Interfacing neurons with nanoelectronics : from silicon nanowires to carbon devices

Farida Veliev

Farida Veliev. Interfacing neurons with nanoelectronics : from silicon nanowires to carbon devices. Materials. Université Grenoble Alpes, 2016. English. NNT : 2016GREAI001 . tel-01281637

Communauté
UNIVERSITÉ Grenoble Alpes

THÈSE

Pour obtenir le grade de

DOCTEUR DE LA COMMUNAUTÉ UNIVERSITÉ GRENOBLE ALPES

Spécialité : **Matériaux, Mécanique, Génie-Civil, Electrochimie**

Arrêté ministériel : 7 août 2006

Présentée par

Farida Veliev

Thèse dirigée par **Vincent Bouchiat**
et codirigée par **Cécile Delacour**

préparée au sein **Institut Néel**
et de **I-MEP2**

Interfacing neurons with nanoelectronics: from silicon nanowires to carbon devices

La nanoelectronique pour l'interfacage neuronal: des nanofils de silicium á des dispositifs de carbone

Thèse soutenue publiquement le **28 janvier 2016**,
devant le jury composé de :

M. Marc BLOCK
Professeur, Université Joseph Fourier, Grenoble, Président
M. Andreas OFFENHÄUSSER
Head of the institute, Peter Grünberg Institute, Forschungszentrum Jülich, Rapporteur
M. Sven INGEBRANDT
Professeur, University of Applied Sciences, Zweibrücken, Rapporteur
Mme. Claire WYART
Directeur de recherche, Institut du Cerveau et de la Moëlle Epiniére, Paris, Examinatrice
M. Vincent BOUCHIAT
Directeur de recherche à L'Institut Néel, Directeur de thèse
Mme. Cécile DELACOUR
Chercheur à L'Institut Néel, Co-Directeur de thèse

Acknowledgements

Here I wish to express my sincerest gratitude and appreciation to all the people, who in many ways contributed to this thesis.

In grateful memory, I thank **Franck Omnés** for providing me the opportunity to pursue my PhD thesis at Institut Néel. His catching enthusiasm for biotechnologies was a great motivation for this work.

I owe my deepest gratitude to my supervisor **Cécile Delacour** for giving me the possibility to work on this fascinating research project. I was incredibly fortunate to have the freedom to explore on my own, and at the same time to obtain the unconditional support and guidance when it was required. Thank you for establishing the entire framework of this project and numerous collaborations with biology labs.

I would like to express my sincere gratitude to my advisor **Vincent Bouchiat**, who kindly agreed to accept the supervision of my thesis after the tragic loss of Franck. This thesis would not have been completed in its present form without his scientific advice, insightful discussions and suggestions for experiments and the manuscript. I am most thankful to him for his continuous encouragement and guidance.

It is difficult to find words to express my gratitude to **Anne Briançon-Marjollet**, who conducted numerous neuron cultures on my samples and made this thesis possible. I also thank **Mireille Albrieux** for calcium imaging and patch clamp measurements.

I am grateful to the members of **HYBRID** group for their support, especially Nedjma Bendiab for her kind help in Raman spectroscopy. I would also like to thank Vitto Han, Dipankar Kalita, Alexandre Artaud, Shashank Mathur, Sudipta Dubey, Simone Lisi, Gouthan Nayak, Pauline Ronseaux, Yani Chen and Cornelia Schwarz for being not just super cool colleagues, but also good friends. I was happy, although if not officially, to be a part of this versatile and most awesome research group.

I wish to thank my colleagues from the research group **Wide Bandgap Semiconductors** (SC2G), especially David Eon and Clément Hébert for their support in CVD growth of diamond and carbon nanotubes as well as the fabrication of diamond based microelectrode arrays. I am also grateful to Laurie-Amandine Garçon and Pascal Mailley for their help in electrochemical characterization of microelectrodes.

Many thanks to the members of the research group **Thermodynamics and Biophysics of Small Systems** (TPS). I owe particular thanks to Catherine Villard, Caterina Tomba and Céline Braini for their help in neuron culturing, patterning and imaging, Tiphaine Belloir for her help in patch clamp measurements and calcium imaging, and Antoine Bourrier for graphene growth, development of the experimental set-up, and many helpful discussions.

I would like to thank Cécile Berne, Simon Le-Denmat, Sébastien Pairis, Valerie Reita, Pierre Giroux, David Barral, Graziella Kavaklian, Laurent Cagnon, Philippe David, Emmanuel André and Richard Haetel for their technical support. Special thanks also to **NanoFab** team: Thierry Crozes, Sébastien Dufresnes, Bruno Fernandez, Gwénaelle Julie, Jean-francois Motte and Thierry Fournier. Without their help I would not have been able to complete this thesis.

I also thank Florence Pois, Sabine Gadal, Louise Infuso and Christine Martinelli for their help in all administrative procedures.

Many thanks to all the awesome people I met at Institut Néel, who made my stay in Grenoble unforgettable and who I can call my friends now: Sven Rohr, Anja Backen, John Landers, Dipankar Kalita, Yani Chen, Cornelia Schwarz, Vitto Han, Katrin Zimmermann, Johanna Seidemann, Joachim Schönle, Tobias Bautze, Iza Petrykiewicz, Kitti Ratter and Sayanti Samadar. Thank you for the great time!

I want to thank my family, who always believed in me and supported my decisions. I am deeply grateful to my father for encouraging my scientific interests and ambitions from the very young age, and I am sad that he did not live to see the day I have obtained the PhD.

At last, I thank my fiancé Hanno Flentje, who despite of his ongoing thesis was always there for me to discuss about my experiments and to cheer me up, when I had hard time on my research. I was extremely lucky to find the right person, who shares my way of life and on whom I can completely rely in any situation. I am happy to call myself your wife soon!

Contents

Introduction

In 1780, Italian scientist Luigi Galvani demonstrated that it was possible to activate the motor nerves connected to a frog's leg muscles by introducing a small electrical current, revealing for the first time the electrochemical nature of body functions. This fascinating finding unleashed the scientific curiosity and conducted an emerging study of nervous system, leading to the discovery of neurons and their electrical activity. Since then, the technological progress brought neurosciences to a fully new level, allowing real-time monitoring of brain activity with few to single neuron resolution, and revealing the possibility to translate the brain activity into easily processable electrical signals, which gave rise to development of brain-machine interfaces (BMI) and neuroprosthetics. At the same time, the ongoing miniaturization of sensing devices enabled the detection of single neuron activity with unprecedented spatial resolution.

Building on this progress, transnational research initiatives, such as *Human Brain Initiative* in EU (2013) and *BRAIN Initiative* in the USA (2013), were founded to promote the development of new technologies, theoretical models and computational methods for a deeper understanding of fundamental brain functions and disorders, such as Alzheimer's and Parkinson's diseases, depression and brain injuries. One of the declared objectives of these initiatives is to build a detailed brain activity map, reaching from the activity of large brain regions to single neuron signaling. In this context, the development of nanoscale sensor devices would provide the spatial resolution required for the understanding of signal processing in neural networks on a sub-cellular level.

On the other hand, a particular interest is devoted to the realization of long lasting neural interfaces for neuroprosthetics, deep brain stimulation electrodes for patients with epilepsy, and brain-machine interfaces to help paralyzed people to lead more independent lives by being able to control external robotic devices using brains electrical signals. However, despite the remarkable development in the last ten years, the breakthrough of bioelectronics is constrained by the performance of currently available sensor devices. Thus new electrically active materials with high neural affinity are evaluated for a seamless integration into the nervous system and a reliable long-term performance.

In this work, we address both fundamental issues. For a better understanding of signal initiation, processing and transmission in defined neuronal networks, we focused on the improving of the spatial resolution of electrical recordings using 100 nm wide silicon-nanowire field effect transistors (SiNW-FETs). For long-term neural interfacing we considered two possible materials: graphene and nanocrystalline diamond. While diamond based microelectrodes and SiNW-FETs were fabricated and electrically characterized in this work, the main focus was set on the realization and evaluation of graphene based field effect transistors for bioelectrical interfacing with neurons.

This thesis is organized as follows:

In **Chapter 1**, we will introduce the general concepts of bioelectrical interfacing for recording and stimulation of neural activity. First the organization of nervous system and the generation of neural signals in large brain areas and single neurons will be presented. Then the state-of-the-art technologies for electrical detection of these signals and their limitations will be discussed. Finally, we will propose possible solutions to overcome some of the issues of existing neural interfaces.

Chapter 2 highlights the main motivation of using synthetic nanocrystalline diamond for neural interfacing, and presents the realization of all-diamond microelectrode arrays, including the synthesis of intrinsic and doped nanocrystalline diamond films and the fabrication flow. Also the possibility to improve the performance of diamond microelectrodes using carbon nanotube coatings will be discussed.

In **Chapter 3**, we will first present the transistor technology for detection of neural activity and then focus on silicon nanowire field effect transistors (SiNW-FETs). We will highlight the specific advantages of top-down fabricated silicon nanowires, detail the fabrication process and present the electrical characterization.

Chapter 4 focuses on graphene based field effect transistors (G-FETs). Based on the unique crystal structure of graphene, we will reveal its outstanding physical and electrical properties, which make it a promising material for highly sensitive biosensors. Here, we will present the synthesis and characterization of large scale monolayer graphene sheets, detail the fabrication flow and demonstrate the electrical characterization of G-FETs in liquid environment. Moreover, we will show the suitability of our G-FETs to detect small potential pulses, similar to biological signals, and evaluate their performance in combination with biocoatings and long-term neuron cultures.

Chapter 5 presents an extensive biocompatibility study of different materials and reveals the outstanding neural affinity of pristine graphene. This chapter also describes the methods used for culturing and imaging of primary hippocampal neurons, and presents the techniques for in-vitro patterning of defined neural networks.

Chapter 6 focuses on the detection of the activity of cultured neurons. First the recordings of neuronal activity using conventional techniques, such as patch clamp and calcium imaging, will be demonstrated. Then the electrical recordings of neuronal activity obtained using SiNW- and G-FETs will be presented and discussed.

A general conclusion and perspectives will be given in **Chapter 7**.

CHAPTER 1

Bioelectrical Interfacing

In this chapter we will present the concepts of bioelectrical interfacing. After a general introduction of mechanisms underlying the generation of electrical signals in neurons, we will discuss the sensor requirements for long lasting reliable recordings of neural activity in cultures and in living organisms, and present the state-of-the-art technologies for bioelectrical interfacing. Also the principles and the main limitations of brain-machine-interfaces will be explained.

1.1 Neuronal organization and signaling

Nervous system is a complex network, consisting of nerve bundles and neurons, that coordinates all body functions and transmits signals from one body part to another. In vertebrates it consists of two components: the central nervous system (CNS), composed of brain and spinal cord, and the peripheral nervous system (PNS), including sensory neurons and nerves connected to each other and to CNS. Functionally, the nervous system can be divided in two categories: somatic and autonomic nervous system. The autonomic nervous system regulates the basic involuntary body functions, such as heart beating, blood pressure and gastrointestinal system. The somatic system is represented by nerves that connect the brain and the spinal cord to the muscles and sensory neurons, regulating the voluntary body functions, such as movement, and the processing of sensory information (hearing, sight, touch). The generation of somatic response can be described by a very simple model, consisting of a detector, which detects an environmental stimulus or inner will, transmitter (nerve), which transmits the detected electrical signal to the target, and receiver, which translates the electrical signal into an action or sense. For example, the order to move a limb originates in the brain region responsible for locomotion and is transmitted via nerves to the muscles, resulting in a muscle contraction. The vision on the other hand is the information detected by the photo-active neurons in the retina and transmitted via nerves to the vision center in the brain, where the received electrical code is translated into an image. In this context, eventually lost body functions due to severed nerves or loss of limbs or sensory organs can be partially restored using artificial signal pathways or organs (robotic limbs, retinal implants) connected to the corresponding brain region, as illustrated in Figure 1.1. This concept is known as brain-machine-interface (BMI) and is currently one of the most investigated research areas in neurosciences. Particularly important is hereby a long lasting (chronical) bioelectrical interfacing of the brain tissue with a sensor device.

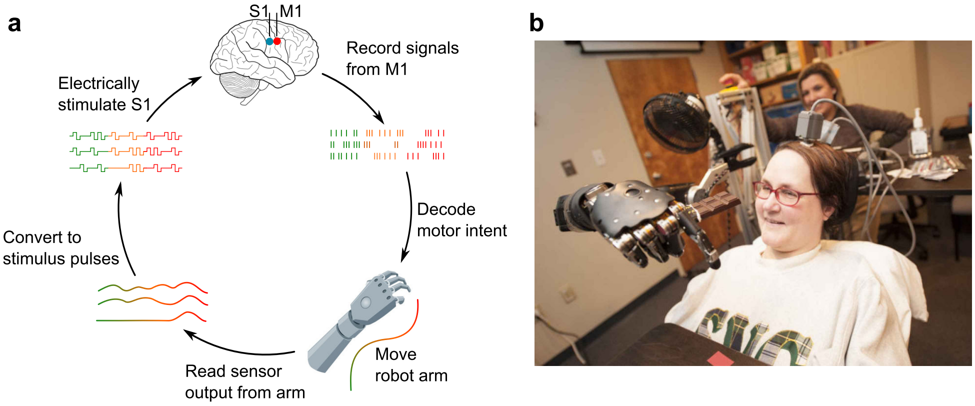

Figure 1.1: Brain-Machine Interface. a) Idealized bidirectional brain-machine interface for neuroprosthetic control. Neuronal signals generated in the motor center in the brain (M1, primary motor cortex) are transmitted to the robotic arm and decoded into movement. Sensors of the prosthetic limb convey the information about the movement to the sensory center (S1, somatosensory cortex), creating a feeling of touching an abject. Adopted from [1]. b) Patient with tetraplegia controls a robotic arm via implanted array of electrodes [2].

On the cellular level the nervous system consists of neurons, glial cells and nerves. Glia, derived from the Greek word for "glue", represents a collection of specialized cells that mechanically support the neural growth, form the immune system, supply the neurons with nutrients and electrically isolate the neurons from each other [3–5]. They also provide scaffolds for neuronal growth and are involved into the healing process after an injury [6]. Neurons are the electrically excitable cells of nervous system, which receive, process and transmit information. They exhibit a specific morphology, shown in Figure 1.2 a, with a compact cell body called *soma* and thin branched outgrowths called *neurites*. Soma represents the metabolic center of the neuron and contains all typical organelles required for the cell maintenance, including the cell nucleus. The longest neurite, a thin highly branched filament, is the *axon*. The axon transmits the electrical signals, also called *action potentials* (APs), to the target neurons. The branching of the axon allows hereby the communication with several neurons. The axons are usually fragmentary covered with insulating myelin sheaths built by specialized glial cells (Fig. 1.2 a). Since the action potentials can only occur on the free membrane, the signal transmission is faster in myelated axons. Cable-like bundles of long axons build nerves, which connect different body parts to the brain and spinal cord. Shorter outgrowths emerging from the soma, called *dendrites*, receive the signals from other neurons and transmit them to the cell body. The electro-chemical connection between two neurons is called a *synapse*. Once the signal from the emitter neuron arrives at the synapse, certain chemical molecules (neurotransmitters) are released and dock on the membrane of the target neuron, resulting in the initiation of the post-synaptic action potential.

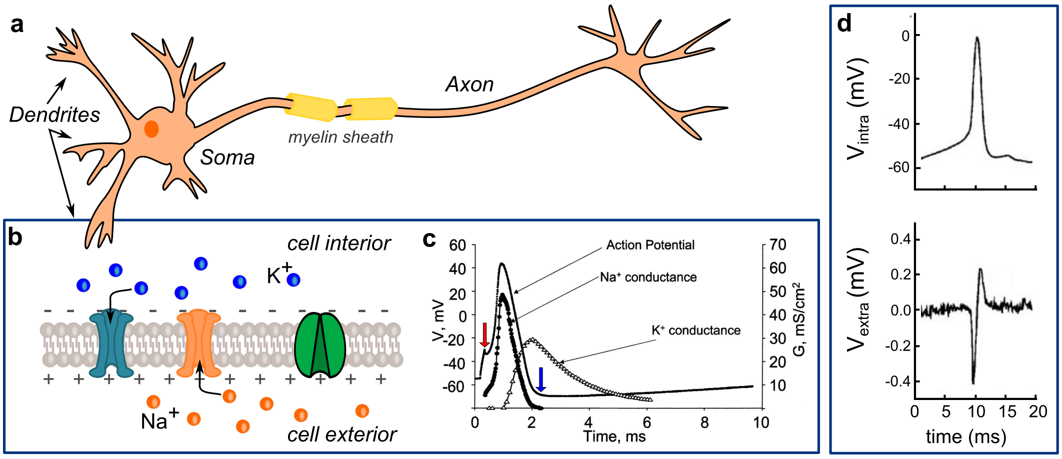

Figure 1.2: Morphology and electrical activity of neurons. a) Schematic illustration of a mammalian neuron with cell body (soma) containing the cell nucleus, axon and dendrites. The axon of adult neurons is fragmentary isolated by myelin sheaths. b) Neuronal membrane containing voltage gated K$^+$ ion (blue) and Na$^+$ ion (orange) channels, as well as K$^+$-Na$^+$ pumps (green). The subsequent opening and closing of the ion channels, once the membrane potentials achieves the threshold value, generates a Na$^+$ ion flux into the cell interior, followed by a K$^+$ ion outflow to the cell exterior. These ionic currents across the cell membrane result in an action potential spikes. The ion pump is then activated to exchange the excess intracellular Na$^+$ ions with extracellular K$^+$. c) Coarse of the membrane potential and the channel conductance of Na$^+$ and K$^+$ ion channels during an action potential. Red arrow indicates the threshold value and blue arrow the afterhyperpolarization. Figure adopted from [7]. d) Intra- and extracellular action potentials measured simultaneously using a patch clamp (intra), and a Si-FET (extra) interfaced to the axon of a leech neuron. Adopted from [8, 9]

The electrical activity of neurons within a certain brain region gives rise to transmembrane currents in the extracellular medium. The current contributions of single neurons superimpose at given location in the extracellular medium and generate a potential difference with respect to a reference potential. This potential gradient across the brain tissue results in an electrical field, which can be detected by extracellularly placed electrodes. Depending on the electrode position, the recorded potentials are called electroencephalogram (EEG), when detected from the scalp, electrocorticogram (ECoG), when recorded from the cortical surface and local field potential (LFP), when recorded with small electrodes inside the brain [10]. Local field potentials are generated through the superimposition of all ionic processes, including fast action potentials, synaptic activity and neuron-glia interactions. The characteristics of the detected collective oscillations, such as amplitude and frequency, depend on the proportional contribution of the multiple sources, the properties of the brain area and the distance of the recording electrode, since the potential amplitude scales with the inverse of the distance from the source. Typically, LFP has a frequency of 10 - 300 Hz and an amplitude of few hundred μV [10, 11].

On a single neuron level, action potential spikes are generated through voltage gated ion channels distributed in the cell membrane (Fig. 1.2 b) [12]. The main contribution comes hereby from positively charged sodium and potassium ions, Na$^+$ and K$^+$, but also calcium ions are involved into the generation of action potentials [12, 13]. The ion channels are gated by the membrane potential V_M of the neuron. At the resting state the membrane potential is in the range of -85 mV to -60 mV, and the ion channels are closed. However an external stimulus can increase V_M to a specific threshold value, resulting in the opening of sodium channels, as illustrated in Figure 1.2 c. When the channels open, Na^+ ions flow inside the cell, which generates a positive intracellular and a negative extracellular potential change (Fig. 1.2 d). The reversed membrane potential results in a closing of sodium channels and activates the potassium channels. The outflow of K^+ ions sets the intra- and extracellular potentials back to the resting state. Once a single AP spike is initiated on a small section of the membrane, it triggers an action potential in the subsequent section, ensuring the signal propagation along the membrane. At the same time a transient negative shift, called the afterhyperpolarization due to additional potassium currents prevents the back-propagation of the signal. After each action potential, sodium-potassium pumps bring Na^+ ions out and K^+ ions back into the cell. In mammalian neurons, the expected amplitude of the extracellular potential spikes is in a range of 100 - 200 µV with occasional signals up to 1 mV [14], and the spike duration is around 1 ms.

In the following we will introduce different approaches for monitoring the neuronal activity, reaching from the recordings of local field potentials to the detection of action potentials at a single neuron level.

1.2 Neuronal activity: From collective oscillations to single action potentials

The recording of neural activity can be divided into various types. Firstly, depending on the recording condition we distinguish between **in-vivo** detection, when the measurements are performed on a living organism, and **in-vitro** detection, when the recordings are performed on isolated brain slices or cultured neurons. Further, depending on the resolution we distinguish between single action potential detection and collective neuronal activity, also called field potentials (EEG, ECoG, LFP). While *in-vivo* action potential detection is currently being evaluated, field potential recordings have been already widely used in humans, as for example ECoG recordings in patients with epilepsy [15]. As already mentioned above, we distinguish among low frequency EEG signals (5 - 300 µV, $<$ 100 Hz), which can be recorded non-invasively from large electrodes placed on the scalp, medium frequency ECoG signals (0.01 - 5 mV, $<$ 200 Hz) recorded using electrodes placed directly on the brain surface, LFP ($<$ 1 mV, $<$ 200 Hz) and action potentials ($<$ 500 µV, 0.1 - 7 kHz), which can be detected using penetrating electrodes [15] (Fig. 1.3).

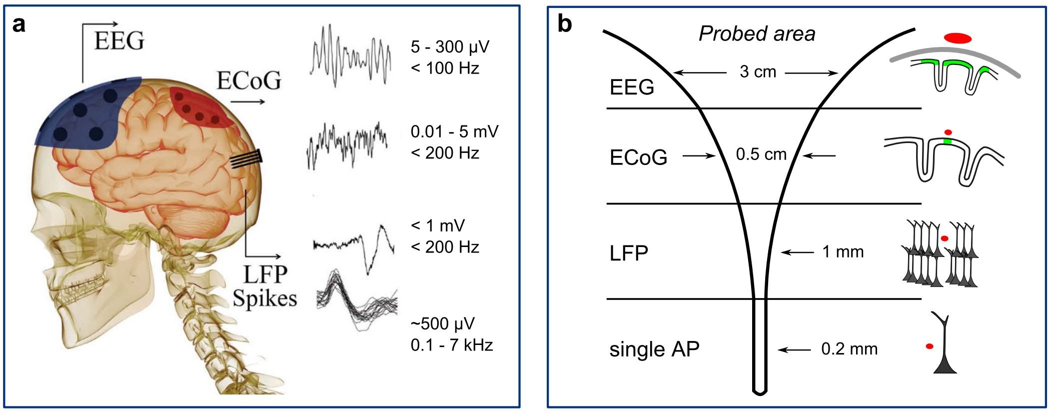

Figure 1.3: *In-vivo* detection of neuronal field potentials and single spike events. a) Schematic of sensor position with corresponding neural signals and their properties. Adopted from [15]. b) Spatial resolution of different detection techniques: EEG electrode (red circle) in a distance of around 2 cm above the cortex averages brain activity over 3 cm spatial extend (green area), ECoG electrodes exhibit a spatial resolution $<$ 5 mm, and penetrating electrodes sample even smaller areas of neural tissue, resulting in a higher spatial resolution. Adopted from [16].

Despite of their non-invasiveness and the partial success in paralyzed human patients, EEG recordings suffer under limited signal bandwidth due to scalp filtering, unstable sensor contacts, multiple wiring and high electrical noise due to the complex instrumentation. On the other hand, due to the closer proximity to the cortex ECoG recordings can provide low noise signals with higher bandwidth. However ECoG electrodes are not available for long term neural interfaces yet, and are currently used only for short term implantation, for example in patients with epilepsy. Recording EEG and ECoG signals provides a general information about the neural activity of certain brain areas. However due to overlapping of different signals it is difficult to extract a specific information, which is usually hold by a small number of neurons in form of single potential spikes. For example, complex hand movements in 3D space are created by the activity of around 50 neurons in the motor cortex [17, 18]. Signals from such a small neural populations easily vanish within the EEG/ECoG activity. Thus penetrating electrodes with high spatial resolution are used to record the spikes and field potentials from a small number of neurons. Although penetrating electrodes were successfully used for movement restoration [2, 19, 20], their long term implantation is critical due to the inflammatory response of the brain tissue, which will be discussed in more detail later in Chapter 1.4.

Single neuron recordings provide more specific information on membrane voltage, postsynaptic potentials, and potential spikes with high temporal and spatial resolution (up to single ion channel), and are widely used in fundamental research to monitor the information processing and the response of the neurons to various environmental stimuli. The action potentials can be detected either inside (**intracellular**) or outside the cell (**extracellular** recording). While the intracellular signal is very high (up to 80 mV) and consequently easier to detect, the recordings are performed inside the cell, and thus, despite the high signal-to-noise ratio, this recording method damages the cell membrane, allowing only short term measurements, and results unavoidably in cell death. Currently, several research groups work on less invasive intracellular recordings using topographically modified microelectrode arrays, which allow a very close contact to the cell without a permanent membrane damage [21, 22]. In contrast, the extracellular recordings are non-invasive, making extended *in-vivo* and *in-vitro* studies possible. However, the extracellular signal, which resembles the time derivative of the intracellular action potential [12], is two orders of magnitude lower (V_{extra} = few 100 μV), and thus more difficult to detect.
Although single spikes can be separated from *in-vivo* recordings using penetrating electrodes, single unit recordings are usually performed *in-vitro* on cultured or isolated neurons, which allows a better control over neuronal network size and external stimuli.

As we see, various types of neuronal signals exist, such as EEG, ECoG, LFP, as well as single intra- and extracellular spikes. Depending on the research interest, these signals can be monitored *in-vivo* or *in-vitro* using adapted sensor devices. In the following we will discus the interest of neuronal recordings in cultured neural networks or brain slices, and the specific sensor requirements for chronical implantation and *in-vitro* monitoring of neural activity.

1.3 In-vitro neuronal models for neuroscience

Currently existing *in-vivo* recording techniques, such as EEG/ECoG, fMRI (functional magnetic resonance imaging) or positron emission tomography, provide a practical tool to monitor whole brain activity, reveal the role of specific brain regions in various body functions and help to understand neurological disorders. However the detected signal represents a low bandwidth superimposition of the activity of large neuron populations with a relatively low information density. To increase the spatial and temporal resolution penetrating implants with small recording sites can be used (Utah array, Michigan array). Despite the small electrode size, the recorded signal usually originates from several neurons and spike sorting algorithms must be used to separate the detected spikes to the level of a single neuron. While penetrating electrodes allow localized recordings from specific brain areas, such as motor or visual cortex, their application in neuroscience is limited due to the highly invasive nature of the recordings. Additionally, due to the complex three-dimensional (3D) inter-connectivity of neurons in the brain, a detailed study of signal processing, synaptic connections and neuron physiology is impossible in *in-vivo* conditions.

On the other hand, brain slices and small neural networks cultured on an array of sensing devices offer a unique tool for studying fundamental concepts of neuroscience. Usually planar microelectrode arrays (MEAs, see Chapter 1.5.1), containing a large number of small recording electrodes, are used to electrically interface the cultured neurons and to record their activity [23–28]. Compared to *in-vivo* experiments, *in-vitro* recordings provide a fast and cheap platform to perform complex pharmacological studies in controlled environments. Thus cultured neuron populations and brain slices are commonly used to monitor information processing in defined neural networks [25–27], to model and understand neurological diseases (stroke, epilepsy, schizophrenia) [29–32], and to investigate the learning process and memory development [28]. Learning in neurons is associated with improved synaptic connections, leading to an increased response to the "learned" stimulus. For example, random neuron networks grown on a MEA could be "taught" to recognize a specific stimulation pattern. As shown in Figure 1.4 a, after a training period (learning) with repeated L pattern stimulation, the neurons were able to distinguish this pattern, showing a higher firing rate (number of action potential spikes due to the stimulus) [28]. Moreover, neuron populations cultured on MEAs can maintain their electrical activity for periods up to 1 year [33], allowing long-term studies of neuronal development, adaptation and synaptic plasticity.

Using neuron cultures it is also possible to model the interplay of different brain regions by growing the corresponding neuron populations (for example cortical and thalamic neurons) on the same recording MEA, but in separate chambers connected through microfluidic channels, as illustrated in Figure 1.4 c. This basic *in-vitro* model of brain connectivity provides a simple tool to investigate the sub-circuitry of the brain and to reveal the role of different brain regions and neuron populations [26, 27].

Compared to the brain tissue, *in-vitro* neuron cultures considerably reduce the number of synaptic connections and restrict the networks to a two-dimensional (2D) surface providing an easy access to specific neurons. Yet, in random neuron cultures the number of synapses is still very high, and the individual neuronal connections are difficult to identify, hindering the investigations of signal transmission and processing on a few neuron level. This problem can be overcome by defining confined neuronal networks with controlled number of neurons and synaptic connections. Currently different methods, including topographic and chemical patterning, are known to design controlled neural networks *in-vitro* [34]. While in topographic designs physical constrictions are used to control the neuron position and outgrowth, in the chemical confinement techniques the neurons attach and grow along an adhesive polymer patterned on the growth substrate [35]. It was shown, that the spatial confinement is not affecting the electrical excitability of neurons (Fig. 1.4 b) [36]. Thus in combination with a suitable recording system, patterned neural networks provide an exciting platform for a detailed investigation of signal processing and synaptic connectivity (Fig. 1.4 d) [23–25].

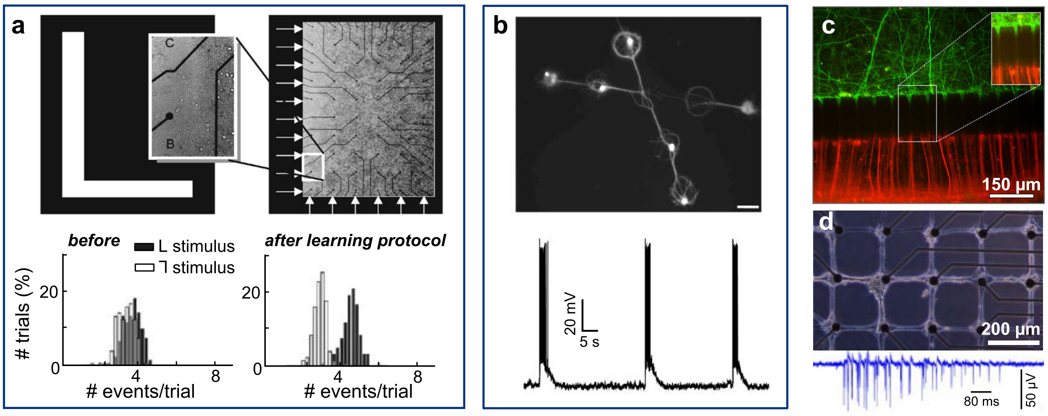

Figure 1.4: Cultured neuron networks. a) Learning of random neural networks. Top image: the outer 10×6 electrodes in L-shape are used to stimulate the neuron population, while other electrodes record the electrical response. Bottom image: after a learning period the response to L-shape stimulation is higher than to the inverted stimulation pattern [28]. b) Neurons confined in a small network still exhibit spontaneous electrical activity (bottom image) [36]. c) Two different neuron populations interconnected through microfluidic channels. [26]. d) Detection of the electrical activity of patterned neural networks [25].

Despite of the utility of neuron cultures, it is important to note, that the neuron properties may alter due to the 2D confinement and missing interconnections to other neuron populations. However despite the difficulty to mimic *in-vivo* neuronal environment, *in-vitro* cultures offer a versatile tool for complex neurological studies.

1.4 Sensor requirements

In contrast to EGG and ECoG electrodes, penetrating brain implants provide the spatial resolution required for a reliable BMI, such as used for restoring motor functions. The stability of the recording however strongly depends on the distance between the electrode and the neurons, since the amplitude of the extracellular potential spike decreases rapidly with the distance to the recording site. This distance is usually further increased by mechanical trauma induced by the electrode insertion and the following foreign body response of the brain tissue. The inflammatory reaction to the implant occurs hereby in two subsequent phases: acute and chronic responses (Fig. 1.5). The acute inflammation is set directly after the implant insertion and is mainly due to the mechanical mismatch of the of the stiff implanted electrode (elastic modulus of ∼ 150 GPa) and the soft brain tissue (∼ 100 kPa) [15]. Due to its stiffness, during the insertion, the electrode damages the neurons and small blood vessels in the brain tissue. In response to this, activated microglia will accumulate at the site of the injury and release various neurotoxic factors to degrade the cellular debris. After 6-8 days of implantation most of the dead tissue around the inserted electrode will be processed by microglia. However since the acute response usually causes neuronal death, only few neurons can be found within 100 µm distance from the electrode, as shown in Figure 1.5 c. Usually it takes around 4-6 months for neurons to grow closer to the implant.

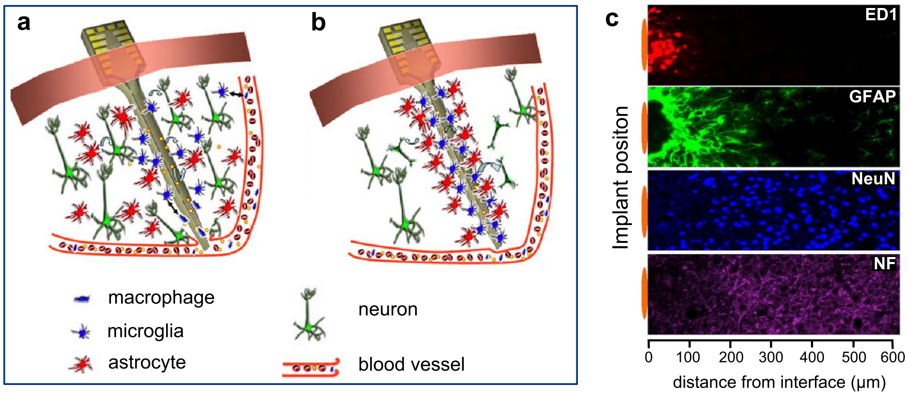

Figure 1.5: Inflammatory response of the brain tissue to inserted implants. a) Schematic illustration of the acute response, characterized by accumulation of activated microglia and reactive astrocytes around the injury, and b) chronical inflammatory response, characterized by condensed sheath of cells around the inserted electrode (from [16]). c) Immunoreactivity images obtained using cell-type specific markers at the electrode/brain tissue interface after 4 weeks long implantation. Foreign body response is characterized by the minimally overlapping inflammatory (ED1) and astrocytic (GFAP) phenotypes at the electrode interface. The inflammation area contains a reduced number of cell bodies (NeuN) and a loss of neurofilament (NF) (from [37]).

After the acute inflammation declines, chronic response is initiated. It is characterized by the presence of reactive astrocytes and activated microglia, which colonize the implant surface and try to degrade and finally remove the foreign material. Since the degradation of the implant is not achieved, the individual cells form a glial scar around the implant as a protection from further injuries, which encapsulates the electrode and deteriorates the electrical recording. The inflammatory response and the long-term viability of chronical implants are well described in several studies [38–41].

The mechanical mismatch leading to the massive inflammatory response can be improved using flexible electrodes. However a stiff sacrificial support is needed to enable the implantation (for example biodegradable polymers). While compared to stiff implants, flexible electrodes have a significantly lower stiffness of around 5 GPa, an optimal neural interface should have an elastic modulus close to that of the brain tissue. A sufficiently soft intermediate layer at the electrode/tissue interface could be realized for example by using synthetic hydrogels [15].

On the other hand, the foreign body response is also partially due to the low biocompatibility of the used electrode materials. While the implant geometry, including the electrode size, tip shape and cross-sectional area, as well as the rigidity and the surface roughness strongly affect the acute tissue response and the wound healing process, it was demonstrated that they have no significant influence on the formation of glial scars. Using biocompatible materials, which promote neuronal adhesion and growth, could prevent the formation of a glial scar and improve the electrical coupling between the device and the tissue.

Another important requirements for a long-term implantation are chemical and mechanical stability, and stable electrical performance. While electrically stable *in-vivo* recordings up to 18 months were reported using microwire arrays, for the majority of implants the stable recording period is significantly shorter [15].

To summarize, a chronical implant should be small to minimize brain injury and have a large number of small sized recording electrodes. To reach the required few neuron resolution, the electrode size should be comparable to that of a neuron with a diameter of $\sim$30 µm. Ideally only biocompatible materials should be used for the implant fabrication, and the recording electrodes should be integrated onto a flexible substrate and exhibit high electrical, mechanical and chemical stability in biological environments.

The requirements are less strict for *in-vitro* recording platforms. Here the inflammatory response is not a limiting factor and thus the sensor rigidity is not as important. However the biocompatibility of the used materials may play a role, since it affects the neural adhesion and thus the electrical coupling between the device and the cell. *In-vitro* biosensors should offer a long-term non-invasive recordings of single action potentials with high spatial/temporal resolution and high signal-to-noise ratio. Thus their performance is mainly characterized by the electrode size required for the subcellular recordings of neural activity (recording site $\ll$ neuron size), and the strength of the electrical coupling, which is primarily given by the physical distance between the cell and the device.

1.5 Bioelectrical interfacing: State-of-the-art

Currently, bioelectrical interfacing and in particular the realization of brain-machine-interfaces for restoration of lost body functions, attracts a growing interest in the scientific community. For example, several research groups investigate the possibility to restore the locomotion in paralyzed patients and amputees. Due to severed nerve pathways, the signals from the brain of a paralyzed human are not able to reach the muscles. A system, which can electrically detect the brain signal and transmit it to a stimulation electrode in the muscles would bypass the severed nerve and trigger the desired movement. Alternatively, the brain signal can be transmitted to a robotic arm or prosthetic limb. Most prominent projects on BMI for movement restoration are conducted by the group of J. P. Donoghue at Brown University (USA), and the groups of S. Micera and G. Courtine at Ecole Polytechnique Fédérale de Lausanne (EPFL, Switzerland). While the BrainGate project at the Brown University addresses the possibility to facilitate the daily routine of paralyzed patients by using mind controlled robotic arms [19, 20], the researchers at EPFL design neuroelectrical circuits to restore the locomotion after a spinal cord injury (NEUWalk project) [42] and develop neuroprosthetic limbs with sensory feedback, allowing the amputees not only to move the artificial limb, but also feel the texture of touched objects [43].

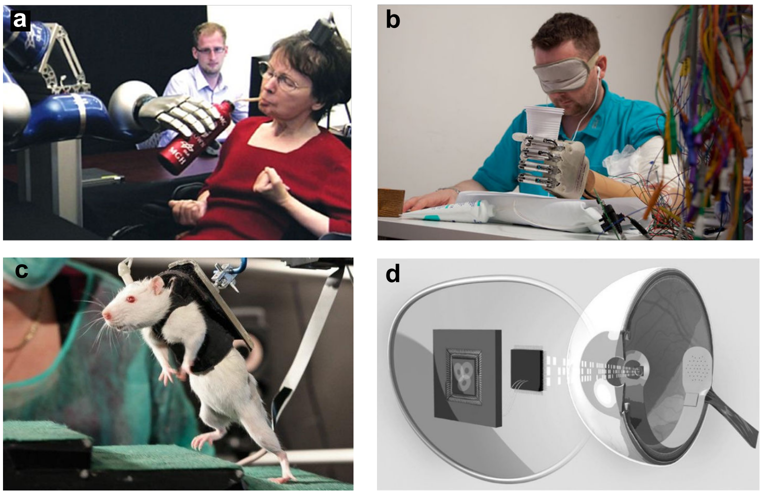

Figure 1.6: Neuro-engineered solutions for locomotion and vision restoration. a) Paralyzed women controls a robotic arm [20]. b) Bionic hand with sensory feedback [43]. c) Restoration of locomotion in a rat with severed spinal cord [42]. d) System for vision restoration consisting of a visual processor on the eye glass and a retinal stimulation array inside the eye [44].

Major efforts are also devoted to restoration of vision in blind and injured patients. The vision occurs as follows: the optics of the eye projects an image on the inner cellular layer (retina), composed of photosensitive cells and neurons (retinal ganglion). The incident light initiates an electro-chemical reaction and triggers a neuronal signal, which is sent to the visual cortex via the optic nerve. In the visual cortex the retinal signal is then translated back into the initial image. Depending on the location and the extend of the injury, different approaches for vision restoration are investigated. For example, if the optic nerve is damaged, the visual cortex can be stimulated using a camera via implanted electrodes [45]. Total or partial blindness can also occur due to a retinal degeneration. This however does not affect signal transmission from the retinal ganglion cells to the visual cortex [46]. Thus the remaining ganglion cells can be electrically stimulated using retinal implants. The stimulating electrodes are usually integrated on a soft flexible polymer support and connected to a camera, which receives and transmits the incoming light signal to the stimulating sites. One such device, the Argus II retinal implant with 60 stimulating electrodes, commercially available from Second Sight (USA), has been shown to improve reading [47] in patients with profound vision loss, and to partially restore the motion detection [48] in blind patient. Recently a subretinal implant (Alpha IMS) containing 1500 embedded photodiodes and corresponding stimulating electrodes was reported [49]. Here, the point-to-point stimulation bypasses the need of an external camera and increases the visual resolution.

In-vivo neural recordings for brain-machine interfaces as described above require the detection/stimulation of neural activity with few to single cell resolution. For single cell addressing, currently two main sensor types exist: microelectrode (ME) and field effect transistor (FET) arrays, which are also used for high resolution neuronal monitoring in cultures. During the electrical activity of the cell, the ions which cross the cell membrane give rise to the extracellular current I_{extra}. This current spreads across the cleft (a naturally formed gap between the cell and the surface of the recording device) with resistance R_{cleft}, resulting in a potential difference V_{extra} with respect to the bath solution. This voltage difference can be measured between the microelectrode in contact with the cell and the reference electrode immersed into the bath solution. Here, the extracellular potential change leads to a charge transfer at the electrode surface, resulting in a small capacitive/faradaic current through the microelectrode. The performance of recording electrodes is typically characterized by their impedance at 1 kHz ($\sim$ frequency of action potentials). For field effect transistors, the interfaced neuron acts as a gate and the extracellular potential modulates the conductivity of the transistor channel through changing the charge carrier concentration. This conductance change can be easily detected by recording the net current through the FET channel at a constant bias voltage. The detected current change depends hereby on the transconductance of the device. For both ME and FET, the detection quality is mainly given by the cleft resistance. Higher R_{cleft} values result in a higher extracellular potential and increased signal-to-noise ratio. The cleft resistance can be improved by a closer neuron/device coupling. A simplified electrical circuit for both detection techniques is shown in Figure 1.7. A more detailed description of the detection mechanism for ME arrays and FETs can be found in Chapter 2.1 and Chapter 3.1 respectively.

Although a remarkable progress in bioelectrical interfacing was achieved in last decades, the performance of commercially available biosensors is still limited for example due to the poor biocompatibility of implant materials, electrical stability issues or low spatial resolution. Thus biosensors are still under ongoing development exploiting new materials to improve their performance. Recent developments of microelectrode and FET technologies will be presented below.

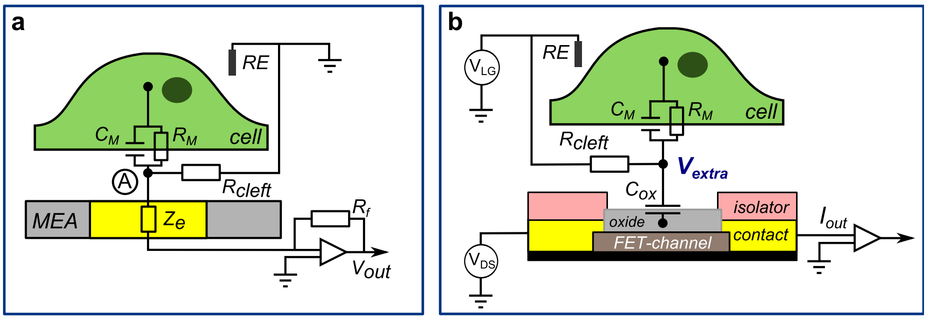

Figure 1.7: Cell/sensor electrical coupling. a) A simplified equivalent circuit of the ME/neuron coupling. The cell membrane is characterized by the membrane potential V_M, capacitance C_M and resistance R_M. The microelectrode is described by the electrode impedance Z_e. RE indicates the reference electrode in the bath solution, and R_{cleft} the cleft resistance. The measured current is amplified using a current to voltage converter with a feedback resistance R_f. Figure reproduced from [50] with modifications. b) A simplified equivalent circuit of the FET/neuron electrical coupling. A constant DC bias voltage V_{DS} is applied to transistor, and the transistor working point is set through the bath potential at the reference electrode RE. The extracellular potential V_{extra} modulates the measured current I_{out} through the transistor channel via gate oxide capacitance C_{ox} (reproduced from [51] with modifications).

1.5.1 Microelectrode Arrays

Microelectrode arrays are by far the most commonly used biosensors in clinical and fundamental research. Since their first realization [52], a large amount of research has been conducted to improve the performance of MEAs, and with nearly 40 years of development, the MEA has been already successfully commercialized and is distributed with different designs and active electrode materials by for example MultiChannelSystems (Germany), Panasonic (Japan), and Ayanda Biosystems (USA). MEA consist of a high number of individually addressable small conductive electrodes with a typical diameter of 10 - 50 µm. The electrodes are usually realized using noble metals (Pt and Au) or metal alloys (for example Pt/Ir) patterned on an insulating substrate (SiO_2, polymers). However due to the foreign body response of the brain tissue to the implant, currently other electrode materials with higher neuronal affinity, such as diamond, graphene or soft conductive polymers are investigated [15].

The variety of existing microelectrode arrays can be briefly divided into implantable MEAs and *in-vitro* MEAs. Implantable electrodes are used for short term investigations of the brain activity and long-term implantation, such as in case of BMI or deep brain stimulation. The most prominent examples of implantable MEAs are metallic microwire arrays, silicon based penetrating electrode arrays (Utah array and Michigan electrodes) and flexible MEAs. Microwire arrays consist of up to 100 thin coated metallic wires (tungsten, stainless steel, Pt, Pt/Ir) with diameters of 20 - 50 µm embedded in a polymers support [15]. The neural recording occurs through the non-insulating wire tip. Silicon based penetrating electrode arrays can be divided into two main types: Michigan electrodes with multiple recording sites arranged along a flattened shank (Fig. 1.8 a, b), and Utah electrode arrays composed of conducting needle electrodes with exposed tips for recording (Fig. 1.8 c). Utah arrays were for example successfully used for BMI in paralyzed patients, allowing them to control a robotic arm [2, 20]. Finally, the flexible MEAs are realized by patterning conductive electrodes on parylene [53], polyimide [54, 55], benzocyclobutene [56], or biodegradable silk tissue [57]. Commonly planar flexible MEAs are used for superficial interfacing of the cortex [57], retina [58], spinal cord [59], or individual peripheral nerves [43]. However efforts are conducted towards flexible soft MEAs for subcortical implantation [56, 60], which would alleviate the injury and the foreign body response due to the mechanical mismatch.

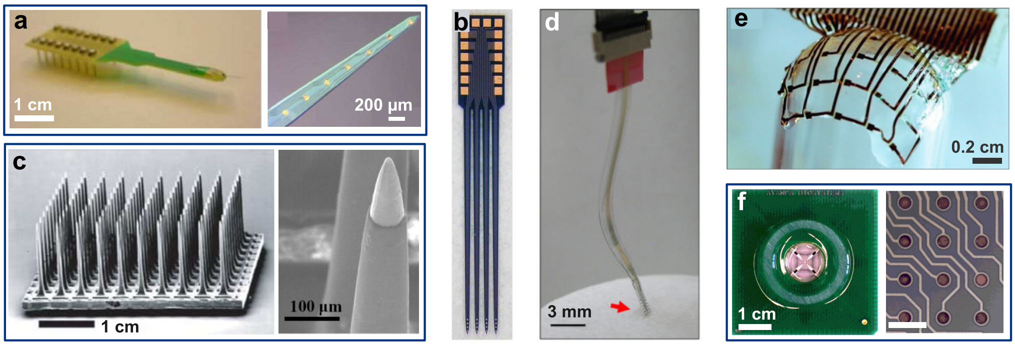

Figure 1.8: Diffrent types of MEAs. a) Eight-channel silicon substrate Michigan type electrode with multiple recording sites [61]. b) An array of Michigan electrodes [62]. c) Silicon based Utah array with 100 metallized recording electrodes [19]. Zoomed view of the exposed tip [63]. d) Penetrating flexible electrode [60] e) Flexible MEA patterned on a biodegradable silk tissue [57]. f) Planar *in-vitro* MEA [64]. Scale bar in the zoomed image is 100 µm.

In implantable MEA technology, the current research focus lays in the development of stable electrode/tissue interfaces with reduced chronical inflammatory response. Integrating highly biocompatible electrode materials, such as graphene [65, 66], conductive polymers [67, 68] or nanocrystalline diamond, on flexible platforms seems to provide a potential solution for chronical implants. A detailed review of different biomaterials currently used for neural interfaces is given by R. Fattahi et al. [15].

In this context, diamond appears as promising candidate [69–73] due to its chemical inertness, mechanical stability, and biocompatibility. The possibility to tune the electrical conductivity of synthetic diamond from insulating to metallic by changing the doping concentration, allows the fabrication of all-diamond biocompatible MEAs with doped diamond for active electrodes and intrinsic diamond films for the insulating layer/substrate. Despite the natural hardness of diamond, nanocrystalline diamond films are compatible with soft flexible electronics [74, 75], including planar MEAs with potential use as retinal implants [72, 76, 77] and flexible penetrating electrodes with multiple recording sites for brain implantation [78, 79], as shown in Figure 1.8 a, b. Considerable progress of diamond based biosensors was recently made at Diamond Sensors

Laboratory in Gif-sur-Yvette, France. For example, using carbon nanotubes (CNTs) grown on the electrode surface and subsequently encapsulated in a boron-doped diamond film by chemical vapor deposition, the researchers could drastically improve the electrode performance [80] (Fig. 1.8 d).

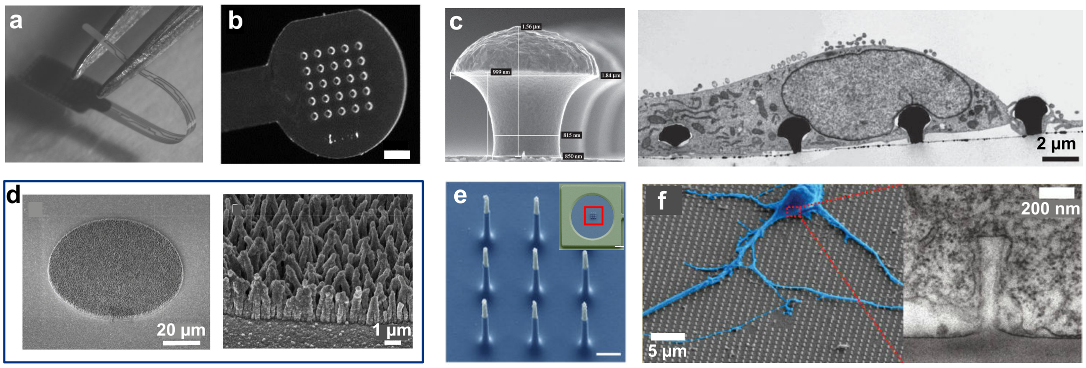

Figure 1.9: Diffrent types of MEAs. a) Flexible diamond MEA [81] (electrode length 5 cm). b) 3-D diamond electrodes patterned on flexible polyimide substrate for retinal implantation [77]. Scale bar 100 µm. c) Spine-shaped gold protrusions on the microelectrode surface to improve the adherence and electrical coupling of neurons to the electrode with corresponding transmission microscopy image of cell/electrode interface [21]. d) Planar diamond microelectrode covered with 3D nanocrystalline diamond [80] e) Vertical silicon nanowire array [22]. Scale bar 1 µm. f) Transmission microscopy image of cell/nanopillar interface [82].

In-vitro MEAs are usually used for pharmacological studies on cultured neurons, brain slices and other electrogenic cells. For example, the effect of various chemical substances with excitation or inhibition properties has been shown using MEAs, including neurotransmitters (dopamine) [83], different receptor antagonists [84–86] and ethanol [87]. Other examples include the drug-induced cardiotoxicity studies [88] and the response of ganglion cells to different electrical stimuli to asses the rehabilitation of retinal diseases [89]. Non-invasive planar microelectrode arrays are also used for long-term recording of the activity of neuron cultures [90] and the signal transmission between different neural networks [91].

The main limitation of ME performance is the relatively high impedance, which makes it difficult to detect small extracellular potentials. The impedance scales with the reverse of the electrode surface. However increasing the planar surface would reduce the spatial resolution. Thus the commonly used solution is a 3D modification of the electrode surface, such as shown in Figure 1.8 d. The effective electrode surface can be increased by adding for example platinum black [92] or CNTs [93]. Another approach is to improve the signal-to-noise ratio by recording the higher intracellular potential. For this, the electrodes are loaded with small vertical electrodes, which partly penetrate the cell membrane. Spine shaped protrusions [21] or vertical silicon nanowires with metallized tips [22] were shown to reliably detect the intracellular action potentials.

Despite the major performance improvements in recent years, the spatial resolution of conventional microelectrodes still remains limited. Due to the impedance scaling, reducing the electrode dimensions would drastically decrease the device sensitivity and hinder the detection of small potential changes, such as neural spikes.

1.5.2 Field Effect Transistors

In contrast to microelectrodes, field effect transistors exhibit a significant potential for miniaturization since their sensitivity (transconductance) merely depends on the width-to-length ratio (see Chapter 3.1, Equation 3.2). The first recording from living tissue using a transistor device was performed in 1976 by Bergveld et al. [94], who measured the electrical signals from muscle fibers. The next landmark in using FET technology for bioelectrical interfaces was set by Fromherz et al. in 1991 by changing the detected biological object from tissue to a single cell [95]. After this pioneering experiment, the mutual interaction of cell/transistor hybrid devices was broadly investigated by several research groups.

Usually arrays of field effect transistors are fabricated on selectively doped single crystalline silicon wafers. The mature silicon technology allows hereby large scale fabrication of FETs with varying dimensions (down to nanoscale) and reproducible electrical properties. While Si based FET technology has been already extensively studied, recently more biocompatible materials, such as graphene, are attracting a growing interest for bioelectrical interfacing [96]. In the following we will introduce the current development of silicon based transistors, including silicon nanowire technology, and graphene FETs.

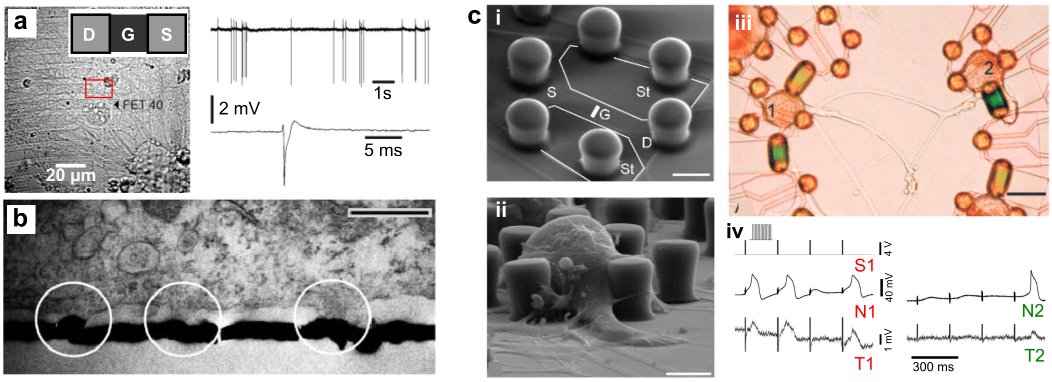

Figure 1.10: FET/Neuron coupling. a) Left image: Hippocampal neurons cultured for 25 day on an array of 6×7 µm^2 field effect transistors. The inset shows a schematic of an individual FET with source (S) and drain (D) electrodes and the transistor channel gated by the neuron (G). Right image: Transistor recordings of neural activity spikes. From [14]. b) Transmission microscopy image of cell/device interface, showing a ~100 nm cleft. Scale bar 1 µm. From [97]. c) Detection of signal transmission in small neural network: i) polyimide fence is patterned to trap neurons above the FET (ii) and form small neural networks. (iii)Two synaptically connected neurons. iv) Signal transmission between two snail neurons. Left panel represents the signals of neuron 1: stimulation voltage bursts (S1), intracellular voltage (N1), and extracellular voltage on the transistor (T1). On the right are the signals of the postsynaptic neuron 2: intracellular voltage (N2) and extracellular voltage (T2), revealing the data transmission from the first neuron. Scale bar 20 µm in (i), (ii), and 50 µm in (iii). From [98].

A large amount of research on silicon based FETs for cell interfacing was conducted by P.

Fromherz (Max Plank Institut Munich, Germany) with significant contributions from A. Offenhausser (Forschungszentrum Jülich, Germany) and S. Ingebrandt (University of Applied Sciences Kaiserslautern, Germany). After the first detection of electrical activity from leech neurons [95], recordings from individual mammalian neurons [14, 51], cardiac muscle cells (cardiomyocytes and HL1 line cells) [99, 100] and human embryonic kidney (HEK) cells [101, 102] followed. The cell/transistor coupling was characterized by its physical and electrical interfaces. Fluorescence interferometry [103, 104] and transmission electron microscopy [97] were used to asses the physical coupling of cells to the underlying sensor device, revealing the existence of a 50 - 100 nm gap at the cell/device interface, which is commonly referred to as *cleft* (Fig. 1.10 b). From the variety of detected voltage waveforms, an elaborate model of the ionic current, which flows through the cleft during neural activity and modulates the transistor signal, was developed [8, 105]. Moreover, signal transmission in small patterned neuronal networks could be monitored using silicon FETs [98, 106] (Fig. 1.10 c).

The further development of the planar silicon FETs is represented by the realization of transistor needle chips [107] (Fig. 1.11 a) for potential *in-vivo* applications and the implementation of high-density multitransistor arrays (MTA) by extended complementary metal–oxide–semiconductor (CMOS) technology [108] (Fig. 1.11 b). Multitransistor arrays (MTA) with 128×128 individually addressable transistors packed on 1 mm^2 chip surface were used for mapping the electrical activity of individual snail neurons and small neural networks with a spatial resolution of 7.8 µm [109]. Later MTA recordings were also applied to brain slices to obtain detailed maps of field potentials with high temporal and spatial resolution [110], as shown in Figure 1.11 c.

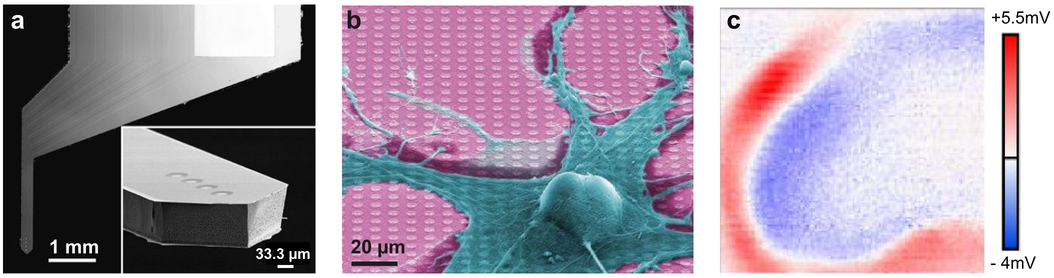

Figure 1.11: Versatile integration of silicon FETs. a) Scanning electron micrograph of a transistor needle chip with four transistors [107]. b) Neuron interfaced to multitransistor array (MTA) containing 128×128 on 1 mm^2 with 7.8 µm pixel size [108]. c) 1×1 mm^2 activity map of a hippocampus slice *in-vitro* obtained using MTA shown in b [110].

The spatial resolution of the recordings depends on the sensor size. The dimensions of silicon transistors presented above vary from 22×24 µm^2 to 2×8 µm^2 [14, 51, 100, 102], already allowing the detection of neural activity with single cell resolution. However, as mentioned above, the miniaturization of transistors does not affect their sensitivity. Thus the spatial resolution could be further improved by employing silicon nanowires (SiNW). Additionally, the sensitivity of SiNWs increases due to their high surface-to-volume ratio.

SiNW-FETs offer the sensitivity and temporospatial resolution required for monitoring the neuronal activity at a subcellular level. First demonstration of the detection and stimulation of neural activity using SiNW-FETs was provided by the research group of C. M. Lieber (Haward, USA) in 2006 [111]. In the same study, the propagation of a single action potential along the axon and dendrite was recorded using a high-density SiNW-FET array, composed of bottom-up[1] grown silicon nanowires with diameters of <100 nm and inter-device spacing of 50 µm (Fig. 1.12 a). Same research group demonstrated the integration of SiNW-FETs on polymer substrates for flexible electrical recordings from cardiomyocytes [113], and realization of kinked selectively doped silicon nanowires on a flexible device support for minimally invasive intracellular recordings with few hundred nm resolution [114] (Fig. 1.12 b).

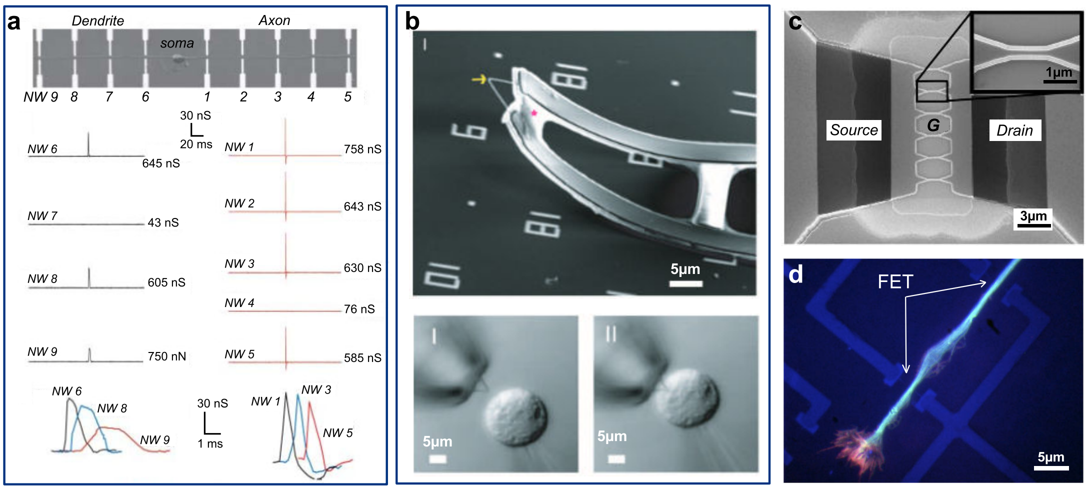

Figure 1.12: SiNW-FETs for bioelectrical interfacing. a) Nanowire recordings of action potentials progagating along the axon and the dendrite of a single hippocampal neuron [111]. b) Kinked silicon nanowire probe for intracellular recording of cell activity [114]. c) Top-down fabricated SiNW-FETs [115]. d) Neuronal guidance above the nanowires using adhesive patterning [116].

While bottom-up grown nanowires exhibit the required electrical properties for interfacing single electrogenic cells, their processing and exact positioning on a support substrate remains challenging. Top-down[2] fabricated silicon nanowires, on the other hand, exhibit similar electrical performance [115, 117] and offer large scale integration on silicon-on-insulator substrates and controlled positioning and scaling of FET devices. Their suitability for electrophysiological measurements was demonstrated by electrical recordings of the spontaneous activity of cardiac muscle cells (HL-1 line cells) with an improved signal-to-noise ratio compared to planar silicon transistors [99]. Additionally, combining different SiNW-FET arrangements, which are easily realized by top-down fabrication techniques, with neuronal patterning using adhesive polymers (see Chapter 5.1.3) would provide a versatile platform for monitoring neural activity in defined

---

[1] In the **bottom-up** approach, vertically aligned nanowires are grown using chemical vapor deposition [112] and then dispersed on a support substrate for further processing.

[2] In the **top-down** approach, the nanowires are formed by etching the single crystalline silicon layer using a hard mask defined by e-beam lithography or nanoimprint technique [115, 117].

networks [116].

Regarding the chronical implantation, silicon based sensors exhibit several issues, such as rigidity, which damages the surrounding tissue, poor biocompatibility and stability issues in biological environments. Thus alternative semiconductor materials for electrical interfacing with cells are investigated. Among them, graphene attracts the greatest attention [96, 118]. Graphene is a single layer of carbon atoms organized in a honey-comb structure. Large size single layer graphene sheets of high crystalline quality can be currently obtained on copper foils using chemical vapor deposition (CVD) technique [119–121] and transferred onto a variety of rigid substrates and soft flexible polymers. Based on its unique properties, including chemical inertness [122], elasticity [123], outstanding electrical properties [124] and biocompatibility [65], graphene is believed to be an excellent candidate for the realization of long term neural interfaces. Furthermore, graphene FETs (G-FETs) do not require any gate oxide for liquid operation in cell interfacing applications. Due to the high capacitance of the extremely thin electric double layer (EDL, see Chapter 4.3) [125], which forms at the graphene/liquid interface, even small potential changes result in a significant conductance modulation of graphene, making G-FEts to extremely sensitive potential sensors. Table 1.1 summarizes the electrical properties of different materials proposed for bioelectronic applications and reveals the superior performance of graphene based transistors due to the high mobility and high interfacial capacitance of EDL [126]. As shown the sensitivity of graphene based FETs exceeds the performance of conventional semiconductor materials by one order of magnitude.

Table 1.1: Properties of filed effect transistors prepared using different material systems, which have been proposed for bioelectrical applications (adopted from [126]).

Material	Mobility (cm^2/Vs)	Interfacial Capacitance ($\mu F/cm^2$)	Sensitivity (mS/V)	Biocompatibility	Flexibility
Silicon	450	0.35	0.20	0	0
Diamond	120	2	0.29	+	-
AlGaN/GaN	1200	0.32	0.51	+	-
Graphene	4000	2	5	+	+

First demonstration of the ability of G-FETs to electrically interface with cells was provided by the research group of C. M. Lieber in 2010 [127], followed by J. A. Garrido (Max Plank Institut Munich, Germany) in 2011 [128]. In these studies G-FETs were used to detect signals from cardiomyocytes and HL-1 cell lines respectively. However, electrical recordings from neurons using G-FETs are not reported yet.

1.5.3 Other techniques

Commercially available MEAs are well established tools for neurophysiological studies on cultured neuronal networks. However due to their low spatial resolution (pitch > 30 µm) and limited electrode size (typically less than 300) due to the connectivity problems, passive MEAs are not suitable for single cell monitoring. Recently, a new approach was developed to overcome these issues by implementing complementary metal-oxide-semiconductor technology [108, 129–131]. Here the connectivity problem is solved by integrating the circuitry on the same substrate as the recording electrodes and using electronic switches to asses shared signal wires. Thus, thousands of electrodes can be closely packed on a small detecting area, allowing high resolution mapping of neuronal activity. Moreover, since the signals are amplified and filtered close to the signal source, the detection quality is improved due to the elimination of the additional noise from the cables. By combining MEA and CMOS technologies, a new class of biosensors arose: high density microelectrode arrays (HD-MEAs). Among others, significant contribution to development of HD-MEAs for neuronal interfacing was made by the research group of A. Hierlemann (EHT Zurich, Shwitzerland), who realized high-resolution platforms for mapping neural activity at subcellular, cellular and network levels, allowing spatial tracking of action potentials [132] and even an exact reconstruction of neural architecture on the basis on electrical recordings [133], as shown in Figure 1.13 a. Here, the recording electrode size was around 9×5 µm^2 with center to center pitch of 17.5 µm. CMOS technology is compatible with both microelectrode arrays and field effect transistors [108–110], building a powerful tool for *in-vitro* tracking of signal propagation in complex neural networks.

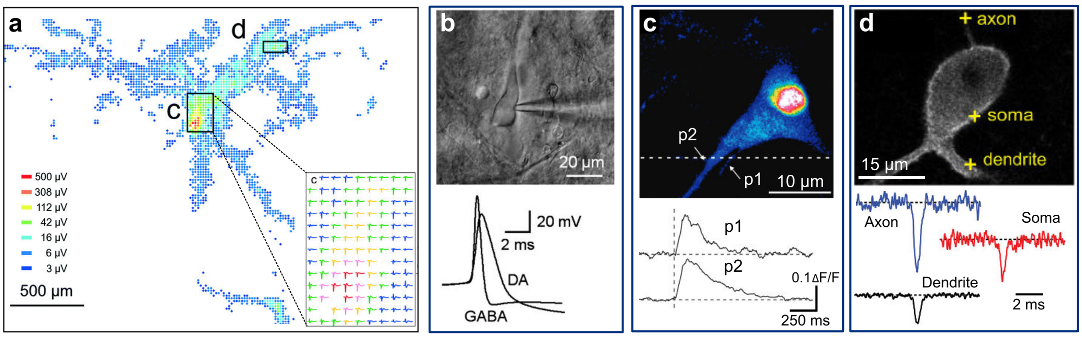

Figure 1.13: Other techniques for monitoring neural activity. a) Neural architecture reconstruction using electrical recordings from a CMOS-MEA [133]. b) Example of patch clamp detection of action potentials in different neuron types [134]. c) Map of Ca^{2+} ion concentration in a neuron (top), and calcium spiking at different positions (bottom) obtained using calcium imaging technique [135]. d) Voltage-sensitive dye imaging provides fast localized detection of action potentials [136].

Other commonly used techniques in neurophysiology are patch clamp recordings and optical imaging of neuronal activity. In the patch clamp method, a small patch of membrane is electrically isolated from the external solution, and the current through the patch is measured using a thin glass pipette filled with a suitable electrolyte solution. Depending on the pipette dimensions, the isolated patch may contain only few or even a single ionic channel, providing unitary information of cell activity [137, 138]. Compared to relatively big conventional microelectrodes, patch clamp technique provides a higher spatial resolution and allows the monitoring of single cells and cell compartments, which are too small for electrical recordings with MEs. However, only one measurement at a time is possible, which makes patch recordings inconvenient for monitoring neuronal network activity and signal propagation. An example of intracellular potentials spike

measured using patch clamp method is shown in Figure 1.13 b.
Optical recording of neural activity includes calcium and voltage-sensitive dye imaging (Fig. 1.13 c, d). Calcium imaging technique is based on the great impact of Ca^{2+} ions on the neuronal activity, including the generation of action potentials and neurotransmitter release [139–141]. Thus the electrical activity of neurons can be monitored by imaging the intracellular Ca^{2+} ion concentration both *in-vivo* and *in-vitro*. The principles of calcium imaging and its recent development are well reviewed by Grienberger et al. [142]: briefly, the neurons are loaded with calcium indicators, which respond to binding of Ca^{2+} ions by changing their fluorescence properties. This fluorescence signal can be simultaneously detected from hundred to thousands of neurons while keeping track on the activity of each neuron individually. However due to the slow ion diffusion dynamics and saturation effects of calcium indicators, fast membrane potential changes are difficult to detect. The temporal resolution of optical recordings was significantly improved by using voltage-sensitive dye imaging (VDSI). Here the dye molecules bind to the membrane of the neurons without interrupting their normal functions and transform the variation of the membrane potential directly into a measurable fluorescence signal [143, 144], providing a high resolution mapping of neuronal activity with submillisecond precision [136]. The dye can be applied *in-vitro*, *in-vivo* and *in-utero* (at the embryonic stage in the womb). Recently a variety of different organic and genetically modified fluorescence proteins exist, allowing the recording of specific neuron population without background signals from other cell classes [144, 145].
Patch clamp recordings and calcium imaging were also used in this work to assess the spontaneous activity of cultured neurons (see Chapter 6.1).

1.5.4 Conclusion

As discussed above, commercially available neural implants exhibit several issues, such as rigidity, which damages the brain tissue, poor biocompatibility, resulting in the encapsulation of the electrodes by glial scar, and stability issues in biological environment. Thus special efforts are devoted to implementation of biocompatible electrode materials for chronical implantation. Ideally these materials should also provide chemical and electrical stability in biological surroundings and the compatibility with soft flexible platforms. These requirements are well met by CVD grown nanocrystalline diamond films and graphene. Due to its tunable conductivity nanocrystalline diamond is a suitable candidate for realization of single material biocompatible MEAs for long term neural interfacing. Graphene, on the other hand, can be easily transferred on flexible polymers and used for both ME and FET based bioelectronics.

Compared to ME, FET technology provides a greater potential for miniaturization, allowing electrical recordings of neural activity with sub-cellular resolution. This is especially important for *in-vitro* monitoring of signal propagation within a neural network. In this context, ultra high spatial and temporal resolution can be achieved by using silicon nanowire transistors, which can be readily obtained by standard nanofabrication techniques and are compatible with large scale production.

From this, the motivation of this work was to develop a silicon nanowire based platform for high resolution monitoring of neural network dynamics and to evaluate the potential of nanocrystalline diamond MEAs and graphene based FETs for chronical neural interfaces.

CHAPTER 2

All-Diamond Microelectrode Arrays

In this chapter, we will present all-diamond microelectrode arrays fabricated in this thesis. First we introduce the general principles of MEA technology for the detection of neuronal activity. We discuss the detection mechanisms as well as the major performance limitations and review the recent developments. Then we propose to introduce nanocrystalline diamond as a material to produce microelectrode arrays (D-MEA) for bioelectrical interfacing, followed by the presentation of the growth of intrinsic diamond on Si substrates using chemical vapor deposition (CVD), in-situ boron doping and characterization techniques, in particular Raman microspectroscopy. Then, the fabrication of our all-diamond microelectrode arrays and their possible applications in electro-chemical and electrical detection of neuronal activity will be discussed. Finally we will see how a mechanically stable combination of nanocrystalline diamond with another carbon nanophase (nanotubes) can be realized.

2.1 MEA fundamentals

In MEA technology, conductive electrodes are used for sensing electrical fields associated with the ion dynamics outside the cell during electrical activity. A simplified illustration of the origin of the extracellular potential measured by the electrodes is given in Figure 2.1 a. Neurons interfaced to any kind of devices naturally form an extracellular cleft between the cell membrane and the substrate, to which they adhere. The cleft is filled with ionic solution. During the electrical activity, ions, which cross the cell membrane, give rise to the extracellular current I_{extra}. This current spreads across the cleft with resistance R_{seal}, resulting in the development of a potential difference V_{extra} between the cleft and the bath solution. To detect V_{extra}, a reference electrode with zero potential is immersed into the bath solution and the potential difference across R_{seal} is measured between the electrode in contact with the cell and the reference electrode.

Depending on the electrode material we can distinguish between capacitive (the microelectrode is described only by its capacitance), faradaic (only by its resistance) and pseudocapacitive (by both resistance and capacitance) MEAs (Fig. 2.1 b). The shape of the measured signal will strongly depend on the operation regime.

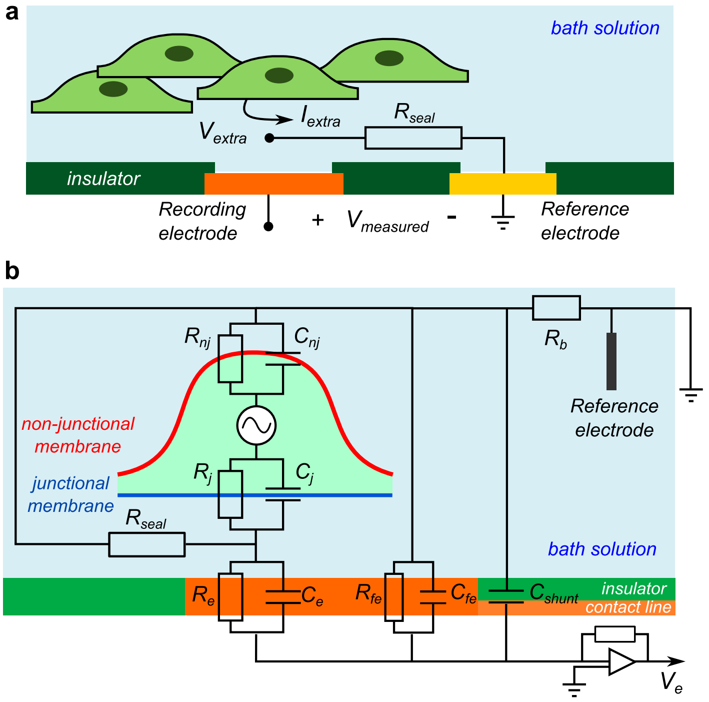

Figure 2.1: Extracellular recordings using microelectrodes. a) Schematic illustration of the origin of the extracellular potential V_{extra} recorded by MEA. Ionic current I_{extra} generated by action potentials flows through the cleft resistance R_{seal}. Local potential V_{extra} accross R_{seal} is measured with respect to a bath reference electrode. b) Equivalent electrical circuit of the neuron/electrode interface (adopted from [146]). The electrode is partially covered by the neuron. The cell body of neuron forms a cleft filled with culture medium above the electrode. The neuron membrane is divided into two parts: junctional membrane with resistance R_j and capacitance C_j facing the electrode, and non-junctional membrane with resistance R_{nj} and capacitance C_{nj} facing the bath. The ionic solution within the cleft generates the seal resistance R_{seal}. The electrode impedance is represented by the resistance R_e and the capacitance C_e for the part covered by the cell, and R_{fe} and C_{fe} for the free electrode area. R_b is the resistance of the bath solution, and C_{shunt} the shunt capacitance. The potential V_e at the electrode is measured versus the reference electrode and amplified.

When recording signals from cells cultured on MEA, individual cells may only partially contact the electrode, as shown in a more complex equivalent circuit model in Figure 2.1 b. The free electrode area is then in contact with the bath solution and connected to ground. The amplifier connected to the conducting line records not only the extracellular potential from the cell, but the sum of the potentials at the surface of the free electrode and the surface covered by the cell, as well as the potential at the contact line. For a capacitive coupling, the fraction of the extracellular potential detected by the electrode is then approximately given by [147]:

$$V_{measured} = \frac{C_e}{C_E + C_{shunt}} \cdot V_{extra} \approx \frac{A_e}{A_E} \cdot V_{extra} \tag{2.1}$$

where C_e is the capacitance of the covered electrode area A_e, C_E the total electrode capacitance with area A_E, and C_{shunt} the shunt capacitance. With $C_{shunt} \ll C_E$, the recorded signal linearly depends on the ratio of the covered electrode surface to the total electrode area.

The amplitude and the shape of the recorded signals are critically affected by the electrical properties of the overall route from the cell membrane to the external amplifier. The recorded signal will strongly depend on the seal resistance, the electrode impedance and the resistance of the junctional membrane. Also, the shunt capacitance as well as the amplifying circuitry may have an effect on the detected signal.

The measured V_{extra} is determined by the current that flows across the seal resistance R_{seal}. The ratio between the extracellular and intracellular voltage V_{extra}/V_{intra} is given by [148, 149]:

$$\frac{V_{extra}}{V_{intra}} \cong \frac{R_{seal}}{R_{seal} + R_j} \tag{2.2}$$

with the resistance of junctional cell membrane R_j. A strong cell-electrode coupling with high seal resistance ($R_{seal} \gg R_j$) will therefore result in a higher amplitude of the detected signal and increased signal-to-noise ratio. Consequently, intensive efforts are dedicated to increase the value of R_{seal} by improving the cell adherence to the sensor [21].

Another important factor affecting the detection, is the input impedance of the sensing electrode. The current induced by the cell is formed by ions in the solution and thus fundamentally different from the electron current in the device. This difference results in the impedance of the device, which is attributed to the "blocking" ion bilayer (referred to as the electric double layer, which will be explained in more detail in Chapter 4.3) formed at the interface to the ionic solution. For example, commercially available planar gold electrodes with a radius of 30 µm have impedances of 50 kΩ at 1 kHz [146]. Ideally, the recording of neural activity should provide a high spatial resolution (electrode size < neuron) and high signal-to-noise ratio (low impedance). However, these two fundamental requirements are conflictive, since reducing the electrode area would inevitably lower the interfacial capacitance and increase the impedance. Thus other approaches to increase the effective sensing surface are investigated. For instance, by using nanostructures such as platinum black [92], gold nanoflakes and nanopillars [150, 151], or carbon nanotubes [93, 152] the surface area can be increased without affecting the spatial resolution.

Also, a reduction of junctional membrane resistance would improve the electrical coupling between the cell and the device. Reducing the membrane resistance to increase the detected signal is commonly used by classical approaches of sharp electrodes or whole-cell patches [137]. Recently, local increases in the membrane conduction by electroporation using vertical nanowire electrode arrays were demonstrated to increase the cell/device coupling, associated with intracellular recording [22]. However these recordings are highly invasive and could induce cell apoptosis.

While MEAs are routinely used by neuroscientists for *in-vitro* investigations, their utilization for long term clinical implants still remains difficult. MEA-based implants already have shown partial success in restoring hearing and vision, treating neural disorders and developing brain-machine interfaces [20, 59, 153, 154]. However, long term performance of such implants remains poor due to their stiffness, poor biocompatibility of used materials and degradation of the electrode performance in the harsh biological environment [38–41, 155]. In this context, nanocrystalline diamond based MEAs compatible with soft/flexible platforms [72, 74, 75] appear as promising candidates due to their high biocompatibility as well as chemical and mechanical stability, which we will discuss below.

2.2 Nanocrystalline diamond microelectrodes for sensing

Microelectrode arrays are powerful devices with a wide range of applications for *in-vivo* and *in-vitro* neuronal interfacing. Among others, a particular research interest lays in the development of long lasting computer brain interfaces. Despite the outstanding electronic properties, such as large injection current, low noise as well as high temporal and spatial resolution, the majority of materials used for MEAs suffer from poor biocompatibility, encapsulation of electrodes by glial scar caused by the inflammatory reaction of the brain tissue, or mechanical/electrical degradation of the electrode material under *in-vivo* conditions [39–41, 155]. In this context, due to its chemical inertness, mechanical stability and biocompatibility, diamond appears as a promising material for the realization of chronical implants [69, 70]. Over the past decades diamond-based electronics have become a topic of great interest. Since the development of CVD synthesis of diamond, doped diamond materials of single-, micro- and nanocrystallinity have been realized for a variety of novel electronic devices [156–163]. The biocompatibility and the wide potential window of these materials make biochemical and biological applications particularly relevant [156, 160–163]. Moreover, the possibility to tune the conductivity from insulating to metallic by simply varying the doping concentration, makes doped diamond a suitable material for MEA fabrication.

Since the first realization of a boron-doped diamond (BDD) MEA in 2002 [164], diamond-based electrodes have been thoroughly developed for electrochemical detection of redox active compounds by cyclic voltammetry [165–168] and increasingly tested for *in-vivo* applications, including flexible implants [72, 79] and the restoration of sensory functions such as in retinal implants [72, 76, 169, 170]. Besides the successful recordings of electrical activity of cardiomyocyte cultures [71], diamond MEAs have been not yet established for extensive use to interface electrically with neurons. Mainly due to the low signal to noise ratio, the electrical recordings with single cell resolution using unmodified diamond electrode surface are challenging.

The signal-to-noise ratio of diamond MEAs can be improved by increasing the effective surface area, for example by simply adding carbon nanotubes (CNTs) on the microelectrode surface, or by growing a thin nanodiamond film above the attached CNTs [80, 171, 172].

2.3 Crystalline and electronic structure of diamond

Carbon is a group IV element in the periodic table with half-filled valence shells. Their electronic configuration is s^2p^2. In diamond these s and p states hybridize to tetrahedral sp^3 directed hybrid bonds and form a body centered cubic structure (bcc, Fig. 2.2 a). This structure has two basis atoms in the primitive cell and represents two inter-penetrating face centered cubic (fcc) sublattices displaced by the translation vector (1/4, 1/4, 1/4).

Carbon atoms arranged in the diamond structure give rise to exceptional properties, such as for example extreme mechanical hardness, highest bulk modulus, highest thermal conductivity and chemical stability [173]. The remarkable performance of diamond arises from the very strong short range covalent bonds of relatively small carbon atoms.

The theoretical band structure calculated by tight-binding Hamiltonian, using sp^3 basis set with first- and some second neighbor interactions [174], is shown in Figure 2.2 b and reveals the good insulating properties of diamond with a large bandgap. The experimentally obtained bandgap is $E_{gap,exp}$ = 5.47 eV [173, 175], which is much higher than the thermal energy (0.025 eV). Diamond is therefore referred to as a wide bandgap material.

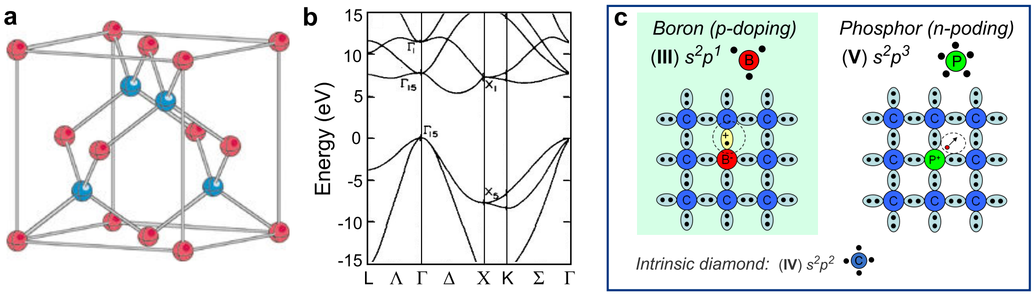

Figure 2.2: Crystalline and electronic structure of diamond. a) Crystallographic unit cell (unit cube) of the diamond structure [175]. b) Bandstructure of diamond [174]. c) Doping of diamond by boron and phosphorous incorporation.

Although intrinsic diamond is an insulating material, its conductivity can be easily tuned to the metallic state by replacing carbon atoms in the diamond crystal by group III (boron, B) or group V (phosphorous, P) elements, which have one electron less or more than carbon respectively (Fig. 2.2 c). This results in an increased concentration of charge carriers (hole or electron) available for conduction, and the introduction of allowed energy states within the band gap. Acceptor atoms, such as boron, form energy levels close to the valence band, donor atoms, group V elements, close to the conductance band. For example, phosphorous-doping results in a n-type conductivity with a donor level 0.56 eV below the conduction band [176].

Due to its lower activation energy, boron has been widely used for obtaining hole-doped *(p-doped)* diamond. Boron doping can be achieved by adding for example diborane to the gas mixture during diamond synthesis, as we will describe in more details in Chapter 2.4.5. The activation energy of the boron acceptor atoms is relatively high, 0.37 eV. However when the doping concentration reaches values higher than 10^{20} cm^{-3}, the conduction mechanism changes and the activation energy approaches zero [177], resulting in a fully metallic behavior.

The tunable conductivity of diamond provides the possibility to realize single material microelectrode arrays by using boron-doped diamond for active electrodes and intrinsic diamond film for electrical insulation.

2.4 Nanocrystalline diamond synthesis and characterization

Synthesis of diamond by chemical vapor deposition (CVD) has been extensively studied by different research groups since the early 1980s [178, 179]. This technique is based on the deposition of carbon atoms dissociated from a carbon-containing gas precursor on a solid substrate. The substrate can be either bulk diamond or a non-diamond material, such as silicon. While using bulk diamond allows the synthesis of single crystalline films, the latter case results in polycrystalline diamond layers. Since the fabrication and proper performance of MEAs does not require a high crystallinity, diamond films used in this work were grown on low cost silicon substrates. However, diamond does not grow spontaneously on non-diamond substrates and its deposition on foreign substrates requires an extra nucleation step. In this step, the substrate surface is covered with diamond seeds. The following deposition of carbon atoms leads to a 3 dimensional growth of seeds into diamond grains until they merge in a continuous diamond film. The nucleation density hereby determines the final crystallinity level of the diamond layer reaching from ultrananocrystalline at high nucleation density to microcrystalline at lower nucleation density. Several nucleation techniques are reported in the literature, such as **mechanical abrasion** [180] of the substrate with a diamond grit resulting in diamond residuals in the scratched grooves, which act as seeds for diamond growth, **nanoseeding** [181], where a suspension of nanodiamond powder is deposited on the substrate by ultrasonic treatment, and **bias enhanced nucleation** [182]. The latter one was also used in this work and will be explained in the following in more detail.

2.4.1 Chemical vapor deposition set-up

Diamond films used for the fabrication of MEAs were grown by plasma-enhanced CVD technique using carbon species (CH_4) mixed in low concentration with hydrogen. Since neutral molecules do not contribute to the growth, a plasma is used to produce highly reactive atomic hydrogen and hydrocarbon radicals involved in the diamond synthesis. In our set-up, the plasma is generated by a microwave discharge (Microwave Plasma CVD, MPCVD), which has a number of advantages over the other methods. Microwave deposition is an electrodeless process and avoids therefore the contamination of the film due to electrode erosion. Microwave discharge at 2.45 GHz produces a plasma with electrons with higher energy than RF plasma (13.5 MHz), and generates more atomic radicals involved in the diamond growth. Additionally, the plasma is confined into a plasma ball at the center of the deposition chamber, preventing carbon deposition on the chamber walls. A schematic view of the growth chamber is shown in Figure 2.3 a. Two different growth chambers were used: a SEKI (Seki Technotron, AX 5200), which allows in-situ nucleation, and a NIRIM type MPCVD for the growth of doped diamond films.

2.4.2 Mechanism of CVD diamond growth

Despite the simple methane/hydrogen gas mixture in the growth chamber, a number of molecules, ions and radicals are generated by the plasma and impinge on the substrate surface. Hydrocarbon concentration measurements during diamond growth show that besides methane (CH_4), one

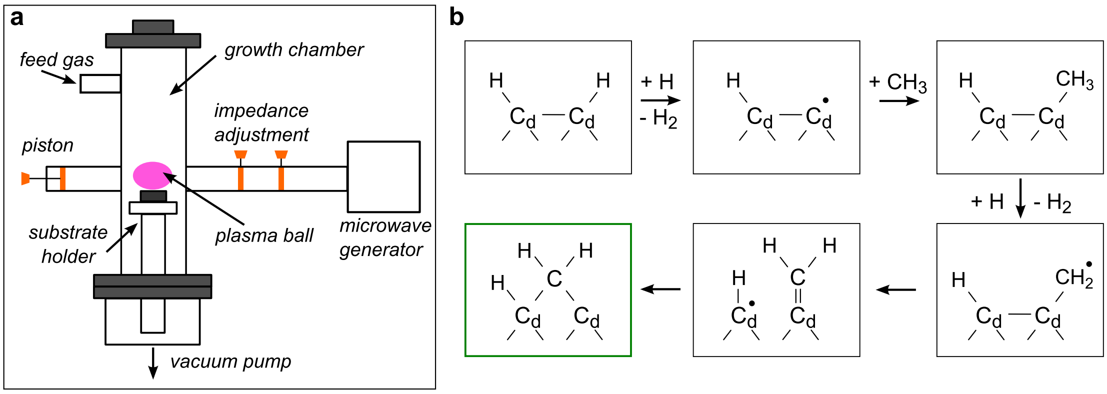

Figure 2.3: Growth of diamond by chemical vapor deposition. a) A schematic view of the growth set-up. b) Diamond growth mechanism [183].

finds acetylene (C_2H_2), methyl radicals $\bullet CH_3$ and a lower concentration of ethylene (C_2H_4) [184, 185]. The distribution of the species depends hereby on their stability. Since the C_2 species are more stable than C_1, reactions such as $C_2H_2 + H_2 \rightarrow C_2H_3 + H$ or $C_2H_2 + H_2 \rightarrow C_2H_4$, require higher energies and are consequently very slow leading to a low concentration. Consequently, only CH_4, $\bullet CH_3$ and C_2H_2 are present in sufficient quantities to play a dominant role in diamond growth.

Also atomic hydrogen radicals, which are directly produced by high temperatures and high energy electrons in the plasma, $H_2 + e^- \rightarrow H + H + e^-$, are crucial for obtaining high quality diamond films. The diamond surface consists of dangling bonds C_d, which need to be terminated to prevent carbon cross-linkage leading to graphite (sp^2 hybridization). The presence of atomic hydrogen is thus needed to prevent graphitic phases to be formed by passivation of dangling bonds and to favor the diamond allotropic phase with respect to the other forms. A model growth mechanism of CVD diamond [183] is presented in Figure 2.3 b.

2.4.3 Bias Enhanced Nucleation

The technique of bias enhanced nucleation (BEN) was pioneered by Yugo et al. [182] and could drastically increase the nucleation density (i.e. number of diamond crystallites per unit area) on non-diamond conductive substrates, such as Si. Due to the high surface energy of diamond and the large lattice mismatch, the spontaneous nucleation of diamond on a Si surface is extremely low (10^4 cm^{-2}). The spontaneous nucleation is due to the development of an interfacial silicon carbide layer (carburisation), which promotes the formation of amorphous carbon islands, and subsequently local areas of sp3-bonding which grow to form nanosized diamond seeds. A negative substrate bias accelerates the deposition of carbon species and increases the nucleation density up to 10^{11} cm^{-2} [186].

In this work, a BEN step was carried out in the same CVD chamber as for intrinsic diamond growth under similar conditions, but prior to the normal deposition. The substrate was first heated to 700°C in hydrogen plasma (285 sccm, P = 1400 W) under 16 torr for 10-20 min to clean the Si surface. Then 15 sccm CH_4 were added to the hydrogen plasma and a pre-bias carburisation step to form a carbide layer on Si surface was performed, followed by applying a negative DC bias (-200 V to -300 V) to the substrate to accelerate positive ions in the plasma toward the substrate. The growth parameters (substrate temperature, pressure and plasma power) were kept constant for all BEN steps. The duration of nucleation was varied to control the nucleation density and the seed size, but in general 20-30 min were enough to obtain a sufficient nucleation density. Typically nucleation densities of 10^{10} cm^{-2} to 10^{11} cm^{-2} were obtained. However, the distribution of diamond seeds was not uniform all over the sample due to the inhomogeneity of the plasma ball.

In-situ diamond film deposition is performed directly after the nucleation by breaking the substrate bias and adjusting the growth parameters (see below).

2.4.4 Intrinsic nanocrystalline diamond: Growth and Characterization

Directly after nucleation, an intrinsic diamond (ID) film can be grown in the same chamber without electrical bias. The typical methane concentration for the growth is 1 % (3 sccm CH_4 in 297 sccm H_2), the pressure is set to 30 torr, plasma power to 1300 W and the measured substrate temperature is around 700°C. For these conditions, the growth rate is around 6-8 nm/min. As discussed above, the diamond film is formed by coalescence of growing diamond grains. The thickness and the crystallinity of the formed diamond layer depends hereby on the nucleation density. As shown in Figure 2.4 a, at higher nucleation densities, diamond grains merge faster, resulting in a thinner film with smaller crystal size. For low nucleation densities, the grains can grow longer without merging, resulting in a higher film thickness with bigger crystals. For the rather dense nucleation used in this work (Fig. 2.4 b), the diamond film thickness would be around 200 nm. However, the continuous deposition results in secondary nucleation of diamond grains and further growth of the film. Since the nucleation density on diamond is very high, the obtained diamond film is nanocrystalline with crystal size < 200 nm. A cross section of the typical nanocristalline diamond layer grown in this work is shown Figure 2.4 c.

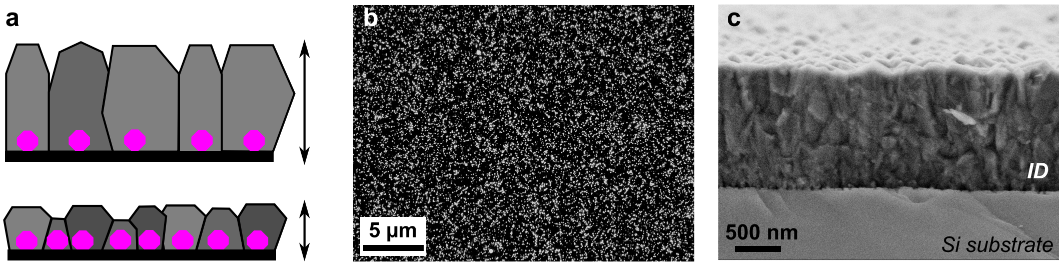

Figure 2.4: CVD growth of diamond on Si substrates. a) A schematic view of the diamond growth on substrates with different nucleation densities (nucleation seed in purple). Higher nucleation density results in thin diamond films with smaller grains. b) SEM image of a Si substrate after nucleation. The nucleation density is around 10^{10} cm^{-2}. c) SEM image of the cross section of nanocrystalline diamond realized in this work, clearly indicating secondary nucleation of diamond grains.

The surface morphology and crystalline structure of the obtained diamond layers were then characterized using scanning electron microscopy and Raman microspectroscopy. Figure 2.5 shows the surface of a typical intrinsic diamond layer with randomly oriented crystals grown in this work. Since the nucleation density is not homogeneous all over the sample (with dimensions 1.6× 1.6 cm^2), sometimes a total merging of diamond grains at the sample edges is not achieved due to the lower nucleation density. However, this is usually observed below 100 μm distance from the sample edge and is not critical for the following chip fabrication.

Depending on the orientation of the crystallites nucleated during BEN, diamond film surfaces with different roughness can be obtained. The diamond nuclei are sometimes oriented with the crystalline structure of the Si wafer [187]. This causes diamond crystals formed during BEN to align with the crystallographic planes of the Si substrate, allowing growth of "oriented" diamond films, as shown in Figure 2.5 c. These diamond films have one particular crystal facet parallel to the substrate surface, and hence can be made very smooth.

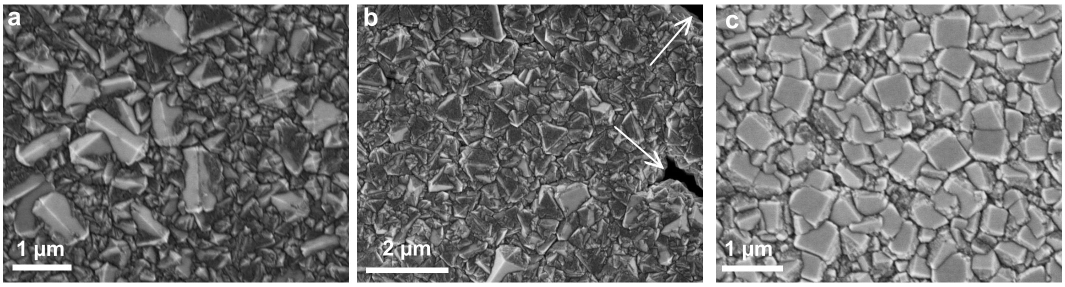

Figure 2.5: Surface of nanocrystalline CVD diamond grown in this work. a) SEM image in the center of the sample. b) SEM image taken on the same sample in 100 μm distance from the edge. c) Polycrystalline diamond film with aligned crystals.

Raman microspectroscopy analysis was then performed in order to assess the crystalline structure of the obtained diamond films. This is a fast and non destructive method, which provides information about specific vibrational modes, and thus the atomic configuration in molecules and solid matter. Raman spectroscopy [188] uses a monochromatic light source (laser) to excite the molecules in the sample and the radiation scattered from the molecule is detected. Unlike infrared absorption, a matching of incident radiation to the energy difference between the ground and excited states is hereby not required. The light interacts with matter and polarizes the electron cloud around the nuclei to form a short lived state (virtual state). This state is unstable and the incident photon is quickly re-radiated.

The majority of the scattered light is of the same frequency as the excitation source. This is known as Rayleigh or elastic scattering, where only the electron cloud distortion is involved in scattering and the photon is scattered with a very small frequency change due to the small mass of electrons. However if a collective nuclear motion (phonon [1]) is induced during the scattering process, energy will be transferred either from the incident photon to the phonon *(Stokes)* or from

---

[1] A phonon is a collective excitation in a periodic, elastic arrangement of atoms or molecules in condensed matter.

the phonon to the scattered photon *(Anti-Stokes Raman inelastic scattering)*, and the energy of the scattered photon will be one vibrational unit different from the incident photon: $\Delta E = \pm h\nu$. At room temperature, Stokes scattering is more probable, because thermal activation leads to a significant phonon population. Since the phonon information is specific to the chemical bonds and the crystal symmetry, Raman spectroscopy is commonly used to identify the crystal structure and to control the crystalline quality.

The Raman "fingerprint" of intrinsic diamond with typical scattering peaks is summarized in Table 2.1 [189]. The quality of the grown diamond film can be assessed by comparing the intensities of the 1332 cm^{-1} peak, which represents the sp^3 hybridization typical for diamond, and peaks corresponding to graphitic sp^2 hybridization (D and G peaks). High quality intrinsic CVD diamond exhibits a high peak at 1332 cm^{-1} and very low D and G peaks at around 1350 cm^{-1} and 1520-1580 cm^{-1}.

Table 2.1: Raman peaks commonly observed in CVD diamond (adopted from [189])

Position cm^{-1}	FWHM cm^{-1}	assignment
1100-1150	40-80	most likely transpolyacetylene at grain boundaries often observed in nanocrystalline CVD diamond films
1332	5-10	first-order diamond Raman line; sp^3 carbon
1345	250	sp^2 amorphous carbon (the D peak)
1430-1470	80	most likely transpolyacetylene at grain boundaries
1520-1580	100	sp^2 amorphous carbon (the G peak)

As shown by Wagner et al. [190], the Raman spectrum strongly depends on the excitation wavelength. Figure 2.6 a demonstrates spectra of polycrystalline CVD grown intrinsic diamond extracted using laser wavelengths from 257 to 1064 nm [190]. UV excitation provides hereby the best detection of the first-order diamond peak. While the fraction of sp^3 hybridization remains unchanged, at longer wavelengths, the sensitivity to non diamond sp^2 bonds increases leading a drastically reduced intensity ratio I(diamond)/I(non-diamond) in the infrared. This trend is even more dramatic for nanocrystalline diamond, where the first order diamond peak is completely invisible for wavelengths longer than UV. The peak intensities vary due to the different resonant efficiency of the laser light with sp^3 and sp^2 carbon species. Raman characterization in this work, was performed at laser wavelength $\lambda = 514$ nm. Typical spectra are shown in Figure 2.6 b, c. As it can be seen, the intensity of the first-order diamond peak depends on the crystallinity of the grown ID layer. While the layer thickness is the same (~ 1 µm), diamond films with larger crystals exhibit a stronger diamond signature. Nonetheless both films can be clearly identified as polycrystalline diamond.

ID films were grown to realize an insulating buffer layer between the conductive p-doped Si substrate and the second doped nanocristalline diamond layer used for fabrication of electrodes. Thus, it is important to characterize their insulating properties. For this, metallic pads were

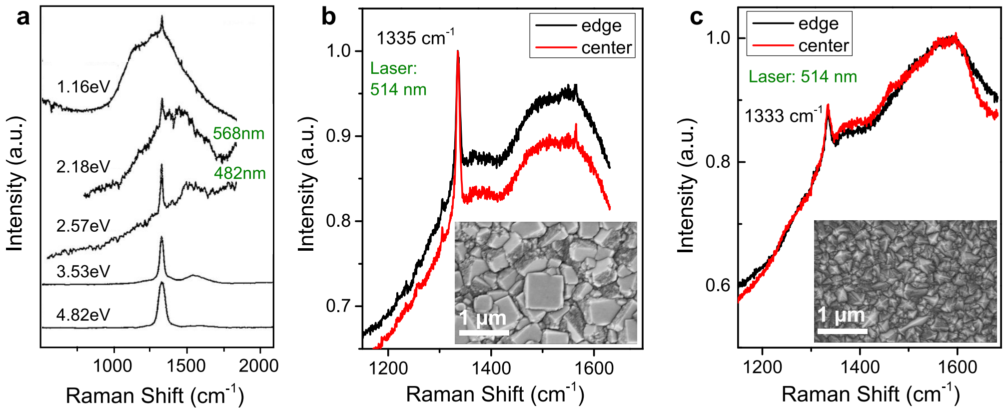

Figure 2.6: Raman spectroscopy of intrinsic polycrystalline CVD diamond. a) Raman spectra of polycrystalline CVD diamond using different excitation wavelength (adopted from [190]). b) Raman spectra of CVD diamond films grown in this work with large and c) small crystals. Excitation wavelength is 514 nm.

defined on the diamond surface using optical lithography and the resistance was measured either between two pads or between the pad and the p-doped Si substrate. All measurements were carried out using a 2 probe technique consisting of a probe station and a Keithley 2100 used in a 2 wire resistance mode. As grown, ID films showed a rather high conductance with resistances less than 2 MΩ both between the pads on the ID surface and from the pad to the substrate (Fig. 2.7 a). This low resistance can be explained by the hydrogenated ID surface during the growth in hydrogen rich plasma. H-atoms bonded to C-atoms of the diamond lattice increase the surface conductivity of the diamond layer. After an ozone treatment of the diamond layer, which suppress the H-bounds, the resistance increases to several GΩ (Fig. 2.7 a). This treatment is performed in oxygen rich atmosphere under high power UV light illumination, which transforms O_2 into highly reactive ozone molecules O_3. For a 1 µm thick ID layer, after UV/ozone treatment 80% of pads have no contact to the substrate.

2.4.5 Boron-doped nanocrystalline diamond: Growth and Characterization

To realize any functional diamond based devices, the used diamond film should be conductive to transmit electrical signals. While intrinsic diamond is an insulating material with a very big bandgap ($E_g = 5.45$ eV), its electrical conductivity can be tuned from insulating to metallic by simply changing the doping concentration. Both doping types, p and n, can be achieved by using boron acceptor- or phosphorous donator-atoms respectively. But due to its low charge carrier activation energy (0.37 eV), boron is by far the most used dopant for conductive diamond films. Boron is introduced into the diamond material during the film growth by adding diborane B_2H_6 to the deposition gas mixture. The toxicity of this gas requires hereby specific safety precautions. Since the boron-doped diamond (BBD) layer was grown on the first intrinsic diamond film, a nucleation step was not required. After a 20 min long cleaning of the sample in a hydrogen rich plasma, methane gas at 1% concentration was added (1.05 sccm CH_4 in 200 sccm H_2). The

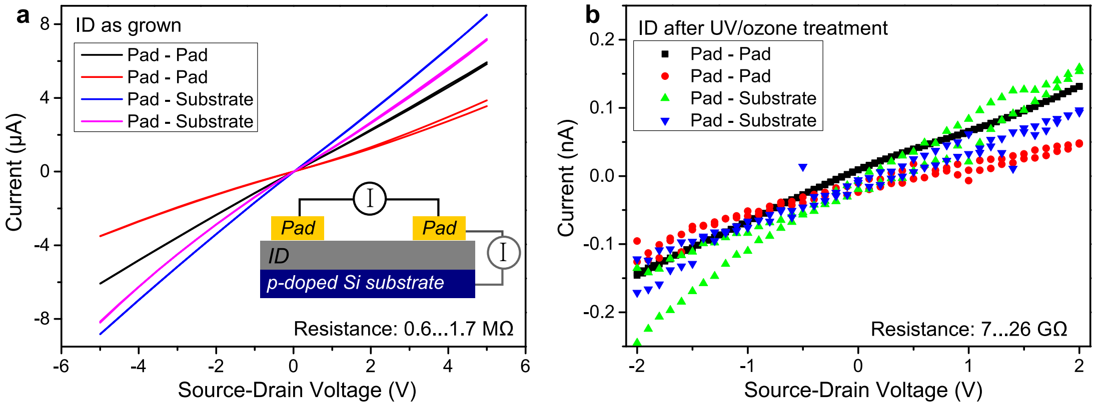

Figure 2.7: Electrical characterization of nanocrystalline ID layer grown on p-doped Si substrate. a) Two point measurement of the resistance of ID layer as grown. As shown in the simplified measurement scheme, the current was measured between two metallic pads on ID surface or between a pad and the Si-substrate by sweeping the source-drain voltage. b) ID layer resistance after UV/ozone treatment. The layer thickness is 1 µm.

growth of doped diamond was carried out at 33 torr pressure and around 280 W plasma power, which heated the sample up to 900°C. According to the previous work at Institut Néel [191], B_2H_6 in concentration $B/C = 5800$ ppm was added to the gas mixture to achieve a doping concentration of $\simeq 2{\cdot}10^{21}$ cm^{-3}. The plasma power was adjusted to reach the required growth temperature and to increase the plasma ball to ensure a homogeneous diamond deposition. The growth time was 3 h to obtain a 1 µm thick BDD layer, and the sample was then treated by a UV/ozone plasma to suppress hydrogen surface bonds. The produced BDD films were characterized in terms of their homogeneity, crystallinity and conductivity. Two probe electrical measurements of an 100 µm wide BDD line result in a resistivity of around $4.4{\cdot}10^{-3}$ Ω.cm. Figure 2.8 shows SEM images and Raman spectra of BDD layers grown at different plasma powers: 300 W and 250 W. The sample size is $1.6{\times}1.6$ cm^2, and the images/spectra were taken at the center and at the edge of each sample. Both SEM and Raman analysis reveal an inhomogeneous deposition of the BBD layer grown at higher plasma power (Fig. 2.8 a). This is due to the fact, that high microwave power produces a plasma ball smaller than the sample, resulting in a poor diamond deposition at the sample edges. Also, Raman spectra of the BBD layers grown at 300 W exhibit a higher sp^2 carbon peak at 1520-1580 cm^{-1}, which increases closer to the edge of the sample confirming poor diamond growth. By reducing the plasma power to 250 W and thus increasing the plasma ball, homogeneous BDD films could be obtained with a reduced amount of sp^2 carbon (Fig. 2.8 b).

Compared to the Raman spectra of intrinsic diamond, increasing the doping concentration leads to significant changes. The first order Raman silicon peak (520 cm^{-1}) disappears as the doped material becomes more opaque at the excitation wavelength, the second order phonon feature from the Si substrate at 1100 cm^{-1} is however still visible in the spectrum. The first order diamond peak shifts to the lower wavenumber (1290 cm^{-1} as indicated in Fig. 2.8 b), and its

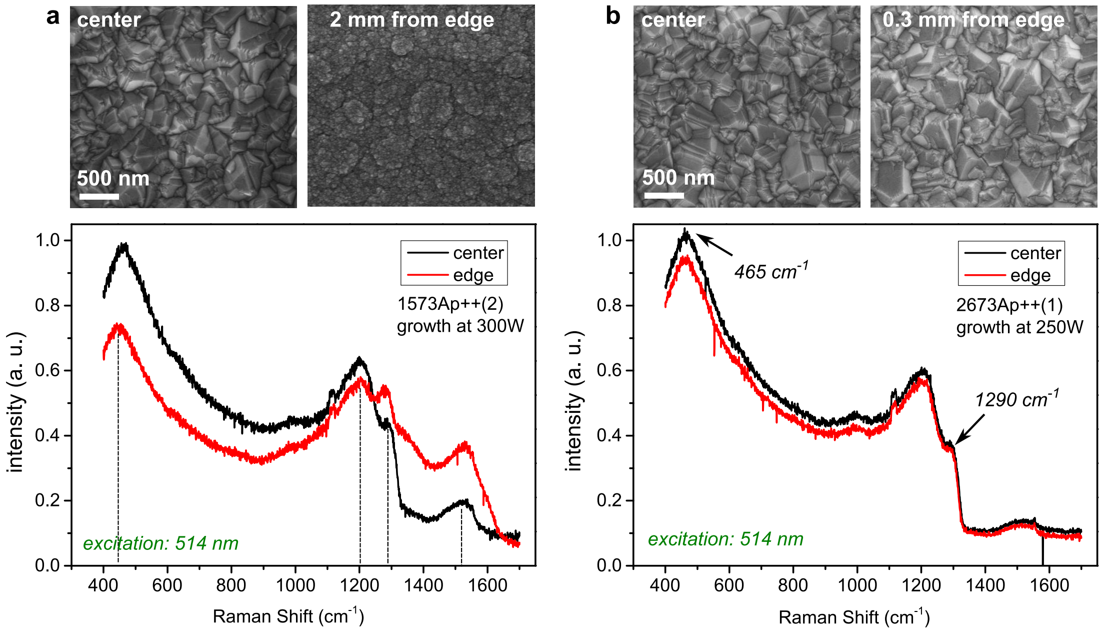

Figure 2.8: Characterization of BDD films grown in this work. a) SEM images and Raman spectra of the center and edge zone of the BDD layer grown on 1.6×1.6 cm^2 ID sample at 300 W microwave power. A very poor crystallinity is observed at the sample edges (∼25% of the sample surface) due to the small plasma ball created by the high microwave power. Typical BDD Raman peaks are indicated by dashed lines. b) SEM and Raman analysis of a homogeneous deposition of BDD obtained by decreasing the microwave power.

intensity decreases. New peaks appear at around 500 cm^{-1} and 1200 cm^{-1} associated with boron incorporation in the diamond lattice [192]. For extremely heavily doped diamond films, Bernard et al. [193] suggested to fit the peak around 500 cm^{-1} with a combination of Gaussian and Lorentzian lineshapes in order to obtain the boron concentration:

$$[B](in\ cm^{-3}) = 8.44 \cdot 10^{30} \cdot e^{-0.048\omega} \tag{2.3}$$

there the wavenumber ω is the center position of the Lorentzian component, which is around 461 cm^{-1} for BDD layers grown in this work. This leads to a boron concentration of $2.1 \cdot 10^{21}$ cm^{-3} as expected. While the original experiment by Bernard et. al. was carried out using a red laser beam (λ = 632 nm), the spectra here are obtained with green laser excitation, which might affect the the position/shape of the peaks. However, it was shown, that by changing the excitation wavelength, the spectral position of the low frequency BDD peak remains unchanged [194], justifying the use of Equation 2.3 for the estimation of the doping concentration.

2.4.6 Conclusion

In conclusion, intrinsic and doped nanocrystalline diamond layers with controlled properties could be produced using the MPCVD technique: 1 µm thick ID films with excellent insulating properties were grown on highly p-doped Si substrates using the BEN technique, followed by deposition of a 1 µm BDD layer. SEM analysis reveals the overall good homogeneity, while Raman spectroscopy exhibits the expected signature for both ID and BDD with with the first diamond peak at 1335 cm^{-1} and 1290 cm^{-1} respectively.

2.5 All-diamond MEA fabrication

For the fabrication of MEAs we use BDD/ID stacks grown on Si substrates. The ID layer is used as an insulating buffer between p-doped Si and BDD, which has a versatile function and will be used to define the active microelectrodes and also the passive leads. Detailed growth and fabrication protocols can be found in Appendix A. The fabrication flow developed by C. Hébert at Institut Néel [195] is presented in Figure 2.9. As shown, the realization of all-diamond MEAs involves 3 main steps: 1) etching of BDD mesa, 2) selective CVD growth of intrinsic diamond to electrically insulate the leads for future liquid operation and 3) the metallization of contact pads and counter electrodes. In the following the individual fabrication steps will be described in more detail.

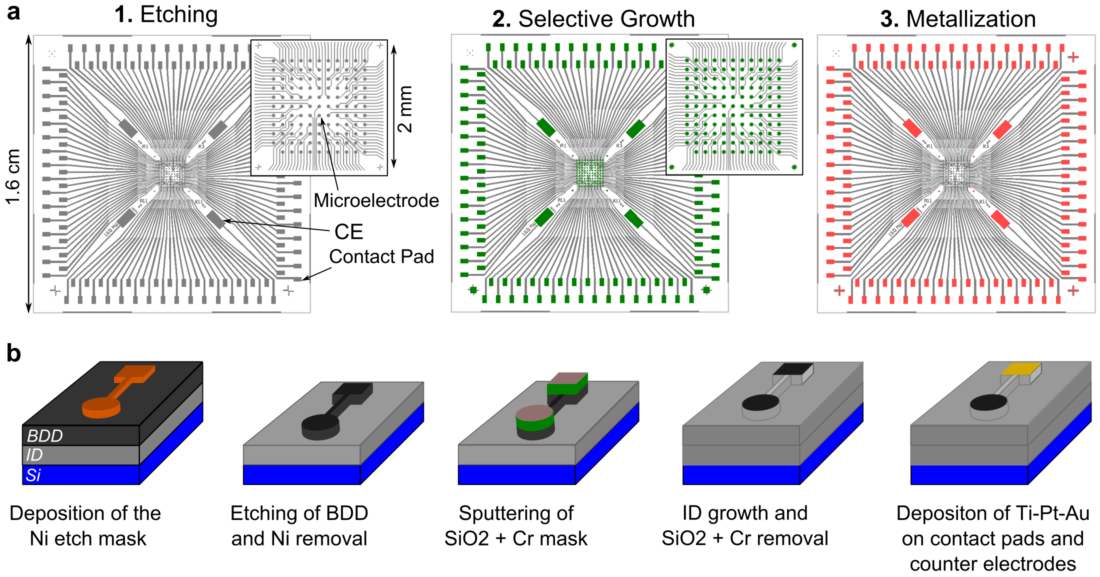

Figure 2.9: Fabrication of all-diamond MEAs. a) Design of photolitographic masks used for fabrication of 1.6×1.6 cm^2 diamond chips: 1) mesa definition and a zoomed view of the active area with 121 microelectrodes with 55 µm diameter, 2) definition of protection mask over microelectrodes, counter electrodes (CE) and contact pads for selective ID growth to electrically insulate the leads, 3) metallization of contact pads and counter electrodes. b) Schematic representation of fabrication flow.

2.5.1 Etching the mesa

First, a 100 nm thick Ni mask for etching BDD layer is defined using standard photolithography. By etching BDD we define an array of electrically separated microelectrodes (ME), leads, counter electrodes (CE) and contact pads. The corresponding mask and chip dimensions are shown in Figure 2.9 : the microelectrodes have a circular shape with a diameter of 55 μm and are connected through the leads to 240×440 μm^2 contact pads. The thickness of the Ni etching mask must be sufficient to sustain the following diamond layer etching. The etching is performed by deep reactive ion etching (DRIE) technique using oxygen plasma. The etching parameters are adjusted to ensure a deep etching of diamond (>1 µm) without damaging the Ni mask or diamond layer itself. Etching at lower rate (around 1 h for 1.4 µm) was found to be more suitable for our process. After the etching, Ni is removed by a commercial Ni etchant. Figure 2.10 shows the MEA after 55 min etching in O_2 plasma using DRIE, and removing the Ni mask.

The etch depth was verified using SEM: the side profile of the leads (Fig. 2.10 c) reveals a complete etching of the BDD film down to the ID layer resulting in electrically separated microelectrodes, which is also confirmed by resistance measurements between different pads. The surface of the microelectrodes remains hereby undamaged and clean (Fig. 2.10 b). It should be mentioned here, that the surface state of diamond microelectrodes is a crucial parameter for accurate electro-chemical detection and must be kept clean over the entire fabrication process.

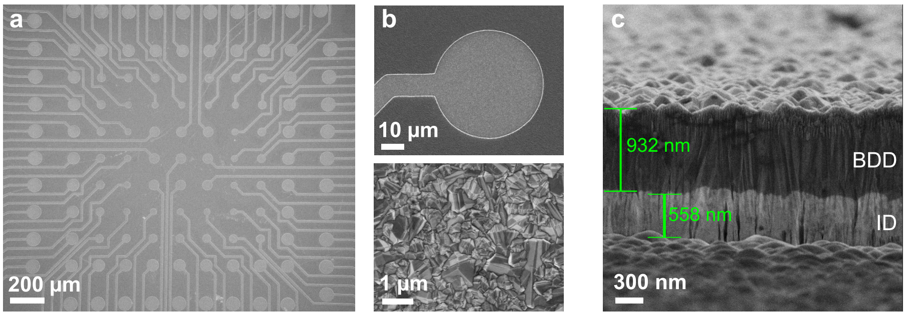

Figure 2.10: Diamond MEA after etching the BDD layer. a) SEM image of microelectrodes with different size after etching. b) Individual ME (top image) with a zoomed view of its surface (bottom image) after etching and Ni mask removal. c) Etch profile after 55 min etching in O_2 plasma.

2.5.2 Selective growth of intrinsic diamond

To ensure the operation of MEAs in biological liquid environment, the contact leads should be electrically isolated from the analyte solution. For this purpose different insulator materials such as insulating polymers (SU8 resist, polyimide) or SiO_2 can be used. However, since the realization of chronical implants requires a chemically and mechanically robust biocompatible material, we chose to use intrinsic CVD diamond deposited on the entire chip except contact pads and electrodes. The selective deposition can be achieved either by protecting the electrodes and pads by a mask during the CVD growth of ID, or by growing ID everywhere and then etching the ID layer above the electrodes and pads. The latter case is less preferable due to the possible surface damage of the electrode surface during the etching. Thus, a stack of SiO_2 and Cr was used above the electrodes and pads to protect them during the CVD growth of the ID layer. The SiO_2 layer is hereby used as a sacrificial layer for easy removal in hydrofluoric acid (HF), while the Cr layer prevents diamond deposition thanks to the reduced nucleation probability. Using each of the layers alone is insufficient due to the poor durability to diamond growth conditions (long time exposure to high power plasma and high temperature) and possible covering of SiO_2 by diamond.

The protection mask for selective growth is defined by optical lithography followed by sputtering of 2 µm of SiO_2 and 200 nm of Cr (Fig. 2.11 a). Then 1 µm of ID is deposited as described above in Chapter 2.4.4, but at lower plasma power (240 W) to reduce the damaging of Cr. The SiO_2/Cr mask is removed using a commercial Cr-etch and HF (Fig. 2.11 b). This results in completely encapsulated BDD contact leads embedded in an insulating layer of ID (Fig. 2.11 d), while the microelectrodes remain exposed to the environment (Fig. 2.11 c). The thickness/quality of sputtered SiO_2/Cr is hereby crucial for sufficient protection of electrodes and pads. If the mask is too thin, it can be destroyed during the ID deposition resulting in carbon composite formation on the electrode surface, which could not be removed by HF or $HNO_3 : H_2SO_4 : HClO_4$ (Fig. 2.11 f). The microelectrode surface after successful selective growth in shown in Figure 2.11 e.

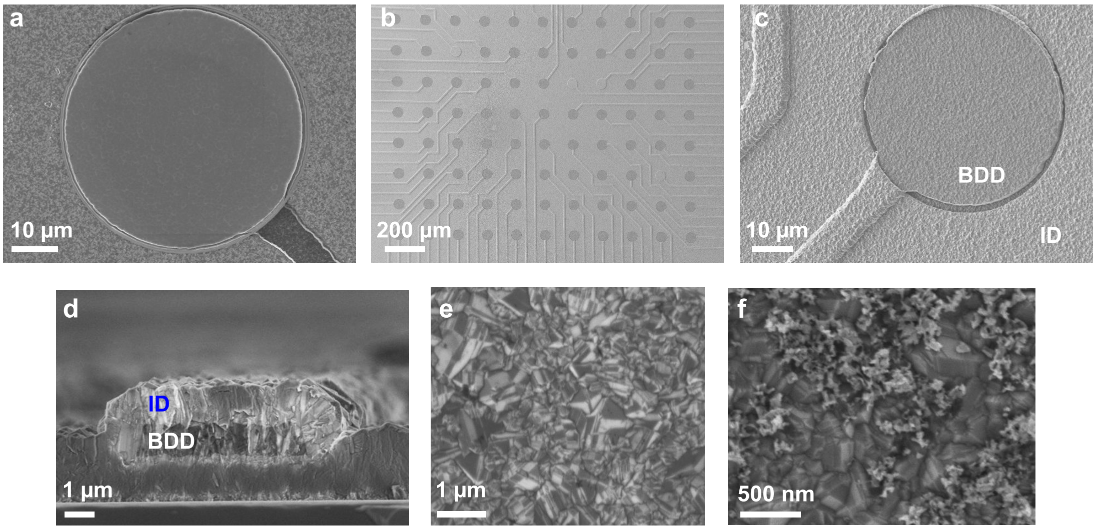

Figure 2.11: Selective growth of ID layer. a) Microelectrode covered by SiO_2/Cr mask to avoid the deposition of diamond b) Microelectrode array after CVD growth of 1 µm of ID followed by etching of the SiO_2/Cr mask using HF. c) Zoomed view of a microelectrode from b). d) Cross section of a contact lead after the selectice growth of ID. Boron-doped diamond lead is encapsulated by ID. e) Microelectrode surface after successful selective growth and mask removal. f) Carbon composite deposition on the microelectrode surface due to the damaged SiO_2/Cr mask during ID growth.

Selective growth of intrinsic diamond layer offers the realization of a mechanically stable all-diamond MEA with excellent insulating properties, as it will be shown later.

2.5.3 Metalization

In the last fabrication step, the contact pads and counter electrodes are defined by optical lithography and evaporation of Ti-Pt-Au (30 nm-40 nm-30 nm). The MEA is then glued to the chip holder and microbonded.

2.6 Electrical characterization

For bioelectrical detection, the MEA should be able to operate with signal frequencies up to 10 kHz and allow a stable recording at sampling rates up to 50 kHz. To verify that the insulating ID layer can sustain such high frequencies and prevent the diffusive current, we performed electrical impedance measurements. The impedance of the diamond microelectrode as well as that of the insulating ID layer were measured in dry environment using a needle probe station. While the first probe was placed onto the metallic contact pad, the second one was connected either to the isolated contact lead (Fig. 2.12 a) or to the corresponding diamond microelectrode (Fig. 2.12 b). AC bias voltage with an amplitude of 30 mV was applied, and the current between these two probes was measured. Figure 2.12 illustrates the representative impedance spectra of the contact leads covered by ID, and the conducting BDD microelectrodes. Up to 10 kHz, the insulating layer acts as a pure resistor with a constant impedance of 25 MΩ. A further increase of the voltage frequency results in a capacitive current through the insulating layer, leading to a lower impedance. The electrical impedance of the BDD microelectrode shows a pure resistive nature up to 100 kHz, with a resistance around $R_{ME} = 3.7$ kΩ. The resistance of the boron-doped electrode is at least 3 orders of magnitude higher than the resistance of the contact lead in the biological frequency range ($\leqslant$ 10 kHz), offering sufficient insulating properties for reliable operation of our MEA in biological applications.

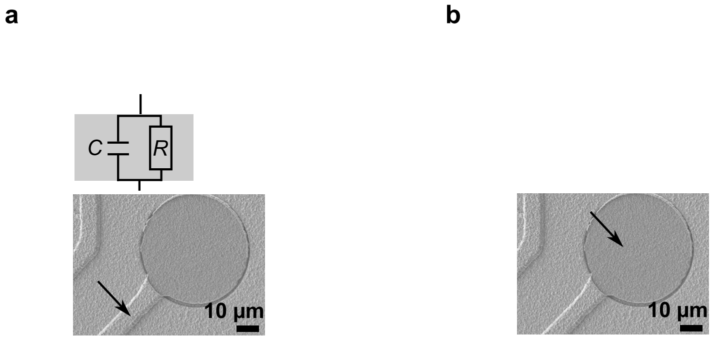

Figure 2.12: Impedance characterisation of a) the insulating ID layer above the contact leads, and b) BDD microelectrode. The inset indicates the probed area and the equivalent circuit model of the diamond surface.

The microelectrodes were further evaluated in terms of detection of redox compounds using cyclic voltammetry (CV). In this technique the microelectrode (working electrode) is exposed to an aqueous solution containing redox active compounds (here 6 mM $\mathrm{Fe(CN)}_6^{3-/4-}$ in 0.2 mM PBS), and the working electrode voltage V_w is swept at a constant rate between two values V_+ and V_- in repetitive cycles, starting from $V_w = 0$ V ($0 \rightarrow V_+ \rightarrow 0 \rightarrow V_- \rightarrow 0$). At the same time the current at the working electrode is measured. The typical CV setup involves three electrodes: the working electrode (here diamond ME), the reference electrode (RE, Ag/AgCl) and the counter electrode (CE, platinum electrode). The RE is used to set a defined reference potential, while CE, usually a highly conductive metal, prevents the current flow to RE. While the voltage at WE is swept with reference to RE, the current is measured between the counter electrode and the working electrode.

The applied potential sweeps induce a reduction/oxidation of the analyte molecules, which involves electron transfer. The electron exchange is then measured as current through the working electrode. At a specific voltage value, the detected current saturates. The saturation value I_{sat} is hereby limited by the electrode dimensions [196]:

$$I_{sat} = 4nrFD_{redox} \cdot c \tag{2.4}$$

with the diffusion coefficient of the redox couple in water D_{redox}, the Faraday constant F, the electrode radius r, the number of exchanged electrons n, and the concentration of the redox couple c. The fact, that the saturation current is proportional to the analyte concentration allows the detection of small concentration changes, such as induced by neurotransmitter release. For example, diamond electrodes were already used for *in-vivo* detection of dopamine release [197].

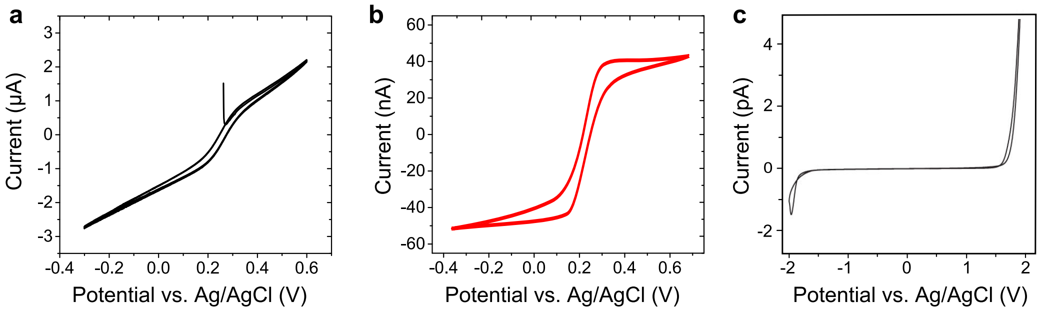

Figure 2.13: Electrochemical characterization of all-diamond MEAs. a) Cyclic voltammetry on a leaking, and b) on a functioning nanocrystalline boron-doped diamond microelectrode in $\mathrm{Fe(CN)}_6^{3-/4-}$ (6 mM) in PBS (0.2 mM). c) Potential window measured in PBS (0.2 mM). Measurements presented in b) and c) were performed by C. Hébert [73].

The CV measurements performed on the diamond MEAs obtained in this work exhibit very high currents though the microelectrode with no saturation value (Fig. 2.11 a), which is a clear indication of a leaking insulating layer or interconnected microelectrodes (for example through the Si substrate). Although improved MEAs were realized later in this work, the electrochemical characterization could not be performed. Figure 2.11 b shows representative CV measurements of similar MEAs successfully fabricated by C. Hébert at Institut Néel. The voltammograms exhibit the typical sigmoidal shape with limiting currents in cathodic and anodic regimes corresponding to the electron transfer on the microelectrode surface. The limiting current of 40 nA is in good agreement with the theoretical value of 46 nA given by Equation 2.4 with $r = 30$ µm and $D_{redox} = 6.67 \cdot 10^{-6}$ cm^2/s [73]. This indicates that the current is detected only by the exposed microelectrode. These microelectrodes show a wide potential window of 3.2 V (Fig. 2.11 c), and there electrical performance was shown to be comparable with previous reports on diamond

MEAs [79]. However, compared to other materials the diamond microelectrodes similar to those fabricated in this work and presented in [73] exhibit a relatively low double layer capacitance and high electrode impedance in liquid environment, which are 70 µF/cm^2 and 400 kΩ at 1 kHz respectively. For example, the impedance of a standard planar gold microelectrodes with a radius of $r = 30$ µm is around 50 kΩ [146].

2.7 Surface modification by carbon nanotubes

Diamond was already shown to be an attractive material for biological and chemical sensing applications [71, 73, 79]. However it suffers from a relatively low double layer capacitance and high impedance. Since the detected signal is proportional to the electrode surface, one possibility to improve the electrode performance is to increase its specific detection area. At the same time, the electrode diameter must remain constant to keep the initial spatial resolution. This can be achieved by using carbon nanotubes (CNT) directly grown on the diamond electrodes, which by increasing the roughness will boost the effective area for the capacitance.

The standard method to produce CNTs is the catalytic chemical vapor deposition (CCVD) in H_2/CH_4 atmosphere at low pressure and high temperature [198]. The most frequently used catalysts are transition metal nanoparticle, such as Fe, Co or Ni. The catalyst particles are used for decomposition of the carbon source and its new nucleation to form CNTs. When CH_4 vapor comes in contact with a hot metal nanoparticle, it decomposes into carbon and hydrogen species, and carbon gets dissolved into the metal. After reaching the carbon-solubility limit, the dissolved carbon atoms segregate to the metal surface and crystallize in form of a stable cylindrical network with no dangling bonds. This continuous process results in the formation of a carbon nanotube. The diameter of the nanotube is hereby related to the size of the metal particles [199]. Two growth models are distinguished depending on the catalyst-substrate interaction: tip growth, where the CNT forms on the bottom of the catalyst, pushing the metal particle off the substrate, and the base growth with the CNTs growing on the top of the rooted catalyst [200]. The base growth is schematically shown in Figure 2.14 a.

By controlling the growth parameters CNTs with different diameters and number of sidewalls, such as single walled (SWCNT), double walled (DWCNT) or multiwalled (MWCNT) can be produced [198]. Depending on its chirality, a given nanotube shell can be either metallic of semiconducting. [201]. Therefore MWCNT are more probable to express metallic characteristics, while SWCNT and DWCNT can be either metallic or semiconducting.

The CNTs grown in this work are multiwalled with random orientation. Using Pd as catalyst we realized a local growth of CNTs embedded in boron-doped nanocrystalline diamond. The embedding of CNTs results in a stronger attachment and encapsulation of potentially toxic metal catalyst by biocompatible diamond.

For the growth, first a pattern of circles with 55 µm diameter was defined by standard photolithography techniques on a nanocrystalline diamond substrate followed by evaporation of

3 nm of Pd and lift-off in acetone. The sample was then transferred to a hot filament CVD reactor (HFCVD) and heated to 850°C substrate temperature (with a corresponding filament temperature 1950°C). The hot filament is used to produce atomic hydrogen and reactive carbon species. The etching was performed in hydrogen atmosphere at 60 torr for 10 min. During the heating, the Pd layer melts forming small particles on the diamond surface. These hot particles dissolve the carbon atoms from the diamond substrate, which then segregate to the metal surface and react with the hydrogen atmosphere to hydrocarbon, as illustrated in Figure 2.14 a. This process creates pinholes in the diamond surface with the radius of the Pd catalyst particles. Figure 2.14 c clearly illustrates the local etching of Pd particles. While the uncovered diamond surface remains unchanged, the circles, which were covered by Pd, exhibit pinholes created by catalyst particles. This embedded Pd particles were then used as catalysts for CNT growth. As shown in Figure 2.14 d, a CNT forest could be locally grown on the predefined areas. The cross-section of the diamond/CNT composite reveals the CNTs emerging from the embedded Pd particles (Fig. 2.14 e).

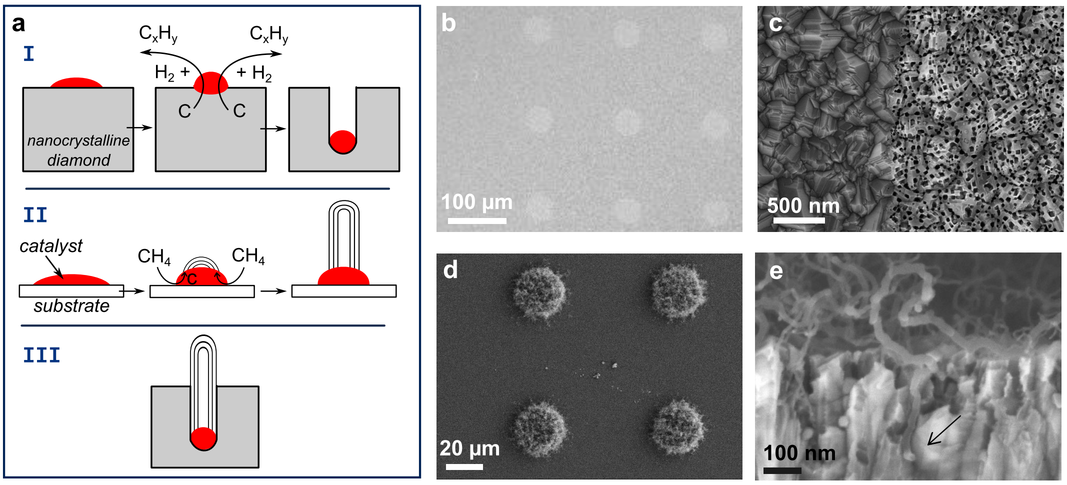

Figure 2.14: Localized growth of CNTs embedded in nanocrystalline diamond. a-I) Schematic illustration of catalytic etching of nanocrystalline diamond: the carbon species from the diamond substrate are dissolved by the catalyst and react with hydrogen to hydrocarbon. a-II) CNT base growth model: carbon species from the growth chamber are dissolved by the catalyst particle and precipitate out to form CNTs. a-III) Combination of both results in the growth of embedded CNTs. b) Photolithographically defined Pd circles on diamond. c) Diamond surface after catalytic etching, showing pinholes in the area which was covered by Pd, while the uncovered diamond surface remains unchanged. d) Locally grown CNT forest. e) Cross-section of the diamond/CNT composite, demonstrating a CNT embedded in the diamond substrate. The arrow indicates the catalyst particle.

The CNT growth was carried out in the same HFCVD, as for catalytic etching. To lower the carbon absorption, the tungsten filament was carburized in CH_4/H_2 (9 sccm/100 sccm) atmosphere for 1h at 60 torr and a substrate temperature of 300°C. For the CNT growth the substrate temperature was increased to 800°C (filament temperature 1800°C) at otherwise unchanged conditions for 15 min. The gas pressure was found to have a significant influence on the morphology of produced CNTs. As shown in Figure 2.15, the diameter of CNTs increases with increasing gas pressure, indicating a higher wall number, which is directly related to the CNT conductivity [202]. The corresponding Raman spectra exhibit the characteristic band peaks [203]: the disorder related D band peak at around 1300 cm^{-1}, and the carbon sp^2 hybridization related G band peak at around 1600 cm^{-1}. The Raman spectra of CNTs grown at lower gas pressure reveals a narrower D band peak and a slightly higher intensity ratio I_G/I_D of D to G band peaks. This indicates a slightly lower amount of defects in CNTs grown at lower pressure.

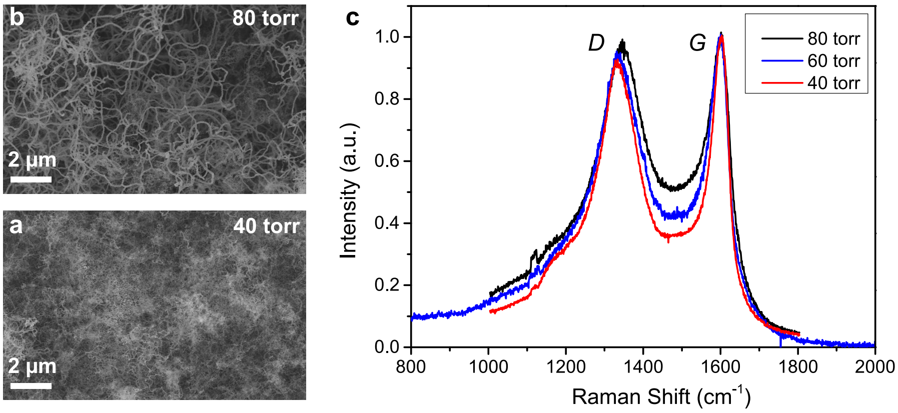

Figure 2.15: CNT forest grown at different gas pressures. a) SEM image of CNTs grown at a total gas pressure of 40 torr and b) 80 torr. c) Raman spectra of CNT forest grown at different gas pressures with characteristic peaks: D band peak at 1300 cm^{-1}, and G band peak at 1600 cm^{-1}.

While we were able to locally grow embedded CNTs with controlled morphology, a detailed investigation of their electrical properties and the effect on the MEA quality could not be performed in this work. However, different studies show a significant improvement of MEA performance [93, 152], and even an increase of neuronal activity [204–206] by using CNTs. But despite the improved attachment of CNTs using embedded catalyst particles, the CNTs still remain toxic for $in-vivo$ applications [207, 208]. In this context, a promising idea is to cover the CNTs by a thin layer of CVD grown nanocrystalline diamond, which combines both the surface enhancement by CNTs and the bioinertness of diamond. For diamond based MEAs, an increase in double layer capacitance from 70 $\mu\text{F/cm}^2$ to 3 mF/cm^2, and an electrode impedance $\leqslant$ 100 kΩ at 1 kHz could be achieved by using this method [80].

2.8 Conclusion

Here we presented a reliable fabrication process of all-diamond microelectrode arrays using boron-doped nanocrystalline diamond for active electrodes and intrinsic diamond films for electrical insulation. Diamond films for the fabrication of MEAs were grown using MPCVD technique on p-doped silicon substrates. In-situ high concentration boron-doping was used to obtain metallic conductivity, required for the realization of microelectrodes. While a detailed electrical characterization of diamond MEAs fabricated in this work could not be performed, similar microelectrodes ($r = 30$ µm) realized previously at Institut Néel exhibit relatively low double layer capacitance (70 $\mu F/cm^2$) and high impedance (400 kΩ), which is one order of magnitude higher than that of the commercially available gold microelectrodes with similar electrode size.

To improve the impedance, a composite material with carbon nanotubes embedded into nanocrystalline diamond was developed. Carbon nanotubes increase the effective electrode surface, which will lower the impedance by increasing the interfacial capacitance. The embedding occurs via catalytic etching of diamond by metal nanoparticles used for CNT growth and improves the mechanical stability of the composite. While a reproducible local growth of embedded CNTs was achieved in this work, their effect on the electrode performance and the electrical interfacing with living tissue remain to be done.

In conclusion, diamond microelectrode arrays offer a practical solution for realization of single-material biocompatible probes for long-term neural implantation with applications reaching from real time detection of neurotransmitter release to stimulation and recording of electrical activity of neurons. However due to their high intrinsic impedance ($\hat{=}$ low interfacial double layer capacitance) detection of neural activity with single cell resolution remains challenging. A possible solution to improve the electrode performance is to increase its effective surface by local growth of embedded carbon nanotubes on the exposed electrode surface.

CHAPTER 3

Silicon nanowire field effect transistors (SiNW-FETs)

In this chapter we will present the FET based technology for detection of neural activity. After a general introduction, we will focus of silicon nanowire field effect transistors, detail the top-down fabrication flow and present the electrical characterization measurements in ambient and liquid environments.

3.1 FET fundamentals

In FET recordings, the semiconductor channel is exposed to the electrogenic cell, which effectively acts as a gate and modulates the channel conductance and consequently the net current flowing through the FET-channel. The transistor thus translates the bioelectrical activity of the cell into a measurable current signal. The transistor device used for first recording from living tissue in 1976 by Bergveld et al. [94] was defined by the authors as oxide semiconductor field effect transistor (OSFET), in analogy to MOSFET (metal oxide semiconductor FET) without the metal gate. A typical n-channel MOSFET is shown in Figure 3.1 a.

The substrate is a p-doped semiconductor (for example Si), containing two highly n doped regions called source and drain. The highly doped regions are isolated from the substrate by p-n junctions. If a positive voltage is applied to the metal gate, negative charge carriers are attracted to the semiconductor/oxide interface creating an inversion layer. Applying a voltage V_{SD} between the source and drain results in a current flow through the transistor channel. The $I-V$ characteristics of a MOSFET are shown in the lower panel of Figure 3.1 b. There are two different regimes: the linear ($V_{SD} \ll V_G$) and the saturation ($V_{SD} \gtrsim V_G$) regime. In the linear regime, the inversion layer connects both n-doped regions, and the transistor behaves like a simple resistor with the source-drain current I_{SD} proportional to the source-drain voltage V_{SD} [209]:

$$I_{SD} \;=\; \mu c_{ox} \frac{W}{L} \left(V_G - V_{th}\right) \cdot V_{SD} \tag{3.1}$$

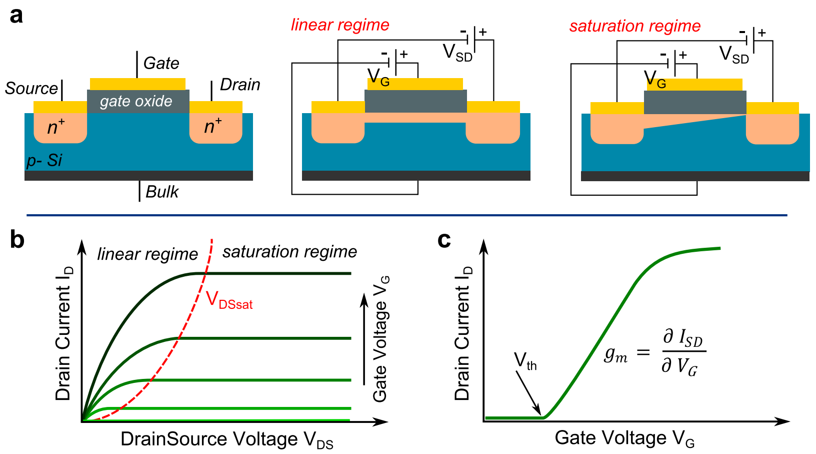

Figure 3.1: MOSFET fundamentals (from [209]). a) Scheme of a typical n-channel MOSFET. The p-type semiconductor containing two highly n-doped, which form the drain and source contacts. A metal gate is placed on top of the semiconductor, isolated by a gate oxide. A positive voltage V_G at the gate attracts the electrons from the bulk forming a conductive channel between the source and drain. Increasing positive voltage at the drain narrows the channel. b) Source-drain current I_{SD} vs. source-drain voltage V_{SD} at different gate voltages V_G. For small V_{SD}, the current increases linearly with the source-drain voltage, and saturates above V_{SDsat}. The dashed line indicates the transition between the linear and saturation regime. c) Transfer curve $I_{SD}(V_G)$. The current is linear with the gate voltage above the threshold current V_{th}. The slope is called transconductance g_m.

where μ is the charge carrier mobility, c_{ox} the gate oxide capacitance per unit area, W the channel width, L the channel length, V_G the gate voltage, and V_{th} the threshold voltage. This simple linear model is only valid for small source-drain voltage $V_{SD} \ll V_G - V_{th}$. The saturation regime occurs at higher V_{SD} due to the narrowing of the inversion channel at the drain electrode [209]. The current is now nearly independent on V_{SD}.

The transfer characteristics of a MOSFET are presented in Figure 3.1 c. A transfer characteristic is obtained by measuring the source-drain current I_{SD} as function of the gate voltage V_G at constant source-drain voltage V_{SD}. To switch the current flow on, a sufficiently large inversion channel is required, which is reached above the threshold voltage V_{th}. Further increase of the gate voltage, increases the current through the transistor channel. The current modulation by the gate voltage is called *field effect*. The slope of the $I_{SD}(V_G)$ represents the transconductance g_m. The transconductance describes the sensitivity of the transistor to the voltage changes at the gate. The higher g_m, the better the device performance. In the accumulation regime, the transconductance g_m and the sensitivity S of the transistor are given by [209]:

$$g_m = \frac{\partial I_{SD}}{\partial V_G} = \mu c_{ox} \frac{W}{L} \cdot V_{SD} \qquad \text{and} \qquad S = \frac{g_m}{V_{SD}} = \mu c_{ox} \frac{W}{L}. \tag{3.2}$$

According to the equation 4.2, the FET sensitivity depends on the semiconductor channel material, on the gate dielectric, and on the width-to-length ratio W/L of the transistor channel.

The field effect can be also used as a detection mechanism for electrical activity of cells in bioelectronics. Here the metal gate is replaced by the living cell (see Fig. 3.2 c). As already described before, the electrical activity of the cell generates an ion current, which flows across the seal resistances R_{seal} in the cleft, resulting in an extracellular voltage V_j. This voltage modulates the current through the transistor channel. Thus the transistor translates the physiological activity of the cell into a measurable current signal ΔI. The measured signal depends on the extracellular potential as follows: $\Delta I = g_m \cdot V_j$ (in voltage biased configuration), revealing the great potential for device engineering. By choosing a suitable material for the transistor channel and adapted gate oxide, the transconductance can be increased resulting in a higher signal-to-noise ratio.

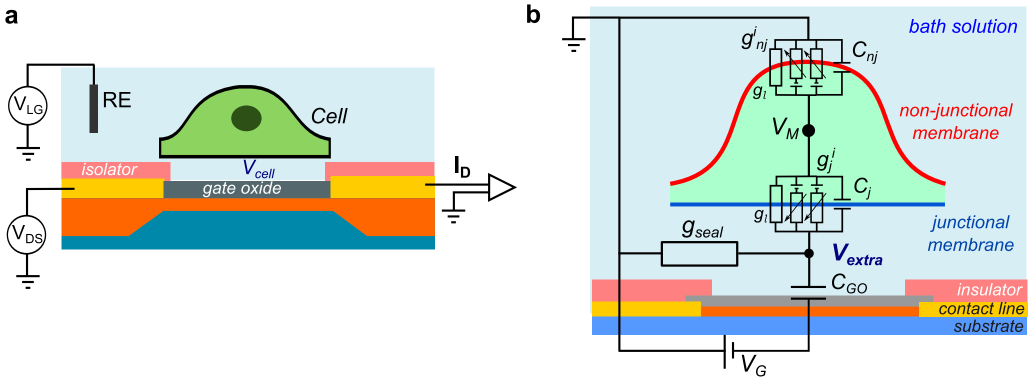

Figure 3.2: FET-cell interface. a) Detection principle: constant bias voltage V_{SD} is applied, and the current I_{SD} trough the transistor channel is monitored. If a local potential change due to the electrical activity of the cell occurs, a small variation in I_{SD} can be observed. The liquid potential is set to a constant value using a reference electrode. b) Equivalent circuit model of the neuron/transistor interface (adopted from [100]). The junctional (non-junctional) membranes of the cell is described by the capacitance C_j (C_{nj}), the leak conductance g_l, and the specific ionic conductance g^i_j (g^i_{nj}). The gate oxide is described by the capacitance C_{GO}. The ionic current generated by the cell activity flows through the cleft with conductance g_{seal}, resulting in the extracellular potential V_{extra}. V_M is the intracellular potential of the cell.

The first FET-recordings of the activity of isolated neurons were performed by Fromherz et al. [95] using leech neurons interfaced with silicon FETs. After that, recordings from isolated mammalian neurons [14], cardiomyocytes [100] and HL cells [99] followed. From this variety of experimental observations, a simple model was developed to describe the junction between the cell membrane and the transistor [105]. This model, also called the point contact model, combines the effect of the capacitive junction, ohmic junction and the voltage gated ion channels. According to Kirchhoff's law, the extracellular potential in the cleft is equal to the current passing through the membrane:

$$g_{seal} \cdot V_{extra} = \underbrace{C_j \cdot \frac{\partial V_M}{\partial t}}_{\text{capacitive junction}} + \underbrace{\sum_i g^i_j (V_M - V^i_{eq})}_{\text{voltage gated ion channels}} + \underbrace{g_l \cdot V_M}_{\text{ohmic junction}} \tag{3.3}$$

where g_{seal} is the seal conductance in the cleft, V_{extra} the extracellular potential, C_j the membrane capacitance, g_l the average membrane conductance (leaking conductance), g_j^i the specific conductance of ion species i, V_M the intracellular potential, and V_{eq}^i the equilibrium potential of ionic species i.

Depending on the cell-transistor coupling strength, the cell-transistor overlap fraction and due to the inhomogeneous distribution of ionic conductance in the cell membrane, differently shaped extracellular potentials V_{extra} can be measured [8, 148, 210], as illustrated in Figure 3.3. When no ionic currents are present in the junction, the cell-transistor coupling is purely capacitive, and the measured extracellular potential is proportional to the first derivative of the intracellular potential V_M (Fig. 3.3 b, A). In case of a leaky membrane, ohmic conductance dominates the capacitive current, and V_{extra} is proportional to V_M (Fig. 3.3 b, B). The majority of detected V_{extra} is however due to the selective accumulation or depletion of voltage-gated ion channels: for complete depletion, V_{extra} corresponds to the capacitive coupling (Fig. 3.3 b, C) [8]: for partially depletion, the response resembles a capacitive detection with lower amplitude; and for accumulation, the capacitive response is inverted, as shown in Figure 3.3 b C. The detected extracellular potential exhibits a biphasic nature with a negative polarity, corresponding to the opening of sodium channels, which induces a lack of positively charged ions in the cleft, and the subsequent opening of potassium channels resulting in an inflow of positive ions into the cleft and increasing the positive potential as described in Chapter 1.1. For all coupling types, the amplitude of V_{extra} increases with the cleft resistance [95]. For hippocampal rat neurons in culture, the measured extracellular potential varies from 200 µV to 4 mV [14].

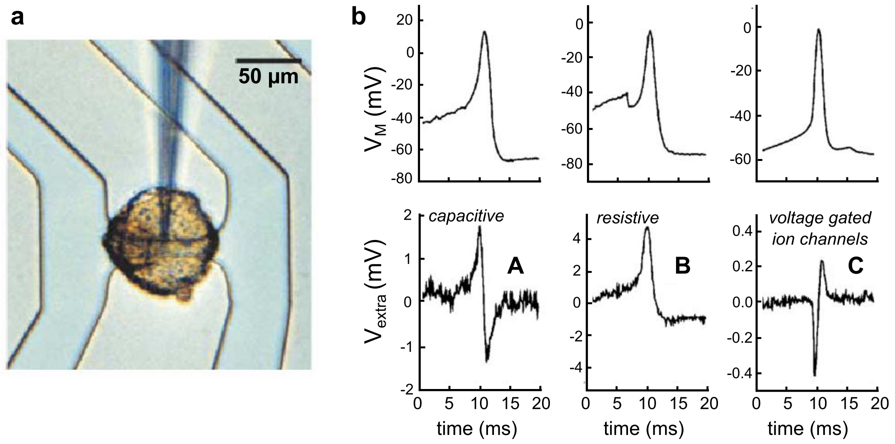

Figure 3.3: Transistor recording of stimulated activity of leech neurons (from [9]). a) The cell body of a leech neuron interfaced with a Si-FET. Micropipette is used for intracellular recordings. b) Different cell-transistor coupling types with extracellular recordings V_{extra} in the lower row and the corresponding intracellular potentials V_M in the upper row. The extracellular potential is induced by (A) capacitive coupling, (B) ohmic coupling, and (C) voltage-gated ion channels. While A and B were obtained on the cell body, C was measured on the axon, which exhibits more voltage gated ionic channels.

Since the first recordings, intensive efforts were devoted to increase the spatial resolution and the number of recording sites. Now, state-of-the-art silicon technology can be used to fabricate multitransistor arrays with over 16,000 recording elements and a resolution of 7.8 µm on an area of 1 mm^2 [110]. Moreover, since the performance of FETs depends merely on their width-to-length ratio (Eq. 3.3), the spatial resolution of the recordings can be increased even further to the *sub-micron* range. For example, using silicon nanowires with diameters $\leqslant$ 100 nm as transistor channel allowed an accurate detection of the propagation of action potentials along the axon [111]. However, the monitoring of information processing within a defined neural network still remains challenging. In this context, combining *in-vitro* chemical patterning of neural networks with corresponding top-down fabricated SiNW-FET arrays is a promising approach to realize a stable platform for stimulation of neural activity and detection of signal propagation in the network [116].

Currently, the FET technology is also being investigated for *in-vivo* applications and chronical implants [107, 113]. For this purpose, more biocompatible materials such as single crystalline diamond [156], graphene [128], or conductive polymers (PEDOT - (3, 4-ethylenedioxythiophene)) [211, 212] are being evaluated. Among these materials, graphene appears as a most suitable candidate for chronical implants due to its biocompatibility [65, 213], chemical inertness, robustness and mechanical flexibility [122, 123, 214], which is required for a long term electrical interfacing soft biological tissue.

In the following, we will present both the possibility to probe neural activity within a defined neural network using top-down fabricated SiNW-FET arrays with matching geometries, as well as the realization of graphene based field effect transistors for detection of neural activity in Chapter 4.

3.2 SiNW-FETs for sensing applications

Since the introduction of ion sensitive field effect transistors (ISFETs) [215], these devices are widely investigated as potential biosensors, which convert chemical reactions into electrical signals. The sensing occurs hereby in analogy to the top gate induced conductance change in metal gated MOSFETs. In case of ISFETs however the gate dielectric material is directly interfaced with the analyte, which modulates the FET conductance via electrostatic gating by chemical or biological species as described above.

Further miniaturization and scaling down the ISFETs to the nanoscale using a silicon nanowire (SiNW) [216] led to an immense improvement of its sensing properties and revealed the potential of SiNW to realize an ultrasensitive, fast, label-free sensor for a variety of applications including pH detection, chemical and bio-sensing [217–220]. The geometry of SiNWs increases the surface to volume ratio and restricts the current flow in a very thin region, such that only a small amount of charge is needed to induce a measurable signal. The small dimensions of SiNW-FETs reduce the response time [221] of the sensor due to lower capacitance and allow a higher covering fraction by the cell increasing their sensitivity and enabling the detection of even very small signals. The surface of SiNWs can be functionalized with different catcher molecules such as antibodies, single DNA strings or proteins to enable a specific detection of analytes [222–224]. Besides the chemical detection, SiNW-FETs also enable a noninvasive detection of the activity of electrogenic cells [99] and of the signal propagation along the neurites [111].

Two different approaches for the realization of SiNWs are reported in the literature: the **bottom-up** approach, where the SiNWs are usually grown using a vapor-liquid-solid method and gold nanoclusters as catalyst [216]; and the **top-down** approach, that is based on standard electron beam lithography and chemical or reactive ion etching of a single crystalline SOI wafer. While bottom-up grown SiNWs offer excellent electrical performance, their integration in electronic circuits and controlled positioning still remains technically difficult. However, currently similar electrical properties can be achieved also using top-down fabrication techniques [99, 115, 117], which additionally offer a precise control of the geometry and position of nanowires. Taking advantage of the mature silicon industry processing, large scale SiNW-FET arrays can be fabricated on silicon-on-insulator (SOI) substrates in different arrangements, allowing investigations of differently shaped neural networks, which can be chemically patterned directly above the nanowire FETs [116].

3.3 Fabrication of SiNW-FETs

The SiNW-FETs realized in this work are fabricated on SOI substrates following the top down approach. Using state of the art micro- and nanofabrication techniques, the top down approach allows the fabrication of large scale integrated devices with reproducible electrical properties, controlled device positioning and high resolution. The fabrication flow is illustrated in Figure 3.4. Briefly, starting from a selectively doped SOI substrate with predefined alignment marks, first the ohmic contact leads are defined followed by e-Beam lithography definition and dry etching of NWs. The surface of the SiNW is then covered with a gate dielectric material (HfO_2 or Al_2O_3) and the metallic leads are passivated using parylene-C to avoid any leakage current in future liquid gate operation. In the following, the individual fabrication steps will be described in more detail. The precise recipes can be found in Appendix B.

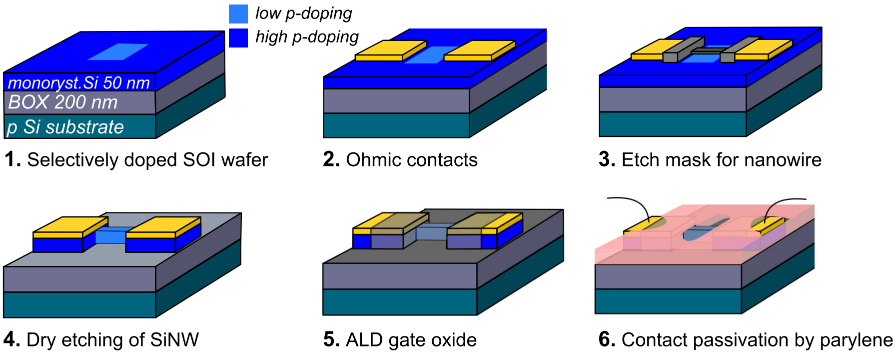

Figure 3.4: Fabrication flow of SiNW-FET arrays. Starting from a selectively doped single crystalline SOI wafer, first the ohmic contacts are evaporated, followed by the definition of the etch masks for nanowires. After etching the excess Si and removing the etch mask, the gate oxide is deposited and the contact leads are electrically insulated with parylene.

High quality SOI substrates (SOITEC, France) with single crystalline top Si-layer for the fabrication of SiNW were selectively doped with boron atoms at Ion Beam Services (IBS, France) to form low doped SiNWs with highly conductive contact areas. First the undoped SOI substrate (200 nm BOX / 100 nm Si) was covered by a thermal oxide layer (200 nm BOX / 50 nm Si / 110 nm thermal oxide) and doped with boron at a lower implantation dose (10^{17} – 10^{19} at. per cm^3) by plasma assisted ion implantation technique. Then, a laser lithography step was performed to form a protective resist pattern above the future nanowire positions and alignment marks followed by a second ion beam implantation step with a higher boron concentration for contact areas. The future nanowire positions remained hereby at the initial low doping concentration due to the resist protection. The thermal oxide was then etched using HF followed by resist removal and resulting in a thermal oxide pattern above the NW positions and alignments marks for the following lithography steps.

Next the ohmic contacts are defined by optical lithography using a bilayer positive resist structure: LOR3A topped by UV3 (MicroChem). Since the first resist has a higher solubility in the developer, the resist stack forms an undercut avoiding sidewall deposition. Considering the high thickness of the contact metals (ca. 90 nm) a sidewall formation would be crucial for a homogeneous deposition of the Al-etch mask for NWs in the later e-Beam step. The ohmic contacts are exposed at both sides of the low doped region followed by evaporation of 17 nm Ti, 40 nm Pt and 30 nm Au. Shortly before the metal deposition, the sample is immersed into buffered HF solution for 10 s to remove the native oxide layer and improve the metal-Si contact. The thermal oxide above the future NWs is chemically etched either before or after forming the ohmic contacts. However since Ti can be partially etched by HF, its preferable to remove it before.

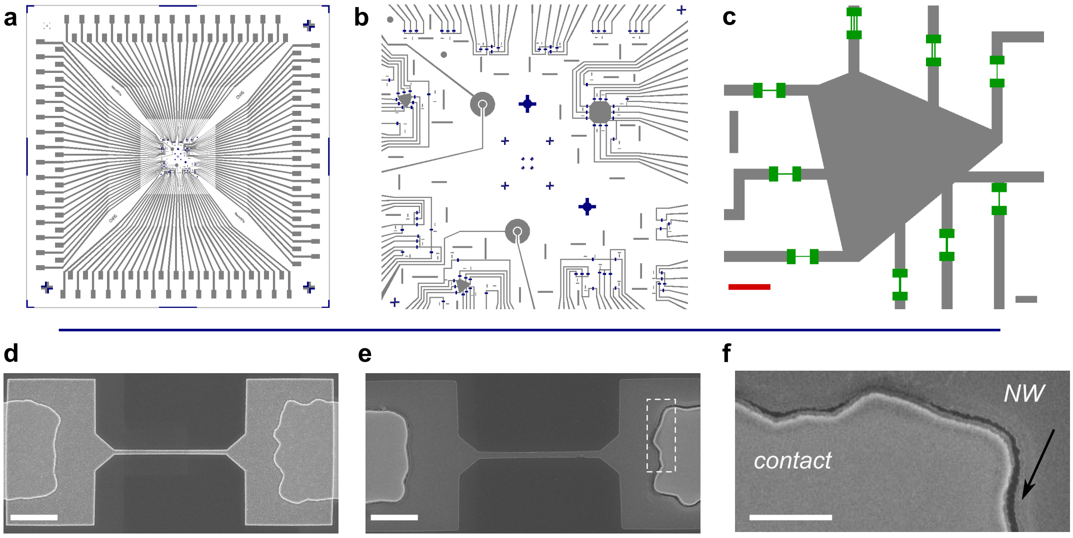

Figure 3.5: SiNW-FET fabrication. a) Photomask for ohmic contacts. The chip size is 1.6×1.6 cm^2 b) Zoom of the 2×2 mm^2 active area with 89 nanowires. The lower doped nanowire positions are indicated in blue, the contact lines in grey. c) Zoom of a triangular NW-FET array with differently shaped nanowires indicated in green (scale bar = 20 µm). d) Al mask for dry reactive ion etching of nanowires (scale bar = 2 µm). e) An example of a disconnected Si nanowire after etching due to an inhomogeneous covering by Al layer (scale bar = 2 µm). f) Zoom of the nanowire illustrating the disconnected region (scale bar = 1 µm).

In the same lithography step as for the ohmic contacts, also the alignment marks for the following e-Beam lithography of SiNWs are defined. Using e-beam lithography, nanowires with different dimensions and geometries can be realized on the same chip. The width of the NWs varies hereby from 100 nm to 1 µm and the length is around 7 µm. Also a parallel configuration of 2-3 nanowires separated by 0.5 - 1 µm from each other and connected to the same drain/source electrodes were employed to increase the success rate. Typically 89 NWs per chip are exposed followed by evaporation of 40 – 70 nm of Al as etch mask. The NWs are then etched using reactive ion etching (RIE) in SF6 plasma and the Al mask is removed with MF-26 (MicroChem). The homogeneous covering of the ohmic contacts by the Al layer is hereby of major importance to assure an intact transition between the NW and the contacts. A too thin Al layer or high sidewall metal deposition on ohmic contacts can lead to an interrupted etch mask forming a cleft between the NW and the metallic contacts after etching. A disconnected NW is illustrated in Figure 3.5.

To improve the contact resistance, a rapid thermal annealing at 400°C for 4 min is performed in Ar/H_2 atmosphere. The annealing forms a conductive titanium silicide alloy, which lowers the Schottky barrier height between Ti and Si [225]. While the NWs initially exhibit a resistance > 10 MΩ, after annealing the resistance drops to $0.1 - 2$ MΩ depending on the width and the doping concentration (Fig. 3.6 a). Next a thin gate oxide is deposited using atomic layer deposition (ALD) above the nanowires. Typically 10 nm HfO_2 or Al_2O_3 is used. The entire chip surface is then covered by parylene-C to electrically isolate the contact lines during liquid operations. Using a photoresist mask, parylene is etched in oxygen plasma just above the nanowires and contact pads. A representative AFM image in Figure 3.6 shows the final nanowire FET structure. The insulating properties of the gate oxide could be confirmed using tunneling atomic force microscopy. The current from the device surface to the tip is only a few pA at 1 V bias voltage, which is small enough to be neglected.

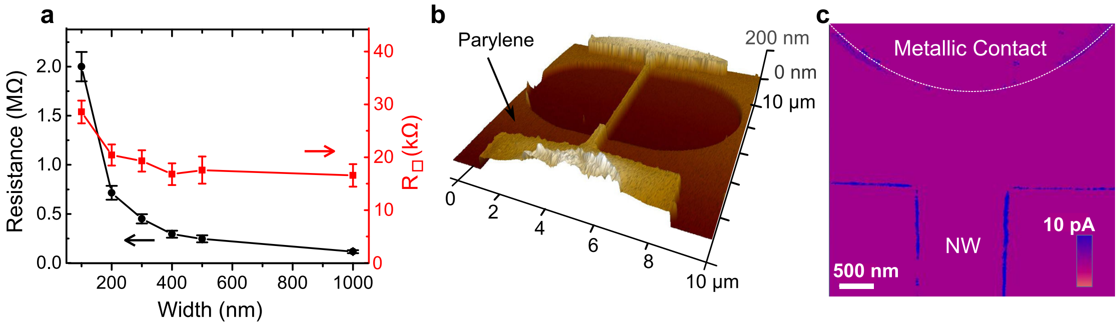

Figure 3.6: SiNW-FET characteristics. a) Two point resistance (black line) and square resistance (red line) of nanowires with varying width after deposition of 10 nm of HfO_2. b) AFM image of the final NW-FET. Insulating parylene layer is etched just above the nanowire. c) Tunneling atomic force microscopy of the final device (measured in collaboration with I. Ionica, INP Grenoble).

3.4 Electrical characterization of SiNW-FETs

The electrical characterization of the fabricated SiNW-FET arrays was performed using a needle probe station connected either to a Keithley source-meter or FPGA (fast programmable gate array) interfaced to a PC via a LabView measurement program. Nanowires of different width and doping concentrations were characterized in terms of conductance modulation by source-drain voltage, back-gate effect, front liquid gate effect, pH detection and the ability to detect small, rapid potential pulses applied to the liquid gate.

3.4.1 SiNW-FET performance in ambient environment

The transistor properties of the nanowires were first characterized under ambient conditions. The measurement scheme is shown in Figure 3.7 a, the source-drain current through the channel Isd is measured at varying polarization voltage V_{SD} and back-gate voltage V_G. While for low doped nanowires the source-drain current saturates with increasing negative V_{SD} due to narrowing the channel at the drain contact, highly doped nanowires exhibit a rather ohmic behavior as shown in Figure 3.7 b, c. The net current through the nanowire increases hereby with its width (Fig. 3.7 d).

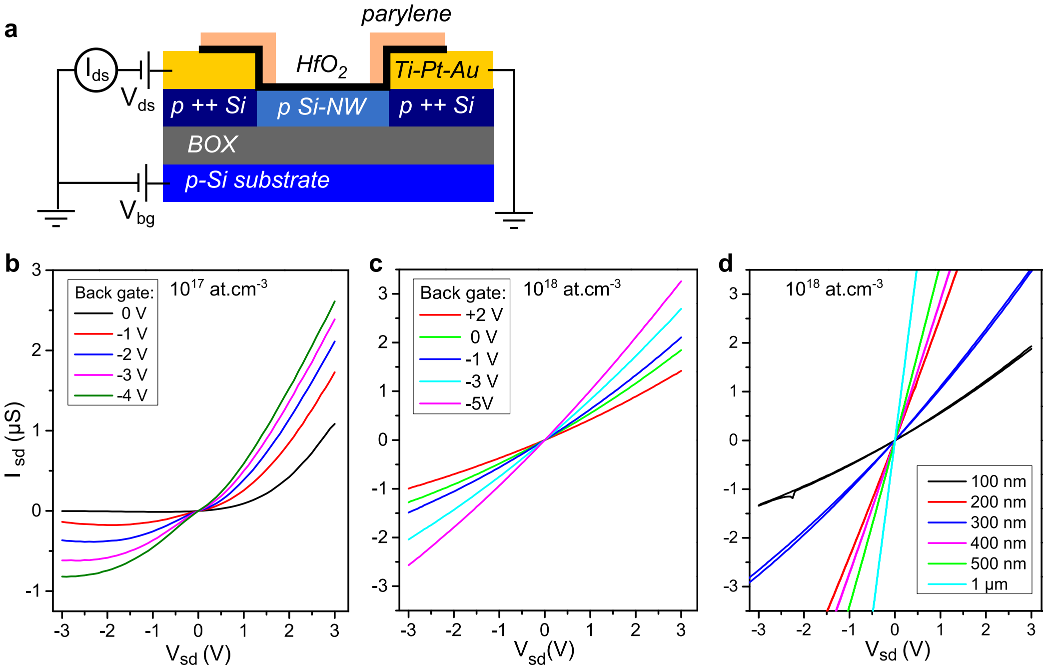

Figure 3.7: I/V-characteristics of the fabricated NW-FETs. a) Schematic of the measurement setup. b) $I(V)$ curves of a low doped SiNW-FET. c) $I(V)$ curves of a highly doped SiNW-FET. d) $I(V)$ curves of SiNW-FETs with varying channel width.

The transfer characteristics of fabricated SiNW-FETs can be seen in Figure 3.8. A small DC source-drain bias voltage $V_{SD} = 100$ mV is applied to the nanowire and the source-drain current through the channel I_{SD} is measured at the varying back-gate voltage V_G. When a negative voltage is applied to the back-gate, the majority carriers, i.e. holes in the p-doped case, are accumulated increasing the conductivity of the nanowire channel until the free carries are exploited entirely and the conductance saturates (Fig. 3.8 a). For more positive back-gate voltages the nanowire is depleted, and no current is flowing through the channel due to forming of p-n junctions between the depleted nanowire and heavily p-doped contact regions. The back-gate induced conductance modulation is stronger for low doped SiNWs, and the current through the channel scales with the width of the nanowire (Fig. 3.8 b). Consequently the sensitivity (transconductance) of the SiNW-FETs scales with the width-to-length ratio W/L, as shown in Figure 3.8 c. The ratio W/L corresponds to the inverse of the number of squares, which is a commonly used descriptive in transport measurements.

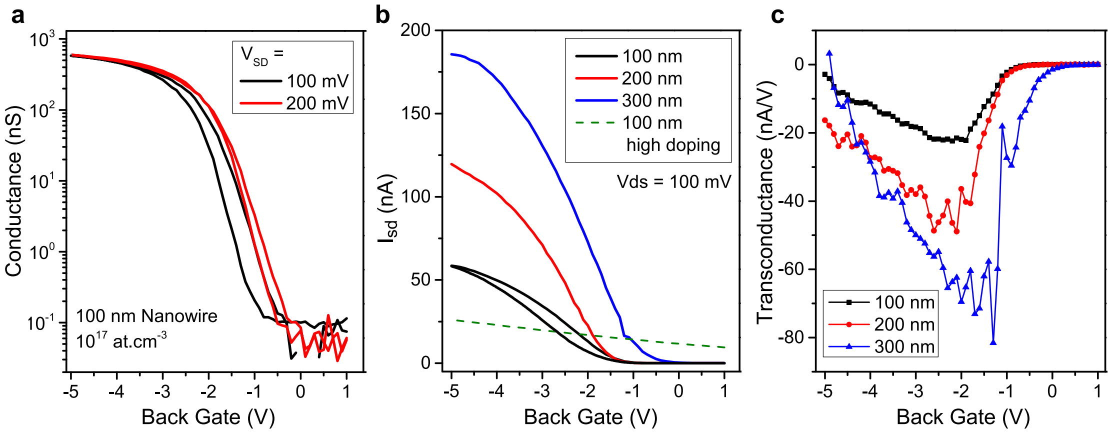

Figure 3.8: Transport characteristics of SiNW-FETs under ambient conditions. a) Back-gate induced modulation of the conductance of a 100 nm wide NW-FET. b) Back-gate effect on nanowires with different widths. The hysteresis is exemplary shown in the black curve for the 100 nm wide nanowire. The dashed green line corresponds to a highly doped 100 nm SiNW-FET. c) Transconductance of nanowires with different widths at $V_{SD} = 100$ mV.

The effective carrier mobility of the device can be estimated from the transfer characteristics shown in Figure 3.8. In the linear regime the current is proportional to the applied gate voltage [209]:

$$I = \frac{W}{L}\mu c_{ox}(V_G - V_0)V_{SD} \tag{3.4}$$

with the nanowire width W, length L, the hole mobility μ, the gate oxide capacitance c_{ox} per unit area A, the applied gate voltage V_G, onset gate voltage V_0 and the source-drain voltage V_{SD}. Using the nanowire conductance $G = I/V_{SD}$, we can rewrite Equation 3.4 to $dG/dV_G = W/L\mu c_{ox}$. From this, the hole mobility is given by:

$$\mu = \frac{L}{W}\frac{1}{c_{ox}}\frac{dG}{dV_G} \tag{3.5}$$

and can be easily calculated using the known geometrical size and the transconductance of the nanowire $dG/dV_G = dI/dV_G/V_{SD}$ at the given bias voltage V_{SD} (Fig. 3.8 c). The only remaining unknown parameter in Equation 3.5 is the gate oxide capacitance c_{ox}. In the first approach, considering only the field lines perpendicular to the oxide, the gate capacitance can be estimated to $c_{ox} = C_{ox}/A = \epsilon_0 \epsilon_{SiO_2}/d$. With the back-gate oxide thickness $d = 200$ nm and $\epsilon_{SiO_2} = 3.9$, we get $c_{ox} = 1.73 \cdot 10^{-4}$ F/m^2, which represents the lower bound as the field penetration all around the nanowire is not considered. A more exact estimation can be found in [226, 227], where the nanowire is considered as a metallic wire of radius R embedded in a dielectric ϵ_r on an infinite metal plate in distance d. An analytical expression of gate capacitance in this case is given by: $C_{ox}/L = 2\pi \cdot \epsilon_0 \epsilon_r / ln(2d/R)$ with less than 1% error for $d/R > 6$ ($d/R = 5.3$ for nanowires realized in this work). In our case however the nanowire is lying on the silicon dioxide and is surrounded by air, which leads to a smaller effective dielectric constant $\epsilon_r^{eff} = 2.45$ [226]. The effective radius R of the nanowire can be defined as the radius of a circle with the same area as the nanowire cross section. For our trapezoidal nanowires with widths of 100 nm and 80 nm and the height 50 nm, the effective radius is 37.8 nm. The gate oxide capacitance can be now calculated to

$$c_{ox} = \frac{1}{W} \cdot \frac{C_{ox}}{L} = \frac{1}{W} \cdot \frac{2\pi \cdot \epsilon_0 \epsilon_r}{ln(2d/R)} = 5.6 \cdot 10^{-4} \text{ F/m}^2. \tag{3.6}$$

For a 7 µm long and 100 nm wide nanowire with a transconductance of $dI/dV_G = 20$ nA/V at $V_{SD} = 100$ mV (Fig. 3.8 c), this leads to an effective hole mobility:

$$\mu = 250 \text{ cm}^2\text{V}^{-1}\text{s}^{-1},$$

in agreement with the values reported for the bulk silicon and slightly higher than for the top-down fabricated nanowires in the literature [117, 228, 229]. While a direct comparison with the literature is difficult, since the carrier mobility strongly depends on the nanowire dimensions, doping concentration and the fabrication process [117, 228], the fact that the mobility extracted for our nanowires is on the range of the bulk values with similar doping concentration reveals the quality of our fabrication process.

3.4.2 SiNW-FET performance in liquid environment

After the successful electrical characterization of fabricated SiNW-FETs in ambient environment, now the active oxide interface of the nanowires is exposed to an electrolyte solution. The ionic/liquid gating properties are tested in solutions of different pH-values and in cell culture medium (Neurobasal, Invitrogen) for future neuron interfacing applications. For the liquid operation, a PDMS chamber is fixed on the chip and filled with the electrolyte. A source-meter is used to apply the DC source-drain voltage and to measure the source-drain current through the NW channel, the liquid gate voltage V_{lg} is applied to a Pt electrode immersed in the aqueous solution above the NWs. At the same time, a silver chloride reference electrode might be used to measure the liquid potential as shown in Figure 3.9 a. For pH detection, the reference liquid gate potential is set to 0 V, the liquid chamber is subsequently filled with a solution of different hydrogen ion concentration and the pH-induced conductance change is measured. With increasing pH, i.e. decreasing concentration of positively charged hydrogen ions c_{H^+} [$\text{pH} = \log_{10}(1/c_{H^+})$], there is an increase in the negative charge on the NW surface, which acts as a negatively charged top gate and leads to a carrier accumulation in the nanowire channel increasing its conductance. The conductance modulation is hereby fully reversible and stable in time, as shown in Figure 3.9 b. The pH-sensitivity of the nanowires is around 210 nS/pH. The response time is very high, which is mostly due to the manual changing of different pH solutions. From this measurement, we can also estimate the sensitivity of the nanowire to potential changes. Using the Nernstian pH response of 60 mV/pH [218] or the Subnernstian response of 30 mV/pH [230], the nanowire sensitivity to potential changes of the liquid gate can be estimated to 3.5 µS/V and 7 µS/V respectively.

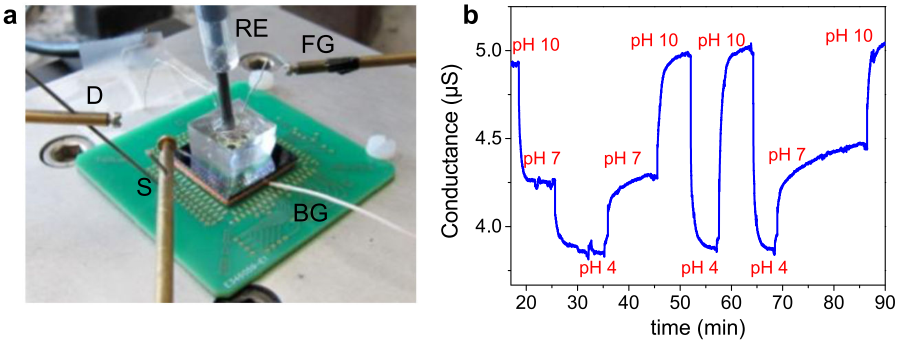

Figure 3.9: Liquid gate operation of SiNW-FETs. a) Experimental setup: a PDMS chamber is glued onto the chip and filled with an electrolyte solution. A needle probe station is used to apply a bias voltage V_{SD} between the source (S) and drain (D) contact. A back-gate electrode (BG) and a Pt electrode (LG) are used to set the back-gate V_{bg} and vary the front liquid gate voltage V_{fg}. A silver chloride reference electrode (RE) is used to record the liquid potential b) Detection of pH changes using a SiNW-FET (100 nm wide, 10^{17} at.cm^{-3}) at the reference liquid gate potential set to 0 V.

An estimation of the sensitivity to voltage changes was also performed by directly sweeping the liquid gate potential and measuring the source-drain current at fixed bias voltage V_{SD}. An example of a measurement in cell culture medium is shown in Figure 3.10 a. In analogy to the back-gate, the conductance increases due to the charge carrier accumulation by applying more negative voltages to the liquid gate. The sensitivity to the potential change can be calculated as the slope of the conductance vs. gate voltage (Fig. 3.10 a) to −6 µS/V, which is in good agreement to the value estimated using the pH-detection measurements. Compared to the back-gate induced modulation of the nanowire conductance (−0.2 µS/V), the effect of the liquid gate is considerably higher due to the thinner gate oxide, leading to a higher capacitance.

Next the ability of SiNW-FETs to detect AC signals, similar to action potentials in neurons, was tested. For that purpose, 1 ms long Gaussian potential pulses with varying amplitude were applied to the cell culture medium through the Pt-gate electrode, and the voltage drop at the nanowire was measured at fixed polarization current I_{SD} = 100 nA. The DC-offset of the gate electrode was kept at 0 V to ensure the highest sensitivity (see Fig. 3.10 a). The potential pulses detected by nanowires can be seen in Figure 3.10 b. The detected current signal exhibits a slightly biphasic shape, indicating that the field effect induced current modulation (monophasic negative pulse: $I_{field} = g_m \cdot V_{pulse}$) is superimposed with capacitive current due to the rapid potential change: $I_{cap} = C \cdot \partial V_{pulse}/\partial t$. The capacitive contribution is however lower than the monophasic current change induced by the field effect.

The calibrated sensitivity $S = \Delta C/\Delta V_{lg} \approx$ -3 µS/V is lower than the one obtained previously by sweeping the DC voltage at the Pt-electrode (Fig. 3.10 a). The discrepancy can appear due to the response time of SiNW-FETs, which might be higher than the pulse duration, or due to the shifted working point with the highest sensitivity. The response time was not explicitly measured, however the capacitive contribution observed in voltage pulse detection reveals a rather high interfacial capacitance, which could increase the response time τ given by $\tau = \sqrt{R \cdot C}$ with the capacitance C and resistance R.

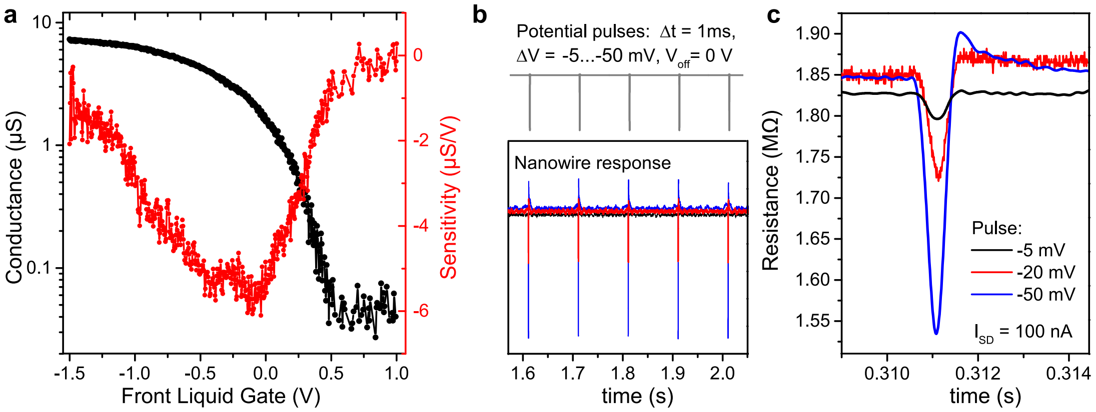

Figure 3.10: Liquid gated SiNW-FETs. a) Modulation of the conductance of a 100 nm wide NW-FET by varying the front liquid gate voltage through the Pt-electrode. b) Detection of short (Δt = 1 ms) potential pulses applied to the front liquid gate using SiNW-FET. c) Zoom of the potential pulses with different amplitudes detected by the SiNW-FET at bias current I_{SD} = 100 nA. The potential pulse induces a resistance/conductance change of the nanowire channel.

In general, the sensitivities of SiNW-FETs fabricated in this work are almost one order of magnitude lower than for SiNW-FETs that have been used for biointerfacing by the Lieber group [111, 113, 231–234]. The discrepancy may arise from the fabrication process of the nanowires. SiNW-FETs of similar dimensions (around 100 nm width) are usually fabricated by a bottom-up approach, which produces nanowires with mobilities reaching 1350 cm^{2}V^{-1}s^{-1} [232], leading to a higher sensitivity. On the other hand, compared to the top down fabricated devices with similar dimensions [99, 115], our SiNW-FETs show similar performance.

3.5 Conclusion

In conclusion, SiNW-FET arrays with varying geometries could be fabricated with reproducible electrical properties. The nanowire FETs exhibit charge carrier mobilities and sensitivities expected for top down fabricated devices of similar dimensions. They show good response to pH changes and to short potential pulses, revealing their suitability for detection of neural activity. To improve the performance of our SiNW-FETs, the relatively low sensitivity can be improved by increasing the width-to-length ratio W/L of the nanowires. However it would decrease the spatial resolution for monitoring the propagation of action potentials. Also, RIE etching of silicon nanowires is known to degrade the device performance [235–237]. Instead, TMAH (tetramethylammonium hydroxide) could be used to etch the nanowires, which was shown to produce nanowires with excellent electronic properties compared to the same device fabricated by RIE [238].

CHAPTER 4

Graphene field effect transistors (G-FETs)

While the general principles of FET technology for bioelectrical interfacing are already presented in Chapter 3.1, here we will directly introduce liquid gated graphene field effect transistors, realized using CVD grown monolayer graphene sheets on Cu. First, the fundamental electronic properties of graphene monolayers and their characteristics observed in transport measurements, such as field effect, will be presented. Then, a novel CVD growth technique used for the production of continuous monolayer graphene sheets in this work will be described, followed by a transfer method and cross-characterization techniques such as AFM and Raman microspectroscopy. Finally the fabrication flow of liquid gated G-FETs, developed in this work, as well as the electrical characterization of realized FETs in liquid environment will be presented, and the suitability of our G-FETs for interfacing with biological entities will be discussed.

4.1 G-FETs for bioelectronics

Besides the silicon technology for the realization of field effect transistors, recently graphene has emerged as an alternative material for bioelectrical interfacing [96, 118]. Graphene, the atomically thin honey-comb carbon lattice, is a conductive material of high carrier mobility, whose exposed surface offers an ideal platform for sensing applications. Compared to other commonly used semiconductors, graphene based biosensors provide a number of advantages, such as chemical stability, robustness and flexibility [122, 123, 214] required for interfacing soft biological tissue and realization of long term neural prostheses. The absence of dangling bonds on the graphene surface associated with the high crystalline quality, and the 2D hole/electron gas directly exposed to the cell without any gate dielectric results in a critical improvement of the electrical coupling between the cell and the device and an enhanced signal-to-noise ratio.

The sensitivity of the transistor to external potential changes is described by its transconductance, which is proportional to the charge carrier mobility and the interfacial capacitance at transistor/-gate interface. While in case of liquid gated Si-FETs, the capacitance depends on the thickness and material of the gate dielectric, for graphene no such insulating layer is used. The interfacial capacitance is then given by the electric double layer (EDL, details in Chapter 4.3), which forms at the graphene/liquid interface. Due to this extremely thin EDL, which results in a high interfacial capacitance, and high charge mobilities, the performance of graphene based transistors exceeds the conventional semiconductors by more than one order of magnitude [126, 128, 239]. At the same time, continuous graphene monolayer sheets of high qualities and large size can be routinely obtained by CVD growth on copper foils [119–121] and then transferred on a wide range of rigid, transparent or flexible substrates, paving the way to large scale integration of graphene electronics. In addition, as we will show, graphene offers high biocompatibility and significantly improves the neuronal growth in cultures. Graphene coating improves neuronal attachment and sprouting [240], increases the stem cell differentiation into neurons [241] and enhances the electrical activity of neural networks in culture [242]. Even without any additional protein for neuronal adhesion, pristine graphene promotes the attachment and growth of neurons [65, 213], revealing a strong neuron/graphene coupling and offering promising perspectives for *in-vivo* recordings. During the past few years, graphene has indeed been shown to be an extremely promising material for tissue engineering, regenerative medicine [243] and was successfully used to record electrical signals from cardiomyocytes [127, 128], hinting at the feasibility of a neuron-graphene interface and its possible applications for neural prostheses.

4.2 Graphene: from crystal structure to field effect transistor

Graphene is a single layer of carbon atoms organized in a honey-comb crystal lattice, as illustrated in Figure 4.1 a. The primitive cell of graphene consists of two different atoms A and B arranged in a triangular sublattices with a carbon-carbon distance $a = 1.44$ Å [244]. Each carbon atom in the hexagonal lattice has 4 electrons with a ground-state electronic shell configuration of [He]$2s^2 2p^2$. The superposition of $2s$ with $2p_x$ and $2p_y$ forms hereby energetically stable and localized σ-bonds to three nearest-neighbor carbon atoms. These planar σ-bonds are responsible for most of the binding energy and elastic properties. The remaining free $2p_z$ orbitals form π-bonds and extend vertically above and below the graphene plane, as shown in Figure 4.1 c. The overlap of these orbital states between neighboring atoms plays a major role in the electronic properties of graphene.

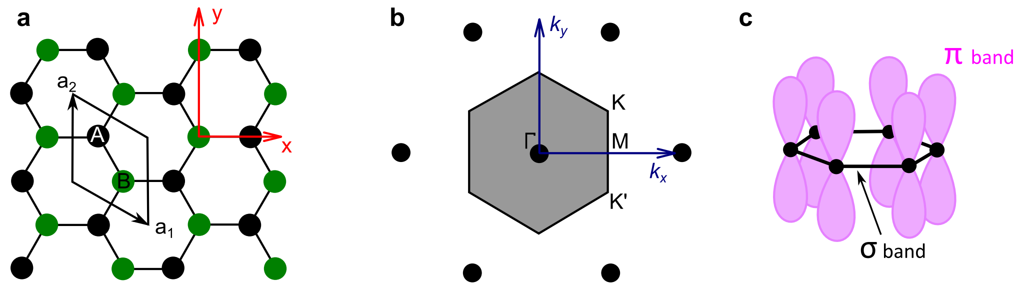

Figure 4.1: Schematic illustration of graphene lattice (adopted from [244]). a) Graphene lattice in real space with basis atoms A and B. b) First Brillouin zone with specific points K, K', M and Γ in reciprocal space. c) σ and π bounds of graphene.

Thus, the electronic structure of graphene can be described by an orthogonal nearest-neighbor tight-binding model with electronic states simply represented by a linear combination of $2p_z$ orbitals. Solving the Schroedinger equation leads to the energy dispersion relation in k space for the upper π^* (+) lower π (-) band [245]:

$$\begin{aligned} \epsilon_{\pm}(\mathbf{k}) &= \pm t\sqrt{3+f(\mathbf{k})} - t' f(\mathbf{k}), \\ f(\mathbf{k}) &= 2cos(\sqrt{3}k_x a) + 4cos(\sqrt{3}k_x a/2)cos(3k_y a/2), \end{aligned} \tag{4.1}$$

where k_x and k_x are the components of the k vector folded onto the first Brillouin zone and $\epsilon \cong 2.75$ eV is the hopping energy. The value of t' is not well known and varies in the range $0.02t \lesssim t' \lesssim 0.2t$ depending on the tight-binding parametrization. For $t' = 0$, the energy dispersion is symmetric for the valence and conductance band. Figure 4.2 a shows a 3D plot of the band structure of graphene obtained for the symmetric condition with respect to the Fermi energy set to 0 eV.

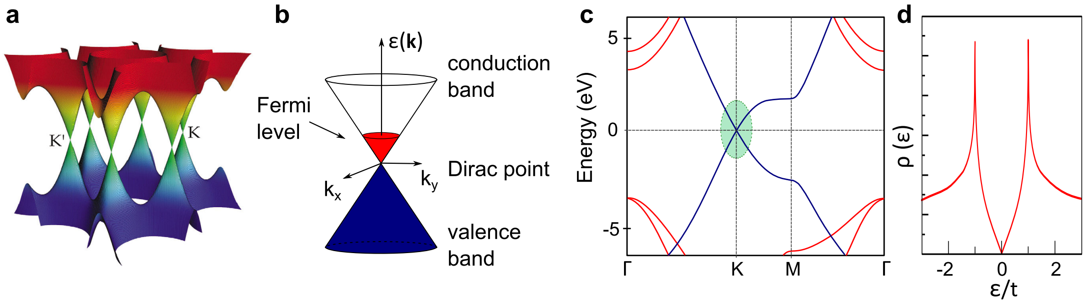

Figure 4.2: Energy dispersion of graphene. a) 3D representation of energy band diagram of graphene [246]. b) Zoom of the low energy region at K point with linear dispersion. For neutral graphene, the Fermi level is at the Dirac point c) Energy dispersion as a cut of 3D diagram in a) along the high symmetry direction Γ-K-M-Γ (adopted from [247]). Red lines are the σ bands and blue lines - the π bands. The linear regime around K point is indicated by a green circle. d) Density of states $\rho(\epsilon)$ as function of energy ϵ (adopted from [245]). DOS is 0 at the Dirac point and is proportional to ϵ in the low energy regime.

Graphene conduction and valence bands are degenerate at the corners of the Brillouin zone, also called K and K' valleys, resulting in a gapless transition (Fig. 4.2 b). Unlike the conventional 2D gas with a parabolic energy dispersion, graphene exhibits a liner dispersion at low energies and has a point contact between upper and lower bands. This point is also called charge neutrality point (V_{NP}) or Dirac point. Close to the Dirac point the energy dispersion and the density of states (DOS) $\rho(\epsilon)$ per unit cell area A_c are given by [245]:

$$\epsilon(\mathbf{k}) = \hbar v_F \mathbf{k} \qquad \text{and} \qquad \rho(\epsilon) = \frac{2A_c}{\pi} \cdot \frac{|\epsilon|}{v_F^2} \tag{4.2}$$

with the Fermi velocity $v_F = \partial\epsilon/\partial k = \sqrt{3}at/2 \approx 10^6$ m/s. The density of states available for transport exhibits a symmetrical electron-hole nature and is obviously zero at the Dirac point. For the low energy region, the DOS can be approximated to $\rho \propto \mid \epsilon \mid$ (Fig. 4.2 d). The density of state determines the conductance of the graphene sheet σ, which can be expressed as [245]:

$$\sigma = D \cdot \rho(\epsilon) \cdot \mathrm{e}^2 \tag{4.3}$$

with the diffusion constant D and elementary charge e.

Due to the linear band structure combined with the absence of charge screening in atomically thin graphene layers, the charge can be experimentally adjusted in density and sign by simply tuning the Fermi level (shadowed cut in Fig. 4.2 b) using a gate voltage V_g. This makes graphene the first atomically thin ambipolar field effect transistor. The density of states and thus the conductance σ of graphene can be directly tuned from the electron to hole conductance regime with a minimal conductance at the charge neutrality point. This gate induced conductance modulation is called field effect. Theoretically the DOS and thus the conductivity at the Dirac point should be zero (Fig. 4.2 d), but due to the presence of charge traps in the substrate, so-called charge puddles are formed in graphene [248], resulting in a non-zero minimum conductivity. Also, usually the Dirac point is not centered at zero gate voltage, but shifted to more negative or positive gate voltage values, indicating a positive or negative doping.

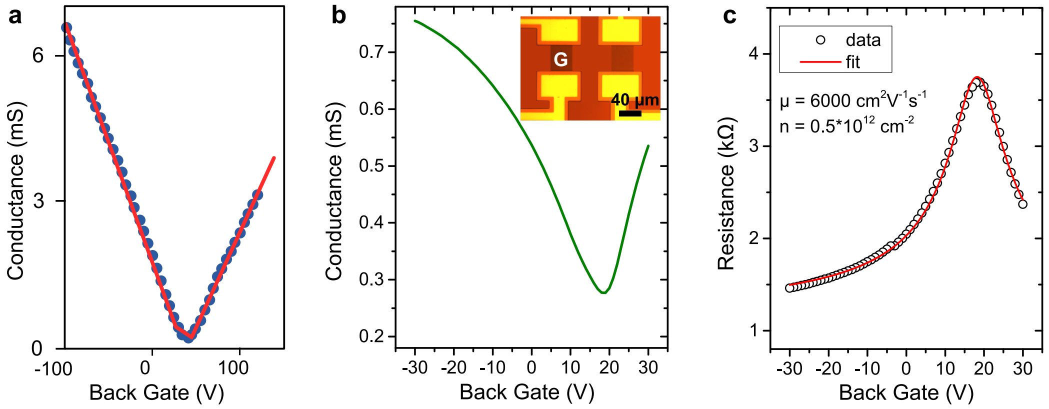

Figure 4.3: Field effect in graphene transistors a) Field effect curve measured at 70 K, data from [249]. b) Two point measurement of field effect curve on 40×60 µm^2 graphene transistor from our CVD grown continuous single layer graphene. The measurement was performed in air at room temperature. The conductance is modulated by a p-doped Si back-gate with 285 nm thick SiO$_2$ gate oxide. The device is shown in the inset: a 40 µm wide graphene stripe (G) was etched by oxygen plasma followed by contact metal deposition [Ti (5nm)/Au (45 nm)] and contact passivation using photoresist for future liquid operations. c) Field effect curve measured on similar device at same conditions as in b). Data are plotted as resistance vs. gate voltage and fitted using Equation 4.6 for mobility extraction.

According to Equation 4.2 and 4.3 the ideal conductance vs. gate voltage σ - V_g curve should be symmetrical for the electron and hole regime as illustrated in Figure 4.3 a. However, often, the σ - V_g field effect curve is not symmetrical (Fig. 4.3 b) due to different scattering mechanisms [250], inhomogeneities in the graphene layer, or asymmetric Schottky barriers formed between the electrodes and graphene for electron and hole sides [251].

Experimentally, a graphene field effect transistor is realized by transferring graphene on a thick dielectric material (285 nm SiO_2 on Si substrate in our case). The charge is then modulated by a capacitive coupling $Q = C_{ox}V_g$ with charge Q, oxide capacitance C_{ox} and applied gate voltage V_g. The charge carrier concentration induced per unit area, per unit Volt, is given by:

$$n_{unit} = \frac{\epsilon_{ox}\epsilon_0}{d \cdot e} \sim 7.56 \cdot 10^{10}\mathrm{cm}^{-2}\mathrm{V}^{-1} \quad \text{(for 285 nm SiO}_2\text{)} \tag{4.4}$$

where e is the elementary charge, d the thickness and ϵ_{ox} the dielectric constant of SiO_2.
A good quality indication of graphene transistors is the mobility μ. To extract the mobility different scattering mechanisms, such as elastic scattering including charge impurities, neutral defects and charge transfer from doping, substrate or surface roughness, as well as inelastic scattering on graphene or substrate phonons, should be taken into account [250]. However, the fitting technique [252] presented below also gives a good approximation. One can extract the mobility in the diffusion region using the conductivity G and the charge carrier concentration n:

$$G = \frac{1}{R - R_c} = \sigma\frac{W}{L} = ne\mu\frac{W}{L} \quad \text{and} \quad n = \sqrt{n_0^2 + [n_{unit}(V_g - V_{NP})]^2} \tag{4.5}$$

From this, the graphene resistance R is:

$$R = \frac{L/W}{e\mu\sqrt{n_0^2 + [n_{unit}(V_g - V_{NP})]^2}} + R_c \tag{4.6}$$

where W/L is the width divided by length (aspect ratio) of the device, R_c is the contact resistance, and n_0 the residual carrier concentration. Using the formula above one can fit the mobility, R_c and n_0 by measuring the resistance vs. gate voltage curve as shown in Figure 4.3 c.

4.3 Electric double layer in liquid gated G-FETs

Usually, the charge carrier concentration in graphene field effect transistors is modulated by using the back or top gate technique. According to Equation 4.4 the additional charge induced by the gate is proportional to the dielectric constant ϵ_{ox} and to the inverse of the thickness d_{ox} of the gate oxide. Thus reducing the oxide thickness while using so-called high k dielectrics, would increase the gate effect. However, due to the low breakdown voltages V_{BD} of these materials, the maximum induced carrier concentration n can reach 10^{13} cm^{-2}.
Besides the conventional back/top gate technique, the charge concentration can be modulated by an electrolyte solution in direct contact with graphene, which is also often referred to as liquid gating. The electrolyte consists of a liquid or gel matrix with dissolved ions. Many different electrolyte solutions with optimized characteristics for particular applications are known. But even water or any other liquid would act as a liquid gate. When a device, here graphene, is exposed to the liquid, an electrical double layer (EDL) forms at the surface [253]. The EDL is an array of charge particles and orientated dipoles at the interface. In the case of a conductive

surface, it consists of a layer of electrons, a layer of adsorbed atoms and a thin diffusive layer, in which the positive or negative ions are in excess. A schematic of the EDL is shown in Figure 4.4 a. By applying an external electrical field to the liquid, the ionic concentration in the EDL and thus the potential at the liquid/device interface can be tuned. The liquid is now acting as a gate and the EDL as a gate dielectric. Due to the extremely low EDL thickness, which around 1 nm, the gate capacitance is much higher than for back or top gate operation with 285 nm SiO_2 or $\sim$ 10 nm top gate dielectric thickness respectively. Thus, using liquid gating, much lower gate voltages are required to induce the same charge carrier density as in case of a back-gate, as shown in Figure 4.4 c. Using ionic solution gating, charge carrier concentration can be tuned up to $4{\cdot}10^{14}$ cm^{-2} in graphene [254, 255].

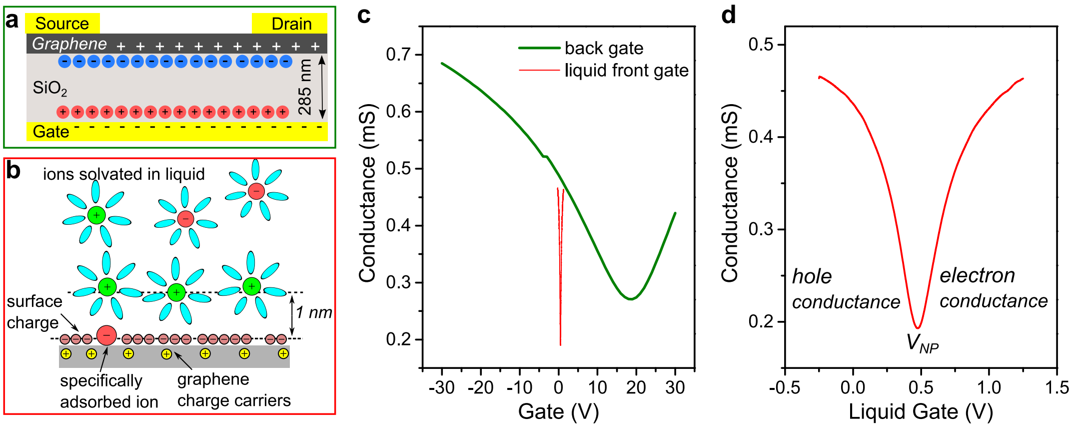

Figure 4.4: Liquid gated graphene field effect transistors. a) Schematic illustration of electrostatic doping using conventional back-gate with SiO_2 oxide. Opposite charges are separated by the thickness of the oxide. b) Schematic of electric double layer formed at graphene/ionic liquid interface. EDL thickness is around 1 nm. c) σ - V_g field effect curves obtained by back and liquid gating (green and red line respectively). d) Liquid gating of graphene transistor with identified hole and electron conduction regime, and charge neutrality point at around 0.5 V, indicating a slightly hole doped nature of our graphene. Same data as in c) red line.

The EDL capacitance C_{EDL} can be estimated by comparing the back-gate and liquid gate induced conductance modulation on the same G-FET [125]. The conductance σ varies with the gate voltage in proportion as: $\partial\sigma/\partial V_{bg} = C_{bg} \cdot \mu_{bg}$, and $\partial\sigma/\partial V_{lg} = C_{EDL} \cdot \mu_{lg}$, where μ is the field mobility and subscript bg (lg) means back (liquid) gate. Assuming a constant mobility for both operation regimes, C_{EDL} can be expressed as:

$$C_{EDL} = \frac{\partial\sigma/\partial V_{lg} \cdot \mu_{bg}}{\partial\sigma/\partial V_{bg} \cdot \mu_{lg}} \cdot C_{bg} = \frac{\partial\sigma/\partial V_{lg}}{\partial\sigma/\partial V_{bg}} \cdot C_{bg}. \tag{4.7}$$

With the back-gate capacitance given by the 285 nm thick SiO_2 layer: $C_{bg} = \epsilon_0 \epsilon_{SiO_2}/d_{SiO_2} =$ 12 nF/cm^2, and the maximal conductance variation $\partial\sigma/\partial V_g$ calculated from the curves in

Figure 4.4 c for both, back and liquid gate, the EDL capacitance can be estimated to:

$$C_{EDL} = \frac{0.977\ \mathrm{mS/V}}{0.015\ \mathrm{mS/V}} \cdot 12\ \mathrm{nF/cm^2} = 0.78\ \mathrm{\mu F/cm^2}. \tag{4.8}$$

The EDL capacitance is in good agreement with values obtained by using complementary back/liquid gate measurements and reported in the literature [125], and is more than one order of magnitude higher than the conventionally used gate oxide capacitance.

4.4 CVD growth of graphene on Cu

Monolayer graphene was first produced in 2004 by repeated mechanical exfoliation of graphite using scotch tape [249]. Since then several techniques have been established for graphene synthesis, such as chemical exfoliation [256, 257], chemical synthesis [258], and thermal chemical vapor deposition [259]. Although the mechanical exfoliation allows production of very clean single crystal graphene, the exfoliated flakes are very small and not suitable for large scale integration. Also chemical exfoliation, where solution dispersed graphite is exfoliated by inserting large alkali ions between the graphite layer, or chemical synthesis, which produces graphene by reduction of graphene oxide, suffer from the same drawback. One of the best processes for large-scale fabrication of high quality graphene is chemical vapor deposition [260]. Two kinds of CVD techniques for graphene synthesis are known: plasma assisted CVD and thermal CVD. The latter one was also used for the synthesis of graphene sheets used in this work.

In a thermal CVD process, the growth substrate is exposed to thermally dissociated precursors and the desired product is deposited onto the substrate at high temperature. First the deposition of monolayer graphitic material by thermal CVD was reported in 1975 on Pt [261], and later in 1979 on Ni [262], followed by a significant amount of research to improve the growth conditions [214, 259, 263, 264]. However, large-scale monolayer graphene fabrication was still in demand, until the catalytic graphene deposition on Cu was discovered [119]. With regards to commercially available high quality Cu foils, the large-scale graphene synthesis became feasible. For example, the largest graphene sheet reported so far was grown on Cu and is 30 inches wide [120], paving the way to mass production.

When choosing the transition metal substrate for CVD growth of graphene, the carbon solubility of the material has to be considered. Carbon solubility means, that carbon atoms not only attach on the surface, but can also diffuse into the bulk material, and its value varies for different metals in the range from 10^{-4} to 10^{-2} atomic fraction [265]. However due to the low activation energy of bulk diffusion, the exchange of bulk atoms and surface adatoms can take place, meaning that some of the dissolved carbon atoms are segregated from the bulk to the surface. At a certain amount these atoms start to nucleate at the surface, building the source for graphene growth. As long as the nucleation conditions are met (certain temperature, gas flow and pressure) segregation continues regardless of whether there is already a graphene layer on the surface or not, and gives rise to the formation of multilayer patches or even thick graphite flakes, which is usually observed for the growth on Ni substrates [259].

Thus, to obtain a monolayer graphene sheet, a metal with low carbon solubility is needed, such as Cu, Ag or Au. Obviously because of cost reasons, Cu is the most attractive candidate for CVD fabrication of graphene. Besides, Cu foil is available in different sizes and thicknesses, and it is fully soluble in standard etchants, making the graphene transfer onto different substrates possible.

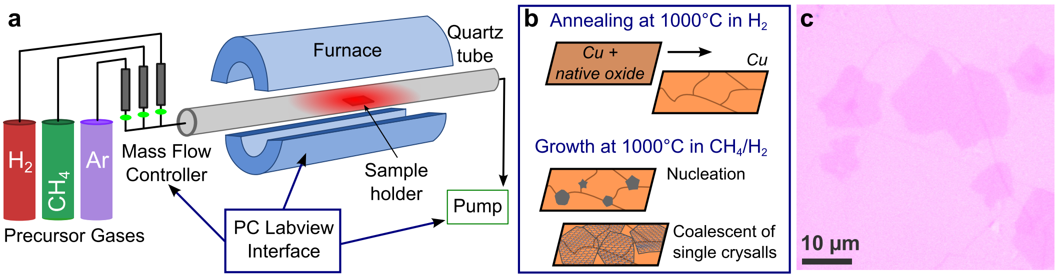

Figure 4.5: CVD growth of graphene on Cu. a) Schematic of the home made CVD reactor with 4 inch quartz tube and effective heating length of about 30 cm. A labview interface was designed for real time control of growth parameters. b) Schematic illustration of growth mechanism. c) Formation of multilayer patches under the continuous monolayer graphene grown by a conventional CVD process. Picture is taken by optical microscope after transferring graphene onto Si/SiO_2 substrate.

Graphene on Cu is grown by decomposition of methane gas over the Cu surface at high temperature in diluted hydrogen atmosphere. Usually H_2 is diluted in an inert gas, such as Ar, which is also used to reduce the partial pressure. A schematic of the CVD setup used in this work is illustrated in Figure 4.5 a. A typical growth protocol (Fig. 4.5 b) starts with annealing of a 25 μm thick Cu foil (Alfa-Elsar) at 1000°C in diluted H_2 environment for around 2 hours to reduce the native Cu oxide. Then, a small flow rate of CH_4 is injected as a carbon source. The carbon atoms form nucleation centers, preferentially at Cu grain boundaries, from which graphene crystals with different orientations emerge. Depending on the pressure and gas concentration, differently shaped single crystals of graphene can be obtained. For longer deposition time, single crystals coalescence and form a homogeneous single layer of graphene.

Due to the low carbon solubility, graphene growth on Cu is believed to be a self-terminated process, i.e. once a single layer of graphene is formed over Cu and no catalytic surface is available, no more carbon deposition takes place. However, the graphene layers grown on Cu foil still exhibit multilayer patches (Fig. 4.5 c), which affect the physical and electrical properties of graphene. It was shown by Zheng (Vitto) Han, a former PhD student at Institut Néel, that these multilayer patches are formed under the first graphene layer [266], meaning that segregation of carbon atoms from Cu bulk occurred during the deposition. The source or these dissolved carbon atoms was found to be in Cu defects. A novel growth technique (pulsed CVD) was then developed by Z. Han et al. to obtain large area homogeneous single layer graphene by in-situ removal of the multilayer patches [267] (Fig. 4.6).

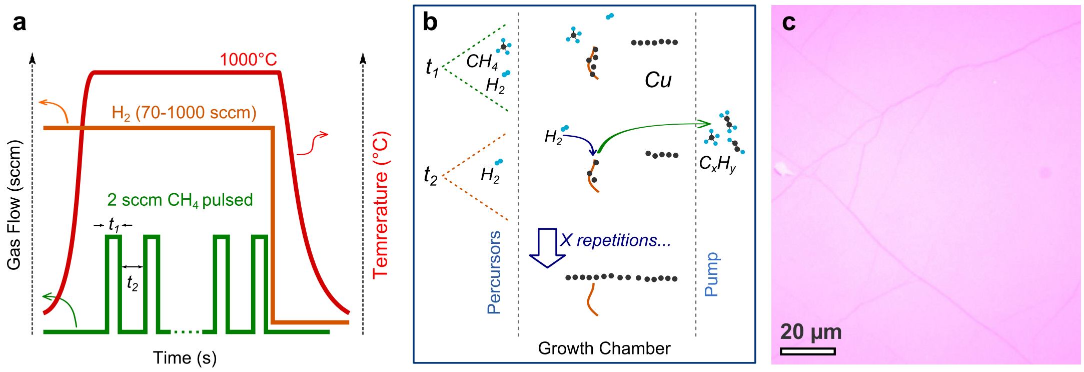

Figure 4.6: Pulsed CVD growth of graphene on Cu (schematics adopted from [266]). a) Schematic illustration of pulsed CVD growth of graphene. While the hydrogen flow is kept constant, t_1 long pulses of methane are injected into growth chamber. During the idle time, t_2, Cu substrate with graphene growing on the surface is exposed to hydrogen atmosphere. b) Schematic of growth mechanism using pulsed CVD method. In the idle time, t_2, carbon atoms trapped in the defects (orange line) are removed by forming C_xH_y species with H_2. c) Optical image of graphene layer obtained by pulsed CVD and transferred onto Si/SiO_2 substrate.

This growth method is based on the fact, that hydrogen partially etches graphene. However, due to the very stable sp^2 lattice, the etching preferentially occurs on crystal edges and unbound carbon atoms dissolved in Cu defects. The schematic of the growth process is shown in Figure 4.6 a, b. While in the conventional CVD growth of graphene, a continuous flow of CH_4 is added to the diluted H_2 environment in the growth chamber, here pulses of CH_4 flow with duration of t_1 are used. In the time, t_2, no carbon species are present in the chamber, and the Cu surface is directly exposed to hydrogen. H_2 molecules can then bind dissolved/segregated C atoms to C_xH_y species, which are carried out from the growth chamber. By adjusting the t_1/t_2 ratio, large monolayer graphene films with mobilities up to 6700 $cm^2V^{-1}s^{-1}$ can be obtained. More details on pulsed CVD growth of graphene can be found in [267].

4.5 Transfer of graphene layers on arbitrary substrates

Besides the great interest in graphene for fundamental research, large scale CVD production has long taken it to industrial level with applications in optical systems [268], nanomechanical engineering [269], transparent electronics [120, 270] or biomedical platforms [271, 272]. However for all these applications, CVD graphene has first to be transferred onto arbitrary substrates, either a polymer, or an insulator (SiO_2, sapphire, quartz, etc.).

One of the most common transfer methods used in research and industrial graphene production, is polymer assisted wet transfer, illustrated in Figure 4.7 and in Figure 4.8 a-d. Here, graphene is first covered by a supporting polymer layer, such as PMMA, and the underlying Cu is then etched in an aqueous solution, containing a specific Cu etchant. Once the Cu foil is completely dissolved, graphene-PMMA stuck remains floating on the surface of the etchant solution. After several deionized (DI) water baths, carried out in order to remove the etchant, graphene-PMMA is scooped out from below (fished) onto a substrate. Directly after fishing, there is a water film between graphene and the substrate, which allows to adjust the position of graphene. The substrate with graphene-PMMA is then dried at room temperature for 1-2 hours, followed by a heating step at 120°C for 10 min to dehydrate the sample. Finally, PMMA is removed in an overnight acetone bath, the sample is then rinsed in isopropanol and dried with nitrogen gun. To increase the adhesion of the graphene layer to the substrate, the sample is then heated to 180°C for 3 min.

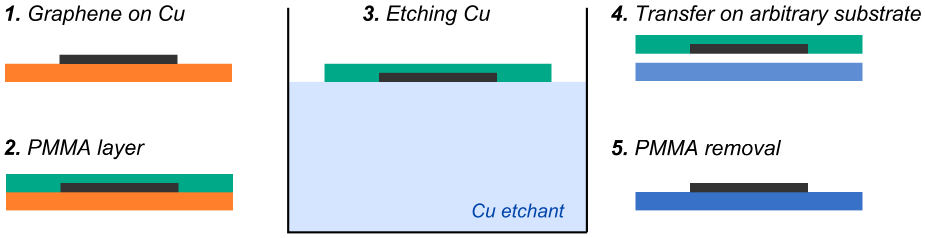

Figure 4.7: Schematic illustration of wet transfer technique.

Several etchants, such as ammonium persulfate $(NH_4)_2S_2O_8$, sodium persulfate $Na_2S_2O_8$ or iron (III) chloride $FeCl_3$, are known to efficiently remove Cu. However, it was found in our group, that long time etching in sodium persulfate will induce disorder in graphene, and using $FeCl_3$ results in a poor graphene quality compared to $(NH_4)_2S_2O_8$ [266]. Consequently, in this work, Cu foil was etched using an aqueous solution of $(NH_4)_2S_2O_8$ with a concentration of 0.1 g/ml. Usually, it requires about 2 h at room temperature and 30 min at 40°C to etch the Cu foil. Since both, copper and ammonium persulfate, are toxic for biological applications, great care was taken to assure a complete Cu etching and removal of etchant residuals (6 subsequent washings in DI water).

For a successful graphene transfer, the substrate surface has to be clean and hydrophilic. A clean/smooth surface is required to avoid mechanical stress, folding or ripping of the graphene layer, and to reduce the amount of scattering centers induced by surface contamination/roughness, therefore preserving good electrical properties of as grown graphene. The hydrophilicity is important to form a water film on the substrate surface, on which the graphene-PMMA stack can float. Thus, prior to transfer, substrates are cleaned using subsequent ultrasonic baths in acetone, isopropanol and DI water, followed by oxygen plasma treatment, which makes the surface more hydrophilic.

Using wet transfer technique as described above, graphene layers could be easily transferred onto a variety of substrates, such as Si/SiO$_2$, sapphire, quartz, glass coverslips, polyimide, PDMS and parylene. More precisely, in this work graphene FETs could be realized by transferring graphene on Si/SiO$_2$, sapphire, glass and polyimide (on Si/SiO$_2$ substrate). Some examples of transferred graphene are shown in Figure 4.8.

The main drawbacks of this transfer method are the PMMA residuals on the graphene surface and the water residuals (probably loaded with ions) trapped between the substrate and graphene, which act as scattering centers for electron transport. While the ions trapped under the graphene layer are impossible to avoid, PMMA residuals can be reduced by using low molecular weight PMMA or by annealing the sample at high temperature (300-500°C) under UHV or in inert atmosphere.

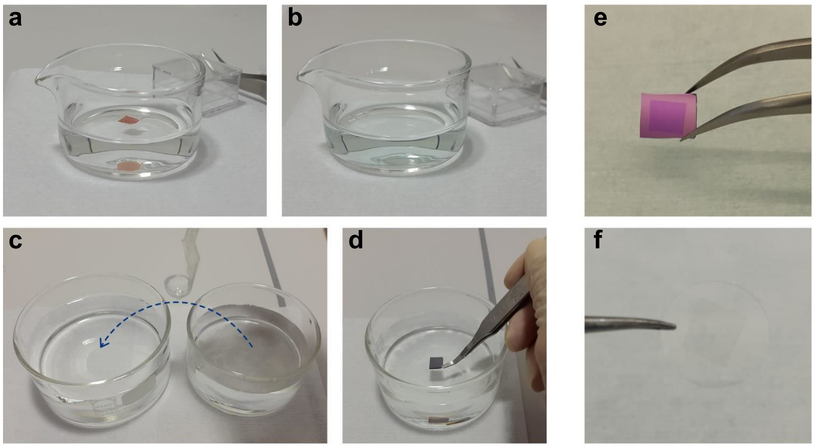

Figure 4.8: PMMA assisted wet transfer of graphene on Cu onto different substrates. a) Etching Cu foil in $(NH_4)_2S_2O_8$ solution. b) By dissolving Cu, the color of etchant turns from transparent to light blue. Graphene with PMMA floats on the surface with graphene in direct contact with the solution. c) Graphene-PMMA is then subsequently washed in DI water to remove the etchant. Using a "spoon", graphene with PMMA is transferred from one beaker to the next. d) Graphene is fished from below onto substrate. e) Graphene can be transferred onto different substrates, here on Si/SiO_2 and f) on glass coverslip.

A very promising method of transferring CVD grown graphene onto parylene was recently developed at Institut Néel by Dipankar Kalita [273]. Here, parylene is directly deposited on graphene on Cu foil under high vacuum conditions followed by Cu etching and rinsing in DI water. In contrast to wet transfer technique, the active graphene surface (at the interface to Cu foil) is never in contact to a sacrificial PMMA layer, bypassing the problem of possible PMMA residuals. Also, no water residuals can be trapped between the substrate and graphene. Thus, this technique allows a simple production of high quality graphene layers on parylene for flexible transparent electronics. Since the electrode flexibility is also required for interfacing soft biological tissues, this transfer method has a great potential for biomedical applications.

Unfortunately, since this work is focused on development of rigid sensors for *in-vitro* cell interfacing, and due to the time limitation, graphene on parylene could not be further investigated in biomedical context. All samples in this work are realized by PMMA assisted wet transfer technique.

4.6 Characterization of graphene sheets

Before the fabrication of devices, transferred graphene is characterized in terms of its homogeneity, surface state and crystalline quality. Some information about the quality of CVD produced graphene can be already obtained prior to the transfer. Usually, directly after growth, graphene on Cu is observed using SEM. Typical images are shown in 4.9. SEM analysis allows a fast observation of sheet homogeneity and presence of contaminations or multilayer patches, but also individual grains of polycrystalline Cu foil can be seen by SEM due to the different crystal orientation and therefore different conductivity. A typical feature of CVD graphene on Cu is the formation of graphene layer folds. These folds are not interrupted by grain boundaries of Cu foil (Fig. 4.9 b), revealing the homogeneity of the graphene layer.

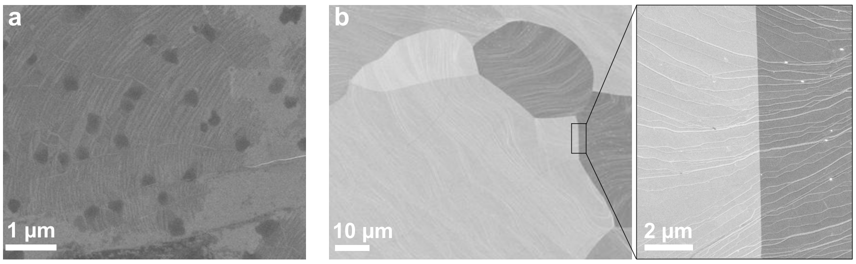

Figure 4.9: SEM images of graphene on Cu foil. a) Graphene layer with a high density of small multilayer patches/amorphous carbon, formed due to defective Cu foil. b) Graphene layer grown on good quality Cu foil using pulsed CVD method with typical graphen folds and individual Cu grains. The zoomed view shows graphene uninterrupted graphene folds at Cu grain boundaries. Also some contaminations, bright dots, can be seen (SEM image by C. Berne).

4.6.1 Atomic force microscopy

After the transfer, graphene layer can be observed using an optical microscope, which gives a brief idea about the homogeneity and the surface cleanliness of the transferred layers (for example, Fig 4.6 c). But to have a more detailed analysis of the surface morphology, atomic force microscopy (AFM) is clearly a better choice. This relatively easy technique can scan large surface areas (up to 100µm) with a topographic resolution of below 0.5 nm. Using the AFM technique, surface contaminations, such as PMMA residuals or nanoparticles, and typical graphene wrinkles can be seen. Moreover, due to the high resolution, even the number of graphene layers can be determined, making AFM a powerful tool for characterization of graphene layers. In this work, AFM analysis is mostly used to determine the cleanliness of the graphene surface. Especially, as a direct consequence of the wet transfer technique, PMMA residuals play a major role in surface state of our graphene. These residuals can increase the contact resistance of fabricated FETs, but also affect the interface of graphene to the living tissue. Thus, a detailed analysis of surface morphology is of great importance.

One way to efficiently remove PMMA residuals, is to anneal graphene at high temperature either under low pressure or in a forming gas, such as H_2/Ar. Figure 4.10 shows surface scans of different graphene layers before and after annealing at 300°C/$5{\cdot}10^{-7}$ mbar for 3 hours. As can be seen in Figure 4.9 a, b PMMA residuals are removed by annealing. Resist residuals are more often found on defects, such as multilayer patches, amorphous carbon or wrinkles, somehow forming carbonated PMMA, which is difficult to remove by annealing, as shown in Figure 4.10 c.

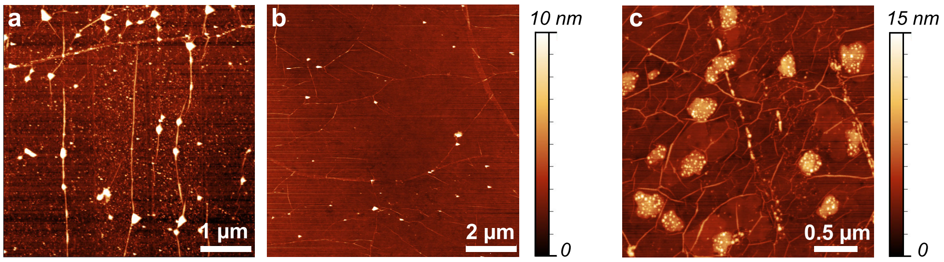

Figure 4.10: AFM analysis of graphene surface. a) Graphene surface directly after transfer exhibits large amount of PMMA residuals (small bright dots) and some bigger contaminations under garphene layer, probably originating from the used Cu foils. Also, the typical wrinkles are observed. b) Same graphene after annealing at 300°C/5·10^{-7} mbar for 3 hours. While the bigger contaminations remain, PMMA residuals are removed. c) Graphene with multilaer patches/amorphous carbon (as in Fig. 4.9 a) after the same annealing procedure. PMMA residuals preferentially remain on graphene defects. These carbon-PMMA compounds are more resistive to annealing.

Both, SEM and AFM, give information about the macroscopic quality of graphene, leaving out its crystalline structure. On a small scale (around 100nm), the crystallinity of graphene can be characterized by transmission electron microscopy (TEM). This technique has single atom resolution and allows to see the honey-comb lattice (with eventual defects) of monolayer graphene or Moire pattern in case of bilayer graphene. However, the TEM scans are time consuming and provide only localized observations. Also, the sample preparation is difficult, especially in case of the CVD graphene due to the high amount of PMMA residuals. Another powerful technique to characterize graphene is Raman spectroscopy, which will be discussed below in more detail.

4.6.2 Raman spectroscopy

Raman spectroscopy is a powerful tool to probe graphene quality on a large scale. It is applicable at both research labs and industrial mass-production, and offers a fast, non-destructive characterization of atomic structure and electronic properties of graphene. It is able to identify the number of layers [274], structural defects [275], functional groups and chemical modifications [276] introduced during the preparation/processing of the sample, which make Raman spectroscopy an ideal tool for quality control of produced graphene.

Raman scattering of phonons can be coupled to internal and external perturbations, which will then be apparent in the measured spectra. For example, information about doping [277], edges [278, 279], strain and stress [280, 281], disorder [275, 282], electrical mobility [283], oxidation [284] or hydrogenation [285] can be extracted from Raman spectra.

A brief introduction to Raman spectroscopy can be find in Chapter 2.4.4. Here, a detailed presentation of the Raman processes in graphene will be given. In Raman spectroscopy [188], the incident light with frequency ω is inellastically scattered on the lattice vibrational modes of the probed material (Fig. 4.11 a). The detected frequency of scattered photon is one vibrational mode ω_0 different from the incident photon: $\omega - \omega_0$ *(Stokes)* and $\omega + \omega_0$ *(anti-Stokes)*. This

frequency change is often referred to as Raman shift. The Raman spectra reported in the literature are usually due to Stokes scattering, since the anti-Stokes process is not likely at the room temperature.
The mechanism of Stokes scattering can be described as following. An incoming photon ω excites an electron-hole pair $e - h$, which rapidly decays into a phonon ω_0 and another electron-hole pair $e' - h$. The latter recombines, emitting a photon $\omega - \omega_0$. This process can involve multiple phonons or even defects with wavevectrors $q_{n,m}$ and d respectively (n and m indicate different phonons). Quantum-mechanically, the selection rules for Raman processes are based on energy and momentum conservation, so that $q_n \mp q_m \sim 0$, or $q_n \mp d \sim 0$, must be fulfilled, as schematically shown in Figure 4.12 b-e.

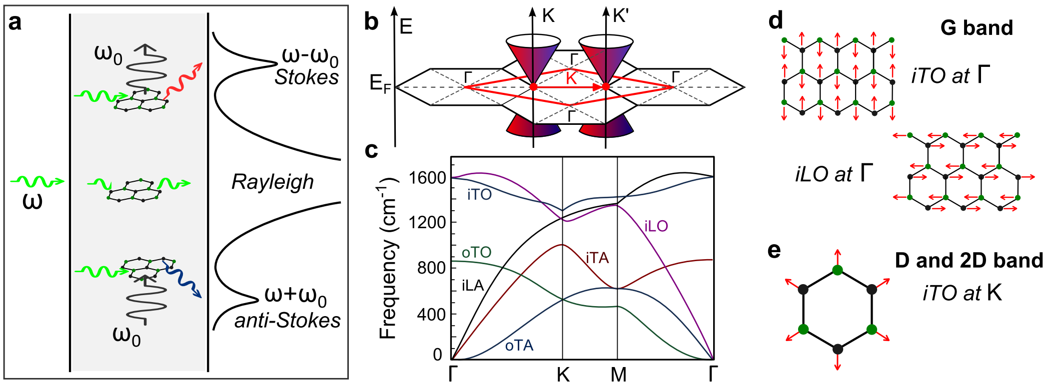

Figure 4.11: Raman spectroscopy on graphene. a) The incoming photon is scattered in graphene either elastically with no change in the frequency ω (Rayleigh), or inelastically (Raman) by emission or absorbtion of a phonon ω_0 and corresponding frequency shift: $\omega - \omega_0$ (Stokes), and $\omega + \omega_0$ (anti-Stokes). b) Electronic Brillouin zones of graphene with schematic of electron dispersion (Dirac cone). Red lines indicate the phonon wave vectors connecting electronic states in different valleys (from [286]). c) Phonon dispersion of graphene (adopted from [274]). d) Displacement pattern of graphene atoms at Γ-point, contributing to the G band peak, and e) at K point, also called breathing mode, contributing to the D and 2D band peak (from [287]).

The phonon dispersion of graphene is shown in Figure 4.11 c. Since the graphene unit consists of two sublattices, there are six phonon branches [274]: three optical (O) and three acoustic phonons (A). Two of these phonon branches (one optical and one acoustic) are out of plane (o), and the other four in plane (i). Depending on whether the direction of the zone-center mode is along the carbon-carbon bond (C-C) or perpendicular, the modes are called transverse (T) or longitudinal (L). The iLO and iTO phonon branches are responsible for most of the Raman peaks observed in graphene. A schematic illustration of these lattice vibrational modes in real space can be seen in Figure 4.11 d and e.

In this work, the micro-Raman spectroscopy on graphene was always performed with a commercial Witec Alpha 500 setup and laser excitation wavelength $\lambda_{exc} = 532$ nm. A typical Raman spectrum of our defective monolayer CVD graphene on 285 nm SiO_2 is presented in Figure 4.12 a. The characteristic Raman peaks of graphene [287], D, G, D' and 2D, will be presented below.

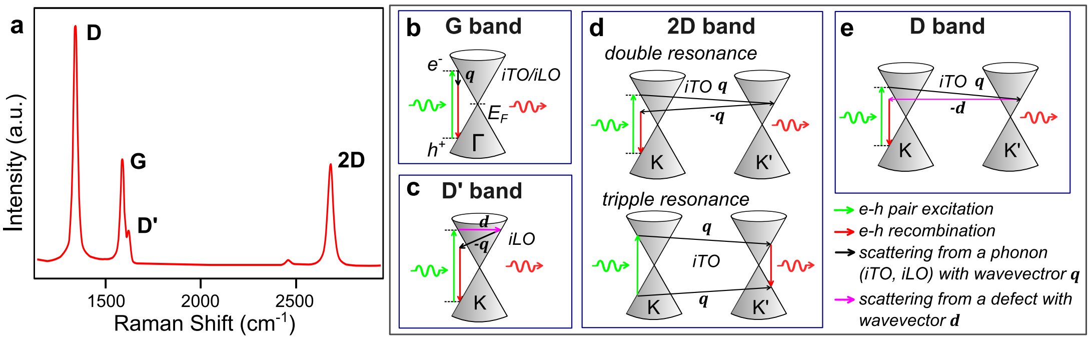

Figure 4.12: Characteristic Raman peaks of graphene. a) Raman spectrum of our defective CVD monolayer graphene with identified peaks (measured by Z. Han). b - e) Sketch of Raman processes [287] b) G band, generated through scattering from iLO or iTO phonons at Γ - point, c) D' band, generated at Γ- point by scattering from a defect and iLO phonon d) 2D band generated at K - point trough a second-order process, that includes two iTO phonons and is either double resonant or triple resonant. e) D band double resonance process including a scattering from a defect.

G band (~ 1580 cm^{-1}): The G band is the main first order band in graphene. It is a doubly-degenerate in plane sp^2 C-C stretching mode [288], and exists for all sp^2 carbon materials, including graphite, amorphous carbon and carbon nanotubes, with varying lineshape. The G band originates at Γ - point in the center of the first Brillouin zone (Fig. 4.11 c, d). The G band Raman process is shown in Figure 4.12 b: an incident photon excites a virtual electron-hole pair in graphene; the electron (or hole) is then scattered by either a iLO or a iTO zone-center phonon, and the electron-hole pair recombines emitting a photon with shifted frequency. The phonon involved in this process has a very small momentum. The shape and the spectral position of the G band peak depends on several factors, which can affect the C-C bonds, such as strain [281, 289], doping [277, 289] or temperature [290], and the intensity increases linearly with the number of graphene layers [291].

D' band (~ 1620 cm^{-1}): D' band, sometimes seen as a shoulder of the G band peak, requires a defect and is due to double resonance of intravalley process connecting two points of the same Dirac cone (K or K'), as shown in Figure 4.12 c.

2D band (~ 2700 cm^{-1}): The 2D peak is the strongest peak in graphene. It is a second order Raman process originating from the in-plane breathing mode of the carbon lattice at K (or K') point in the first Brilliouin zone. The mechanisms giving rise to the 2D band can be seen in Figure 4.12 d: an electron-hole pair is created by an incident photon near the K point, and the electron is scattered by a iTO phonon to K' point. Due to the momentum conservation in Raman processes, the electron must scatter back to K point by a second iTO phonon before recombining with the hole. This process is known as double resonant (upper panel in Fig. 4.12 d). Alternatively, in a triple resonant process (lower panel in Fig. 4.12 d), both carriers are scattered from K to K' by an iTO phonon and then recombine. The 2D peak is specific for graphene, and its shape can be used to determine the number of graphene layers [274, 291–293]. For example, for monolayer graphene, the 2D band is a single Lorentzian, while for bilayer graphene it splits into four peaks.

D band ($\sim$ 1350 cm^{-1}): The disorder-induced D band involves an iTO phonon around the K point. The mechanism is similar to the 2D band generation. However, unlike the 2D band, the D band requires a defect for momentum conservation. As shown in Figure 4.12 e, the electron is inelastically scattered by an iTO phonon to the K' point and then elastically back-scattered to K by a defect. Since only one phonon is involved in this process, the energy shift is half of that for 2D. A defect can be any breaking of graphene lattice symmetry, such as sp^3-defects [294], grain boundaries, vacancy sites [275] or edges [295]. The high sensitivity to defects, makes the D band an important feature for quality control of graphene.

Other Raman bands, which might be present in graphene spectrum, are a defect induced combination D+D' centered at around 2900 cm^{-1}, and the 2D' band at 3250 cm^{-1}. The 2D' peak is the overtone of D', same as 2D is the overtone of D. Both, 2D' and 2D originate from a process, which doesn't require defects, and are always present in the graphene spectrum.

Raman spectra obtained from different graphene batches produced during this work are shown in Figure 4.13. Graphene was transferred on SiO_2 substrates and analyzed using AFM and Raman microspectroscopy. From this figure, it is clear, that AFM analysis is not efficient to compare the quality of graphene.

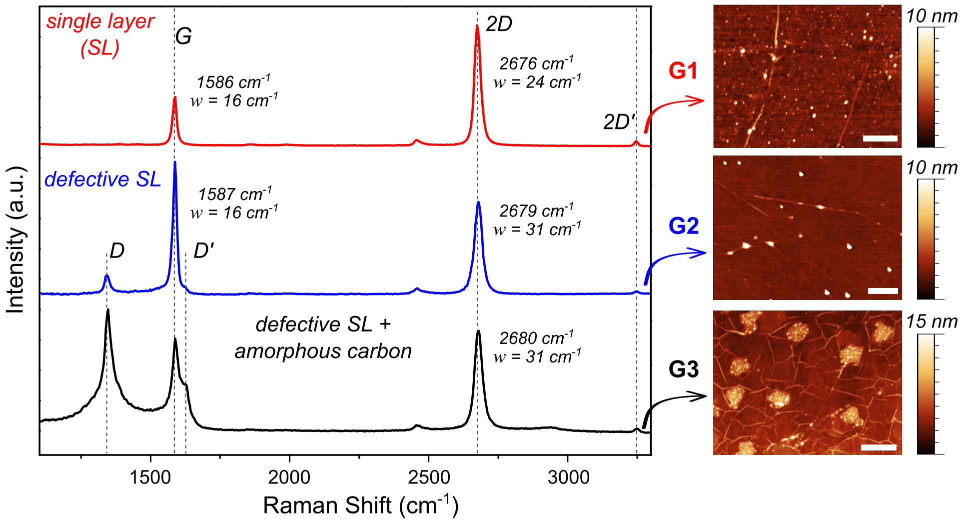

Figure 4.13: Raman microscopy and corresponding AFM analysis of different graphene layers. The structural quality decreases from top to bottom. Graphene was transferred on 285 nm SiO_2 substrate. G2 and G3 were annealed at 300°C/$0.5{\cdot}10^{-7}$ mbar. The scale bar is 500 nm.

All AFM scans show the typical wrinkles, confirming the presence of graphene on the substrate. Obviously, the graphene layer labeled G3 has the worst quality. It exhibits large contamination areas (even seen by optical microscopy), which can be attributed to deposition of amorphous carbon. While, by means of AFM, the graphene layer G2 is of comparable quality, or even better than G1 due to the cleaner surface, Raman spectroscopy clearly demonstrates the presence of lattice defects in G2, which generate the D band peak at 1350 cm^{-1}, and the D' band peak seen as a shoulder of the G peak. The intensity of the D peak, which is proportional to the amount of defects, is lower than for G3, corresponding to less defects. The Raman spectrum of G1 represents the typical signature of high quality monolayer graphene. The defect bands, D and D’, are completely absent. The integrated intensity ratio of G band and 2D band peak $I_G/I_{2D} = 0.3$, the position of the G peak at 1586 cm^{-1} and the FWHM of the 2D peak $\omega = 24\ \text{cm}^{-1}$ confirm the values reported for single layer graphene [291]. Also, G2 and G3 exhibit a monolayer nature, which is determined by the single Lorentzian shape and FWHM $\leqslant 0.3\ \text{cm}^{-1}$ of 2D peak, as well as by the frequency of G band >1585 cm^{-1}. However, the intensity of the G peak is unusually high, while the width is comparable with monolayer graphene G1. Since the intensity of the G band peak is proportional to C-C bonds, most likely some carbon atoms are trapped on graphene surface or between graphene and the substrate.

4.6.3 Electrical sheet characterization

Electrical properties of obtained graphene films were characterized in terms of square resistance $R_\square$ and the mobility of charge carriers μ. To estimate the square resistance we transferred graphene onto 285 nm SiO_2 substrate and etched 40 µm stripes with a varying length L. The graphene stripes were then contacted by Ti/Au, and their two-point resistance was measured. The resistance of the stripes was found to increase linearly with the length. The slope of the linear fit dR/dL, shown in Figure 4.14 a, can be used to estimate the square resistance: $R_\square = dR/dL \cdot 1/W$ with the stripe width W. The square resistance of our graphene could be calculated to $R_\square =$ 0.4-0.6 kΩ.

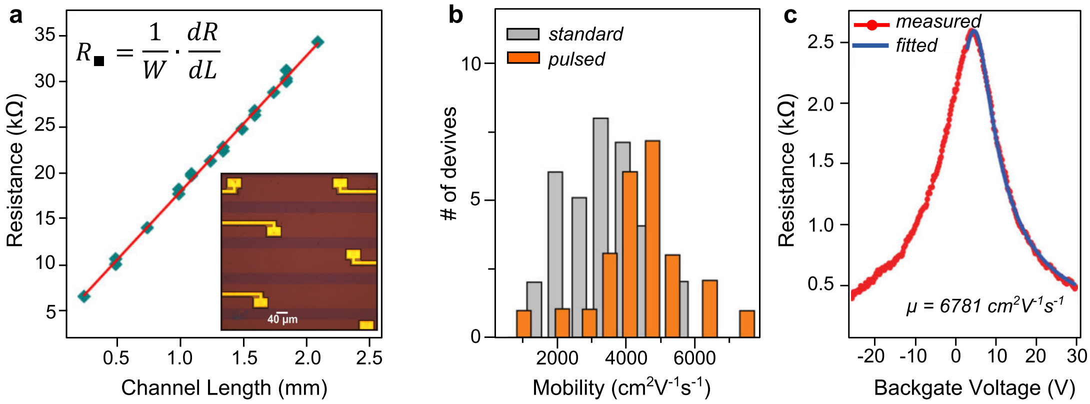

Figure 4.14: Electrical characterization of obtained graphene sheets. a) Determination of the square resistance using W = 40 µm wide graphene stripes of varying length L (see inset). The resistance increases linearly with the length. The square resistance can calculated from the slope of the liner fit. Graphene was transferred onto 285 nm SiO_2 substrate, and the stripes were etched using oxygen plasma and contacted by Ti/Au. b) Distribution of electronic mobility of graphene grown using standard and pulsed CVD method. The mobility of 5×10 μm^2 graphene transistors was extracted using the fitting method. c) To estimate the mobility, the resistance of graphene transistors was measured at varying backgate voltage at room temperature and the obtained curve was fitted using Equation 4.6 in Chapter 4.2. Figures b and c are taken from [266].

The mobility was extracted from 5×10 μm^2 graphene transistors in four point configuration at room temperature. Again, graphene was transferred onto 285 nm SiO_2 substrate, followed by etching the transistor channel and evaporation of Ti/Au contacts. The transistor resistance was then measured at a varying backgate voltage, and the mobility was estimated using the fitting method described in Chapter 4.2, Equation 4.6. A representative measurement with the corresponding fit curve is demonstrated in Figure 4.14 c. The mobility distribution of 37 individual graphene transistors, realized using graphene sheets grown by the novel pulsed CVD technique, exhibits a mean mobility of $\mu = 5000$ $cm^2V^{-1}s^{-1}$ with peak values up to 6700 $cm^2V^{-1}s^{-1}$, which is significantly higher than the mobilities obtained for conventionally grown CVD graphene (see Fig. 4.14 b).

4.6.4 Conclusion

In conclusion, using pulsed CVD growth, large area continuous monolayer graphene sheets with low square resistance and high carrier mobilities could be obtained on copper foils. The multilayer patches, which usually affect the electrical performance and are present in graphene sheets grown by standard CVD technique, could be efficiently suppressed by selective etching in pure hydrogen atmosphere. The obtained graphene sheets can be transferred onto a variety of substrates using wet PMMA assisted transfer technique. A following thermal annealing at 300°C in vacuum for 3 h could significantly reduce the amount PMMA residuals, as confirmed by AFM surface analysis. Furthermore, Raman microspectroscopy analysis reveals the high crystalline quality and the single layer nature of our graphene.

4.7 Fabrication of G-FET arrays

For the fabrication of graphene FETs, CVD graphene was transferred by the wet transfer technique as described above onto SiO_2, sapphire or glass substrates with predefined alignment marks, and annealed to remove PMMA residuals. The chip dimensions are around 1.5×1.5 cm^2 with an active area of 2×3 mm^2 and transistor channel size varying from 5×15 μm^2 to 40×60 μm^2. 38 G-FETs are fabricated per chip using standard photolithography techniques. The schematic illustration of the fabrication flow and designs of photolithographic masks are shown in Figure 4.15. The fabrication involves three main steps: etching of the transistor channel, definition of ohmic contacts and passivation of metallic leads for liquid operation. The individual steps will be discussed below in more detail, the exact recipes can be found in Appendix C.

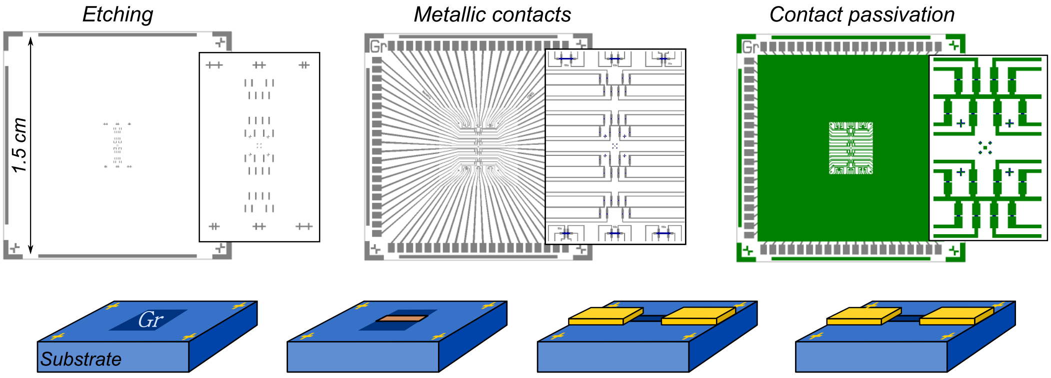
Etching *Metallic contacts* *Contact passivation*

1. Graphene on substrate **2.** Dry etching of graphene ribbon **3.** Ohmic contacts **4.** Contact passivation

Figure 4.15: Fabrication of graphene field effect transistor arrays. Designs of used photolithographic masks (upper panel) with zoomed view of the active area, and schematic fabrication flow (lower panel): after transferring the graphene sheet (G), an etching mask is defined and graphene ribbons are etched in oxygene plasma, followed by stripping of the etch mask and connecting graphene ribbons with metal contacts. In the last step, the contact leads are passivated.

An important issue for processing graphene, is the effect of solvents and resist developers on graphene quality. While, simple solvents, like acetone or isopropanol are safe to use, NMP (N-Methyl-2-pyrrolidone) treatment results in a delamination of the graphene layer from the substrate. The same effect occurs in case of deionized (DI) water and certain photoresist developers (for example, MF-26, MicroChem). Here, we prevented the use of DI water as much as possible, and used diluted Microdeveloper (MicroChem), which is in our experience less aggressive to graphene. After each fabrication step, the sample was heated to 180°C for around 3 min to dehydrate the surface and increase the adhesion of graphene to the substrate.

4.7.1 Etching of graphene ribbons

After transferring the graphene sheet onto a substrate with predefined alignment marks, graphene ribbons of variable dimensions were etched in oxygen plasma. Different etching masks were tested to obtain a clean transistor surface and decrease the contact resistance. A clean graphene surface is essential for low contact resistance and a homogeneous capacitance at the liquid interface. First, we used a simple photoresist mask, which should be easily removed in acetone. However, often after a short oxygen plasma treatment, the resist somehow changed its chemical structure and was extremely difficult to remove from graphene surface. As shown in Figure 4.16 a, massive resist residuals remain on graphene surface, which affect the transistor performance and drastically increase the contact resistance. Even thermal annealing was not sufficient to remove these residuals. To obtain a clean graphene surface, two other etching techniques were developed. In the first one, the PMMA supporting layer was kept on the graphene sheet after the transfer, and a photoresist mask was patterned above. After the etching, both PMMA and photoresist, were removed in acetone over night, followed by thermal annealing to remove the PMMA residuals. In the second method, a 10 nm thick gold layer was used as etching mask and then dissolved in KI solution. Both techniques result in a cleaner graphene surface after etching and improved graphene/metal contact resistance.

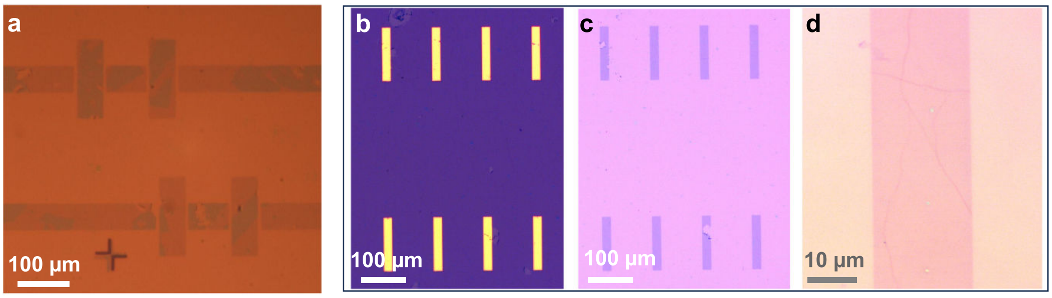

Figure 4.16: Dry etching of graphene ribbons. a) Graphene stripes (dark brown) after etching in oxygen plasma and removing the photoresist mask. Massive photoresist residuals (blue) can be seen on graphene. b) Gold mask patterned on graphene sheet. c) Graphene ribbons after etching and removing gold. d) Zoomed view of etched graphene ribbon. Using gold etch mask no apparent residuals remain on graphene surface.

Figure 4.16 b-d shows graphene ribbons etched using a gold mask. Compared to a photoresist mask, this etching method results in a much cleaner graphene surface with no visible contamination. However, the optical microscope cannot resolve the eventually remaining gold nanoparticles or small photoresist residuals. Thus, AFM analysis was performed to characterize the graphene surface after the etching step. As shown in Figure 4.17 a, the surface seems to be covered by a granular layer and its roughness increases compared to the initial graphene layer (Fig. 4.17 b). The granularity may arise either from the photoresist, which was used to pattern the gold mask, or from the remaining gold particles. The latter one could be clearly excluded by means of SEM, since there was no signal from backscattered electrons. An additional annealing step could only partially remove the residuals.

Good quality of graphene surface and low contact resistance can be also obtained using a PMMA-photoresist stack as described above. The advantage of this method is, that the PMMA layer is not removed after the transfer preventing a direct contact of graphene surface to the photoresist. The PMMA residuals are then removed by thermal annealing (Fig. 4.17 c). Both etching methods (using gold and PMMA/photoresist mask) were used in this work and exhibit similar FET performance.

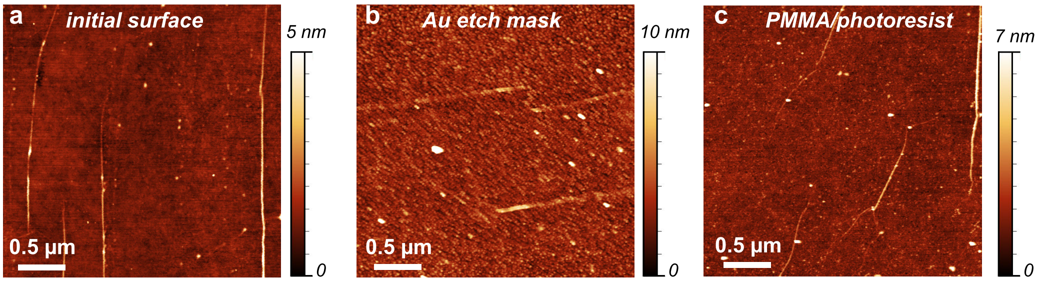

Figure 4.17: Graphene surface a) before fabrication, b) after etching and removing gold mask, and c)after etching, removing the PMMA/photoresist etch mask and annealing at 300°C for 3h under vacuum.

4.7.2 Ohmic contacts

In the second fabrication step, contact leads are patterned using UV mask aligner followed by evaporation of metals. While the quality of CVD grown graphene itself is no more a limiting factor, the realization of low resistance ohmic contacts is one of the main issues to improve the performance of graphene FETs. Low contact resistance increases the on/off current ratio (I_{on}/I_{off}) and consequently the signal-to-noise ratio and the detection quality. Therefore controlling the contact resistance is critical for high performance biosensors used for the detection of very small signals, such as extracellular potentials.

The contact resistance is controlled by two parameters: surface cleanliness of graphene and the contact metal [296, 297]. As already described above, using specific etch masks and thermal annealing, a clean graphene surface can be obtained after the etching. However, the exposure of contacts will unpreventably introduce new resist residuals at the graphene/metal interface. To avoid those, either a hard mask (for example made of parylene) can be used for evaporation, or metals can be evaporated all over the sample and then etched by specific etchants to form the contact leads. While in case of a hard mask, the alignment is very difficult especially for small devices, the latter method is limited to only few contact metals, such as Ni or Au, which can be easily etched by commercial etchants.

In this work, we used standard photolithography and tested two metals at the interface: Ti and Pd. Several samples with arrays of $20 \times 15\ \mu m^2$ G-FETs (Fig. 4.18 a) were fabricated at the same time using exactly the same graphene layer and fabrication recipes. Only, the contact metal was changed. Figure 4.18 b demonstrates the effect of the contact metal on the two-point resistance of fabricated FETs. An absolute decrease of 0.9 kΩ of the contact resistance compared to Ti could be achieved by using Pd as contact metal. The contact resistance could be qualitatively estimated by measuring the two-point resistance of G-FETs with different widths, as shown in Figure 4.18 c. The contact area, as well as the contact width were kept constant at $1000\ \mu m^2$

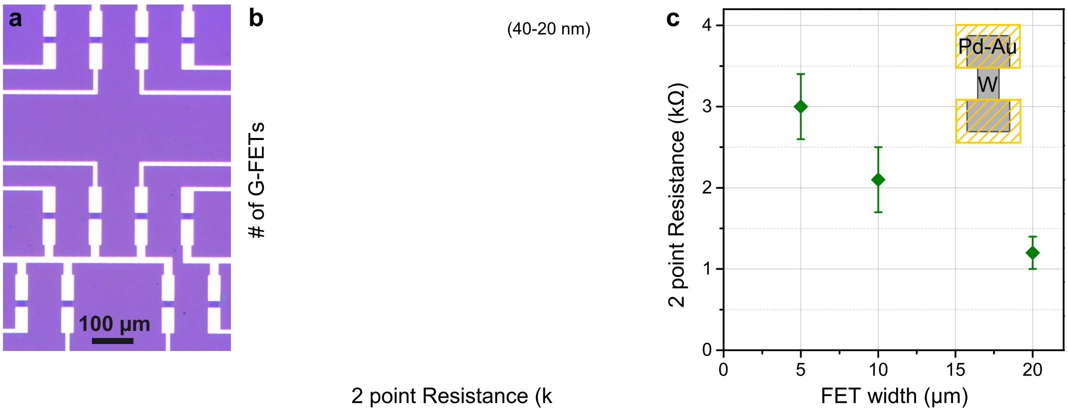

Figure 4.18: Effect of the contact metal at graphene interface on the contact resistance. a) Optical image of G-FET array after the patterning of ohmic contacts. b) The effect of the contact metal at the interface to graphene on the two-point resistance of G-FETs. c) Two-point resistance of graphene FETs with different widths. As indicated in the inset schematic, the contact area was kept constant, while the width W was varied.

and 20 µm respectively. While the FET-channel length was kept at 15 µm, its width was varied. As expected, the resistance decreased exponentially with the width. From this, the contact resistance can be approximately extracted from the saturation value, which is around $2R_C = 0.6$ kΩ, meaning $R_C = 0.3$ kΩ per contact, while the square resistance $R_\Box$ of the graphene sheet could be calculated to $\mathrm{R}_\Box = 0.65 \pm 0.05$ kΩ/□.

In a recent study the low contact resistance in case of Pd was explained in terms of work function of graphene under the contact [298]. When graphene is interfaced to a metal, its work function is shifted depending on the metal at the interface. For the majority of contact metals, the work functions of graphene is pinned to the same value as the metal electrode. For Pd and Au however the work function shifts to an intermediate value ($\sim$ 4.6 eV), which was shown to result in a lower contact resistance. Although both Pd and Au result in similar work function of graphene, Pd has lower contact resistance, which can be attributed to the varying wettability [298]: while thin Au layers evaporated onto graphene easily migrate and aggregate into islands, Pd is widely known to wet carbon materials (such as CNTs). The intermediate work function, which indicates an easier charge transfer, combined with a good wettability results in a lower contact resistance of Pd compared to other metals. Moreover, it was shown that the change of the contact resistance upon a gate voltage variation as well as the maximal contact resistance are smaller for contact metals with an intermediate work function shift [298].

4.7.3 Passivation

In the last fabrication step, the metallic contact leads are insulated using polymers, such as polyimide (PID) or the negative photoresist SU8-2000, as well as a simple positive photoresist S1818. By choosing the material for passivation, several aspects have to be considered: insulating properties, chemical and mechanical stability, and of course in case of biosensors, the biocompatibility. When the surface is covered by cell adhesion proteins, such as poly-L-lysine (PLL), all the materials mentioned above have comparable biocompatibility and are not toxic to the cells (here neurons). Furthermore, after a thermal annealing step, PID and SU8 exhibit the required chemical and mechanical stability, which make them suitable materials for long-term utilization. On the other hand, for one time use experiments, S1818 also provides the required properties. While its robustness is very poor, and it is easily dissolved by several solvents, it still exhibits good insulating properties and is easy to handle. As demonstrated in Figure 4.19 e, the electrical properties of fabricated devices are not affected by the material used for the passivation.

The surface state of the final device was assessed by AFM and is shown in Figure 4.19 c. The device surface is slightly contaminated due to the use of polymers in direct contact to graphene for passivation. A cleaning process would certainly improve the FET performance, but it would also eventually damage the insulating polymer or the graphene surface itself. A reliable cleaning recipe is still under development.

The crystalline quality of the graphene ribbons after the fabrication was assessed by Raman microspectroscopy analysis (Fig. 4.19 d). The integral intensity ration $I_G/I_{2D} = 0.33$ of G and 2D mode peak, as well as the width of the 2D peak $\omega_{2D} = 31$ cm^{-1} confirm the single layer nature of the used graphene sheet. The low intensity of the defect induced D peak reveals the high quality of graphene even after the fabrication. The right shoulder of the G-peak, however, indicates the presence of resist residuals.

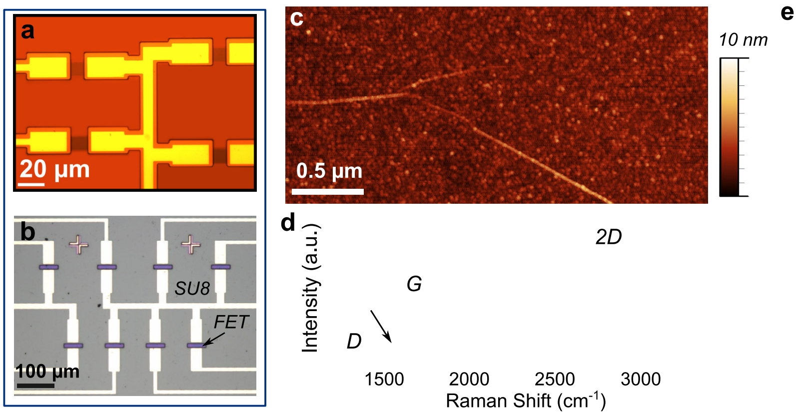

Figure 4.19: Passivation of metallic contacts for liquid operation. a) Optical image of G-FET arrays passivated with photoresist S1818. Notice, that only the leads are covered by the resist. b) Contact passivation using photoresist SU8. The chip is completely covered by SU8, except the area above the FETs. c) AFM image of the graphene surface after passivation by S1818. d) Raman spectra of graphene transistor channel of the final device. Arrow indicates a peak due to resist contamination. e) Front liquid gate effect measured on 20×15 µm^2 G-FET arrays passivated by S1818 and SU8. The measurements were performed in phosphate-buffered saline solution (PBS) at drain-source voltage $V_{SD} = 100$ mV.

Two different photolithographic masks were developed for the passivation, allowing the realization of the passivation pattern only above the metallic lines, or exposing a small window just above the FET-channel, while everything else is covered by the polymer (Fig. 4.19 a, b). Obviously, the latter method will affect the cell-device coupling due to the narrow gap. Also the liquid tension may prevent the liquid flow into the gap, making the deposition of PLL onto the FET-channel more difficult. Especially, due to the high hydrophobicity of SU8, using a passivation pattern only above the metallic leads, as shown in Figure 4.19 a, is more preferable.

4.7.4 G-FETs on different substrates

The fabrication protocol as presented above was used for the realization of arrays of G-FETs of variable size on different substrates with a success rate of over 85%. G-FETs were fabricated on Si/SiO$_2$ substrates, PID, glass coverslips and sapphire (Fig. 4.20). While the electrical characteristics of FETs fabricated on glass, sapphire and Si/SiO$_2$ are comparable to identical, the FETs realized on polyimide (PID deposited onto Si/SiO$_2$ substrates), exhibit much higher contact resistance and a slightly shifted Dirac point. Nevertheless the extracted transconductance values are similar for all substrates presented in Figure 4.20 a, indicating that the main performance limitation of G-FETs fabricated on soft PID substrates is the high contact resistance. The presented measurement on PID represents the first and only attempt in this work to fabricated G-FETs on soft substrates and already reveals the potential of graphene FETs for integration on soft flexible polymers required for *in-vivo* bioelectrical interfacing. On the other hand, G-FETs realized on transparent sapphire or glass substrates offer a transparent sensor, which is compatible with inverted microscopes for in-situ monitoring of recorded neural cultures. As illustrated in Figure 4.20 c, this provides a convenient platform for in-vitro investigations of neuronal cultures with three easily accessible manipulation ports: in-situ optical monitoring, as well as electrical and fluidic manipulation ports.

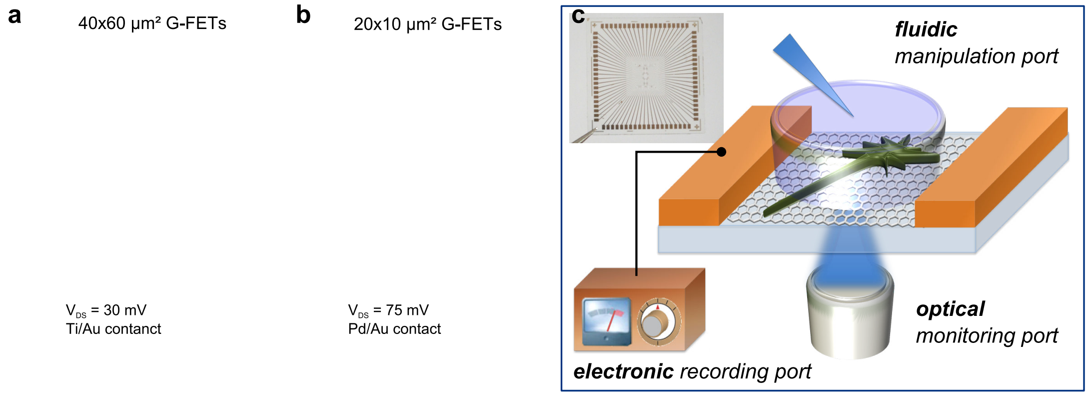

Figure 4.20: G-FET arrays on different substrates. a) Field effect in 40×60 µm^2 G-FETs fabricated on different substrates, measured in liquid gate configuration in PBS solution at $V_{SD} = 30$ mV. Ti was used as contact metal. b) Field effect in 20×15 µm^2 G-FETs fabricated on different substrates, measured in liquid gate configuration in PBS solution at $V_{DS} = 75$ mV. Pd was used as contact metal. c,d) G-FET arrays fabricated transparent glass or sapphire substrates provide a convenient experimental set-up for *in-vitro* recordings of neural activity with three easily accessible manipulation ports: optical control, electronic recordings and fluidic manipulation of investigated neuron culture.

4.8 Electrical sensing properties

The fabricated G-FETs were characterized in terms of their sensitivity to external potential fields in liquid environment. For liquid gating, a PDMS chamber was fixed on the chip and filled with either cell culture medium (Neurobasal) or PBS (phosphate-buffered saline) solution. The measurement scheme is shown in Figure 4.19 a. The measurements presented below are carried out using a needle probe station interfaced with a FPGA. The liquid gate voltage V_{LG} is applied to a Pt electrode immersed into the solution. A constant DC source-drain bias voltage V_{SD} is applied to the G-FET and the source-drain current through the transistor channel I_{SD} is measured at the varying V_{LG}. The transistor current is amplified using a commercial Femto amplifier (Femto DLPCA-200). To decrease the input noise, voltage dividers and low pass filters are used. The output signal is filtered using a low pass filter with a cut-off frequency $f_c = 5$ kHz, which would still transmit a signal generated by an action potential with a typical frequency $<$ 1 kHz. As shown in the inset of Figure 4.19 b, the peak-to-peak noise amplitude is limited by the Femto amplifier operation regime, being 20 nA for 10^5 gain setting, and only 5 nA for 10^6 gain. Since the bandwidth×gain product is constant for a given amplifier, increasing the gain reduces the probed bandwidth and results in lower noise. A customer designed low noise current amplifier was ordered to decrease the setup noise, but could not be finalized during this thesis.

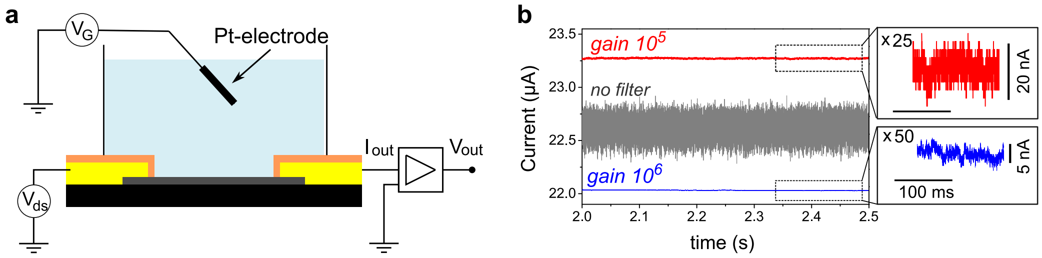

Figure 4.21: Measurement setup. a) A schematic illustration of the electrical measurement setup. The liquid gate voltage V_G is tuned using a Pt-electrode, a constant DC bias voltage V_{SD} is applied to the G-FET, and the output current I_{out} is amplified using a current-voltage converter. b) Measurement of output noise of G-FET in liquid gate configuration. To decrease the noise, V_{SD} was filtered using a *1/100* voltage divider, and V_G using a *1/10* voltage divider and a low pass filter with $f_c = 1.5$ kHz. The output signal V_{out} was filtered by a low pass filter with $f_c = 5$ kHz. The inset shows the effect of the gain operation regime of the Femto amplifier on the peak-to-peak noise of the output signal.

The measurements presented below were performed either in cell culture medium or in PBS solution. The FET performance was not affected by the used liquid. As gate electrode either a platinum wire or silver/silver chloride (Ag/AgCl) reference electrode was used. While both gate electrodes showed identical slope of conduction modulation, the Dirac point was shifted by +0.3 V when using a Pt gate electrode.

4.8.1 Field effect in liquid gated G-FETs

As already discussed in chapter 4.3, the conductance of graphene FETs can be efficiently tuned by using a top liquid gate. By increasing the gate potential, the transistor operation mode can be tuned from hole conduction to electron conduction regime by passing the conductance minimum at the charge neutrality point (or Dirac point). Figure 4.22 a illustrates typical measurements of the field effect in liquid gated G-FETs. With increasing gate potential, the conductance first decreases due to depletion of hole charge carriers, and reaches its minimum value at the Dirac point around $V_{CNP} = 0.4$ V. With further increasing gate voltage, the capacitance also increases due to the accumulation of electron charge carriers. The saturation value of the curve corresponds to the contact resistance. The slope of the conductance modulation curve is defined as transconductance $g_m = \partial I / \partial V_{LG}$, and represents the conductance modulation strength of the liquid gate. The higher the transconductance, the higher the current response of the FET to the gate variation. In other words, it represents the sensitivity of the transistor to external potential changes. Usually, the sensitivity S is normalized by the bias voltage V_{SD}:

$$S = \frac{\partial I / \partial V_{LG}}{V_{SD}} = g_m / V_{SD}. \tag{4.9}$$

As shown in Figure 4.22, G-FET arrays fabricated in this work exhibit reproducible electrical performance. The mean value of the sensitivity is around S = 3.5 mS/V with peak values reaching $S_{max} = 4$ mS/V, which makes the performance of our G-FETs one of the highest reported in the literature for CVD grown graphene [126, 299].

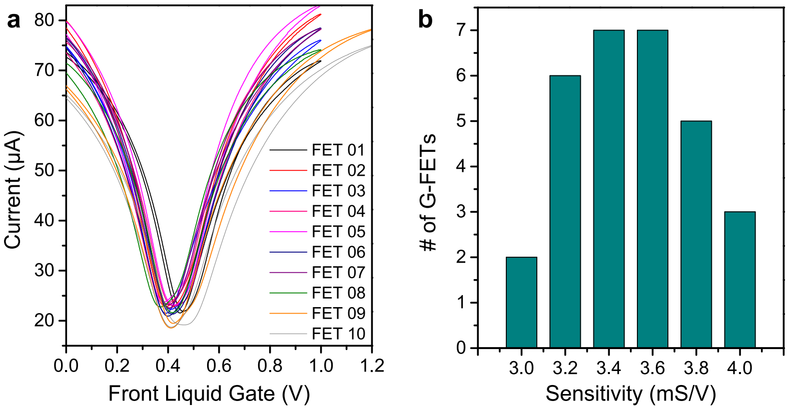

Figure 4.22: Electrical characterization of fabricated G-FET arrays. a) Field effect measured on 10 devices with reproducible behavior. The measurements were performed on 20×15 µm^2 G-FETs fabricated on sapphire in cell culture medium at $V_{SD} = 75$ mV. b) Sensitivity distribution of 30 identical FETs on the same chip.

This high sensitivity was measured on small 20×15 µm^2 devices. The dimensions of the FET channel are important for sensing applications: the size of the device must be in the same order as the size of the interfaced cell to ensure a measurable current modulation by the electrical activity of the cell. According to Equation 4.9, the transistor sensitivity scales with the width/length ratio W/L:

$$S = g_m / V_{SD} = \mu \cdot C_g' \cdot \frac{W}{L}, \tag{4.10}$$

where μ is the carrier mobility, and $C_g^{'}$ - the gate capacitance per unit area.
Figure 4.23 demonstrates the sensitivity scaling with FET dimensions. Reducing the width of the FET decreases the net current through the channel and the sensitivity (Fig. 4.23 a), while reducing the length of the FET-channel obviously increases the net current and the sensitivity of the transistor (data not shown). In agreement with Equation 4.10, the sensitivity of our G-FETs was found to be proportional to W/L, as shown in Figure 4.23 b and c.
As it is shown above, the sensitivity is proportional to the carrier mobility μ, gate capacitance $C_g^{'}$, and the width-to-length aspect ratio W/L. With the mean mobility value of our graphene [267] $\mu = 5000\ \mathrm{cm^2V^{-1}s^{-1}}$, the EDL capacitance calculated in Chapter 4.3 $C_{EDL} = 0.78\ \mu\ \mathrm{F/cm^2}$ and $W/L = 20/15$, the theoretical sensitivity should be $S_{th} = 5.2$ mS/V. The maximal experimental value measured in this work is $S_{exp} = 4$ mS/V, which is in good agreement with the theoretical prediction.

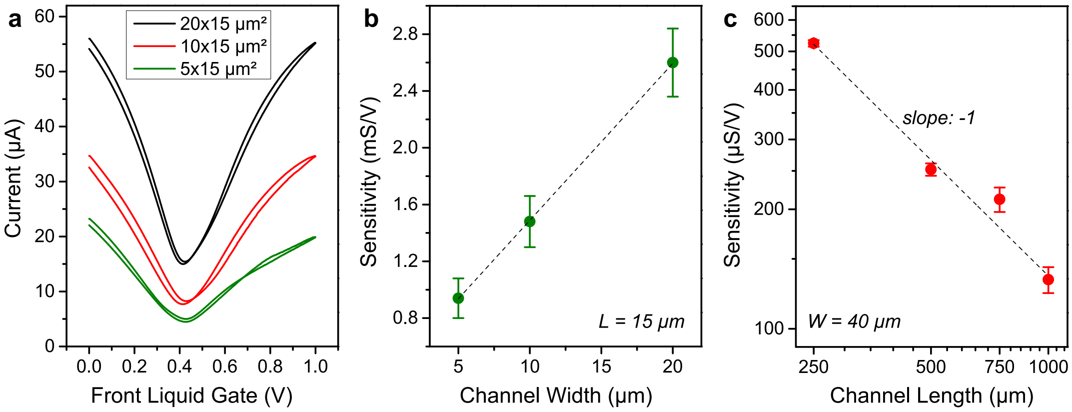

Figure 4.23: Scaling of the transistor sensitivity with the FET-channel dimensions. a) Field effect in liquid gated FETs with a constant length $L = 15$ µm and varying width. The measurements were performed in cell culture medium at $V_{SD} = 50$ mV. b) Sensitivity as function of the transistor channel width. Sensitivity is proportional to the channel width. c) Sensitivity as function of the channel length. Double logarithmic scale reveals a $1/L$ dependence.

According to Equation 4.10, the sensitivity does not depend on the dimensions of the G-FET, but only on the ratio W/L. Consequently, even smaller G-FETs can be realized with the same high sensitivity.

4.8.2 Detection of potential pulses

In order to prove the ability of the devices to detect action potential like pulses, we superimposed 1 ms-short Gaussian voltage pulses onto the DC offset of the liquid gate. The conductance change in response to these rapid potential spikes was reported at different liquid gate offsets. To be as close as possible to the experimental conditions for cell interfacing, the measurements were performed in cell culture medium. A typical current versus liquid gate voltage measurement with corresponding sensitivity is presented in Figure 4.24 a. The sensitivity of the G-FET device can be readily calculated as the slope of the $I - V_{LG}$ curve at a specific V_{LG} value. The sensitivity can be changed by varying the gate offset; it has its maximum value at the inflection points around 0.3 V for hole, and 1 V for electron operation regime, and the minimum at the Dirac point around 0.5 V.

The response of our G-FET to an external potential 10 mV pulse with a duration of 1 ms at different gate offsets is shown in Figure 4.24 b. The baseline and amplitudes of the spikes show a good agreement to the corresponding $I - V_{LG}$ curve (Fig. 4.24 a). The polarity of the detected signal is inversed as the device is tuned from hole conduction to electron conduction regime. The amplitude ΔI of the detected signal is the highest at the points of inflection, and the lowest at the Dirac point, as it can be clearly seen in the zoomed view in Figure 4.24 c. The symmetrical monophasic shape of the detected current signals follows the applied Gaussian pulse with equal rise and decay time, revealing the high fidelity of the recordings and fast response of our G-FETs. Interestingly, close to the Dirac point, the detected current pulse exhibits a biphasic shape. Due to the low transconductance of the G-FET close to the charge neutrality point, here we can observe the small contribution from the capacitive current, which is proportional to the time derivative of the applied voltage pulse.

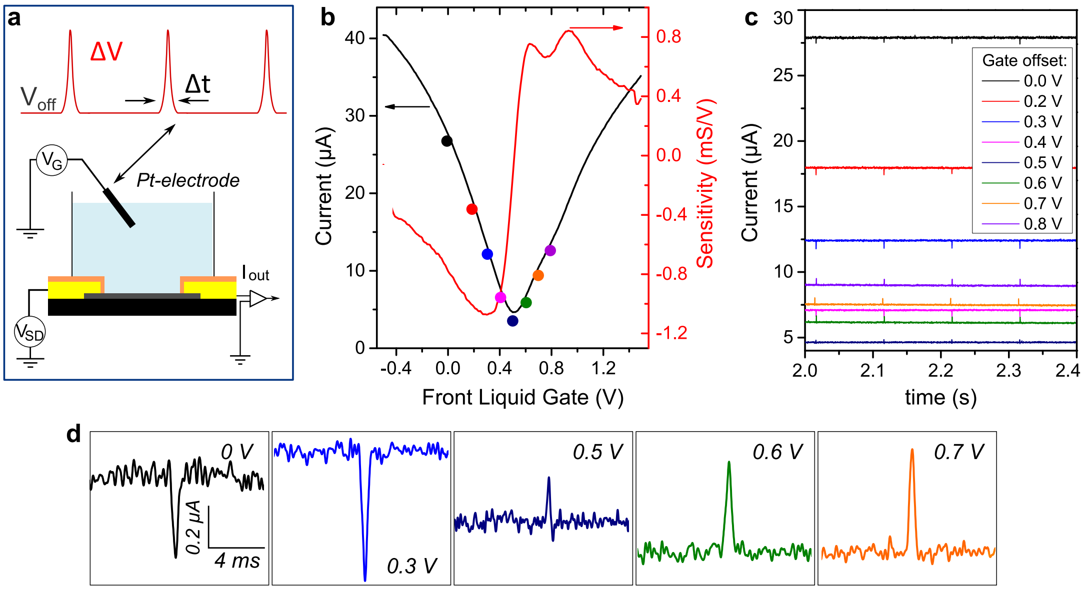

Figure 4.24: Detection of impulsional response of G-FEts. a) Schematic of the experimental setup for detection of potential pulse using G-FETs. Potential pulses with an amplitude ΔV and duration Δt are applied to the liquid gate using a Pt-electrode, and the current through the transistor channel is recorded at a constant bias voltage V_{SD}. The gate voltage offset V_{off} sets hereby the transistor working point and thus the sensitivity. b) Current through the G-FET channel and corresponding sensitivity as function of the liquid gate voltage. The measurement was performed in cell culture medium at $V_{SD} = 50$ mV. The colored dots indicate the representative gate offset values for the following pulse detection in c. c) Detection of 10 mV high and 1ms long potential pulses at different gate offset values using the G-FET device from a). d) Representative expanded peaks for selected gate potentials.

A potential pulse V_P induces a current modulation ΔI proportional to the sensitivity at the given liquid gate voltage $S(V_{LG})$:

$$\Delta I/V_{DS} = S(V_{LG}) \cdot V_P \tag{4.11}$$

with the bias voltage V_{DS}. For a good sensor, the equation above must be true. From the potential pulse detection in Figure 4.24, we can recalculate the applied pulse using the recorded signal ΔI:

$$V_P = \frac{\Delta I/V_{DS}}{S(V_{LG})}. \tag{4.12}$$

The calibrated signal at different liquid gate offsets V_{LG} is shown in Figure 4.25 and is in a very good agreement with the applied pulse, revealing the high fidelity detection of G-FETs.
To correctly detect such a short signal, the response time of the sensor device must be lower than the signal duration. We measured the response time of our G-FETs by applying square shaped potential pulses to the liquid gate. The response time was then estimated as the time required from the signal initiation until the saturation of the G-FET current. For the device presented in Figure 4.25 b and c, the response time is lower than 0.5 ms, which is fast enough to detect action potentials from neurons. The response time depends on the dimensions of the FET and the surface cleanliness, which affect the capacitance at the interface to the liquid gate. The higher the gate capacitance, the slower the FET response. Unfortunately, a detailed statistics on the response time of different G-FET devices realized in this work was not carried out.

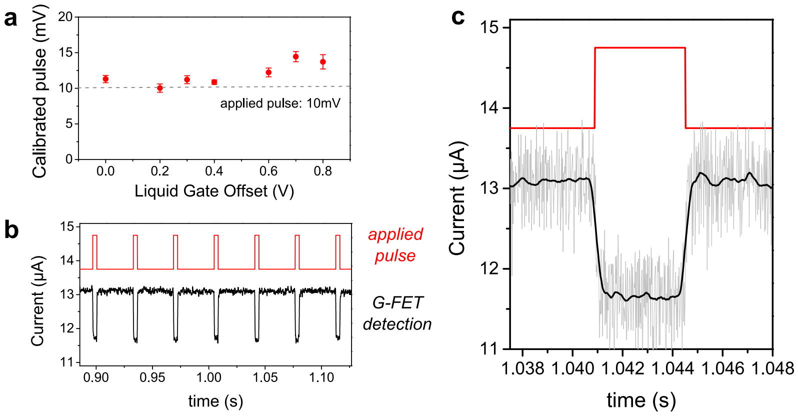

Figure 4.25: Response characteristics of G-FET to potential pulses. a) Calibrated pulse height of the potential pulse $V_P = 10$ mV applied in Figure 4.24 b. The calibrated pulse and the applied pulse are in very good agreement. b) G-FET response (black line) to square shaped potential pulses (red line) in cell culture medium. c) Zoom of a pulse detected by G-FET (black line), revealing a very fast response (less than 0.5 ms) to the applied square pulse signal (red line). Grey line is the unfiltered signal.

The characterization measurements presented above show, that our G-FETs exhibit the required electrical properties for detection of rapid voltage pulses with duration and amplitude similar to neuronal action potentials. The fabricated FETs provide a fast and reliable detection of potential spikes with the minimal amplitude $V_P = 75$ µV, which is on the order of the neuronal spike amplitude, and signal-to-noise ratio 2.5, as demonstrated in Figure 4.26 b. However, the detection performance may vary depending on the cell/device coupling area.

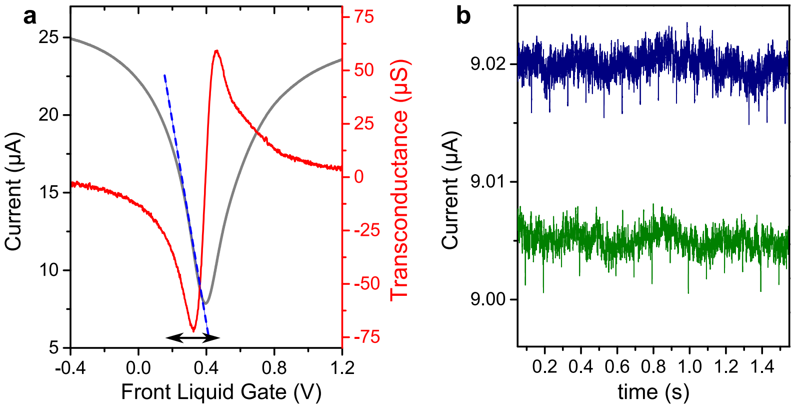

Figure 4.26: Potential pulse detection using G-FETs. a) Field effect in cell culture medium and the corresponding transconductance at $V_{SD} = 50$ mV. Dashed blue line indicates the linear operation regime of the G-FET with the maximal sensitivity. The black arrows highlight the gate voltage range of the maximal sensitivity around $V_{LG} = 0.3$ V. b) Detection of 100 µV (blue) and 75 µV (green) potential pulses by the same G-FET as in a) at $V_{LG} = 0.32$ V and amplifier gain 10^6.

The detection of small potential pulses was performed at the maximal sensitivity point. Thus the stability of the detection depends on the stability of the transistor operation point. Absorption of water molecules or other chemical compounds present in the cell culture medium or in the biological environment can result in a doping of the graphene channel, leading to a shift of the Dirac point and changed sensitivity. A similar shift can be also observed due to the changing pH value of the solution. To minimize the effect of this drifting on the detection stability, an expanded linear operation regime of the G-FETs (as indicated by the blue dashed line and black arrows in Fig. 4.26 a) with a constant sensitivity over a wide range of gate voltages is required. This could be achieved by a further decrease of the series resistance R_s, which is composed of the contact resistance R_C and the resistance of the graphene channel under the polymer used for the passivation R'_G. While the contact resistance can be tuned by choosing a suitable contact metal and keeping a clean graphene surface, the parasitic resistance R'_G depends on the area ratio of exposed graphene to graphene under the polymer. Decreasing the area fraction of graphene under the polymer would decrease R'_G and increase the linear operation regime of G-FETs. However, this possibility could not be studied in this work.

4.8.3 Noise in liquid gated graphene FETs

Another important parameter for a high quality sensor is the signal-to-noise ratio. The noise in our detection is composed of the internal noise of the G-FET device and to a greater part, the set-up induced noise, which was discussed above. The power spectral noise density of G-FET in the two usually used measurement configuration is shown in Figure 4.27 a. As for many semiconductor devices, an inverse dependence on the frequency $1/f$ is observed for the low frequency regime [300]. While the graphene based devices exhibit a relatively low noise level [301–305], the origin of this $1/f$ noise in graphene is still a topic of investigations [306]. Several mechanisms are believed to be involved into its generation, such as generation-recombination noise (G-R noise) or mobility fluctuations within the FET-channel. The G-R noise is observed in all semiconductor devices with a gate oxide. This noise is induced by charge traps in the oxide [307]. Carriers from the semiconductor can tunnel into these traps and generate charge fluctuations in the oxide, which act as scattering centers for the carriers in the semiconductor. For liquid gated graphene transistors no such gate oxide is used, which could be a reason for the lower noise than for example for silicon devices [299, 308]. However, the defects on the edges of graphene channels can act as charge traps and contribute to G-R noise [309].

The noise amplitude exhibits a clear dependence on the liquid gate voltage. As shown in Figure 4.27 b, close to the Dirac point the amplitude follows a V-shape dependence with a minimum at the Dirac point, where the resistance is the highest, in agreement with the noise behavior in graphene reported in the literature [306]. In some reports, the V-shape became M-shape over the extended gate bias range, and the noise amplitude followed the transconductance trend [303, 304]. This M shape of the noise amplitude, which can be also observed in our measurements in Figure 4.27 b, was attributed to the presence of electron and hole puddles in graphene [303], or impurities, such as water molecules trapped on the graphene surface [310]. Recently, the gate-dependence of $1/f$ noise could be also explained within the mobility-fluctuation approach [311].

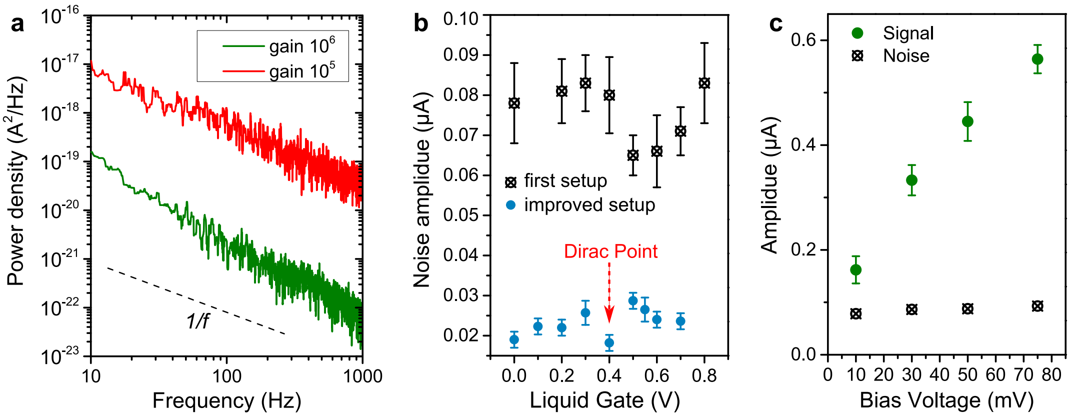

Figure 4.27: Noise in G-FETs. a) Power spectral density of the current noise in liquid gated G-FETs ($V_{LG} = 0$ V) in two amplification regimes. A $1/f$ dependence on the frequency is observed. b) Peak-to-peak amplitude of the noise measured before and after adding analog low-pass filters for input voltage and output current signal. The measurements were performed on two different G-FETs at 10^5 amplification. c) Amplitude of the detected signal as function of the bias voltage. The measurement was performed in cell culture medium at a constant liquid gate offset $V_{LG} = 0.3$ V, and applied pulse amplitude $V_P = 10$ mV. The error bars are calculated form 10 subsequent pulses.

As shown in Figure 4.27 b, the peak-to-peak noise amplitude could be drastically decreased by using low-pass filters for input voltage and output signals. A further noise reduction is however limited by the gain setting of our current amplifier (Femto DLPCA-200), as already discussed in Chapter 4.8. Due to the low resistance of G-FETs, the recordings are usually performed with a gain setting of 10^5, which exhibits a higher noise amplitude, as demonstrated in Figure 4.27 b. The current noise amplitude is around 25 nA. For the mean transconductance value of our G-FETs $g_m = 260$ µS (see Fig. 4.22 b), this results in a effective gate noise of around 50 µV, making the detection of extracellular action potentials challenging. However, the gate noise can be reduced by at least a factor of 5 using 10^6 gain setting (see Fig. 4.21 b), allowing the detection of very small potential signals (see Fig. 4.26 b).

The noise amplitude has no dependence on the source-drain bias voltage V_{SD}. While the net current through the FET-channel, and consequently the amplitude of the detected signal, increase with increasing V_{SD}, the noise amplitude remains constant (see Fig. 4.27 c). Thus to increase the signal-to-noise ratio, a higher polarization voltage can be used

4.8.4 Effect of biocoatings

The surface of G-FETs has to be covered with poly-L-lysine (PLL) to promote the neuronal attachment *in-vitro*. While cell adhesive coatings are essential for neuron cultures on almost every substrate, they could affect the electrical properties of the sensor by creating a charged interface that will partially shield the neuronal signal to be detected by the transistor channel. To estimate the effect of the cell adhesive coatings on the sensor performance, we measured the field effect in liquid gated G-FETs before and after covering with PLL.

PLL-coated G-FETs exhibit a slight asymmetry around the charge neutrality point. While the FET-conductance in the hole operation regime and the position of the Dirac point remain unchanged, the electron conductance is decreased, as can be seen in Figure 4.28 a. The depression of only electron conductance indicates a positive chemical doping of the graphene layer [312], which originates from the positive charged poly-L-lysine molecules. The sensitivity of G-FETs in the hole conductance regime is not affected by the coating, such that PLL can be well used to interface G-FETs electrically with neurons.

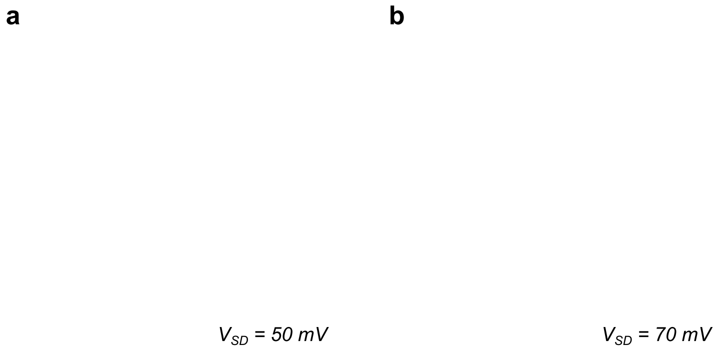

Figure 4.28: Field effect in liquid gated G-FETs before and after covering with different biocoatings: a) poly-L-lysine (PLL), and c) hyaluronic acid (HA). Measured in cell culture medium.

Regarding the great potential of using cell-compatible hydrogels as protective biodegradable coatings [313] for *in-vivo* implants, we also tested the effect of hyaluronic acid (HA) on the FET performance. HA is an immunoneutral polysaccharide and one of the main components of the extracellular matrix involved in a variety of biological functions [314]. HA can be transformed into many physical forms, including hydrogels [315]. HA based hydrogels can be produced with different mechanical properties matching the stiffness of the target tissue [316] and are biodegradable [317, 318], which makes them a suitable material to protect graphene based implants during the implantation and to reduce the inflammatory response.
Preliminary measurements on graphene FETs covered with a hydrophobic modification of HA show a significant change in transistor properties. Figure 4.28 c demonstrates field effect induced conductance modulation in liquid gated G-FETs before and after coating with HA. The effect of HA was measured on several FET devices and is highly reproducible. The coating leads to a 0.4 V positive shift of the Dirac point and broadened field effect curve, which can be attributed to the net negative charge of HA molecules [319] as well as the lowered interfacial capacitance and gate voltage screening due to the relatively thick coating. The change of the slope of the field effect curves can be also attributed to a reduction of the mobility of the charge carriers due to introduction of new scattering centers. As a direct consequence, the sensitivity of G-FETs is decreased to 67% of the initial value. While additional tests with improved coating and measurement protocols have to be carried out, the first results show, that the functionality of G-FETs is not affected by HA layer. Additionally, body's own enzyme hyaluronidase can fully degrade HA *in-vivo* [317, 318], resulting in a clean graphene surface and recovered FET performance.

Further evaluation of HA-hydrogel coated graphene devices is the subject of an ongoing PhD project at Institut Néel (A. Bourrier). However here we have already shown that the fabricated G-FET arrays are compatible with cell adhesive protein and hydrogel coatings. More importantly, using PLL to promote neuronal growth on G-FETs for *in-vitro* recordings of neuronal activity is not affecting the sensing performance of the device.

4.8.5 G-FET characteristics after the neuron culture

Figure 4.29 represents the FET characteristics before the neuron culture, with 21DIV neurons grown on top of the devices, and after removing the neurons from the FETs. The G-FET array was first characterized by measuring the field effect induced conductance modulation using cell culture medium as a liquid gate to estimate the sensitivity of the individual FETs. Same measurements were performed with live neurons cultured on the same chip for 3 week and after cleaning the G-FETs from the neurons. When the field effect curve is measured with live neurons on top of the FET devices, a 0.2 V positive shift of the charge neutrality point can be observed along with a general conductance depression. Also the Dirac point exhibits two local minima, which is usually observed due the charge transfer from the metal contacts [320], creating two differently doped graphene areas. Here however the charge transfer seems to originate directly from the presence of dense neuron networks on the FET surface, since after removing the neurons, the Dirac point shifts back to less positive gate voltage values, and the double conductance minimum almost disappears. This shift of the Dirac point in presence of neurons can be attributed to the negative resting membrane potential (around -80 mV relative to the extracellular medium), which has to be compensated by the liquid gate, and the screening of the gate voltage by the dense neuron networks, which almost completely cover the FET-surface (Fig. 4.29 a).

The sensitivity of G-FETs is reduced by 25% after the culture compared to the sensitivity of the same device measured before (Fig. 4.29 c), which might be due to the damaged graphene surface induced by the tension of growing neurons and resulting in a lower mobility. On the other hand, the decreased sensitivity may arise from the reduced field effect due to the presence of a screening neuron layer on the FETs. Nevertheless, the FETs are able to detect small potential changes (V_P = 500 µV) even with graphene surface fully covered by neurons and reduced sensitivity, as shown in Figure 4.29 d.

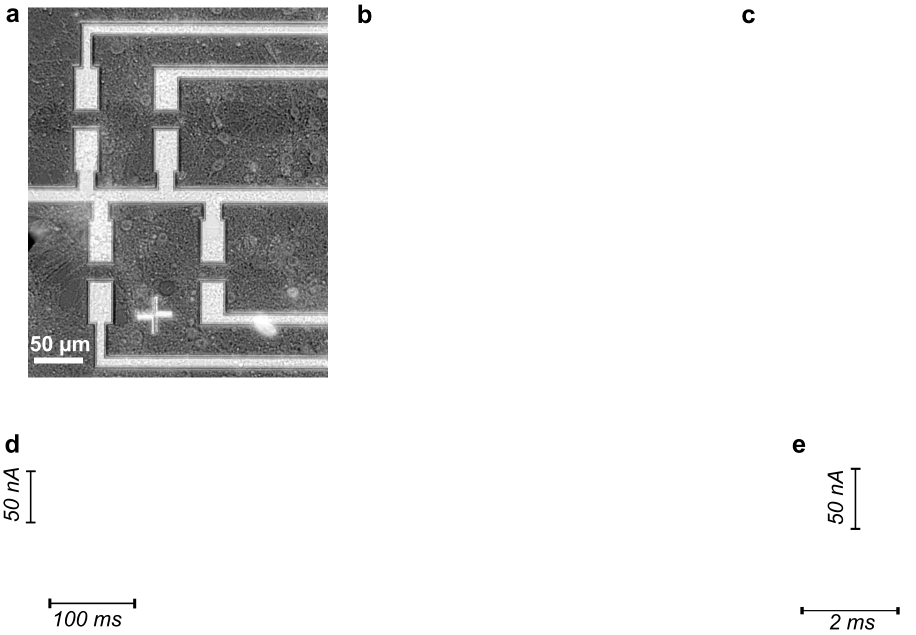

Figure 4.29: G-FET characteristics before and after 3 weeks of neuron culture. a) Dense neuronal networks cultured on G-FETs (21DIV). b) Field effect in liquid gated G-FETs before culture (grey curves), covered with 21DIV neurons (blue curves), and after cleaning the chip (orange curves). The darker curves represent the average field effect curves for each condition. All measurements were performed in cell culture medium at V_{SD} = 50 mV. c) Average sensitivity of G-FETs before the culture (black), covered with neurons (blue) and after cleaning (red). The sensitivity was calculated from the average field effect curves in b). d) Potential pulse detection using G-FETs covered with neurons. A 1 ms long potential pulse V_p = 500 µV was applied to the cell culture medium through a Pt-electrode; the transistor working point was set to the highest sensitivity, and the current through the FET-channel was measured at V_{SD} = 100 mV. e) Zoomed view of an individual current pulse detected in d).

After the electrical recordings with neurons, the chip was immersed into warm DI water, resulting in the burst of neurons due to osmotic pressure. The chip was then rinsed several times with DI water and dried. After this simple cleaning procedure, the transfer characteristics of G-FETs were measured again in cell culture medium. After removing the neurons, the Dirac point shifted back to less positive voltage values. However the conductance and the sensitivity of the FETs were further decreased compared to the initial value and to G-FETs covered with neurons. The decreased sensitivity suggests a reduced mobility of charge carriers due to increased scattering. The scatter centers can originate from structural defects in the graphene layer introduced by the cleaning process, membrane residuals, as well as water molecules or chemicals from the culture medium absorbed on the graphene surface.

The sensitivity of G-FETs was reduced to 50% of the initial value after the cleaning. To re-use the chips for several cultures, the cleaning process has to be improved. First, DI water should not be used for removing the neurons, since the surface tension of water can lead to partial delamination of the graphene layer. Also, a complete dissolving of neuronal tissue should be ensured by using for example trypsine, a digestive enzyme able to degrade the cell membrane. Certain acids [321] were also shown to be efficient in removing organic tissue, however the impact of these treatments on our graphene devices was not tested in this thesis.

4.9 Conclusion

In conclusion, using pulsed CVD growth, we are able to produce high quality continuous monolayer graphene sheets on Cu foil, which can be transferred on a variety of rigid, transparent or flexible substrates by the wet transfer technique. The graphene quality is controlled throughout the entire processing using Raman microspectroscopy, revealing the monolayer nature of our graphene with a very low defect rate even on the final G-FET devices.

We also developed a fabrication process for the realization of graphene based FETs on different substrates with a very high success rate and reproducible electrical properties. G-FETs with sensitivities reaching 4 mS/V could be fabricated in a scalable manner. The suitability of our G-FETs for bioelectrical interfacing with electrogenic cells was confirmed by detection of small 1 ms long potential pulses applied to the liquid gate. The response time of our G-FETs was estimated to $\lesssim 0.5$ ms and a reliable fast detection of potential pulses down to 75 µV could be achieved. Additionally, the fabricated G-FET arrays are compatible with biocoatings, such as hyaluronic acid and poly-L-lysine, which is commonly used to increase the neuronal attachment on the sensor device. Their performance is stable and degrades only slightly during the neuron culture. The presence of live neurons of the FET surface, decreases the sensitivity to around 75% of its initial value. However, the FETs are still able to correctly detect small potential pulses (few 100 µV) applied to the cell culture medium, revealing the suitability of our G-FETs to detect neuronal signals.

However, several drawbacks could be identified during this work. For example, the surface cleanliness of graphene during the processing still remains an issue. While the initial graphene surface is very clean after thermal annealing, it is unavoidably contaminated during the fabrication of G-FETs due to the use of photoresist. A cleaning process has to be developed to further improve the transistor performance. A clean surface would decrease the contact resistance and increase the interfacial capacitance to the liquid gate, leading to a higher transconductance and lower response time of the transistor. Also, the linear operation regime should be expanded to a wider gate voltage range to ensure a stable detection for example by reducing the graphene area under the insulating polymer.

Although some improvements can be made, the performance of G-FETs developed in this work is at the same level as state of the art devices.

CHAPTER 5

Neuron culture: methods and biocompatibility assessment

In this chapter we will describe the methods used for culturing primary hippocampal neurons, including imaging techniques and in-vitro designing of controlled neural networks using chemical patterning. We will also present a detailed study of the bioacceptance of different materials used as a neural growth substrate. In particular, we will focus on the cytocompatibility of pristine monolayer graphene and show, that the crystalline quality of graphene has a major impact on its neural affinity.

5.1 Primary hippocampal neurons as a study object: In-vitro neuronal growth as model of complex in-vivo systems

The fundamental understanding of the functionality and information processing in the brain is one of the most fascinating research areas in our days. Numerous clinical studies are carried out using EEG and ECoG electrodes to detect the brain activity and its response to different stimuli [322–327]. However this method provides only general information about the activity of large brain areas. To increase the spatial resolution and to resolve the interactions between different brain regions, more invasive techniques are required. For example, using subdural implants *in-vivo* recordings with a few cell resolution are possible [328, 329]. Yet not always a complicated experiment involving a live organism is necessary to obtain the desired information, and thus cultured neural networks are routinely used in fundamental neuro-physiological research as a model to study the brain functionality on a single neuron level. As *in-vivo*, cultured neurons develop complex network with synaptically connected cells. At the same time, the monitoring of the network architecture and the signal propagation within the network becomes more simple than in *in-vivo* case. Additionally, the physiology of a single neuron can be studied in a controlled environment with a single ion channel resolution.

The neurons for *in-vitro* cultures are usually obtained from the cerebellum (cortical) or from the hippocampus (hippocampal neurons) of rat/mouse brains. Here, we used primary hippocampal neurons from mouse embryos. The hippocampus is the brain region responsible for the long term and spatial memory, learning and navigation [330–334]. If damaged, it may cause memory loss and disorientation, such as in case of Alzheimer's disease [335, 336]. Due to the specific morphology, hippocampal neurons can be divided into two main types: pyramidal cells and interneurons with additional separations within the both types [337]. Considering the complexity of the hippocampus functions, the neurons obtained from this brain region are expected to develop complex networks with distinct electrical activity and to be suitable to study learning processes and memory development. Moreover, embryonic hippocampus provides relatively homogeneous neuron populations, mainly composed of pyramidal neurons with a small amount of glial cells. As already described, glia are non-neuronal cells in brain, which mechanically support the neuronal organization, electrically isolate the neurons from each other, supply nutrients to the neurons and build the immune systems of the brain [3, 338–340]. While glia do not participate directly in synaptic interactions and electrical signaling, they play an important role in development of synaptic contacts and maintain the signaling abilities of neurons [5, 341, 342]. They also provide scaffolds for neuronal development and are involved into the healing process after neural injuries and protection from foreign bodies by building glial scars around them [41, 343].

Over the past decades, the neural cultures enabled a variety of studies, providing insights into the subcellular morphological organization and physiological functionality of single neurons, as well as the information processing and synaptic plasticity of neural networks. Cultured neurons exhibit similar electrical activity as neurons *in-vivo* and can be electrically interfaced to sensing devices, such as MEAs or FETs. Using specific adhesive/repellent polymers, neural outgrowth can be even guided along predefined chemical pattern [344], allowing the organization of neurons into different networks and an exact positioning of neurons above the individual sensing element. Using cultured neurons, investigations under controlled conditions are possible, and the response to different chemicals/drugs can be studied much easier than in *in-vivo* conditions. However, the separation of neurons from their natural environment may result in an abnormal behavior. In the culture, the three dimensional neuronal organization with high interconnectivity within the brain is replaced by simple 2D connected neurons. Also no sensory input from other brain regions exists. Thus, the activity pattern of cultured neurons may drastically differ from the activity in live organisms.

It was shown, that neurons exhibit the ability to adjust to the environment, changing their shape and morphology [345–348]. Depending on the growth substrate neurons may exhibit different outgrowth and electrical activity [240, 242, 349]. The varying cytocompatibility of different materials will be discussed in more detail in Chapter 5.2.

5.1.1 Culturing methods

For the neuron cultures we used hippocampi from 16 days old (E16) mouse embryos. The pregnant mouse was killed by breaking its neck. Hereby the base of the skull is hold between thumb and forefinger and slightly twisted, at the same time the tail is pulled backwards [350]. The embryos are then isolated from the mouse and kept in ice cooled dissection medium (10×HBSS

+ 1 M HEPES, Invitrogen). The brains are separated from the body. Hippocampus is located in the temporal lobe of each brain hemispheres. To isolate it, first the two hemispheres are separated. Using an optical microscope and fine tweezers and scissors, any non-cortical tissue is removed, followed by peeling off the meningeal tissue, a layer which covers the brain and contains blood vessels and cerebrospinal fluid. Then the hippocampus is dissected. A schematic dissection protocol is illustrated in Figure 5.1. The hippocampi are then chemically dissociated in 0.5 mM EDTA (2%, Life Technologies) solution supplemented 10% trypsin at 37°C for 15 min, followed by several washings in the dissection medium and mechanical dissociation by repeatedly pipetting the cells up and down. The cell suspension is then diluted in the plating medium (MEM with 10% foetal bovin serum (FBS), 1% glutamine and 0.05% peniciline/streptomycine, Gibco) to the desired cell concentration (seeding concentration) and plated onto the growth substrates. After 2-3 hours of incubation at 37°C in humid atmosphere containing 0.5% CO_2, the excess cells are removed and the attachment medium is replaced by a conditioned cell culture medium (Neurobasal/B27, Invitrogen).

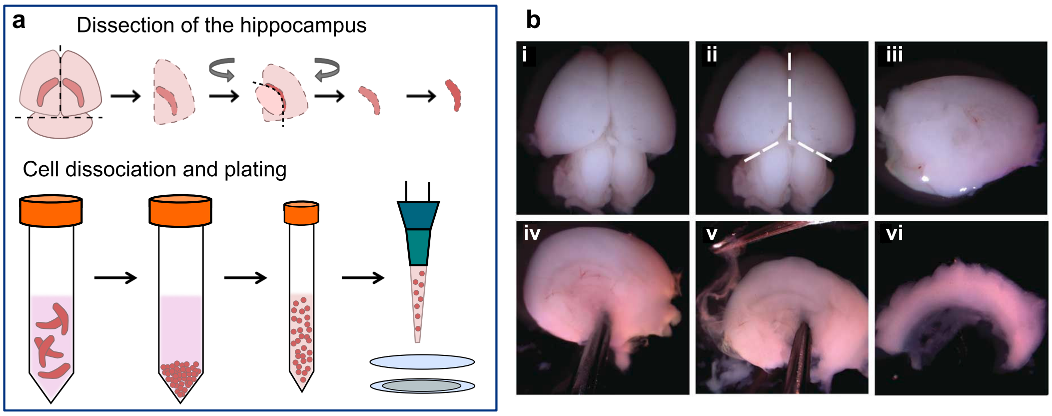

Figure 5.1: Culturing hippocampal neurons. a) Schematic illustration of dissection of hippocampus, dissociation of hippocamal neurons to the desired cell density and plating on growth substrates. b) Optical images of the dissection process: i) place the brain dorsal side up in dissection medium, ii) separate the two hemispheres, iii) place each hemisphere's cortex side down and remove any noncortical forebrain tissue, iv-v) hold the hemisphere carefully and remove the meningeal tissue, vi) dissect out the hippocampus. Figure adopted from [351].

The exact composition of the cell culture medium, as well as a detailed culturing protocol, can be found in [352]. We supplemented the culture medium with 1 µM AraC to inhibit the proliferation of glial cells. During the incubation, the culture medium was changed weekly.

The cell culture medium was conditioned in an astrocyte co-culture. Astrocytes are specific star shaped glial cells involved into a variety of physiological processes in the brain [340, 342]. The proteins secreted by astrocytes were shown to improve the growth and maturation of neurons in culture [353–356]. We obtained astrocytes from cortex of E16 mouse embryos. The cells were plated at concentration $\sim 4{\cdot}10^4$ cells/cm^2 on 100 mm Petri dishes covered with PLO (Poly-L-Ornithine), which improves the cell adhesion, and incubated in MEM + 10% FBS medium until confluency. MEM medium improves astrocyte proliferations and inhibits the neural growth. Next the medium was supplemented with 1 μM AraC to eliminate microglia, and after 48 h replaced by Neurobasal/B27. From this point, the medium was collected every 2 days and replaced by fresh one. The collected astrocyte-conditioned medium was filtered, supplemented with AraC and frozen for subsequent use for hippocampal neuron cultures.

For the majority of materials, including glass coverslips usually used for neuron cultures, neurons do not spontaneously attach on the surface, and the substrates surface has to be functionalized with an adhesive polymer. We used poly-L-lysine (PLL) coating to increase the neuronal attachment. One day before the culture, the substrates were sterilized in ethanol and if possible treated by O_2 plasma to make the surface more hydrophilic and enhance the attachment of PLL. Shortly before use, PLL was diluted at 1 mg/ml in filtered 0.1 M borate buffer (pH 8.5). A droplet of this solution was added to the substrate surface (for hydrophilic surfaces this droplet spreads evenly over the entire surface). The substrates with PLL solution were covered to avoid the evaporation and left stand overnight. On the following day immediately before the culture, the excess PLL was washed out in several sterile water baths.

5.1.2 Immunofluorescence microscopy

To characterize the neural development at different growth stages, we used immunofluorescence (IF) microscopy, which is a powerful technique to visualize the neural anatomy [357, 358]. The principle of IF imaging is based on the specific binding of fluorescent molecules on different neural buildings blocks, such as the nuclei, synaptic vesicles, actin filaments and microtubules. Using various fluorescence wavelengths, each part of the neuron can be observed separately, allowing a detailed investigation of the neural development and maturation.

To perform IF analysis, the neurons were fixed on the substrates and stained with fluorescent antibodies. The fixation was achieved using paraformaldehyde (PFA). More precisely, the culture medium was removed and replaced with 4% PFA solution (diluted in PBS), and after 10 - 20 min in PFA, the cells were washed three times with PBS and directly used for IF staining or stored at 4°C in PBS. Depending on the fluorescent molecule, two different staining protocols exist: direct and indirect IF staining. For the first one, the molecules directly bind on the target neuron location. In the latter case, the binding is mediated by a specific primary antibody, which binds at the target neuron location and builds anchors for the secondary fluorescent antibody. The primary antibody is produced in a specific host animal, which is recognized by the the secondary antibody. To ensure a specific labeling of different neuron parts, primary antibodies from different animal species have to be used.

To enable the antibody binding, first the neural membrane is permeabilized in 0.1% PBS-Triton solution for 10 - 30 min. Then the cells are incubated with primary antibodies diluted in BSA (bovine serum albumin) for 1 h at room temperature, followed by three subsequent washings in PBS and further incubation with secondary antibodies diluted in PBS during 1 h (protected from light). Then the cells are washed again and exposed to DAPI deluted in PBS for 10 min. DAPI is a direct IF dye, labeling the cell nuclei. Lastly, the neurons are washed in PBS, and the substrates are glued onto microscope slides using a specific mounting medium (Dako, Sigma-Aldrich). The antibodies used in this work are supplied by Millipore or Sigma-Aldrich ($*$), and are summarized in the table below.

Table 5.1: Antibodies used for IF staining.

Indirect Immunofluorescence Staining			
Primary Antibodies			
Antibody	Target neuron location	Host animal	Dilution in BSA
Synapsin I	Synaptic vesicles	Rabbit	1:350
YL 1/2	Microtubules	Rat	1:1000
Tau-1	Axon specific microtubules	Mouse	1:150

Secondary Antibodies			
Target Animal	Flourophore	Wavelength	Dilution in PBS
Rabbit	CY3αRab	647 nm	1:500
Rat	CY5αRat	488 nm	1:500
Mouse	CY5αM	infrared	1:500

Direct Immunofluorescence Staining			
Antibody	Target neuron location	Flourophore	Dilution in PBS
DAPI*	Nuclei	Blue	1:1000
Phalloidin*	Actin	Alexa Fluor 594nm	1:150

Immunofluorescence images were acquired using a fluorescence microscope *Olympus BX51* and image processing was then performed with the free software *ImageJ*.

5.1.3 In-vitro control of neuronal growth pattern and connectivity

A deeper understanding of information processing in the brain can be achieved by designing simple neural networks *in-vitro*. The direct interfacing of individual network entities with the sensing devices would allow a complex spatially and temporally resolved study of neural signaling and connectivity. Recently different approaches are developed to design neural networks in cultures, including chemical patterning [359, 360] and topographical constrictions [91, 361, 362]. In this work, we used poly-L-lysine pattern for neural confinement. PLL patterning is a simple technique to realize defined neural networks. Changing the shape and width of adhesive PLL stripes, the axonal polarization can be easily controlled [116], allowing specified positioning of axons and dendrites above the recording/stimulating sites of the sensor device. As shown in Figure 5.2 b, the soma position is defined by a circular shape node, while the neurites are confined on PLL stripes. The width of these stripes determines whether a dendrite or an axon will develop. The narrower stripes result in faster growth dynamics, and once a critical length is achieved, the neurite becomes an axon. Thus the axon/dendrite guiding can be realized by a simple geometrical approach [363]. Already at DIV2 some of the neurons develop axon, as shown by the higher concentration of Tau antibodies (Fig. 5.2 e).

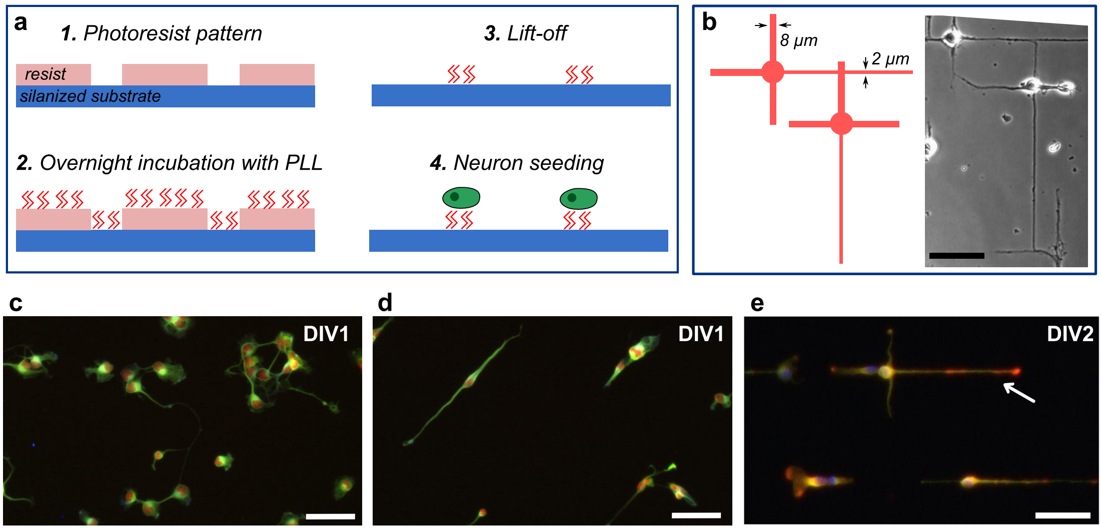

Figure 5.2: Patterning neural networks. a) Schematic illustration of the realization of the adhesive PLL pattern. b) Example of a pattern design, and transmission microscopy image of the obtained neural network at DIV4. c) Random neural growth on PLL coated glass coverslip at day one in culture. d) DIV1 neurons confined on a PLL pattern. Dapi (red) labels the soma, synapsin (green) the synaptic vesicles, and tau (blue) the axon. e) DIV2 patterned neurons. The arrow indicates the already developed axon. Dapi (blue) labels the soma, synapsin (green) the synaptic vesicles, and tau (red) the axon. All image were obtained from the same culture. Scale bar is 50 μm.

The adhesive PLL pattern was realized either on glass coverslips or SiNW-FET arrays using standard photolithography techniques. The substrates were covered with photoresist and the desired pattern was exposed. After short oxygen plasma treatment to clean the exposed area and to make it more hydrophilic, the substrates were incubated with PLL solution over night. The lift-off was then performed using ethanol in ultrasonic bath, and the substrates were rinsed in sterile deionized (DI) water. Since the substrate itself prevents the neural adhesion, the seeded neurons attach on the PLL pattern, forming the desired network. However the neural confinement on PLL pattern realized on untreated glass is not strong enough, and usually after few days in culture, the neurons start to explore the surroundings and finally spread beyond the pattern by generating the supporting extracellular matrix. This can be partially suppressed by using cell repulsive protein coatings [364] or silanizing [360] the substrate before defining the PLL pattern. Here we used APTES molecules (Sigma Aldrich), which covalently bind on the substrate surface and build a cell repellent film, preventing the growth of neurons. Prior to the silanization the glass coverslips were cleaned and subsequent acetone/isopropanol/DI water baths and treated with oxygen plasma, APTES molecules were in-situ deposited using vapor-phase deposition technique.

For long term investigations of the network connectivity up to the maturation stage, the cell migration hast to be prevented. As already mentioned above, after few days in culture, neurons start to grow beyond the PLL pattern. The silanization of the substrate surface can delay, but not completely inhibit this process. Figure 5.3 a shows, that already at DIV7 the neurons start to develop interconnection outside the defined PLL pattern. Up to DIV12, the network remains partially intact, and the individual neurons exhibit healthy growth with a dense distribution of synaptic vesicles (Fig. 5.3 a). However, at DIV19, the initially designed network finally vanishes within the random neural growth all over the substrate (Fig. 5.3 b).

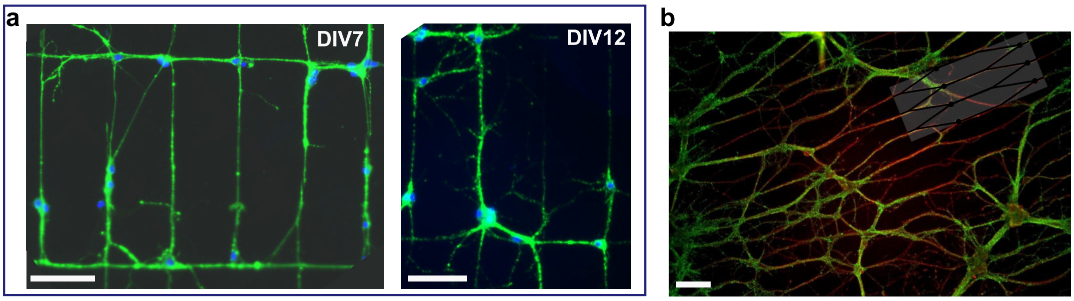

Figure 5.3: Evolution of the PLL patterned neural networks. a) Rectangular neural pattern realized on silanized glass coverslip at DIV7 and DIV12. Dapi (blue) labels the soma, and synapsin (green) the synaptic vesicles. Scale bar is 100 µm. b) DIV19 hexagonal neural network. The inset indicates the original pattern. Dapi (blue) labels the soma, synapsin (green) the synaptic vesicles, and tau (red) the axon. Scale bar is 50 µm.

The morphological and physiological stability of the designed neural networks depends on several factors. For example, isolated networks of few neurons hardy survive and usually do not establish spontaneous electrical activity. Several studies have shown, that the electrical activity of neural networks strongly depends on the population size [365, 366]. Thus to increase the survivability of neural networks up to maturation stage, the small networks have to be integrated into a bigger neuron population. Further, to establish synaptic connections, the axon of the emitting neuron has to be connected to the dendrites of the target neuron. This can be achieved by using the geometrical approach for axonal polarization as described above. Also the neurite path orientations with respect to soma position seems to have a significant effect on the confinement of the network. As shown in Figure 5.4 a, rectangular networks with neurites emerging perpendicularly from the cell body exhibit higher stability than hexagonal networks. Especially with regards to bioelectrical interfacing of individual neurons to sensing devices, the PLL assisted patterning of neural networks is an easily implementable method. This patterning technique is not additionally affecting the device performance, since for most biosensors a PLL coating is anyway used to ensure the neuron attachment. Here, we employed the more stable rectangular network on SiNW-FET arrays, as shown in Figure 5.4 b. The neural network survived up to DIV12. At this stage the neurons start to migrate and to detach from the initial PLL pattern. As already discussed above, the stability of the network can be improved by increasing the neuron population and designing more dense networks. However this possibility could not be investigated during this thesis, and the optimization of the patterning protocol still remains an issue.

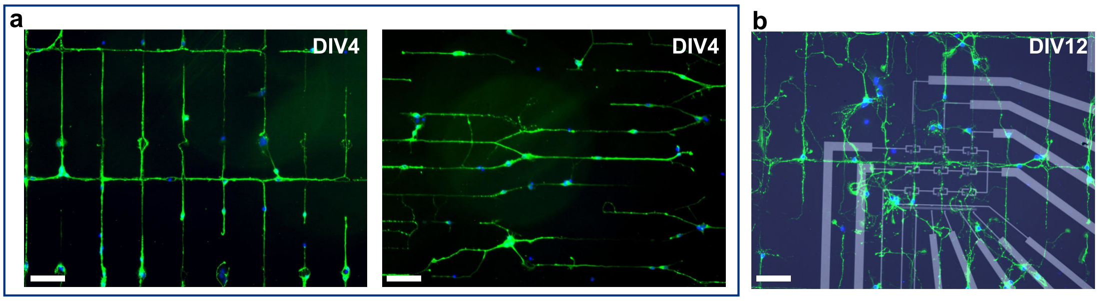

Figure 5.4: Stability of different neural networks. a) Rectangular (left) and hexagonal (right) neural networks at DIV4. b) DIV12 rectangular neural network patterned on SiNW-FET array. Dapi (blue) labels the soma, and synapsin (green) the synaptic vesicles. Scale bar is 100 µm.

5.2 Neural adhesion and growth on different materials: A bioacceptance study

The neural membrane is a complex organelle involved into a variety of cell functions. Beside the generation of electrical signals and exchange of specific molecules and nutrients, it contains adhesion receptors, involved into the building of the extracellular matrix (ECM). ECM is a complex multimolecular material that surrounds the cell. It builds a scaffold on which the cells can adhere and provides an adjusted micro-environment for cellular growth [345]. For *in-vitro* growth of neural cultures artificial ECMs can be designed using adhesive polymer coatings or specific topographical modifications of the substrate.

In-vitro adhesion and growth of neurons on artificial ECMs is controlled by the transmembrane adhesion proteins (primarily the proteins of the integrin family), which can intelligently sense and respond to a wide range of environmental signals, including the chemical composition, topography, strain and rigidity of the underlying growth substrates [345]. This environmental sensing results in the ability of cells to adjust their cytoskeletal organization to the direct surroundings. Thus depending on the topography, rigidity and material of the growth substrate varying adhesion, shape and connectivity of cultured neurons can be observed. For example, neurons grown on randomly distributed silicon nanopillars exhibit less, but longer neurites, elongate faster and differentiate an axon earlier than those grown on flat silicon surface [346]; neurons cultured on softer gels show higher dendrite branching [367]; mechanical stretching/tension can accelerate the axonal polarization [368, 369]; and modification of hydrogels with positively charged monomers improves primary neuron attachment [370].

Neuronal attachment and growth dynamics, including axonal polarization, dendrite branching and formation of synaptic connections, reveal the potential of the material for use in tissue engineering, regenerative medicine or bioelectrical interfacing. In this context, the adhesion strength of the cells to the growth substrate is particularly important for bioelectrical interfacing, since an intimate neuron/device coupling is a crucial parameter to establish a strong electrical link for a reliable detection/stimulation of neural activity.

5.2.1 Strategies for cell adhesion promotion

Currently a variety of electrode materials is used to stimulate and to detect signals from electrogenic cells [15], such as neurons. However, it was shown, that the quality of the detection strongly depends on the cell-device coupling [371]. The commonly observed weak electrical link between the cell and the device is mainly attributed to the property of living cells to form an extracellular cleft between the cell plasma and the substrate, to which they adhere. This cleft increases the dissipation of the ionic current generated by action potentials, resulting in a reduced effective field potential above the sensing device and lower signal-to-noise ratio. Consequently, decreasing the cleft thickness can improve the electrical coupling [21] and allow the detection of even very small signals. Topographical modifications of the electrode surfaces for example with spine shaped protrusions or nanopillars, were shown to significantly decrease the distance between the cell membrane and the electrode surface [21, 82] and increase the signal-to-noise ratio [21]. Similarly, materials promoting a direct neuronal attachment and growth without any additional adhesive coating, can be considered to decrease the cleft thickness due to their high biocompatibility and improve the electrical coupling to the neurons.
For the majority of sensor materials, including the topographically modified electrode surfaces, neuron adhesion is mediated by an adhesive coating, such as poly-lysine, laminin or fibronectin, that mimics the extracellular matrix and improves the cell attachment [372]. However these polymer coatings affect the electrical coupling. They increase the distance to the cell [373] and reduce the sensitivity and the reliability of the recording. Bypassing the adhesive coating using biocompatible materials would improve the detection quality and allow the realization of long-tern neuroprostheses. Thus, besides the excellent electrical properties, the sensor material should also offer a close proximity to the cells.

In following we will present a biocompatibility study of different materials and reveal the high neural affinity of pristine graphene.

5.2.2 Neural growth on different materials

Here we studied neuronal adhesion and growth on following materials: glass coverslips (12 mm diameter, Marienfeld), high quality monolayer CVD graphene, nanocrystalline CVD diamond (NCD), parylene-C and polyimide (PID). Conventional glass coverslips were used as control substrates. Parylene-C and polyimide are often used as insulating materials and flexible substrates for biosensor arrays. For this study both were deposited onto glass coverslips. Also graphene was transferred onto glass coverslips by PMMA assisted wet transfer technique as described in Chapter 4.5. Particularly interesting is the growth of neurons on pristine conductive materials, such as CVD diamond and graphene. As discussed above the possibility to bypass the adhesive coating would improve the electrical coupling and reveal the potential of these materials for chronical implants.

Half of each sample batches were coated with PLL as described above, while the other half remained pristine. Using the previously described protocol, primary E16 mouse hippocampal neurons were cultured on both coated and pristine substrates for 5 days. Two samples of each batch were fixed and immunostained at DIV1, 2, 4 and 5. Since at DIV4 and 5, the neural architecture becomes very complex, the main growth characteristics, such as neurite number and neurite length, were compared only at the early growth stage, i.e. at DIV2.

Figure 5.5 demonstrates representative IF images obtained on different growth substrates after 2 days of culture. While with PLL coating, all substrates exhibit neural attachment with expected shape and neurite outgrowth, without PLL neurons attach only on graphene. While it is not surprising, that no neurons adhere to pristine glass or polymer substrates, the repellent nature of NCD seems to contradict the general impression of its high neural affinity, which arises from various studies reporting cell adhesion and growth on pristine diamond surface. However, this studies either report the adhesion of proliferating cell lines [374–376] or use an additional nanodiamond (ND) coating when combined with primary hippocampal neurons [377, 378]. A disadvantage of using nanodiamond coating is that, despite the same chemical composition as NCD, they may alter the electrode properties. A recent study finally reveals, that primary neurons do not adhere to the pristine NCD surface and provides a possible explanation of the controversial neural adhesion on pristine NCD and nanodiamond functionalized surface [379]. The authors suggest, that varying culture parameters as well as the differences in protein absorption ability of nanodiamond particles and NCD films may affect the neural adhesion.

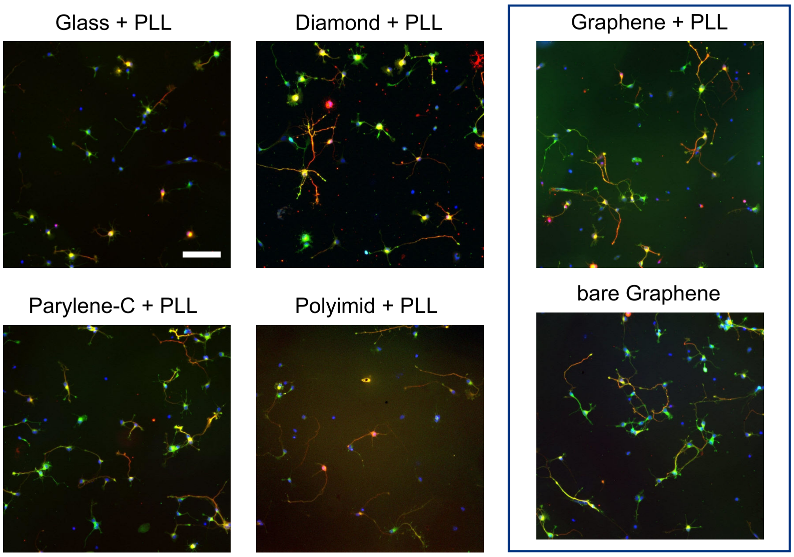

Figure 5.5: Representative IF images of 2 days old neurons growth on different substrates.Note, that in absence of PLL neurons only attach and grow on graphene. IF labeling: dapi (blue) labels the soma, synapsin (green) the synaptic vesicles, and tau (red) the axon. Scale bar is 100 µm.

As can be seen in Figure 5.5, already at DIV2 neurons start to develop axons, as shown by emerging tau staining (red), which labels the axon specific microtubules. However neurons grown on coated glass coverslips exhibit less axon polarization than those cultured on other substrates, including pristine graphene.

A detailed analysis of the neural development on different substrates is given in Figure 5.5. We compared the cell density at DIV1 and DIV2, as well as the neurite number, total outgrowth and the length of the longest neurite per neuron (which is presumably the future axon) at DIV2. The neurons are seeded with the same initial density (124 neurons per mm^2) on all growth substrates, but not all of these neurons attach to the substrate surface. For coated samples, around 66% of seeded neurons attached on the diamond surface, and only 42% to the polyimide, as shown in Figure 5.5 a. The low amount of neurons attached to PID is maybe due to higher hydrophobicity, which was observed prior to PLL deposition and could affect the homogeneity of the final coating. At DIV2, the neuron density decreases for all substrates by around 10 - 15%. More interestingly, the neural adhesion on pristine graphene (without PLL coating) is significantly higher than for PLL coated substrates, while on non-coated glass, diamond, parylene and PID statistically no neurons adhere (less than 5 on the entire sample with substrate diameter of 12 mm). While the results obtained on pristine graphene will be briefly mentioned here, a detailed discussion will follow in the next chapter.

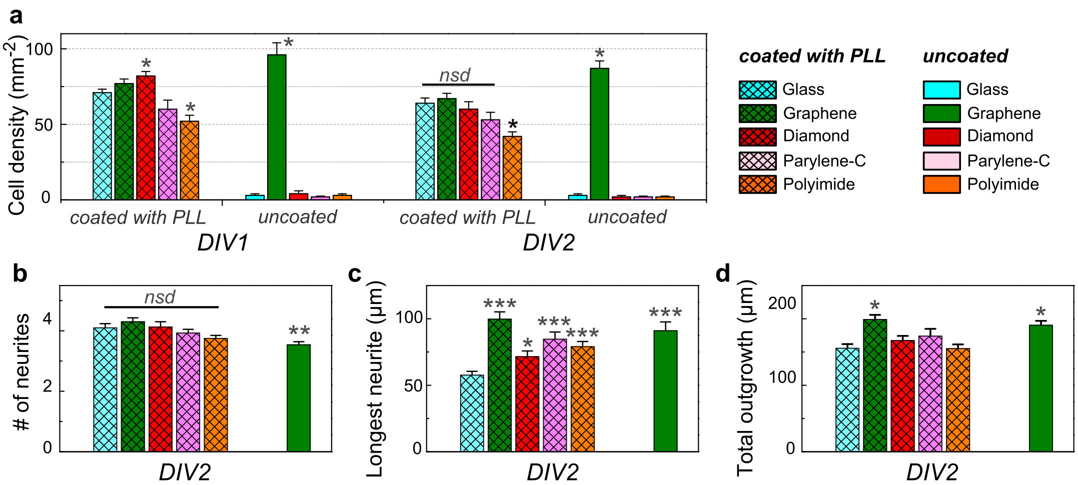

Figure 5.6: Neural adhesion and growth on different materials. a) Cell density at DIV1 and DIV2. b) Number of neurites, c) length of the longest neurite and d) the total outgrowth per neuron at DIV2. The results are obtained from one culture with two samples per batch and expressed as mean values ± s.e.m. (with at least 140 neuron per condition). The results were statistically compared to the control PLL coated glass coverslip using ANOVA followed by Bonferroni test with significance levels: $^{*}p < 0.05$, $^{**}p < 0.005$ and $^{***}p < 0.001$, "nsd" mens no significant difference.

Neurons grown on all investigated substrates exhibit healthy shape and outgrowth. At DIV2, on all PLL coated samples neurons develop in average 4 neurites, and significantly less than 4 on pristine graphene (Fig. 5.5 b). At this development stage also the initiating axonal polarization can be observed on all growth substrates. However, the amount of neurons developing axons are less on glass coverslips than on other samples. While the number of neurites is statistically equivalent on all coated samples, significant differences were found in terms of the neurite length. Graphene as well as parylene and PID seem to promote neuronal growth. As shown in Figure 5.5 c, the neurons cultured on these substrates exhibit significantly higher length of the longest neurite per neuron than those grown on glass coverslips, which reflects the less frequently observed axonal polarization. As already mentioned above, the neurite outgrowth strongly depends on the stiffness of the growth substrate [367]. During their development the neurons continuously probe the surrounding environment via neural growth cones, which are highly motile structures at the neurite ends able to recognize and respond to the mechanical/chemical properties of the growth substrate [380]. It was shown that neurons retract and re-extend their processes in response to the increased stiffness [381]. As a result, the axonal elongation is delayed on stiff substrates, such as glass coverslips and diamond, and accelerated on soft materials, such as parylene and PID. PLL coated diamond exhibits slightly higher maximal neurite length, than control glass coverslip, which can be attributed to the increased substrate roughness [378]. Neurons grown on PLL coated and pristine graphene develop longest maximal neurites. Mechanisms, which might be involved into increased neurite length will discussed in Chapter 5.3.2.

Despite the significant differences in the maximal neurite length, the total outgrowth, calculated as the cumulative length of all neurites emerging from the same soma, is statistically equivalent on all coated substrates, expect graphene (Fig. 5.5 d). Again this observation reflects the accelerated axonal differentiation on soft polymers and diamond. The mass gain/total growth velocity of the neurons seems to be preserved on all substrates: while on glass coverslips all neurites grow almost equally fast, on polymers and NCD the dendrite growth is delayed to benefit the earlier axonal polarization. Graphene however seems to actively promote the neural growth. Neurons grown on graphene not only exhibit the longest maximal neurite, but also the highest total outgrowth, revealing that graphene accelerates all processes in the neuron. More importantly, neurons grown on pristine graphene exhibit similar amount of processes as those grown on PLL coated graphene, and higher total outgrowth than those cultured on other coated substrates. Unlike other substrates, graphene significantly improves the neuronal growth even without an adhesive coating, revealing its exceptionally high neural affinity.

The presented study of neural growth on different materials demonstrates the effect of the growth substrate on the neuronal development and reveals the superior improvement of neuronal growth by using PLL coated graphene, which even extends the performance of soft polymers (parylene and PID) and nanocrystalline diamond. The most important and original finding of this investigation is however that pristine graphene (without any coating) increases neural adhesion and outgrowth and offers a unique growth support for primary neurons. This extraordinary neural affinity of pristine graphene will be discussed below in more detail.

5.3 Pristine graphene interfaced with primary neurons

In previously published works, graphene has already been investigated in terms of its biocompatibility in combination with primary cell cultures, stem cells and purified adult retinal ganglion cells [65, 213, 240–242]. It was shown, that graphene layer indeed supports neuronal attachment and sprouting [240], increases the stem cell differentiation into neurons [241] and enhances the electrical activity of neural networks in culture [242]. However, in these studies either an adhesive coating was used to ensure the cell attachment [240–242], or the demonstration of the superior cytocompatibility of pristine graphene was insufficient. It was reported, that proliferating cells, more specifically retinal ganglions, attach to and survive on pristine graphene surface [65]. However proliferating cells already exhibit effective ECM, and thus it is not surprising that they not only attach to the pristine graphene, but also to the bare sapphire substrate without any adhesive coating [65]. In contrast, culturing primary neurons on glass substrates always requires additional surface functionalization prior to neuron seeding. Up to now, primary hippocampal neurons grown on pristine graphene were shown to built cell body conglomerations [213] indicating a poor adhesion to graphene surface. Here however, we found that pristine graphene is similarly compatible with primary hippocampal neuron cultures as samples coated with an adhesive poly-L-lysine (PLL) coating (see above Chapter 5.2.2).

In the following study, we investigate single layer graphene with and without an adhesive PLL coating in terms of neural attachment and neural development over a period of 5 days *in-vitro*. Glass coverslips (with and without PLL) were used as control samples.

5.3.1 Strong adherence of primary hippocampal neurons to pristine graphene

Surprisingly, while there is neither adhesion nor neurite sprouting on the uncoated glass, the neurons could not only adhere but also grow on bare graphene with highly developed neurite architecture. As shown in Figure 5.7 a, the neurons define a clearly identifiable border between the graphene and the uncoated glass substrate. In contrast to previous culture on sapphire[65], the hippocampal neurons do not attach to uncoated and untreated glass. Thus the neuronal adhesion can be attributed only to presence of graphene.

The adhesion on bare graphene is strong enough to prevent cell migration and neurite sprouting towards the uncoated glass substrate. The neurons stay confined on graphene during 5 days of culture (Fig. 5.7). The suppressed cell migration observed here reveals the extremely strong neural adhesion to bare graphene surface.

Moreover, neither soma clustering nor neurite bundles were observed. Neurons grown on bare graphene exhibit a healthy shape and highly developed dendritic architecture. Their maturation follows the usual stages of development of hippocampal neurons in culture [382]: after 48 h the tau proteins are well expressed in the longest neurites, labeling the axon (see Fig. 5.7 f). At DIV5, neurite branching is widely observed and pre-synaptic vesicles start to agglomerate around somas and at the neurites end. Dendrites are outgrowing and neurons establish contact with neighboring cells (Fig. 5.7 f).

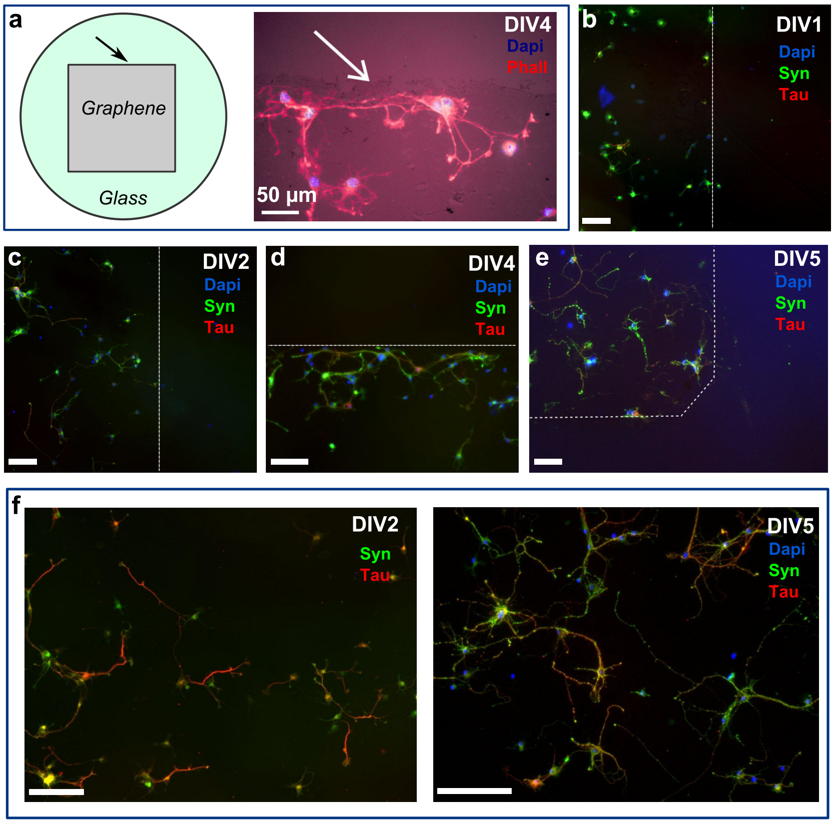

Figure 5.7: Neural confinement on pristine graphene. a) Schematic view of a square shaped graphene sheet transferred onto glass coverslip and IF image of DIV4 neurons cultured on uncoated graphene/glass substrate, showing that neurons attach and grow only on graphene. The arrow indicates the graphene/glass border. b-e) The neurons remain strongly confined on graphene during the entire study from DIV1 to DIV5. dashed lines indicate the graphene/glass border. f) At DIV2 Tau proteins accumulate in the longest neurites, labeling the axons. At DIV5, neurons develop complex dendritic architectures, while synapsin proteins start to agglomerate around the soma and at the neurites ends. Neurons are stained with Dapi (blue, nucleus), Synapsin (green, pre-synaptic vesicles), Phalloidin (red, actin) and/or Tau (red, axon). Scale bar is 100 µm.

To reveal how graphene affects the neural development, the growth dynamics on pristine graphene were compared to neurons grown on PLL coated graphene and on PLL coated control glass coverslips.

5.3.2 Enhanced neuronal adhesion and outgrowth on bare graphene

Figure 5.8 illustrates the neural development at early growth stage (DIV1-DIV2). As can be seen, neural adhesion on pristine graphene layer was found to be significantly higher (80% of the initial seeding density) than on both PLL coated graphene and glass samples (56%) (Fig. 5.8 a). No neurons attached on glass coverslips in absence of PLL. However the neurons cultured on pristine graphene developed in average 3.5 neurites and thus significantly less than those grown on coated samples with an average of 4 neurites for both glass and graphene (Fig. 5.8 b). The lower neurite emergence on pristine graphene seems to be compensated by faster growth dynamics. Indeed, the total area per neuron is identical for all growth substrates, while the maximal neurite length, which represents the longest neurite per neuron, and the total outgrowth at DIV2 were found to be significantly higher on pristine and PLL coated graphene samples compared to PLL coated glass coverslips (Fig. 5.8 c-e).

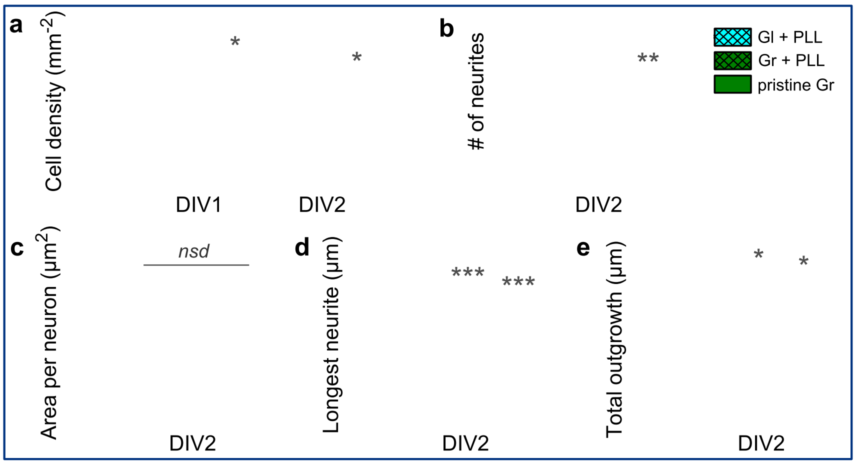

Figure 5.8: Enhanced neural attachment and growth on pristine graphene. a) Cell density at DIV1 and DIV2. b) Number of neurites attached to the surface at an initial seeding density of 124 cells per mm^2. c) Area, d) length of the longest neurite and e) the total outgrowth per neuron at DIV2. The results are obtained from one culture with two samples per batch and expressed as mean values ± s.e.m. (with at least 140 neuron per condition). The results were statistically compared to the control PLL coated glass coverslip using ANOVA followed by Bonferroni test with significance levels: $^{*}p < 0.05$, $^{**}p < 0.005$ and $^{***}p < 0.001$, "nsd" means no significant difference.

Since the longest neurite, presumably the axon[382], is almost 3/2 times longer on bare graphene, graphene may accelerate the axonal polarization while poly-L-lysine rather enhances neurite emergence. Similarly it was reported that neurons grown on native adhesive protein coatings, such as laminin, exhibit less neurites but longer axons (3 and 80 µm respectively) than neurons grown on synthetic polymers such as poly-L-lysine (4.5, and 35 µm) [383]. The PLL coated graphene layer seems to combine both fast neurite emergence (4 neurites) and accelerated axonal development, showing the highest neurite number (4) and longest maximal neurite (2 times longer than on PLL coated glass coverslips).

As already mentioned above, the mechanical properties of the growth substrate significantly affect the neurite sprouting and cell mobility [367, 381, 384, 385]. Recently, Lee and Co-worker have established a way to distinguish mechanical strain and charge doping in graphene by plotting the resonant frequency of 2D band peak as function of G band frequency [289]. If we apply this method on graphene used for neural growth here, it appears stretched and slightly hole doped compared to the neutral freestanding graphene (Fig. 5.9). Thus, it combines both positive and stretched surfaces, which are known to enhance the adhesion and the axon specification respectively [370, 384–388].

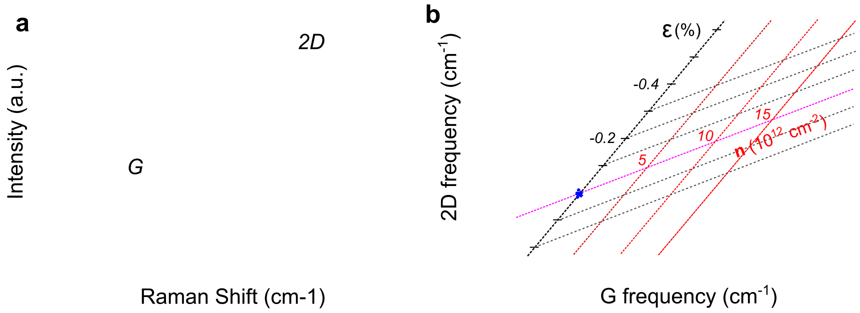

Figure 5.9: Mechanical strain and doping in graphene resoled using Raman spectroscopy a) Raman spectra of monolayer graphene used for neural interfacing. Graphene was transferred on glass coverslip. $\lambda_{exc} = 532$ nm. b) 2D band frequency versus G band frequency obtained from graphene layers used for neural cultures (green dots) plotted with the theoretical projections for strain ε/charge n induced (black/purple dashed lines) frequency dependence from [289]. Blue star indicates the neutral graphene.

While at the early growth stage, the neural density is significantly higher for non-coated graphene layer, it decreases faster with time and seems to saturate at the same cell density as for coated glass coverslips, as demonstrated in Figure 5.10 b. However the total surface covered by neurons as well as the area developed by an individual neuron increased during the culture and remained comparable with neurons grown on PLL coated glass coverslips (Fig. 5.10 c, d). The healthy development of neurons grown on pristine graphene, associated with the increasing neurite emergence and branching during the culture, demonstrates the high cytocompatibility of pristine graphene, which is at least comparable with PLL coated glass samples. Despite the comparable cell densities, the neurons grown on PLL coated graphene develop significantly higher individual and total areas than those grown on pristine graphene and coated glass samples (Fig. 5.10 c, d). This can be explained by the previous observation, that PLL coated graphene combines both, accelerated axon growth and higher neurite emergence attributed to the positive feedback of graphene and PLL coating respectively. However a quantified study of branching and/or neurite growth was not possible due to the high complexity of neuron networks achieved at DIV5. Inhomogeneities of the PLL and the graphene layers could also be involved. Pristine graphene seems to act as a unique adhesive coating for neurons, but due to local structural inhomogeneities this coating may partially fail. The same uneven covering may likewise occur for PLL coating. Thus, the combination of graphene layer and PLL coating could complement each other to further suppress inhomogeneities over the large surfaces scales sensed by the neurons after few days in culture, leading to a higher area fraction covered by neurons.

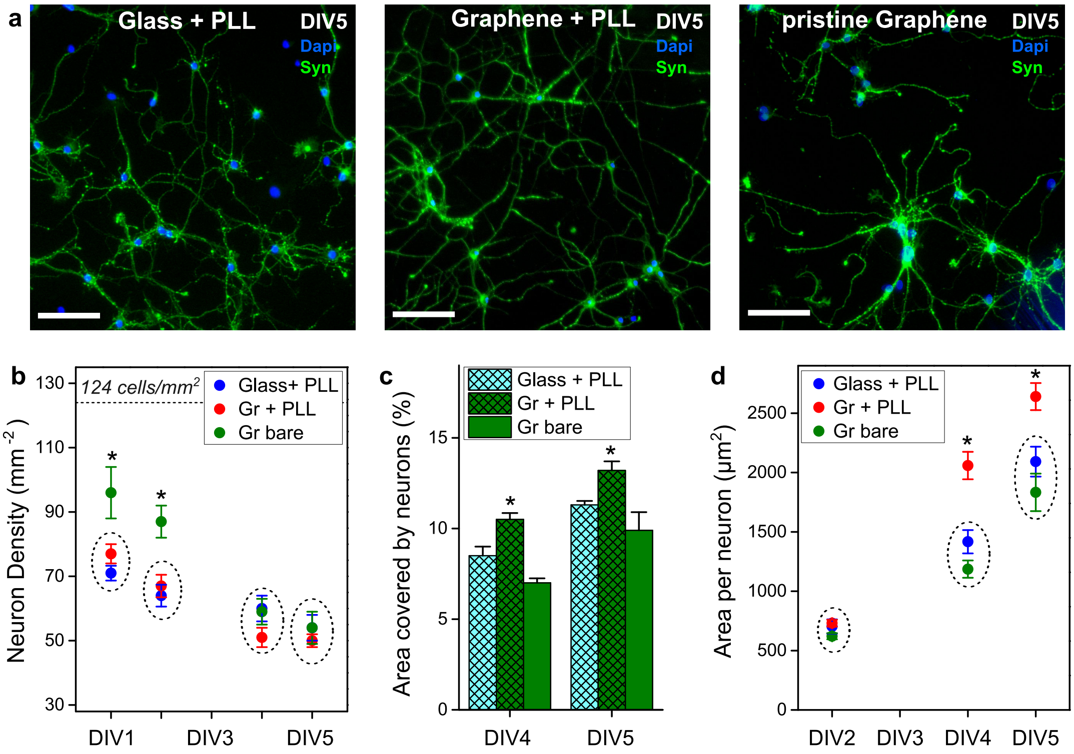

Figure 5.10: Influence of the coating on the dendrite outgrowth of hippocampal neurons. a) IF image of neurons grown: on PLL coated glass and graphene, and on pristine graphene at DIV5. Dapi (blue) and synapsin (green) labeling are superimposed. Scale bars are 100 µm. b) Neuron density as function of the incubation time. The dashed lines indicates the initial seeding density. c) The area fraction covered by neurons and (d) the area developed by an individual neuron. Results are expresses as mean value ± s.e.m., and statistically compared to the control PLL coated glass coverslip using ANOVA followed by Bonferroni test with a significance level of $^*p < 0.05$. Dashed circles represent values with no significant difference.

Summarizing the above, graphene acts as an adhesive layer to neurons and accelerates the axonal polarization. Neurons grown on pristine graphene exhibit stronger adhesion and higher outgrowth at the early stage of culture, while at the later growth stage their development is comparable to those grown on PLL coated glass coverslips.

5.3.3 Graphene quality in the culture

High-quality monolayer graphene, used for neural interfacing here, was grown on copper foil using pulsed CVD growth method [267] as already described in Chapter 4.4. The main characteristics of the obtained graphene layer transferred on SiO_2 substrates are shown in Figure 5.11 a. AFM scans reveal the overall homogeneity of the graphene layer with the specific wrinkles. Some resist residuals remain from the transfer process on the otherwise mostly clean graphene surface, which could be removed by a post transfer annealing. Raman spectroscopy analysis ($\lambda_{exc} = 532$ nm) further assess the crystalline quality of the transferred graphene (Fig. 5.11 a). The intensity ratio between the G- and 2D-band peak, centered at 1585 cm^{-1} and 2674 cm^{-1} respectively, is around 0.28, and the width of 2D-band is 25 cm^{-1} as expected for single layer graphene [291]. Moreover, the absence of D-peak (1300 cm^{-1} - 1383 cm^{-1}) confirms the absence of structural defects and the overall homogeneity of the graphene with extremely low rate of lattice defects.

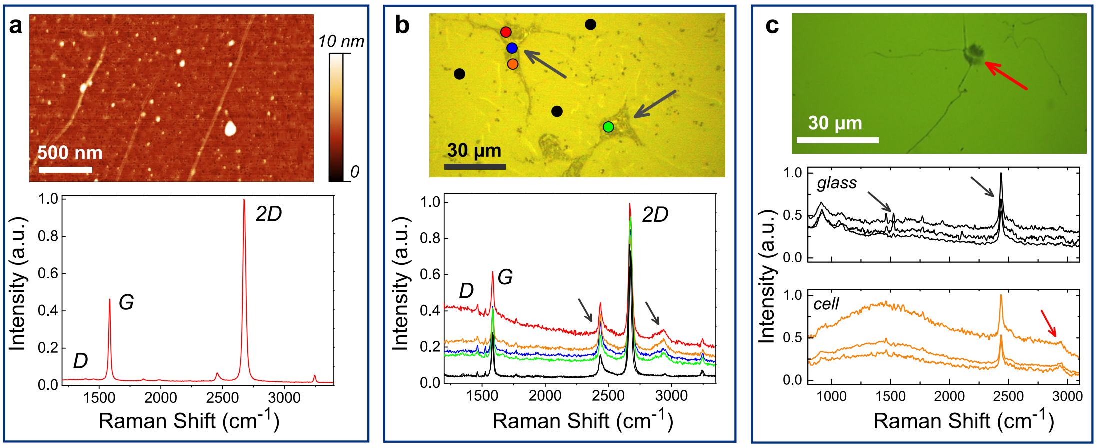

Figure 5.11: Quality control of pristine graphene in culture. a) AFM (top) and Raman (bottom) characterization of single layer graphene used for neural growth. b) Top: optical image of uncoated graphene after 1 day of culture. Arrows and dots indicate neurons and Raman laser spots respectively. Bottom: Raman spectra (3 superimposed spectra for each spot) acquired above the freestanding (black) and the graphene layer under the cell body (colored). Peaks related to the glass substrate and the cells are indicated by the gray arrows (2440 cm^{-1} and 2850 cm^{-1} respectively). c) Image of neurons cultured on PLL coated glass coverslip at DIV2 (top) and Raman spectra obtained on glass (black line) and on neuron (orange line)indicated by a red arrow in the top image. Black and red arrow indicated the specific peaks attributed to glass and neuron respectively.

In return to the high neural adhesion, the strong binding of neurons to graphene surface may potentially damage the underlying graphene layer and induce defects. However, Raman spectra measured after the culture to probe graphene quality still exhibit a clear signature of single layer graphene even under the neurons body with G-band peak always centered at 1585 cm^{-1} and 2D-band peak at 2677 cm^{-1} (Fig. 5.11 b). The still missing D-band peak (1300 cm^{-1} - 1383 cm^{-1}), which represents the presence of lattice defects, confirm the remaining high quality of used graphene. The emergence of new peak (2440 cm^{-1}) originates from the glass substrate (Fig. 5.11 c). Except the baseline offset, increased by the background fluorescence of stained neurons, there is no apparent difference in the Raman spectra taken on free standing graphene layer and on the part under the neuron. The intensity of the D+D'-band peak around 2850 cm^{-1} - 3000 cm^{-1} slightly increases for spectra performed above neurons and could indicate depression of structural quality of the underlying graphene layer. However the absence of the D-band peak clearly disproves this assumption. The origin of this broad peak could rather be attributed to the cells with corresponding CH_2 - and CH_3 - stretching modes [389, 390]. This is indeed confirmed by further Raman characterization of neurons grown on coated glass substrates (Fig. 5.11 c). The crystalline quality of graphene seems not to be affected by the strong neural adhesion.

Additionally, in Chapter 4.8.5 we have already demonstrated that also the electrical properties of graphene are conserved during extended neuron cultures up to 21 days.

5.3.4 Impact of graphene crystallinity on neural adhesion

Similar improvement of neural attachment and electrical activity was reported by adding nanodiamonds and carbon nanotube coating [377, 391, 392] suggesting that carbon based materials in general support neural adherence and their further development. Our results however show that the presence of carbon atoms alone does not ensure a high adhesion, but rather its crystalline quality has a significant impact on the cytocompatibility of graphene. Neuron cultures performed on uncoated low quality graphene layers with a high rate of disordered carbon atoms show no neural attachment (Fig. 5.12 c).

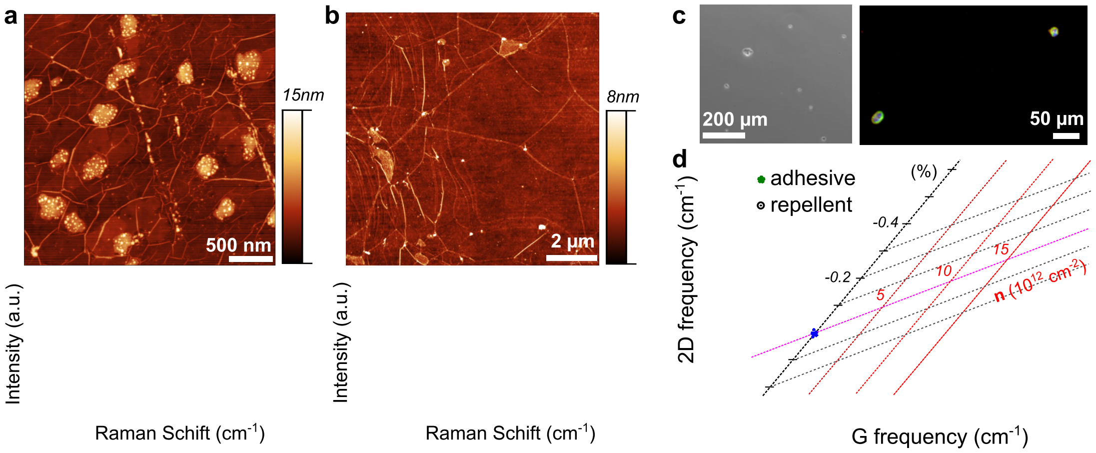

Figure 5.12: Poor quality graphene for neural growth without adhesive coating. a-b) Representative AFM surface scans(top) and Raman spectra (bottom) of two graphene batches with poor quality transferred onto glass coverslips. Around 75 of these graphene samples were used for neural interfacing without adhesive coatings. c) Transmission microscopy and optical image of DIV1 neurons cultured on graphene presented in a-b). Primary hippocampal neurons do not adhere to pristine graphene of poor quality and build clustered somas. Neurons are stained with Dapi (blue), synapsin(green) and tau (red). d) 2D band versus G band frequency diagram for graphene layer presented in b) (repellent graphene, black circles) plotted with the theoretical projections for strain ε/charge n induced (black/purple dashed lines) frequency dependence from [289]. For comparison, data obtained on high quality graphene with strong neural adhesion are also presented (adhesive, green dots). Blue star indicates the neutral graphene.

Since the culture conditions were kept constant, it can not be attributed to presence/absence of particular proteins involved into neural adhesion in the culture medium. The repellent interaction arises with the presence of lattice defects (D-band peak at 1300 cm^{-1} - 1383 cm^{-1}) or multilayer patches (Fig. 5.12 a, b). Two representative graphene batches of poor quality are shown in Figure 5.12 a, b. Around 75 of these graphene samples transferred onto glass coverslips (annealed and not annealed) were used for neuron cultures and showed no primary neuronal attachment after seeding. Graphene layer used is [213] also exhibits a non zero D-band peak, attributed to the presence of defects. Interestingly, they reported poor neuronal adhesion and soma clustering, indicating the need of an additional surface treatment to increase the neural affinity.

The origin of the repellent nature of defective graphene is not clear yet. Several mechanisms might be involved, including topographic and chemical composition. From Raman analysis, we clearly observe a frequency shift for both G and 2D modes between the adhesive (high quality, high neural affinity) and repellent (poor quality, poor neural affinity) graphene of around $\Delta\omega_{2D,G} \sim$ 10 cm^{-1}, which reveals a higher hole doping for the repellent layers (Fig. 5.12 d) [289, 393]. This positive doping could originate from metallic nano-particles (Cu, Cr-oxide which may remain from the etching of Cu foils used for graphene growth, see methods), structural defects or from charged impurities trapped between the substrate and the graphene layer. But atomic force micrographs show only few traces of particles embedded below graphene, and the transfer process (etchant, substrate) remained identical for all samples. Thus it can barely explain the differences that we observe. However, the frequency diagram shown in Figure 5.12 b reveals a significant difference of the mechanical and electrical nature of repellent and adhesive graphene, which could be involved into the varying neural affinity.

Depending on the CVD growth batch, the repellent graphene exhibits more wrinkles, multilayer patches or amorphous carbon grafted on the surface (see Fig. 5.12 a, b). This can directly rise the hydrophobicity of graphene layers, preventing the neural attachment, or increase the amount of structural defects. The defects, also revealed by Raman spectroscopy (emerging D-band) are directly associated with dangling bonds, which promote the grafting of specific molecules from the environment and change the surface state of graphene. The direct result of this could be for example an increase of PMMA residuals, which was indeed observed on poor quality graphene here (the residuals were removed by thermal annealing). Theoretical simulations have also shown, that defects increase the local reactivity of graphene and result for example in enhanced grafting of carboxyl, hydroxyl or other functional groups [394]. In particular carboxyl radicals were shown to decrease neural adhesion and sprouting [388]. The exact grafting can be for example verified using X-ray photoelectron spectroscopy (XPS), which was unfortunately not available.

With regards to its high repellent nature, the defective graphene can be used as a cell repulsive substrate for chemical patterning of neural networks. As already mentioned above, usually the neurons seeded on PLL pattern start to grow beyond the pattern after few days in culture. To increase the cell confinement on the defined network, cell repulsive protein coatings or surface silanization is used prior to PLL patterning [360, 364]. Similar to this approach, here we tested the use of the defective monolayer graphene to prevent the cell migration outside the PLL pattern. A silanized glass coverslip with the same PLL pattern was used as a control sample. As shown in Figure 5.13, the seeded neurons adhere only to PLL pattern and barely grow on the surrounding substrate (outside the PLL patterns). The confinement on graphene seems hereby to promote the neurite outgrowth (Fig. 5.13 a, b). Indeed, the neural networks realized on graphene substrates (Fig. 5.13 c, top image) cover 2/3 more of the substrate area than the same neural networks patterned on silanized glass coverslips (Fig. 5.13 c, bottom image).

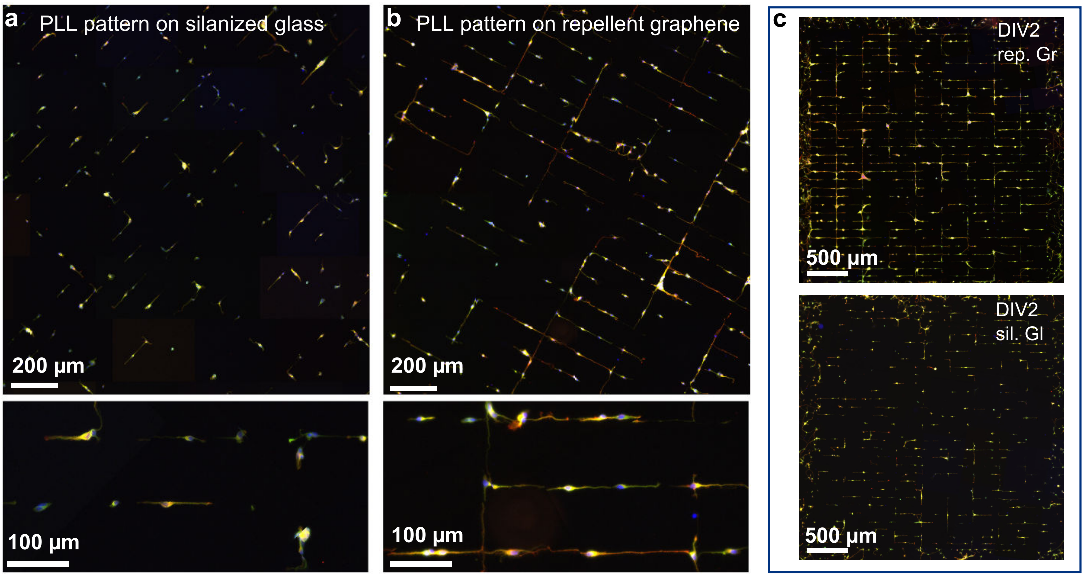

Figure 5.13: Representative IF images of primary hippocampal neurons cultured on adhesive rectangular PLL pattern realized on a) silanized glass coveslips and b) defective (repellent) graphene at DIV1. c) Same pattern on DIV2. Neurons are stained with Dapi (blue), YL1/2 (green, cytoskeletal protein), synapsin I (red).

5.3.5 Conclusion

In conclusion, we investigated the effect of single layer graphene on the development of primary hippocampal neurons in culture. In agreement with previously published studies [240] PLL coated graphene actively promotes neuronal growth. Neurons grown on PLL coated graphene layers exhibit larger size and highly developed dendritic architecture with long, highly branched neurites. Hence, using graphene instead of glass coverslips as growth support for neurons, can significantly improve the viability and connectivity of neural networks. But more importantly, we have shown, that pristine single layer graphene exhibits high neural affinity. At early growth stage, graphene improves the neural attachment even without any adhesive coating, accelerates the axonal polarization and increases the neuron processes. Also at the later development stage, neurons grown on pristine graphene perform exceptionally well and similar to those grown on control coated glass samples. The remarkable adherence of neurons to bare graphene is a unique advantage for achieving a very close proximity and strong electrical coupling with the neurons. Unlike other active materials used at the interface with living cells, neurons could directly bound to the single layer graphene leading to increased detection sensitivity and improved stimulation. Also the high crystalline quality appears as a requirement for high cytocompatibility and is preserved during the culture despite of the strong coupling with neurons. This physical stability of graphene together with the possibility to bypass the protein coating reveals its great potential for long term biocompatible recording of neural activity, which is the fundamental requirement for chronic neuroprostheses.

CHAPTER 6

Recording of neuronal signals

In this chapter we will present in-vitro recordings of neuronal activity using various techniques. After confirming the electrical excitability of cultured neurons using patch clamp measurements and calcium imaging, we will present the detection of local filed potentials in brain slices using SiNW-FETs and the recordings of electrical activity of hippocampal neuron cultures interfaced to silicon nanowire - and graphene FETs.

6.1 Maturation control of cultured neurons

E16 mouse embryo hippocampal neurons were cultured on SiNW- and graphene FETs using the protocol described in Chapter 5.1.1. The chips were sterilized with ethanol and covered with poly-L-lysine. The neurons were seeded onto chips at the concentration of 10^5 cells per cm^2 and incubated for 19 - 21 days, typically required for hippocampal neurons to establish spontaneous electrical activity. For some experiments, the seeding density was increased to achieve a complete covering of the FETs. The cell culture medium was changed once per week and supplemented with AraC (1 µM) to inhibit the proliferation of glial cells, allowing direct coupling between the neurons and the transistor. Glass coverslips were used as control samples to follow the neuronal growth and development.

Before performing electrical recordings of the activity of cultured neurons with SiNW- and graphene FETs, their electrical activity was assessed using conventional neurophysiological tools, such as patch clamp recordings and calcium imaging. These techniques were used to ensure that the neurons indeed achieve the expected maturation stage, characterized by generation of spontaneous action potentials. Patch clamp measurements provide a relatively simple electrical detection of potential spikes, while calcium imaging monitors the intracellular Ca^{2+} ion concentration, which varies with the electrical activity of the cell due to the involvement of Ca^{2+} ions into various cell functions, including the generation of action potentials. Thus calcium imaging provides a supplementary tool to assess the maturation of cultured neurons. Additionally, morphological cues can be used to assess the neural development and viability. In the following we will present the characteristics of hippocampal neurons cultured in this work and reveal the suitability of the used culture protocol to obtain mature neural networks with spontaneous electrical activity achieved after 19 - 21 days in culture (= days *in-vitro* = DIV).

6.1.1 Morphology assessment using immunofluorescence imaging

To assess the morphological development, the neurons were stained at 19 - 21 DIV with specific immunofluorescence (IF) markers, as described in Chapter 5.1.2, and observed using fluorescence microscopy. As expected for mature hippocampal neurons [395], the neurons cultured in this work exhibit a pyramidal shape with a highly developed dendritic architecture and a dense distribution of pre-synaptic markers, indicating numerous synaptic connections (Fig. 6.1). IF staining was also performed on neurons cultured on graphene FETs to reveal their location and viability immediately after the electrical recordings. While live cells show a well defined dendridic structure, dead or suffering neurons usually exhibit a degeneration of cytoskeleton and a granular fragmentation of neurites [396, 397], resulting in a rounded shapes with partially dissolved or completely missing neurites. Figure 6.1 b for example demonstrates an IF image of neurons cultured on G-FETs and electrically recorded for 1 - 2 h. The cells clearly exhibit a healthy shape, meaning that the neurons were alive during the recordings.

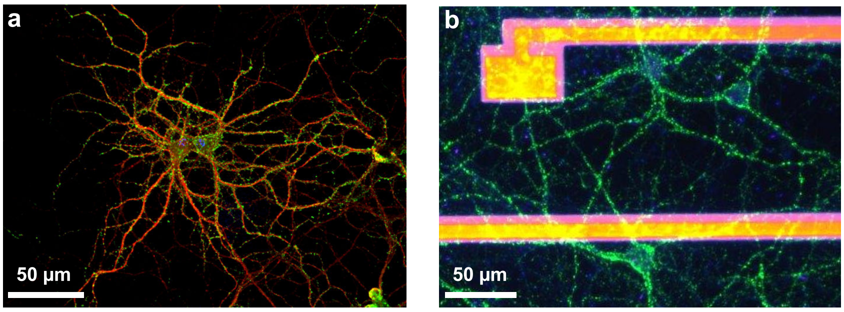

Figure 6.1: Immunofluorescence images of cultured hippocampal neurons. a) Neurons cultured on a glass coverslip (19DIV). Synapsin (green) marks the synaptic vesicles, Dapi (blue) the nucleus/soma, and YL1/2 the cytosceleton. b) Low density neural network cultured on G-FETs for 19 days. The neurons were stained after the electrical recordings and exhibit healthy shape and dense distribution of pre-synaptic markers. Synapsin (green) marks the synaptic vesicles and Dapi (blue) the nucleus/soma.

6.1.2 Patch clamp recordings of spontaneous electrical activity

Cell attached voltage-clamp technique was used to assess the spontaneous electrical activity of the hippocampal neurons at DIV21. In this technique, a glass pipette containing an electrolyte solution is tightly sealed onto the cell membrane and isolates a membrane patch containing one or several ion channels (Fig. 6.2 a). The ion currents generated by the electrical activity of the cells flow through these channels into the pipette and can be recorded by an electrode that is connected to a highly sensitive amplifier. When the membrane potential is not at steady-state, the patch of the membrane under the electrode is presented by a resistor R_p and the capacitor

C_p (Fig. 6.2 b). The capacitor aspect of the membrane patch provides hereby a low impedance pathway trough the patch for fast events, making this method especially suitable for recording action potentials.

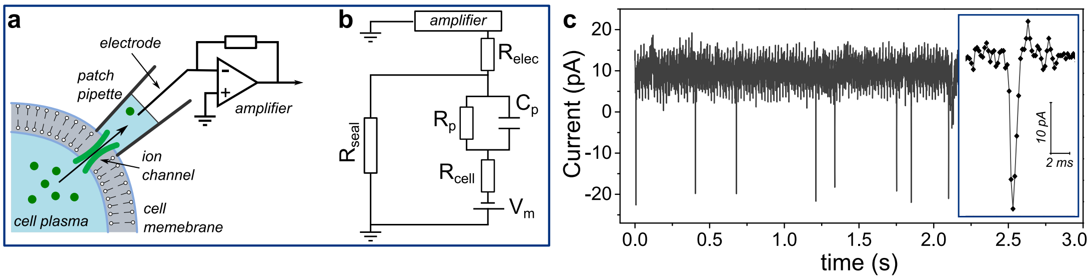

Figure 6.2: Patch clamp recordings. a) Schematic illustration of cell attached voltage-clamp configuration, and b) the electrical circuit involved when the cell potential V_m is changing. The patch is described by the resistance R_p and the capacitance C_p. For fast events, such as action potentials, the capacitor provides a low impedance pathway through the patch. The fraction of the current which arrives at the amplifier depends on the seal resistance R_{seal} and the electrode resistance R_{elec}. c) Patch clamp recording of spontaneous action potentials of 21DIV hippocampal neurons with a zoomed current peak. Measured in collaboration with M. Albrieux, GIN Grenoble.

Figure 6.2 c shows a typical recording trace of spontaneous activity of DIV21 hippocampal neurons. The shape and the duration of the detected signals can be clearly attributed to action potential spikes, which are characterized by a rapid, approximately symmetrical rise and fall of membrane potential within 1 - 2 ms. The amplitude of the recorded current spikes $\varDelta I_{patch}$ must be proportional to the change of the membrane potential $\varDelta V_m$ (for infinite seal resistance R_{seal}) [398]:

$$\varDelta I_{patch} \quad = \quad \frac{\varDelta V_m}{Z_{patch} + Z_{elec}} \tag{6.1}$$

with the patch impedance Z_{patch} and the impedance of the electrode Z_{elec}, which is given by the electrode resistance and is around 5 MΩ. Thus, to correlate the measured current signal to the membrane potential change $\varDelta V_m$, we have to estimate the patch impedance. The patch impedance can be calculated as the inverse of the patch admittance Y_{patch}:

$$Z_{patch} \quad = \quad 1/Y_{patch} \qquad with \qquad Y_{patch} \quad = \quad \sqrt{g^2 + B_C}, \tag{6.2}$$

where g is the patch conductance and B_C the susceptance of patch capacitance. Assuming a patch resistance of $R_{patch} = 2$ GΩ, the patch conductance is $g = 5 \cdot 10^{-10}$ S.
The value of B_C depends linearly on the capacitance of the patch C_{patch} and the frequency f of the transmitted signal:

$$B_C = 2\pi \cdot f \cdot C_{patch}. \tag{6.3}$$

The patch capacitance can be calculated using the specific capacitance per unit area $c = 1\ \mu\text{F/cm}^2$ and the patch area S, which can be approximated as a circle $S = \pi r^2$ with a pipette opening of radius $r = 1\ \mu\text{m}$. This results in a capacitance $C_{patch} = S \cdot c = 3.14 \cdot 10^{-14}$ F.

Then, for fast spiking events, such as action potentials with frequency $f = 2$ kHz (0.5 ms rising time) [398], the susceptance will be $B_C = 3.9 \cdot 10^{-10}$ S, leading to the patch impedance $Z_{patch} = 1.58 \cdot 10^9\ \Omega$. For a membrane depolarization $\Delta V_m = 80$ mV during an action potential this will lead to a current signal:

$$\Delta I_{patch} = \frac{\Delta V_m}{Z_{patch} + Z_{elec}} \approx \frac{80\ \text{mV}}{1.58\ \text{G}\Omega} = 50\ \text{pA}$$

The theoretically estimated current is in good agreement with the measured value $I_{patch} = 30 \pm 2$ pA (Fig. 6.2 c). The small difference can originate from the finite seal resistance R_{seal}. The current coming from the cell has two possible pathways to ground: either through the electrode to the amplifier or through the seal (Fig. 6.2 b). The percentage of the current going to the amplifier is hereby given by the ratio $R_{seal}/(R_{seal} + R_{elec})$. While for $R_{seal} = 10 \times R_{elec}$, more than 90% of the current reach the amplifier, for $R_{seal} = R_{elec}$ it is only 50%.

6.1.3 Calcium signaling in cultured neurons

Additionally calcium imaging was used to assess the excitability and the membrane integrity of cultured neurons. Calcium ions are present in nearly every cell type in biological organisms [139], and are involved in a variety of cell functions, including muscle cell contraction [399, 400] and energy household [401]. In neurons, calcium ions play an an important role in regulating neuronal processes, such as neurotransmitter release [402], synaptic plasticity [403] and generation of action potentials [140, 404, 405]. During neural activity Ca^{2+} channels present in the cell membrane are activated, resulting in an exchange of Ca^{2+} ions between the extracellular medium and cell plasma. Thus monitoring the intracellular Ca^{2+} ion concentration provides an additional tool for detection of neural activity.

In calcium imaging technique, fluorescent molecules are used, which can respond to the binding of Ca^{2+} ions by changing their fluorescence properties. These molecules are injected into the cell and respond specifically to the changes of the intracellular ion concentration by increasing the fluorescence intensity once a Ca^{2+} ion is bounded. Here, we used Fluo-4 AM (ThermoFisher) molecules as calcium indicator. These molecules consist of a fluorescent body (fluorophore, Fluo-4), which is functionalized with non-fluorescent acetoxymethyl (AM) ester [406]. Fluo-4 is a fluorescent chelator molecule, which is able to specifically bind Ca^{2+} ions. The lipophilic AM ester is used to transport the fluorophore through the neural membrane into the cell plasma. Inside the neuron, the cellular esterases will degrade the ester and free the fluorophore, which can then bind the Ca^{2+} ions.

Calcium imaging was performed on neurons cultured on control glass coverslips. After 21 days of culture, 2 - 5 µl of Fluo-4 AM was added to the cell culture medium depending on the neuron density and incubated for 15 - 60 min. The incubation time is critical for a complete release from AM ester to avoid an increasing background fluorescence during the measurements. Then the cell culture medium was changed to remove the excess Fluo-4 AM molecules, and after a short incubation, the neurons were excited by $\lambda_{exc} = 488$ nm laser light, and the emission at the wavelength $\lambda_{em} = 515 \pm 15$ nm was detected. The data were acquired at 4.76 Hz using a confocal microscope and a commercial software EZ2000 (Nikon).

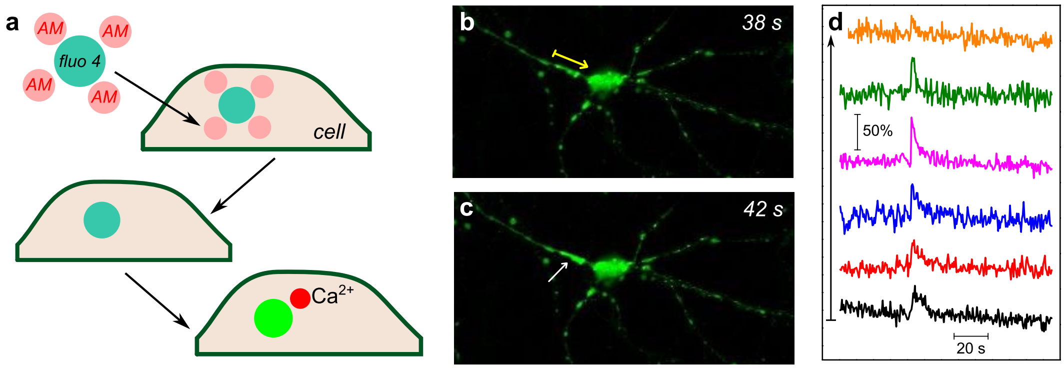

Figure 6.3: Calcium signal imaging in 21DIV hippocampal neurons. a) The neurons are loaded with Fluo-4 AM molecules. The lipophilic AM ester groups allow the fluorescent calcium indicator Fluo-4 to enter the cell, and are then dissolved by the cellular esterases. Once a Ca^{2+} ion is bounded to Fluo-4, the fluorescence intensity increases. b) Image of a neuron loaded with Fluo-4 at t = 38 s. The yellow arrow represents the neurite trace along which the intensity change in d) was measured. c) Same neuron at t = 42 s. Note the increased intensity indicated by the white arrow. d) Recording of calcium signals along the path indicated in b). Peaks correspond to an increase in the intracellular Ca^{2+} ion concentration. Measured in collaboration with M. Albrieux, GIN Grenoble.

Figure 6.3 b-d shows the recordings of spontaneous calcium signals in hippocampal neurons *in-vitro*. The signal propagates from the dendrite to the soma. The recorded calcium spikes exhibit the typical shape with a fast rise and exponential decay. The decay time depends on the involved neuronal process and the acquisition parameters, such as exposure time and the pixel size. The duration of the measured signals is around 10 - 15 s. This value is on the range of the calcium signals in neurons reported in the literature with spike duration from 0.5 s to 20 s [135, 140, 404, 407]. The low frequency of Ca^{2+} signals recorded here can be attributed to the poor temporal and spatial resolution of the used setup. Since the acquisition rate is 210 ms/image, fast events could not be recorded.

Then, to prove the functionality of calcium channels, we supplemented the culture medium with an excitatory neurotransmitter, glutamate, known to activate some Ca^{2+} -channels in the cell membrane [140, 141] and recorded the fluorescence intensity. The effect of glutamate is illustrated in Figure 6.4. Initially, the intensity increases due to the enhanced inflow of Ca^{2+} ions, starting from the ends of the neurites, where the density of glutamate receptors is the highest. However, due to the increased influx of the extracellular medium into the cell, the neuron swells and finally bursts as shown in Figure 6.4 at t = 40 - 50 s. The increased concentration of calcium ions in response to glutamate treatment confirms the functionality of calcium channels and thus the integrity of the neural membrane.

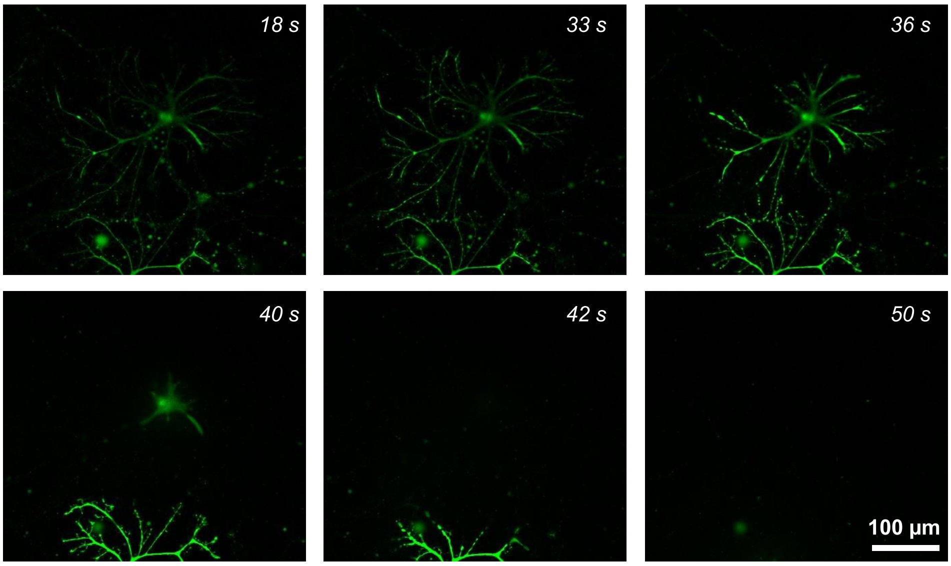

Figure 6.4: Representative fluorescence micrographs obtained from the continuous recording of calcium signal in hippocampal neurons exposed to glutamate. At t = 33 - 36 s, the signal intensity increases due to the enhanced Ca^{2+} influx through glumamate activated calcium channels. Further increase of the inflow of the extracellular medium results in swelling and bursting of neurons at t = 40 - 50 s. Measured in collaboration with M. Albrieux, GIN Grenoble.

6.1.4 Conclusion

In conclusion, we assessed the maturation stage of hippocampal neurons cultured in this work using various techniques, such as immunofluorescence microscopy, calcium imaging and patch clamp measurements. This extensive characterization reveals, that after 3 weeks of culture the neurons exhibit a highly developed dendritic architecture, dense synaptic distribution and typical spontaneous electrical activity. The fact, that cultured neurons express spontaneous electrical activity means, that the culturing protocol as described in Chapter 5.1.1 is suitable for bioelectrical interfacing of neurons with recording devices. The next crucial step is to record the neuronal activity using silicon nanowire and graphene FETs.

6.2 SiNW-FET recordings of neural activity

For interfacing SiNWs with living tissue or cells a special measurement setup was designed. The contact pads of the chip are bonded to a chip holder, which is integrated into a portable incubator (see Fig. 6.5 a). The individual NWs are addressed with a homemade electronic card of 12 parallel acquisition inputs and 5 kHz sampling rate, which is USB-connected to a PC. The nanowires are AC current biased and the sampling rate is adjusted to the bias current modulation, enabling a low-noise recording similar to lock-in technique.

6.2.1 Brain slices

The bioelectrical interfacing of the SiNW-FET arrays was first tested on acute mouse brain slices. More precisely, we looked at the Sunbstancia Negra Reticula (SNR) – the brain region involved in the setting of motor control and learning. Its particularity is to have a pacemaker like activity with a frequency of about 10 Hz *in-vivo*. In brief, the brain was quickly removed from anesthetized mouse, the SNR slice was separated, placed onto the SiNW-chip and adjusted above the nanowire to find a good coupling. The response of the nanowire FET to the electrical activity of SNR is shown in Figure 6.5 b.

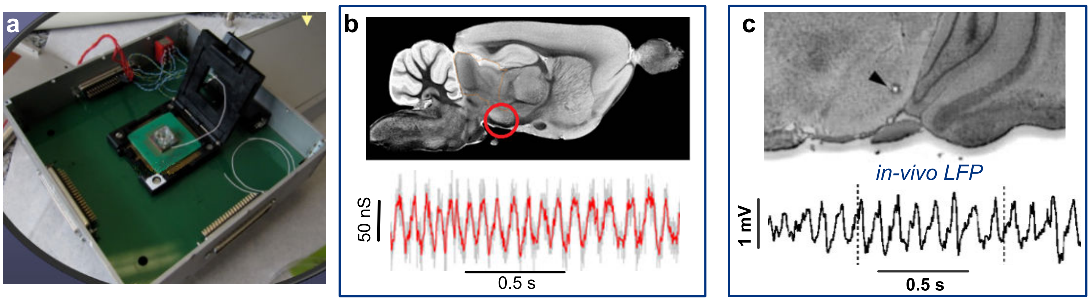

Figure 6.5: a) Portable measurements setup with integrated incubator and electronic card for interfacing with a laptop. b) Detection of the activity of the brain slice from Substancia Negra Reticula (SNR) of a mouse. SNR region is indicated by the red circle in the top image. The bottom image demonstrates the periodic modulation of the conductance of SiNW-FET induced by the activity of the SNR slice. c) *In-vivo* detection of local field potentials (LFP)(bottom image) generated by rats SNR brain region (top image), from [408].

Here the brain slice acts as a gate above the FET, and its local field potential modulates the charge carrier density and thus the conductivity of the nanowire channel. The periodic modulation of the conductance is around 10 Hz and is in good agreement with the frequency of local field potentials measured in live rats [408, 409]. For typical nanowire sensitivities of 3.5 - 6 µS/V, the modulation amplitude is around 8 - 14 mV. This value is almost one order of magnitude higher than the values reported in *in-vivo* experiments. However, the difference could be due to the stronger coupling of the brain slice to nanowires and/or calibration issues since not all nanowires exhibit the same sensitivity.

6.2.2 Hippocampal neuron cultures

The SiNW-FETs were also interfaced with primary hippocampal neurons. The chip surface was sterilized and coated by poly-L-lysine (PLL), a polymer coating to ensure the neuronal adhesion, and the hippocampal neurons from 16 days old mouse embryos (E16) were seeded onto the chip surface and incubated for 19-20 days at 37°C in 5% CO2. More details of cell culture techniques can be found in Chapter 5.1.1. Healthy neuronal growth on SiNW-FET arrays was observed and even an exact positioning of neurons above the NWs could be realized using a photo-lithographically designed PLL pattern (Fig. 6.6).

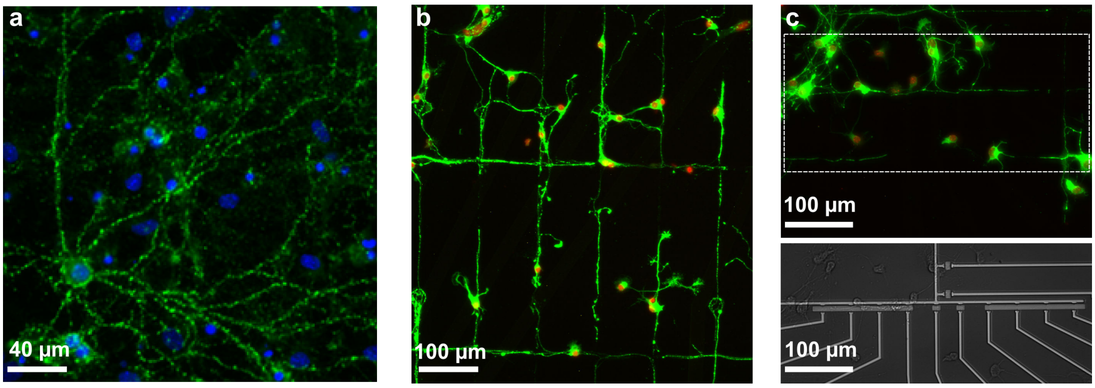

Figure 6.6: Immunofluorescence images of SiNW-FET arrays interfaced with neuron. a) Random neuronal network on SiNW-FET arrays. Blue color highlights the soma and green the synaptic distribution. b) Patterned neuronal network on SiNW-FET. c) Neurite growth above the SiNW-FETs at 7 days of culture: immunofluorescence image and the corresponding optical image to visualize the SiNW-FETs. Red color highlights the soma and green the synaptic distribution.

Detection of neuronal activity on patterned neuronal networks is extremely challenging due to several reasons. Firstly, the neural maturation, i.e. establishing of spontaneous electrical activity, is delayed on isolated networks containing only few neurons [365, 366], while extended culturing periods usually result in cell migration. The detection is usually performed at early growth stage (few days of culture) with additional electrical stimulation [111]. Secondly, the contact area of the neurite with the FET device is very small, around 1/5 of the FET channel, which decreases the effective sensitivity and the potentially detected signal can be vanished within the recording noise. Decreasing the NW length would improve the coupling, but also complicate the neural patterning. Also, no integrated optical system was implemented for in-situ observation of the neuron position during the measurements, making it difficult to find a FET coupled to a cell, and to specifically stimulate an individual neuron. Especially on opaque substrates such as Si/SiO_2, where no transmission microscope can be used, imaging of cells is challenging due to the similar refractive index of the cells and the liquid (see Fig. 6.6 c, bottom image).

Another important parameter, is the expected signal-to-noise ratio for the recordings of action potentials. With sensitivities of our devices, we expect an action potential to induce a conductance change of a few nS. This small signal would be in the range of the electrical noise, and is thus difficult to detect.

The detection of neural activity should be easier on randomly grown dense neural networks. Although the neurons achieve the required maturation stage at 19-21 days of incubation, as confirmed by patch clamp measurements and calcium imaging (see above, Chapter 6.1), a reliable detection of action potentials could not be realized. However, the presence of neurons seems to induce an electrical signal in nanowires. Figure 6.7 a shows conductance traces recorded on two neighboring SiNW-FETs with a spatial separation of $d = 39$ µm interfaced to neurons grown for 21 days.

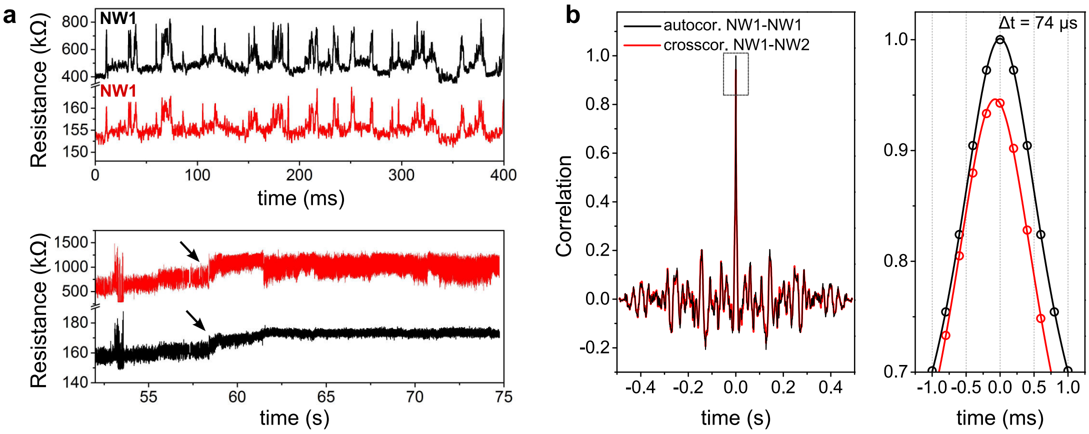

Figure 6.7: Bioelectrical interfacing of SiNW-FETs with neuron cultures. a) Top image: resistance variation of two neighboring SiNW-FETs in presence neurons (cultured for 21 days). Bottom image: at the moment when the neurons die (black arrows), the resistance of p-doped nanowires increases. b) Auto- (NW1-NW1) and crosscorrelation functions (NW1-NW2) of traces shown in (a) with a zoomed view around zero, revealing a delay between the two traces.

The amplitude and the polarity of the detected conduction spikes could not be attributed to action potentials. Nonetheless, the conductance of p-doped nanowires decreases when the neurons die, which is consistent with the vanishing negative membrane potential (Fig. 6.7 a, bottom image). The occurring conductance changes is 0.525 µS and 0.48 µS, which corresponds to a potential change of -87.5 mV and -80 mV for the first and second nanowire respectively (with a typical nanowire sensitivity of -6 µS/V). The calculated potential change is in good agreement with the resting membrane potential. Moreover, the traces detected on the two nanowires are well correlated as shown in Figure 6.7 b. Compared to the auto-correlation of the trace recorded on an individual nanowire (NW1), the cross-correlation function between the two recordings (NW1-NW2) shows a clearly identifiable shift, which corresponds to a time delay of $\Delta t = 74$ µs. Same time delay was also found by comparing the individual shifts between two corresponding spikes detected at each NW. For the conductance modulation due to the potential fluctuations in the cell culture medium or due to the electrical noise of the setup, the cross-correlation function would be centered at zero. The observed shift however suggests a propagating signal. The propagation velocity can be calculated to $v = d/\Delta t = 0.52$ m/s, which is in good agreement to values reported for propagation of neural signals such as action potentials in cultured hippocampal neurons [111].

Although the detected signal can be attributed to neural activity, its exact origin remains unclear. The potential change calibrated from the spikes presented in Figure 6.7 a, is around 12.5 mV and 3 mV for the first (NW1) and the second (NW2) nanowire respectively. These values suggest, that the nanowires record the intracellular potential changes, which can occur in case of a strong ohmic coupling to a leaky neuron membrane [149, 210, 371, 410] (see Chapter 3.1, Fig. 3.3 b).

6.2.3 Conclusion

The fabricated SiNW-FETs were able to detect local field potentials generated in acute brain slices. They were also electrically interfaced to random hippocampal neuron cultures and defined neuronal networks with an exact positioning of neurites above the transistors. While neurons seem to induce a measurable conductance modulation in nanowires, a precise detection of extracellular action potentials was not achieved.

The failed detection of neural action potentials seems to contradict the fact, that planar Si- and top-down fabricated SiNW-FETs were already shown to be suitable for a stable detection of electrical signals from electrogenic cells [14, 99, 100, 102]. However, this kind of recordings strongly depends on the transistor dimensions (which affect the sensitivity), and the cell type interfaced to the FET. While hippocampal neurons exhibit a very small electrical signal (100 -200 µV with occasional responses up to 1 mV [14]), the signals from cardiomyocytes or HL1 line cells reach typically few mV. For example, SiNW-FETs with similar dimensions and sensitivities (350 nm × 10 µm, $g_m/V_{sd} = 2.3$ µS/V [99]) as realized in this work were interfaced to HL1 cells, which form a dense monolayer on the chip surface and exhibit a collective periodic electrical activity, which is easier to detect due to the large cell/device coupling area and higher amplitude of the action potentials. On the other hand, the reported recordings from hippocampal neuron cultures were realized using large planar Si-FETs (22 × 24 µm^2 and 6 × 7 µm^2) with a width-to-length ratio of $W/L \sim 1$ [14] and a neuron/transistor covering fraction of 2/3. These transistors clearly exhibit higher sensitivities, which makes the detection of small neural signals easier, but in return, the spatial resolution is very low. In contrast, the downscaling of our nanowire FETs with $W/L \sim 0.01$ offers high spatial resolution, but a lower sensitivity, which hinders the detection of neural signals, especially at low neuron/device covering area and missing optical control to identify the nanowires coupled to cells.

Thus, to realize a reliable SiNW-FET platform for detection of neuronal activity within a defined neural network, critical improvements of the device sensitivity and the measurement setup have to be considered. For example to improve the set-up, an optical control of the cell position relative to the transistor device during the recordings should be implemented to easily identify a nanowire in contact with a neuron, and an additional detection/stimulation technique, such as patch clamp, could be used to control the cell activity during the recordings with nanowires. Further, the nanowire aspect ratio W/L can be adjusted to increase the area fraction covered by the neuron and to improve the detection sensitivity.

6.3 G-FET recordings of neural activity

The electrical recordings of neuronal activity using G-FETs were performed using the same measurement set-up as in Chapter 4.8. However, the sample holder was heated to 37°C, and the set-up was isolated using a chamber with controlled CO_2 concentration and humidity. These optimized experimental conditions allowed long term electrical recordings without significant pH changes of the cell culture medium, which can cause the death of neurons. A constant DC bias voltage V_{SD} was applied to the FET, and the current I_{SD} through the FET channel was measured. During an action potential the ion flux through the neuron membrane locally changes the liquid potential and results in a conductance change of the FET, which can be measured as a current signal. The working point of the FETs and consequently the sensitivity was set using either a Pt- or silver/silver-chloride (Ag/AgCl) reference electrode.

The recordings were performed on 19-21 DIV neurons. This culturing period is sufficient for neurons to establish spontaneous electrical activity. To increase the firing rate (action potentials per second), 20 µM bicuculline (BIC) was added to the cell culture medium during some recordings. Bicuculline is an excitatory drug, usually used to enhance the network activity and to synchronize the network activity [411, 412]. To confirm the biological origin of detected signals, tetrodotoxin (TTX) was added at 0.5 µM to inhibit/decrease the neuronal activity by blocking sodium channels [413, 414].

6.3.1 Graphene FETs used for recordings

G-FETs with different dimensions were used for recordings. We classify three different designs demonstrated in Figure 6.8: sheet, stripes, and small FETs. For the sheet configuration, we simply put metallic contacts on a graphene sheet transferred onto Si/SiO_2 substrate. In case of stripes, 40 µm wide graphene stripes with length varying from 250 to 1500 µm were etched and contacted by metals. Small FETs had dimensions of 40×50 µm^2, or 20×10 µm^2.

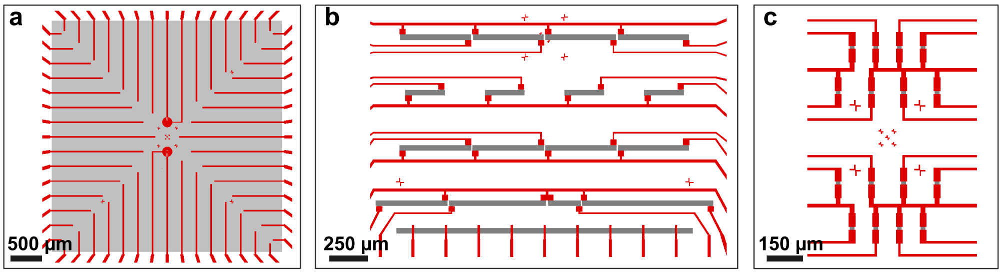

Figure 6.8: Active areas of different G-FET types used for electrical recordings of neuronal activity. a) Graphene sheet: the contact lines (red) on graphene (grey) are separated by a distance of 250 µm. b) Graphene stripes with width 40 µm and varying length. c) Small G-FETs with 20×10 µm^2 exposed FET-channel.

First, we used large (0.5×0.5 cm^2) graphene sheets with multiple ohmic contacts as the simplest configuration for interfacing with neurons to test the compatibility of graphene devices with neuron cultures. For the stripe design, the initial idea was to achieve a guided neuronal growth along the graphene stripes as described in [415], and to detect the network activity at different positions. Then, the dimensions of G-FETs were decreased to allow single neuron interfacing. In the following, recordings of neuronal activity using each type of G-FETs will be presented. These different device types will be referred to as **A** type for graphene sheet, **B** type for graphene stripes, **C** type for $40 \times 50\ \mu\text{m}^2$ and **D** type for $20 \times 10\ \mu\text{m}^2$. The respective indication will appear as inset in the following figures to identify the device type, which was used for the presented recording.

6.3.2 Random telegraph signal in G-FETs interfaced with neurons

When interfaced with neurons, a number of graphene FET devices tested here exhibits random telegraph signal (RTS). This signal, characterized by two discrete conductance states, was measured on graphene FETs with different dimensions and aspect ratios, ranging from $W \times L = 1000 \times 250\ \mu\text{m}^2$ (**A** type) over $40 \times 250\ \mu\text{m}^2$ (**B** type) to $40 \times 50\ \mu\text{m}^2$ (**C** type). Figure 6.9 illustrates the representative conductance traces obtained on each device type in presence of neurons. The conductance switches between two discrete values, which represent the ground and the excited states. In the following we will refer to this states as state I and state II. The switching time is hereby random and varies from few to several hundred milliseconds.

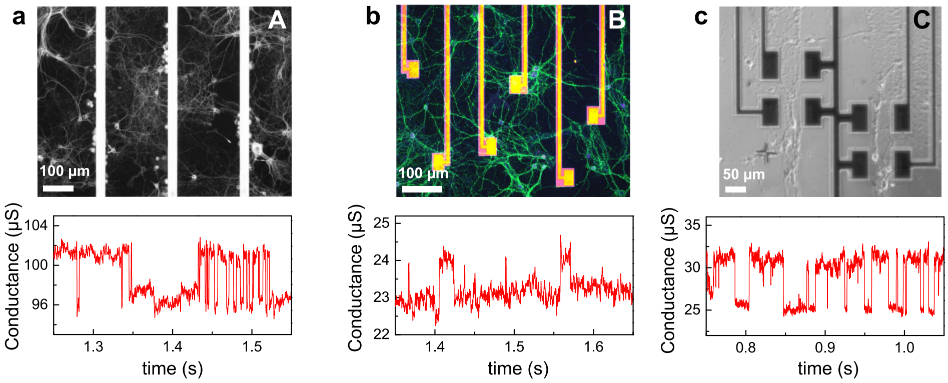

Figure 6.9: Conductance fluctuations in graphene FETs interfaced to neuron cultures measured at 19 - 21DIV on a) type A device (sheet) at $V_{LG} = 0.2$ V, and $V_{SD} = 50$ mV; b) type B graphene FET (stripes) at $V_{LG} = 0.15$ V, and $V_{SD} = 30$ mV; and c) type C graphene FET ($40 \times 50\ \mu\text{m}^2$) at $V_{LG} = 0$ V, and $V_{SD} = 30$ mV. In a) and b) the immunofluorescence images correspond to the measured samples, while c) represents a typical C type device. The neurons were stained with synapsin (grey/green) and Dapi (blue).

An exemplary histogram of the conductance trace obtained on a C-type device is shown in Figure 6.10 a. The histogram exhibits two distinct peaks centered around 25 µS and 30 µS, well illustrating the two-state nature of conductance fluctuations. This conductance behavior clearly resembles the random telegraph signal observed in many devices, including MOSFETs [416], silicon nanowire FETs [417, 418], carbon nanotube FETs [419], as well as graphene based structures [420, 421]. The corresponding current noise power spectrum in Figure 6.10 b exhibits the typical Lorentzian bulge superimposed on the $1/f^2$ spectrum in the low frequency regime. The spectral position of the bulge corresponds hereby to the specific relaxation time τ of the random process, which is equal to the average time the system stays in a state between two transitions [421].

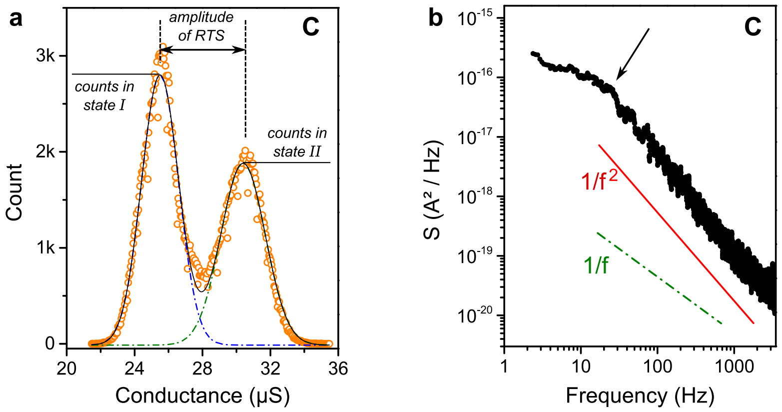

Figure 6.10: Characteristics of the measured telegraphic signal a) Histogram of the conductance fluctuation (orange circles) recorded on C type devices interfaced with live neurons. Black curve represents the fit of multiple Gaussian peaks, and the green/blue curves the individual peaks. b) Current noise power spectral density of C type device interfaced with neurons (black dots) with $1/f^2$ and $1/f$ noise dependence (red/green line) for comparison. The arrow indicates the specific Lorentzian kink. Data are taken from the conductance trace shown in Figure 6.9 c.

The observation of RTS is usually linked to a finite number of impurities in close vicinity to the conductive channel. Some of these impurities have energy levels close to the Fermi energy of the charge carriers in the channel. Consequently, the carriers can jump from the conductive channel to the impurity and after a certain time back into the channel. With increasing number of impurities different random telegraph signal superimpose into a single $1/f$ spectrum. However if only one impurity is present close to the FET channel, the conductance will fluctuate between two discrete values corresponding to the trapping and detrapping events. Especially for small devices, such as SiNW-FETs and CNT-FETs, where the current is carried by a small number of charge carriers, this will result in a significant change of the channel resistance. Thus it is very surprising, that we observe a discrete telegraphic signal on the large graphene devices.

Before discussing the origin of the RT signature observed here, we will present the main characteristics of the measured signal, including the dependence of RTS on the gate voltage, the effect of neurotoxins and the impact of the device size.

Gate voltage dependence

A more detailed analysis of the random telegraph signal measured in G-FETs interfaced to neurons was performed on B type devices (Fig. 6.9 a). Here the conductance traces were measured at different liquid gate offsets V_{LG}. The offset was set using a Pt-wire inserted into the cell culture medium.

The recordings presented below were obtained using a 40×250 µm^2 graphene FET interfaced to

19DIV hippocampal neurons. The transfer characteristics are demonstrated in Figure 6.11 a. The conductance versus gate voltage curve exhibits the expected coarse: with increasing liquid gate voltage $\mathrm{V_{LG}}$ the device is tuned from the hole to the electron operation regime with the charge neutrality point around 0.48 V. The sensitivity S achieves its maximal values at the points of inflection around 0.3 V and 0.7 V, and is -110 µS/V and 30 µS/V for the hole and electron branch respectively. While the position of the Dirac point shifts only slightly during the culture, probably due to the low neuron density (Fig. 6.10 b), the conductance and the sensitivity of the device decrease to 1/5 of the initial values (data not shown).
The FET conductance was recorded at different liquid gate offsets in hole and electron conduction regime (Fig. 6.11 b). As expected, the baseline of the recorded traces varies with respect to the field effect induced conductance modulation presented in Figure 6.11 a. The conductance fluctuation amplitude ΔC varies with the liquid gate offset (see Fig. 6.11 c): the highest conductance change was recorded in the hole branch ($V_{LG} = 0.3$ V), and the lowest close to the Dirac point ($V_{LG} = 0.5$ V), with average peak amplitudes of 1.5 ± 0.2 µS and 0.8 ± 0.2 µS respectively.

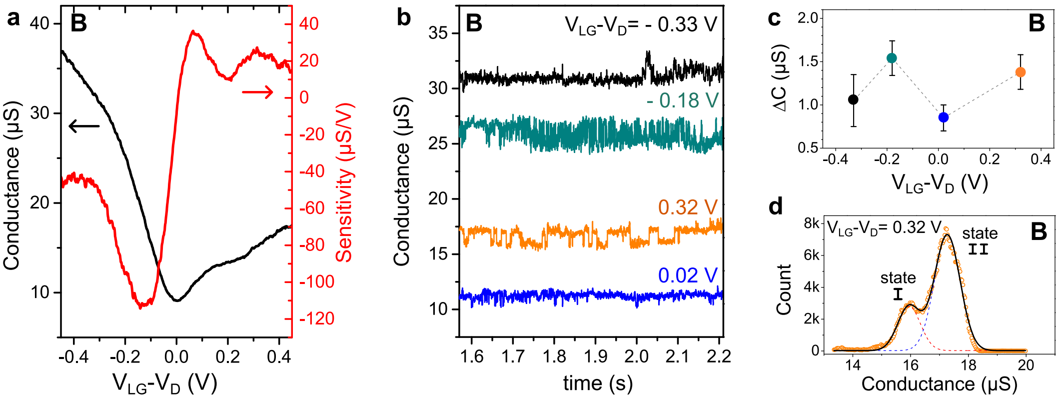

Figure 6.11: Gate dependence of RTS measured on a 40×250 µm^2 graphene FET (B type device) interfaced to 19DIV neuron culture. a) Field effect induced modulation of the conductance (black cure) and the corresponding sensitivity (red curve) of the FET device. Liquid gate voltage V_{LG} is varied with respect to the Dirac point V_D. b) Conductance traces recorded on the same device at different liquid gate offsets V_{LG} ($V_{SD} = 30$ mV). c) Amplitude of the conductance modulation ΔC as function of the liquid gate offset. d) Histogram of the conductance fluctuations (orange circles) recorded at $V_{LG} = 0.8$ V. Black curve represents the cumulative fit of the individual peaks (red and blue dashed lines).

Also the transition frequency f_{RTS} and the ratio of the time τ_{II}/τ_I, which the system spends in the excited and ground states respectively, seems to depend on the liquid gate offset V_{LG} (see Fig. 6.11 b). A quantitative analysis of this observation is illustrated in Figure 6.12. For each V_{LG} value reported in Figure 6.11 b we calculated f_{RTS} as number of events per unit time, and the time ratio τ_{II}/τ_I as the ratio between the two peaks in the conductance histogram (exemplary shown in Fig. 6.11 d). The trace obtained for $V_{LG} = 0.15$ V was not considered due to very low occurrence of events. The state II was attributed to the more occupied conductance state, i. e. the conductance peak with the highest number of counts (see Fig. 6.11 d). As shown in Figure 6.12 a, the transition frequency is proportional to the sensitivity of the device, which is set by the liquid gate offset, revealing a direct relationship between RTS dynamics and graphene mobility. For the time ratio τ_{II}/τ_I however no such clear dependence on the FET sensitivity is observed, and it seems to be more influenced by the net current passing through the transistor channel, which is modulated by the liquid gate offset. Similar dependence of the ratio τ_{II}/τ_I on the drain current was already reported for RTS in liquid gated SiNW-FETs [417, 418].

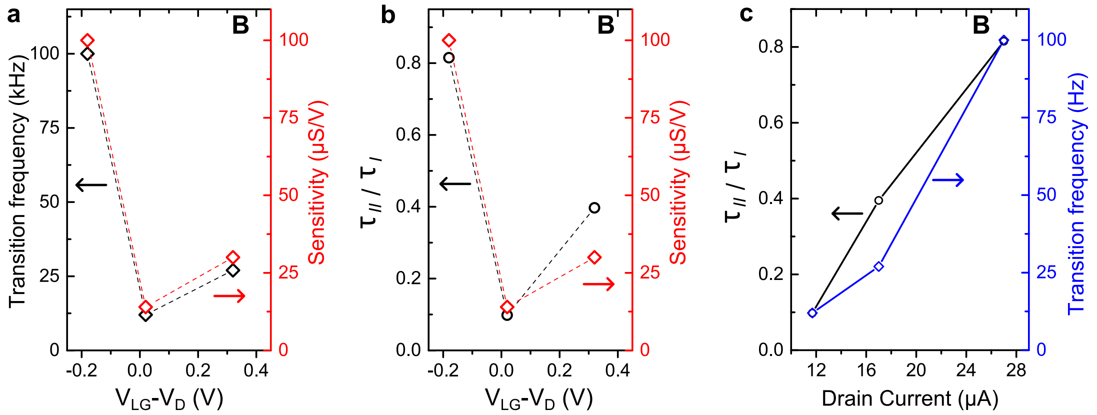

Figure 6.12: RTS dynamics observed at different liquid gate offsets V_{LG} varied with respect to the Dirac point V_D reveal a direct dependence on the sensitivity of the FET. The sensitivity is plotted as function of the liquid gate offset together with a) transition frequency between the two conductance states (excited and ground state) and b) the time ratio τ_{II}/τ_I, which the system spends in each state. c) Alternatively, τ_{II}/τ_I and the transition frequency are plotted as function of the drain current through the transistor channel. To obtain the transition frequency and the time ratio tau_{II}/τ_I, data from recordings presented in Fig. 6.11 b were used.

To summarize, the main characteristics of the measured signal, such as the the conduction modulation amplitude $\varDelta$C, the transition frequency f_{RTS} and the ratio of the time τ_{II}/τ_I, which the system spends in the excited and ground states respectively, exhibit a clear dependence on the gate voltage. While f_{RTS} seems to be linearly proportional to the FET sensitivity (transconductance), the ratio τ_{II}/τ_I is proportional to the net current through the transistor channel.

Effect of neurotoxin

Since this kind of conductance fluctuations was not observed on samples before the culture, it seems to be linked to the presence of the neurons and their activity. To investigate this possibility, we supplemented the cell culture medium during the recordings with tetrodotoxin (TTX), which is a prominent neurotoxin used to inhibit the cell activity by blocking the sodium channels. The effect of TTX is demonstrated in Figure 6.13. The two-state signal observed before was fully suppressed by adding TTX in several devices, revealing a direct relation between the neuronal activity and the RT signal.

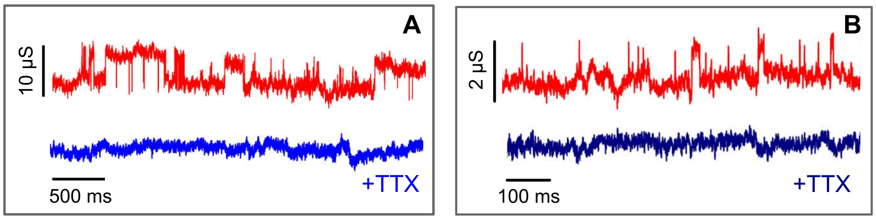

Figure 6.13: Addition of tetrodotoxin (TTX) to cell culture medium during the recording completely exhibits the signal. This effect was measured on several A and B type devices.

Impact of the transistor size

We observed random telegraph signals on a variety of graphene FET devices interfaced to neurons. However the probability to measure the RTS signature in graphene/neuron hybrid was strongly linked to the size of the used G-FET device. While RT signals were frequently detected on large graphene FETs with transistor channel dimensions up to $W \times L = 1000 \times 250$ µm^2, the detection probability decreased drastically with decreasing FET dimension. In fact, RTS was never observed on small graphene transistors with $W \times L = 20 \times 10$ µm^2. On the other hand the relative conductance change $\Delta C/C$ with respect to the baseline conductance C increased with decreasing FET dimensions.

A summary of the dependence of the observation probability and the relative conductance modulation on the FET dimensions is given in Table 1.1.

Table 6.1: Dependence of the observation of random telegraph noise in graphene interfaced to neurons on the size of the recording G-FET.

Device type	$W \times L$ (µm^2)	$\Delta C/C$ (%)	Observation probability
A	$\leqslant 1000 \times 250$	5	$\sim$ 33% (2 cultures, 5 of 15 tested FETs)
B	40×250	6-7	$\sim$ 7% (1 culture, 2 of 28 tested FETs)
C	40×50	10-15	$\sim$ 5% (2 cultures, 2 of $\sim$ 40 tested FETs)
D	20×10	-	$\sim$ 0% (2 cultures, 0 of $\sim$ 40 tested FETs)

Discussion: Noise or Neuronal Signal?

As already mentioned above, the observation of random telegraph signal in solid state devices is usually attributed to the presence of impurities nearby the conductive channel, which can trap and detrap the charge carriers resulting in conductance fluctuations. While the amplitude and the frequency of these fluctuations are specific for each impurity, for an increasing number of charge traps with different characteristic relaxation times, the individual contributions overlap to a single $1/f$ noise spectrum. However when the transistor dimensions are reduced, such that only one impurity affects the current through the transistor channel, the conductance will fluctuate between two discrete levels. A significant change of the conductance due to a single impurity can only occur on very small devices with a low amount of charge carriers involved into transport. Both, the two-state behavior and the high fluctuation amplitude imply small transistor dimensions together with a few to single fluctuator. This contradicts the observation of high amplitude RTS in large graphene devices and implies a large number of impurities with synchronized trapping/detrapping events, which is very unlikely to happen. Thus, it becomes clear, that other processes must be involved into the generation of RTS in graphene. Leakage and hysteresis effects can be clearly excluded, since for the first one, the amplitude would increase linearly with the gate voltage, which is not the case (see Fig. 6.11 c), and the latter one is a slow process and incompatible with the rapid conductance changes observed here.

The inhibition of the signal by TTX shows a dependence of the measured telegraphic signal on the neuronal activity, which suggests that the source of RTS is linked to the cellular activity. The conductance fluctuations could be caused for example by the extracellular potential V_{extra} generated by the ionic current during an action potential. This potential spike could be detected by FET through field effect induced conductance modulation. However the duration and the shape of the measured signal is incompatible with intra- and extracellular action potentials, which would induce a fast rising and decaying spike lasting for only few milliseconds. In other words, the conductance time traces do not look like one expects for neuronal spiking.

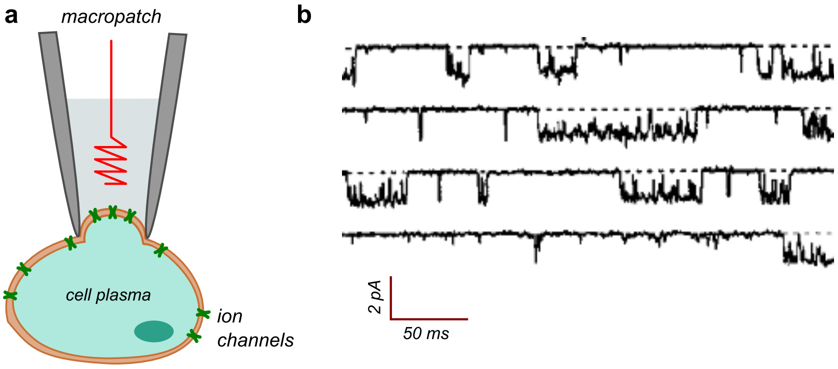

Figure 6.14: Sodium channel activity in macro-patch recordings. a) Schematic illustration of a macro-patch containing several ion channels. b) Na$^+$ channel currents evoked by a 500 ms depolarizing pulses to -30 mV and recorded using a macro-patch containing several sodium channels [422].

However, the shape of the measured signal strongly resembles the fluctuations of single ion channels present in the neural membrane. Indeed, the ion channels exhibit two states, an open and a closed one, and the transition between these two states could generate square shaped signals lasting for up to several hundred milliseconds [422] (see Fig. 6.14). Thus, considering the suppression of the signal by adding TTX, it could be possible, that the conductance fluctuations observed in graphene are due to the random opening and closing of sodium channels. However it is puzzling, how such a small and such a local signal can induce a significant conductance change ($\sim 10\%$) in large graphene devices.

A possible explanation could be provided by the existence of grain boundaries in CVD grown graphene, such as used in this work (see Chapter 4.4). To remind the reader, CVD graphene is

usually obtained on copper foils. Briefly, the copper foil is first nucleated by a local adsorption of carbon atoms. From these nucleation spots, individual graphene grains start to grow until they merge into a single graphene layer. The merging of two graphene grains with different crystal orientations creates a one dimensional grain boundary (GB) consisting of carbon rings containing 5 or 7 atoms, as shown in Figure 6.15 b. These grain boundaries form local weak links with fluctuating transmission properties. Initially these transport gaps can be opened or closed. However due to the one dimensional nature, the transport properties of GBs are expected to be extremely sensitive to local environmental changes, such as local gating or molecule adsorption (Fig. 6.15 d). In this context, recently Yasaei et al. have experimentally shown that the performance of graphene sensors is not necessarily a macroscopic property, but is rather dominated by some sort of sensitivity hot spots formed by GBs [423]. The authors demonstrated that an isolated grain boundary exhibits a 300 times higher sensitivity to molecule adsorption than a single graphene crystal. Consequently if a GB crosses the transistor channel, as illustrated in Figure 6.15 a, the transport characteristics will be dominated by its conductivity and it could be possible, that small conductance fluctuations of ion channels locally trigger the transmission through the GB, resulting in a global resistance fluctuation of the transistor channel. Obviously, the fluctuation amplitude will increase with decreasing transistor dimensions, which is in good agreement with our experimental observation (see Table 6.1).
Typically the dimensions of the single graphene grains obtained with our growth parameters are around $20 \times 30\ \mu\text{m}^2$, as shown in Figure 6.15 c. However individual graphene crystals tend to align their crystallographic structure with the orientation of the underlying copper crystals [424]. Thus the merging of graphene grains grown on the same copper crystal does not necessarily form a grain boundary. Graphene layers used in this work were grown on multicrystalline copper foils. Consequently the probability to have a grain boundary crossing a device with a size well below the average grain size is low, explaining the fact that we never observed RTS on the D type devices with a transistor channel size of $20 \times 10\ \mu\text{m}^2$ (see Table 6.1). Larger graphene devices on the other hand, increase the probability to have a well matching pair of a fluctuating ion channel and a grain boundary, increasing the probability to observe RTS (see Fig. 6.15 a). For all devices, the observation of RTS was accompanied by a drastically increased resistance during the neuron culture. While the conductance of smaller FETs decreased only slightly (Chapter 4.8.5), the square resistance of larger FETs increased up to a tenfold of the initial value for A type devices. This observation is in agreement with the presence of GBs, as they are natural weak spots easily affected by physical stress and chemical adsorption.

The gate dependence of RTS presented above could originate either from the changing sensing properties of the grain boundaries, varying series resistance and conductance regime of the graphene sheet, or from the changing conductance and opened/closed times of the ion channels, which were shown to vary with the amplitude of the depolarization pulse [422]. A more careful analysis of our data and probably additional well controlled experiments, for example with a

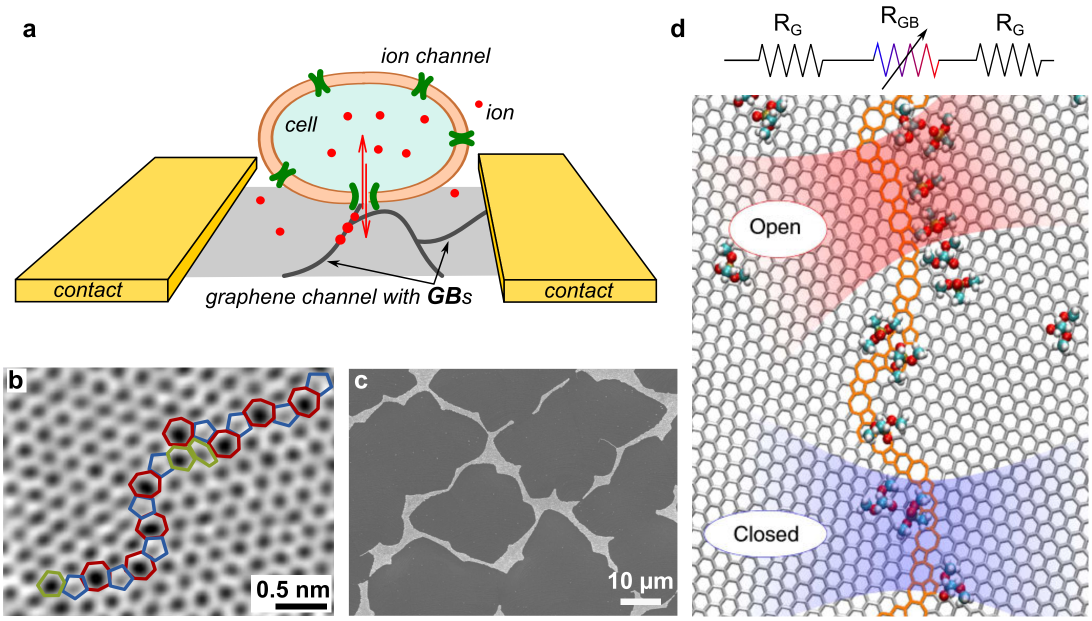

Figure 6.15: Graphene grain boundaries locally increase the sensitivity of G-FET to ion channel fluctuations. a) Schematic illustration of a randomly opening and closing ion channel above a graphene grain boundary. b) TEM image of a grain boundary in graphene [425]. c) SEM image of a typical CVD growth of large graphene sheets stopped shortly before the coalescence, clearly demonstrating the size of individual graphene grains (SEM image from Z. Han [266]). d) Local transmission gaps formed by grain boundaries. Grain boundaries can be represented as local resistors R_{GB} with tunable transmission. While grain boundaries with large transport gaps prevent the current flow (closed channels, blue), grain boundaries with small transport gaps can be easily activated upon chemical adsorption, resulting in an increase of their conductivity (open, red) [423].

single isolated GB, are needed to reveal the exact gate dependence of RTS observed here.

While we strongly believe that the detected RT signal is directly related to the presence of grain boundaries, we can not completely exclude the possibility that the conductance fluctuations are caused by random trapping and detrapping of chemicals/ions dissolved in the extracellular medium. For that latter case, it would imply that the distance between the trap and the sensitive grain boundary is constant in time, a fact that is unlikely at room temperature, unless for a highly confined fluid, such as the cleft formed between the cellular membrane and the device. To clarify this uncertainty, further experimental and theoretical studies will be conducted.

Regardless of the exact origin of the signal, RTS in graphene grain boundaries could provide a high sensitivity platform for detection of biochemical processes, as it was already suggested for silicon nanowires [417].

6.3.3 Neuronal spiking detected with G-FETs

To allow the detection of single potential spikes using our G-FETs, we decreased the FET-dimensions to the size of an individual neuron (20×15 µm^2, 20×10 µm^2), and used higher seeding densities of neurons to increase the probability of FETs interfacing cells. Due to the smaller size, the telegraphic noise in these devices disappeared. Moreover, this batch of G-FETs showed a better stability during the culture, and the device performance decreased only slightly (see Chapter 4.8.5, Fig. 4.29). Figure 6.16 demonstrates the G-FET array interfaced to 21DIV dense neural networks and the transfer characteristics of the G-FETs after the culture. For the detection of neuronal activity, the transistor working point was set to the liquid gate voltage with the highest transconductance, as indicated in Figure 6.16 c, and the source-drain current I_{SD} was recorded at constant V_{SD}.

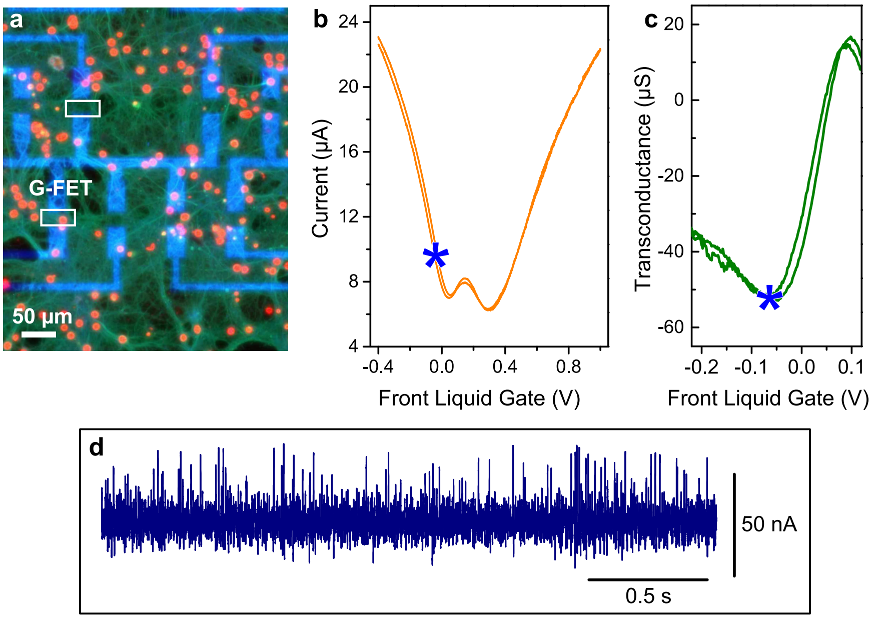

Figure 6.16: 21DIV neurons interfaced with an array of 20×10 µm^2 G-FETs. a) IF image of neurons on G-FETs (dapi (red) marks the neuron soma, and synapsin (green) marks the synaptic vesicles). b) Current versus liquid gate voltage measured on G-FETs shown in a). The liquid gate voltage was set using a Ag/AgCl reference electrode immersed into the cell culture medium. c) The corresponding transconductance curve. The blue star indicates the transistor working point with the highest sensitivity in the hole conduction regime. d) Recording of neuronal activity using G-FET shown in a, at the transistor working point indicated by a blue star in b) and c). The measurements were performed in cell culture medium at $V_{SD} = 100$ mV.

The recorded trace (Fig. 6.16 d) exhibits short positive current pulses, which can be attributed to a short negative potential spikes in the extracellular medium. Using the transconductance g_m at the set transistor working point, the extracellular potential can be calculated to $V_{extra} = I_{SD}/g_m$ with transconductance measured in presence of neurons. The calibrated potential is exemplary shown in Figure 6.17 a. The amplitude is around -570 ± 80 µV, and the spike duration $t_{spike} = 1.5 \pm 0.1$ ms (Fig. 6.17 b).

The polarity and the shape of the detected signals correspond to the expected extracellular potential spike, generated by the opening of sodium channels and influx of positively charged Na^+ ions into the cell resulting in a negative potential change in the cleft. The signal amplitude seems to be rather high compared to values reported using MEAs [146]. However for SiNW-FETs for example, extracellular action potentials with amplitudes up to several mV were reported [14]. Also the high neural affinity of single layer graphene, as demonstrated in Chapter 5.3, could improve the electrical coupling of G-FETs to neurons by decreasing the cleft thickness. This would result in an increased seal resistance and a higher value of detected extracellular potential. The interspike interval (ISI) $\Delta t = 13 \pm 0.8$ ms (Fig. 6.17 c) is in good agreement with values reported for *in-vivo* conditions [426], however slightly shorter than expected for *in-vitro* neuronal cultures. But since the neuron density is very high, it could be possible, that the device is recording action potentials originating from more than one neurons.

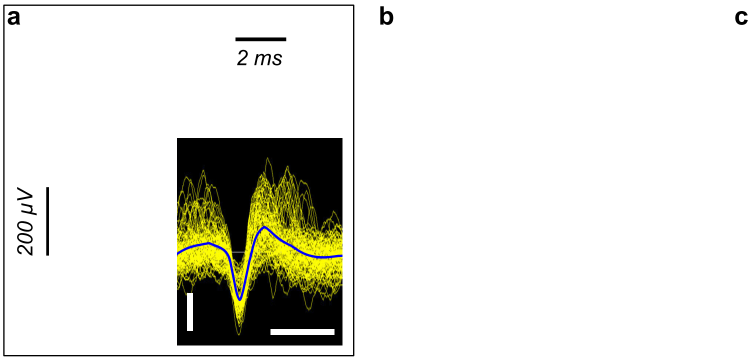

Figure 6.17: Extracellular action potential measured using G-FET interfaced with 21DIV hippocampal neurons. a) The calibrated extracellular potential obtained from a single current spike. The inset shows the superposition of all detected spikes using a commercial spike sorting software "Plexon". The scale bars are 200 µV and 2 ms. b) Histogram showing the distribution of the spike duration. c) Distribution of the interspike interval.

Unfortunately, the control recording with TTX was not performed on this device, since the cell activity collapsed after some time. Similar signals were observed on other G-FETs of the same dimensions, however the firing frequency and the spike amplitude were lower.
To certainly prove the ability of our G-FETs to detect the extracellular action potentials, these recordings have to be reproduced under controlled conditions, and the physiological effect of different drugs on the electrical activity of the neurons has to be shown. Beside TTX, a potassium blocker TEA (tetraethylammonium) could be used to observe the broadening of action potential spikes [427–429].

6.3.4 Conclusion

Due to the small area fraction covered by neurons, single action potentials cannot be detected by large graphene sheet or graphene stripe devices. However, the neuronal activity seems to

occasionally induce some sort of telegraphic signal in this type of graphene transistors. We believe that this signal is attributed to the fluctuating transmission properties of graphene grain boundaries (GBs) induced by the activity of ion channels in the cell membrane. For graphene transistors with channel dimensions larger than the size of a single graphene grain, the transport is dominated by the transmission of the grain boundary, which due to its extremely high sensitivity [423] can be easily modulated by the activity ion channels. However, the exact mechanism of this conductance modulation is not revealed yet and has to be investigated in further experiments.
On the other hand, G-FETs with dimensions similar to the cell size, show better suitability to detect neuronal activity. The traces recorded using 20×10 µm^2 G-FET exhibit current spikes, which can be attributed to the extracellular action potentials. These promising preliminary results have to be reproduced with additional electro-physiological control experiments to finally show the ability of G-FETs to detect neuronal signals.

Recording neuronal activity using graphene FETs seems to be generally difficult. While the detection of the electrical activity of cardiomyocytes using G-FETs was already reported in 2010 [127], followed by the detection of action potentials from HL-1 cells in 2011 [128], up to date there is no publication on recording action potentials from neurons. To our knowledge, the only study, that claims to detect action potentials from neurons using flexible G-FETs [430] is controversially discussed in the scientific community.
The difficulty to create a stable G-FET/neuron interface arises from the challenging neuron culture, complex signal interpretation and the device performance itself. Compared to the relatively easy and fast culturing of cardiomyocytes and HL-1 cells, which requires only few days, primary neuron cultures need long incubation times to achieve the required maturation stage and to establish the spontaneous electrical activity. In this time, the neurons often suffer or even die due to eventually introduced contaminations, or unstable incubator operation. Occasionally, morphologically well developed neurons do not exhibit any spontaneous activity. While the periodic activity of cardiomyocytes and HL-1 cells with high action potential spikes is easy to recognize, the detected activity of neurons often requires additional data treatment and can be easily considered as electrical noise due to the low signal amplitude and irregular behavior. A simultaneous detection of neuronal activity using patch clamp or calcium imaging in addition to FET detection could be necessary as a control experiment. Moreover, the long incubation time may result in device degradation and lowered sensitivity. Although G-FETs realized in this work show good stability in cell culture medium, the fabrication of graphene based devices is very delicate and not always reproducible.
The highest sensitivity obtained for our liquid gated G-FETs is about 4 mS/V (see Chapter 4.8.1, Fig. 4.22 b), matching well the value reported in the literature [299]. The corresponding transconductance is $g_m = 300$ µS. Considering an extracellular potential in the range of < 0.5 mV, in the ideal case the recorded current signal would be around 150 nA. This current signal represents only a 0.4% deviation from the net current flowing through the transistor

channel ($I_{net} \sim 40$ µA, see Chapter 4.8.1, Fig. 4.22 a). After the culture, due to the degradation of the device performance, the current signal induced by neuronal activity would be even smaller. In a more realistic case with sensitivities lower than 4 mS/V, the recorded signal would make $\leq 0.4\%$ of the net current, which is difficult to detect and can be easily vanished within the electrical noise. Thus, the recording noise has to be further reduced by developing of adapted low noise current amplifiers.

CHAPTER 7

Conclusions and perspectives

In conclusion, we fabricated and tested a variety of bioelectrical interfaces including all diamond microelectrode arrays, as well as silicon nanowire and graphene field effect transistors. The fabrication of diamond and graphene based devices started hereby from the very origin by the material synthesis, providing a unique opportunity to control the electronic performance of future devices by controlling the original growth parameters. In the following, we will draw a conclusion to each investigated approach individually, while the main focus will be set on graphene FETs. Before going more into technical details, a general comparison of the fundamental material properties, which can be found in Appendix D (Table .1), reveals the outstanding versatility of graphene compared to silicon or diamond technology, which can be used for realization of a variety of flexible, soft, transparent neural interfaces for *in-vivo* and *in-vitro* applications.

All-diamond microelectrode arrays

All-diamond microelectrode arrays were fabricated using CVD grown nanocrystalline boron-doped diamond for active microelectrodes and intrinsic diamond films for electrical insulation of contact leads for liquid operation. Diamond electrodes with metallic conductivity were obtained by in-situ doping of nanocrystalline diamond with boron. The electrochemical characterization of obtained microelectrodes with a diameter of 55 µm revealed a relatively low double layer capacitance (70 $\mu F/cm^2$) and high electrode impedance (400 kΩ at 1 kHz), which is insufficient for the stimulation and detection of neuronal activity. Thus the possibility to improve the electrode performance by increasing the effective electrode surface by local growth of embedded carbon nanotubes on microelectrodes was introduced. The embedding improves hereby the mechanical stability of the diamond/CNT composite material, and was achieved through sinking of catalytic Pd nanoparticles into diamond layer by dissolving carbon atoms and subsequent growth of CNTs. While a reproducible local growth of embedded CNTs was achieved in this work, a detailed investigation of their effect on the electrode performance and on the interaction with living tissue still remains to be done.

Although nanocrystalline diamond is a promising material for realization of long-term biocompatible neural implants, the detection of neural activity using unmodified diamond electrodes remains challenging due to its high intrinsic impedance. Thus, the electrode performance has to be improved by additional modifications, such as by increasing the effective surface using CNTs or other nanostructures.

Silicon nanowire field effect transistors

SiNW-FET arrays with varying geometries were top-down fabricated using standard e-beam and photolithography techniques. The obtained nanowires with dimensions $W \times L = 0.1{\times}7$ µm^2 exhibit charge carrier mobilities and sensitivities expected for top-down fabricated devices (250 cm^{2}V^{-1}s^{-1} and 6 µS/V respectively). They show good response to pH changes and to short potential pulses. The fabricated SiNW-FETs were successfully used for detection of local field potentials of acute mouse brain slices, revealing their suitability for bioelectrical interfacing with neurons. Also, hippocampal neuron cultures could be grown on the SiNW-FET arrays. Even an exact positioning of neurites above the transistors was achieved using a poly-L-lysine pattern. However, the detection of the electrical activity of cultured neurons has been proved to be difficult due to several issues. For example, no optical control of the cell position was available, making it difficult to find a nanowire in good contact with a neuron. Also, the recordings relied on the spontaneous neural activity with rare spikes, which is more difficult to detect than the stimulated activity. However, no direct electrical stimulation of neural activity could be performed. Additionally, the nanowire geometry with a very low width-to-length ratio $W/L =$ 0.1 µm/7 µm results in a small area fraction covered by a neurite and reduces the detection sensitivity.

Thus to realize a stable platform for detection of neural activity using SiNW-FETs major improvements of the experimental set-up and nanowire performance have to be conducted, including an optical control of the cell position relative to the nanowire, an additional detection/stimulation technique, for example patch clamp, to control the cell activity during the recordings with nanowires, and the adjustment of the nanowire geometry to increase the area fraction covered by the neurites and to improve the detection sensitivity.

Graphene field effect transistors

In this work we presented a stable fabrication protocol for graphene based field effect transistors and revealed their suitability for bioelectrical interfacing with neurons. Large scale single layer graphene sheets were grown on copper foils using a novel pulsed CVD method and transferred onto arbitrary substrates by PMMA assisted wet transfer technique. The quality of obtained graphene layers was primarily assessed by Raman microspectroscopy, revealing highly homogeneous monolayer graphene with low density of structural defects. Additional electrical characterizations showed a square resistance of around 0.4 - 0.6 kΩ, and a mean mobility value of 5000 cm^{2}V^{-1}s^{-1}. These graphene sheets were used for fabrication of field effect transistors with various dimensions.

G-FETs with reproducible electrical properties were realized on a variety of substrates, including Si/SiO$_2$, quartz, glass coverslips and polyimide. The contact resistance was drastically decreased by using Pd as the contact metal at graphene interface. While large G-FETs were used for initial tests with neuron cultures, the FET dimensions were subsequently reduced to the size of a single neuron (20×10 μm^2) to allow single unit detection of action potentials. Electrical characterizations of liquid gated G-FETs revealed a high sensitivity to potential changes with peak sensitivity values reaching 4 mS/V, and a rapid detection (response time less than 0.5 ms) of very small (around 75 µV) potential spikes comparable with neuronal signaling. Additionally, the performance of G-FETs was shown to be compatible with biocoatings, such as poly-L-lysine, and long-term neuron cultures.

Moreover, we demonstrated an unprecedented neuronal affinity of pristine graphene without any additional cell adhesive coating. We found, that primary hippocampal neurons not only attach to pristine graphene, but also exhibit longer neurites and accelerated axonal polarization. The remarkable adherence of neurons to bare graphene reveals a very close proximity and strong electrical coupling. Unlike the majority of other electrically active materials at the interface with living cells, which require an adhesive layer to ensure the coupling, graphene can be directly interfaced to neurons. Consequently, the cleft between a graphene based device and neurons can be qualitatively assumed to be smaller than for any other material, leading to an increased detection sensitivity and improved stimulation. Additionally, Raman spectroscopy analysis performed after the culture suggests, that the strong coupling of neurons to bare graphene surface does not affect the crystalline structure and the electrical properties of underlying graphene layer. This physical stability of graphene together with the possibility to bypass the protein coating reveals its great potential for chronic medical implants.

To assess the suitability of our G-FETs to detect neuronal signals, primary hippocampal neurons were cultured on poly-L-lysine coated graphene transistors for periods of 19-21 days. This culturing period was sufficient for neurons to establish spontaneous electrical activity in well connected networks, as confirmed by patch clamp measurements and calcium imaging. The following electrical recordings on graphene transistors interfaced with neurons revealed two different detection mechanisms. While graphene FETs with channel dimensions smaller than a single graphene grain seem to detect the neuronal spiking via conventional field effect induced conductance modulation, in larger graphene transistors with channel dimensions $\geq 40 \times 50\ \mu m^2$ occasionally neuronal activity seems to induce some sort of two-level random telegraph signal, which is certainly not due to action potentials. Since the transport in graphene devices with channel dimensions well above the size of a single graphene grain is dominated by the grain boundaries (GBs), we attribute the observed two-state conductance fluctuations to the varying transmission properties of highly sensitive graphene GBs induced by the activity of ion channels in the cellular membrane. Additional experiments to confirm this interpretation will be conducted on isolated grain boundaries interfaced to neurons.

On the other hand, conductance spikes detected on smaller graphene FETs ($20\times10\ \mu m^2$) can be attributed to extracellular action potentials. However this preliminary result has to be confirmed in further experiments in combination with additional detection techniques such as patch clamp or optical imaging of neural activity. In this context, since the optical excitation is not affecting the sensing properties of graphene transistors, voltage sensitive dye imaging provides the required spatial and temporal resolution.

Detection of neuronal activity using our graphene transistors was generally difficult due to the relatively high electrical noise in the used current amplification regime. Even for the highest sensitivities obtained in this work, the current modulation induced by an extracellular action potential spike would be on the range of 30 nA for $V_{extra} = 100\ \mu V$, which is comparable with the noise amplitude we usually observe in our recording configuration. Thus, to achieve a reliable recording of neural activity using G-FETs a low noise current amplifier has to be developed.

In conclusion, G-FETs realized in this work show promising results in terms of their biocompatibility, electrical performance, stability in biological environment and electrical interfacing with neurons, but a routine utilization of G-FETs as biosensors for recording neuronal activity still requires further device optimization and development of low noise electronics.

In this thesis, I was offered a unique opportunity to investigate three different types of neural interfaces involving each time a different electronic material, each of them having their particular advantages, such as the mechanical and chemical robustness of diamond, or the unprecedented spatial resolution of silicon nanowires. However, in terms of the diversity of possible applications in biomedical engineering, graphene clearly outperforms both of them. Especially, the peculiar combination of excellent electronic properties with biocompatibility and softness of graphene provides a unique material for a variety of applications, such as the realization of artificial scaffolds for neural regeneration or wearable flexible electronics to monitor specific body functions. While we only evaluated the performance of graphene based transistors, it is also possible to use graphene for soft highly biocompatible microelectrodes, able to intimately conform to the complex surface topology of interfaced brain region or nerves.

In particular, due to its outstanding neural affinity, which we demonstrated here, graphene offers a promising material not only for bioelectrical interfacing, but also for tissue engineering. As a result of its versatility for biomedical applications, in the scientific community graphene is now considered a bionic material, and its potential is worth to be further investigated.

Bibliography

1. Bensmaia, S. J. et al.: ‘Restoring sensorimotor function through intracortical interfaces: progress and looming challenges’. *Nature reviews Neuroscience* (2014), vol. 15(5): pp. 313–325 (cit. on p. 4).
2. Collinger, J. L. et al.: ‘High-performance neuroprosthetic control by an individual with tetraplegia’. *The Lancet* (2013), vol. 381(9866): pp. 557–564 (cit. on pp. 4, 8, 16).
3. Allen, N. J. et al.: ‘Neuroscience: Glia: more than just brain glue’. *Nature* (Feb. 2009), vol. 457(7230): pp. 675–677 (cit. on pp. 4, 100).
4. Streit, W. J. et al.: ‘Functional plasticity of microglia: a review’. *Glia* (1988), vol. 1(5): pp. 301–307 (cit. on p. 4).
5. Nave, K-A. et al.: ‘Axon-glial signaling and the glial support of axon function’. *Annu. Rev. Neurosci.* (2008), vol. 31: pp. 535–561 (cit. on pp. 4, 100).
6. Fitch, M. T. et al.: ‘Cellular and molecular mechanisms of glial scarring and progressive cavitation: in vivo and in vitroanalysis of inflammation-induced secondary injury after CNS trauma’. *The Journal of neuroscience* (1999), vol. 19(19): pp. 8182–8198 (cit. on p. 4).
7. Bezanilla, F.: ‘The action potential: from voltage-gated conductances to molecular structures’. *Biological research* (2006), vol. 39(3): pp. 425–435 (cit. on p. 5).
8. Schätzthauer, R. et al.: ‘Neuron-silicon junction with voltage-gated ionic currents’. *European Journal of Neuroscience* (1998), vol. 10(6): pp. 1956–1962 (cit. on pp. 5, 19, 50).
9. Fromherz, P.: ‘Electrical interfacing of nerve cells and semiconductor chips’. *ChemPhysChem* (2002), vol. 3(3): pp. 276–284 (cit. on pp. 5, 50).
10. Buzsáki, G. et al.: ‘The origin of extracellular fields and currents: EEG, ECoG, LFP and spikes’. *Nature reviews neuroscience* (2012), vol. 13(6): pp. 407–420 (cit. on p. 5).
11. Moran, D.: ‘Evolution of brain-computer interface: action potentials, local field potentials and electrocorticograms’. *Current opinion in neurobiology* (2010), vol. 20(6): pp. 741–745 (cit. on p. 5).
12. Bean, B. P.: ‘The action potential in mammalian central neurons’. *Nature Reviews Neuroscience* (2007), vol. 8(6): pp. 451–465 (cit. on pp. 5, 8).
13. Debanne, D.: ‘Information processing in the axon’. *Nature Reviews Neuroscience* (2004), vol. 5(4): pp. 304–316 (cit. on p. 5).
14. Voelker, M. et al.: ‘Signal Transmission from Individual Mammalian Nerve Cell to Field-Effect Transistor’. *Small* (2005), vol. 1(2): pp. 206–210 (cit. on pp. 6, 18, 19, 49, 50, 130, 141).
15. Fattahi, P. et al.: ‘A review of organic and inorganic biomaterials for neural interfaces’. *Advanced Materials* (2014), vol. 26(12): pp. 1846–1885 (cit. on pp. 7, 11, 12, 15, 16, 107).
16. Schwartz, A. B. et al.: ‘Brain-Controlled Interfaces: Movement Restoration with Neural Prosthetics’. *Neuron* (2006), vol. 52(1): pp. 205 –220 (cit. on pp. 7, 11).
17. Taylor, D. M. et al.: ‘Direct cortical control of 3D neuroprosthetic devices’. *Science* (2002), vol. 296(5574): pp. 1829–1832 (cit. on p. 8).

18. Serruya, M. D. et al.: 'Brain-machine interface: Instant neural control of a movement signal'. *Nature* (2002), vol. 416(6877): pp. 141–142 (cit. on p. 8).

19. Hochberg, L. R. et al.: 'Neuronal ensemble control of prosthetic devices by a human with tetraplegia'. *Nature* (July 2006), vol. 442(7099): pp. 164–171 (cit. on pp. 8, 13, 16).

20. Hochberg, L. R. et al.: 'Reach and grasp by people with tetraplegia using a neurally controlled robotic arm'. *Nature* (May 2012), vol. 485(7398): pp. 372–375 (cit. on pp. 8, 13, 16, 27).

21. Hai, A. et al.: 'Spine-shaped gold protrusions improve the adherence and electrical coupling of neurons with the surface of micro-electronic devices'. *Journal of The Royal Society Interface* (2009), vol. (cit. on pp. 8, 17, 27, 107).

22. Robinson, J. T. et al.: 'Vertical nanowire electrode arrays as a scalable platform for intracellular interfacing to neuronal circuits'. *Nat Nano* (Mar. 2012), vol. 7(3): pp. 180–184 (cit. on pp. 8, 17, 27, 175).

23. James, C. D. et al.: 'Extracellular recordings from patterned neuronal networks using planar microelectrode arrays'. *Biomedical Engineering, IEEE Transactions on* (2004), vol. 51(9): pp. 1640–1648 (cit. on pp. 9, 10).

24. Jun, S. B. et al.: 'Low-density neuronal networks cultured using patterned poly-l-lysine on microelectrode arrays'. *Journal of neuroscience methods* (2007), vol. 160(2): pp. 317–326 (cit. on pp. 9, 10).

25. Marconi, E. et al.: 'Emergent Functional Properties of Neuronal Networks with Controlled Topology'. *PLoS ONE* (Apr. 2012), vol. 7(4): e34648 (cit. on pp. 9, 10).

26. Kanagasabapathi, T. T. et al.: 'Functional connectivity and dynamics of cortical-thalamic networks co-cultured in a dual compartment device'. *Journal of neural engineering* (2012), vol. 9(3): p. 036010 (cit. on pp. 9, 10).

27. Brewer, G. J. et al.: 'Toward a self-wired active reconstruction of the hippocampal trisynaptic loop: DG-CA3'. *Frontiers in neural circuits* (2013), vol. 7 (cit. on p. 9).

28. Ruaro, M. E. et al.: 'Toward the neurocomputer: image processing and pattern recognition with neuronal cultures'. *Biomedical Engineering, IEEE Transactions on* (2005), vol. 52(3): pp. 371–383 (cit. on pp. 9, 10).

29. Liu, Y. et al.: 'NMDA receptor subunits have differential roles in mediating excitotoxic neuronal death both in vitro and in vivo'. *The Journal of neuroscience* (2007), vol. 27(11): pp. 2846–2857 (cit. on p. 9).

30. Sun, D. A. et al.: 'Glutamate Injury-Induced Epileptogenesis in Hippocampal Neurons An In Vitro Model of Stroke-Induced "Epilepsy"'. *Stroke* (2001), vol. 32(10): pp. 2344–350 (cit. on p. 9).

31. DeLorenzo, R. J. et al.: 'Effects of topiramate on sustained repetitive firing and spontaneous recurrent seizure discharges in cultured hippocampal neurons'. *Epilepsia* (2000), vol. 41(s1): pp. 40–44 (cit. on p. 9).

32. Yuan, Q. et al.: 'Regulation of Brain-Derived Neurotrophic Factor Exocytosis and Gamma-Aminobutyric Acidergic Interneuron Synapse by the Schizophrenia Susceptibility Gene Dysbindin-1'. *Biological psychiatry* (2015), vol. (cit. on p. 9).

33. Potter, S. M. et al.: 'A new approach to neural cell culture for long-term studies'. *Journal of neuroscience methods* (2001), vol. 110(1): pp. 17–24 (cit. on p. 9).

34. Wheeler, B. C. et al.: 'Designing neural networks in culture'. *Proceedings of the IEEE* (2010), vol. 98(3): pp. 398–406 (cit. on p. 10).

35. Scholl, M. et al.: 'Ordered networks of rat hippocampal neurons attached to silicon oxide surfaces'. *Journal of neuroscience methods* (2000), vol. 104(1): pp. 65–75 (cit. on p. 10).

36. Wyart, C. et al.: ‘Constrained synaptic connectivity in functional mammalian neuronal networks grown on patterned surfaces’. *Journal of neuroscience methods* (2002), vol. 117(2): pp. 123–131 (cit. on p. 10).

37. Biran, R. et al.: ‘Neuronal cell loss accompanies the brain tissue response to chronically implanted silicon microelectrode arrays’. *Experimental Neurology* (2005), vol. 195(1): pp. 115 –126 (cit. on p. 11).

38. Fernández, E. et al.: ‘Acute human brain responses to intracortical microelectrode arrays: Challenges and future prospects’. *Front Neuroeng.* (2014), vol. 7(24) (cit. on pp. 12, 28).

39. Ereifej, E. et al.: ‘Comparative assessment of iridium oxide and platinum alloy wires using an in vitro glial scar assay’. English. *Biomedical Microdevices* (2013), vol. 15(6): pp. 917–924 (cit. on pp. 12, 28).

40. Griffith, R. W. et al.: ‘Long-term gliosis around chronically implanted platinum electrodes in the Rhesus macaque motor cortex’. *Neuroscience Letters* (Oct. 2006), vol. 406(1-2): pp. 81–86 (cit. on pp. 12, 28).

41. Polikov, V. S. et al.: ‘Response of brain tissue to chronically implanted neural electrodes’. *Journal of Neuroscience Methods* (2005), vol. 148(1): pp. 1 –18 (cit. on pp. 12, 28, 100).

42. Brand, R. van den et al.: ‘Restoring voluntary control of locomotion after paralyzing spinal cord injury’. *science* (2012), vol. 336(6085): pp. 1182–1185 (cit. on p. 13).

43. Raspopovic, S. et al.: ‘Restoring Natural Sensory Feedback in Real-Time Bidirectional Hand Prostheses’. *Science Translational Medicine* (2014), vol. 6(222): 222ra19–222ra19 (cit. on pp. 13, 16).

44. Hornig, R. et al.: ‘A method and technical equipment for an acute human trial to evaluate retinal implant technology’. *Journal of Neural Engineering* (2005), vol. 2(1): S129 (cit. on p. 13).

45. Dobelle, W. H.: ‘Artificial vision for the blind by connecting a television camera to the visual cortex’. *ASAIO journal* (2000), vol. 46(1): pp. 3–9 (cit. on p. 14).

46. Maynard, E. M.: ‘Visual prostheses’. *Annual review of biomedical engineering* (2001), vol. 3(1): pp. 145–168 (cit. on p. 14).

47. Cruz, L. da et al.: ‘The Argus II epiretinal prosthesis system allows letter and word reading and long-term function in patients with profound vision loss’. *Br. J. Ophthalmology* (2013), vol. 97: pp. 632–636 (cit. on p. 14).

48. Dorn, J. D. et al.: ‘The detection of motion by blind subjects with the epiretinal 60-electrode (argus ii) retinal prosthesis’. *JAMA Ophthalmology* (2013), vol. 131(2): pp. 183–189 (cit. on p. 14).

49. Stingl, K. et al.: ‘Artificial vision with wirelessly powered subretinal electronic implant alpha-IMS’. *Proceedings of the Royal Society of London B: Biological Sciences* (2013), vol. 280(1757): p. 20130077 (cit. on p. 14).

50. Wang, P. et al.: *Biomedical sensors and measurement.* Springer Science & Business Media, 2011 (cit. on p. 15).

51. Ingebrandt, S. et al.: ‘Neuron-transistor coupling: interpretation of individual extracellular recorded signals’. *European biophysics journal* (2005), vol. 34(2): pp. 144–154 (cit. on pp. 15, 19).

52. Thomas, C.A. et al.: ‘A miniature microelectrode array to monitor the bioelectric activity of cultured cells’. *Experimental Cell Research* (1972), vol. 74(1): pp. 61 –66 (cit. on p. 15).

53. Metallo, C. et al.: ‘Flexible parylene-based microelectrode arrays for high resolution EMG recordings in freely moving small animals’. *Journal of neuroscience methods* (2011), vol. 195(2): pp. 176–184 (cit. on p. 16).

54. Rubehn, B. et al.: ‘A MEMS-based flexible multichannel ECoG-electrode array’. *Journal of neural engineering* (2009), vol. 6(3): p. 036003 (cit. on p. 16).

55. Lesch, A. et al.: ‘Fabrication of soft gold microelectrode arrays as probes for scanning electrochemical microscopy’. *Journal of Electroanalytical Chemistry* (2012), vol. 666: pp. 52–61 (cit. on p. 16).

56. Lee, K. et al.: ‘Biocompatible benzocyclobutene (BCB)-based neural implants with micro-fluidic channel’. *Biosensors and Bioelectronics* (2004), vol. 20(2): pp. 404–407 (cit. on p. 16).

57. Kim, D-H. et al.: ‘Dissolvable films of silk fibroin for ultrathin conformal bio-integrated electronics’. *Nat Mater* (June 2010), vol. 9(6): pp. 511–517 (cit. on p. 16).

58. Stieglitz, T.: ‘Development of a micromachined epiretinal vision prosthesis’. *Journal of neural engineering* (2009), vol. 6(6): p. 065005 (cit. on p. 16).

59. Borton, D. et al.: ‘Corticospinal neuroprostheses to restore locomotion after spinal cord injury’. *Neuroscience Research* (2014), vol. 78. Neural mechanisms of functional recovery after brain/spinal cord injury: pp. 21 –29 (cit. on pp. 16, 27).

60. Metallo, C. et al.: ‘Silk coating as a novel delivery system and reversible adhesive for stiffening and shaping flexible probes’. *Journal of Biological Methods* (2015), vol. 2(1): e13 (cit. on p. 16).

61. Abidian, M. R. et al.: ‘Experimental and theoretical characterization of implantable neural microelectrodes modified with conducting polymer nanotubes’. *Biomaterials* (2008), vol. 29(9): pp. 1273–1283 (cit. on p. 16).

62. Kipke, D. R. et al.: ‘Advanced neurotechnologies for chronic neural interfaces: new horizons and clinical opportunities’. *The Journal of Neuroscience* (2008), vol. 28(46): pp. 11830–11838 (cit. on p. 16).

63. Negi, S. et al.: ‘Neural electrode degradation from continuous electrical stimulation: Comparison of sputtered and activated iridium oxide’. *Journal of Neuroscience Methods* (2010), vol. 186(1): pp. 8 –17 (cit. on p. 16).

64. Gawad, S. et al.: ‘Substrate arrays of iridium oxide microelectrodes for in vitro neuronal interfacing’. *Frontiers in neuroengineering* (2009), vol. 2 (cit. on p. 16).

65. Bendali, A. et al.: ‘Purified Neurons can Survive on Peptide-Free Graphene Layers’. *Advanced Healthcare Materials* (2013), vol. 2(7): pp. 929–933 (cit. on pp. 16, 21, 51, 64, 111).

66. Kuzum, D. et al.: ‘Transparent and flexible low noise graphene electrodes for simultaneous electrophysiology and neuroimaging’. *Nat Commun* (Oct. 2014), vol. 5: p. 5259 (cit. on p. 16).

67. Luo, S-C. et al.: ‘Poly (3, 4-ethylenedioxythiophene)(PEDOT) nanobiointerfaces: thin, ultrasmooth, and functionalized PEDOT films with in vitro and in vivo biocompatibility’. *Langmuir* (2008), vol. 24(15): pp. 8071–8077 (cit. on p. 16).

68. Chen, Y. et al.: ‘Design and fabrication of a polyimide-based microelectrode array: Application in neural recording and repeatable electrolytic lesion in rat brain’. *Journal of Neuroscience Methods* (2009), vol. 182(1): pp. 6 –16 (cit. on p. 16).

69. Hupert, M. et al.: ‘Conductive diamond thin-films in electrochemistry’. *Diamond and Related Materials* (2003), vol. 12(10-11). Proceedings of the 8th International Conference on New Diamond Science and Technology (ICNDST-8): pp. 1940 –1949 (cit. on pp. 16, 28).

70. Bendali, A. et al.: ‘Distinctive Glial and Neuronal Interfacing on Nanocrystalline Diamond’. *PLoS ONE* (Mar. 2014), vol. 9(3): e92562 (cit. on pp. 16, 28).

71. Maybeck, V. et al.: ‘Boron-doped nanocrystalline diamond microelectrode arrays monitor cardiac action potentials’. *Advanced Healthcare Materials* (2013), vol. 3(2): pp. 283–289 (cit. on pp. 16, 28, 43).

72. Bergonzo, P. et al.: ‘3D shaped mechanically flexible diamond microelectrode arrays for eye implant applications: The {MEDINAS} project’. *IRBM* (2011), vol. 32(2): pp. 91 –94 (cit. on pp. 16, 28).

73. Hébert, C. et al.: 'Microfabrication, characterization and in vivo MRI compatibility of diamond microelectrodes array for neural interfacing'. *Materials Science and Engineering: C* (2015), vol. 46: pp. 25–31 (cit. on pp. 16, 42, 43).

74. Fan, B. et al.: 'Fabrication of polycrystalline diamond on a flexible Parylene substrate'. *Solid-State Sensors, Actuators and Microsystems (TRANSDUCERS), 2015 Transducers - 2015 18th International Conference on.* 2015: pp. 892–895 (cit. on pp. 16, 28, 175).

75. Hess, A. E. et al.: 'Diamond-on-Polymer Microelectrode Arrays Fabricated Using a Chemical Release Transfer Process'. *Microelectromechanical Systems, Journal of* (2011), vol. 20(4): pp. 867–875 (cit. on pp. 16, 28).

76. Hadjinicolaou, A. E. et al.: 'Electrical stimulation of retinal ganglion cells with diamond and the development of an all diamond retinal prosthesis'. *Biomaterials* (2012), vol. 33(24): pp. 5812 –5820 (cit. on pp. 16, 28).

77. Bendali, A. et al.: 'Synthetic 3D diamond-based electrodes for flexible retinal neuroprostheses: Model, production and in vivo biocompatibility'. *Biomaterials* (2015), vol. 67: pp. 73–83 (cit. on pp. 16, 17).

78. Chan, H-Y. et al.: 'A novel diamond microprobe for neuro-chemical and-electrical recording in neural prosthesis'. *Microelectromechanical Systems, Journal of* (2009), vol. 18(3): pp. 511–521 (cit. on p. 16).

79. Varney, M. W. et al.: 'Polycrystalline-diamond MEMS biosensors including neural microelectrode-arrays'. *Biosensors* (2011), vol. 1(3): pp. 118–133 (cit. on pp. 16, 28, 43, 175).

80. Piret, G. et al.: '3D-nanostructured boron-doped diamond for microelectrode array neural interfacing'. *Biomaterials* (2015), vol. 53: pp. 173 –183 (cit. on pp. 17, 28, 45, 175).

81. Chan, H. Y. et al.: 'Fabrication and testing of a novel all-diamond neural probe for chemical detection and electrical sensing applications'. *Micro Electro Mechanical Systems, 2008. MEMS 2008. IEEE 21st International Conference on.* 2008: pp. 244–247 (cit. on p. 17).

82. Hanson, L. et al.: 'Characterization of the cell–nanopillar interface by transmission electron microscopy'. *Nano letters* (2012), vol. 12(11): pp. 5815–5820 (cit. on pp. 17, 107).

83. Eytan, Da. et al.: 'Dopamine-induced dispersion of correlations between action potentials in networks of cortical neurons'. *Journal of neurophysiology* (2004), vol. 92(3): pp. 1817–1824 (cit. on p. 17).

84. Rijal, S. O. et al.: 'Dissociation constants for GABA A receptor antagonists determined with neuronal networks on microelectrode arrays'. *Journal of neuroscience methods* (2008), vol. 173(2): pp. 183–192 (cit. on p. 17).

85. Xia, Y. et al.: 'Differential acute effects of fluoxetine on frontal and auditory cortex networks in vitro'. *Brain research* (2003), vol. 973(2): pp. 151–160 (cit. on p. 17).

86. Sokal, D. M. et al.: 'Multi-neuronal recordings reveal a differential effect of thapsigargin on bicuculline- or gabazine-induced epileptiform excitability in rat hippocampal neuronal networks'. *Neuropharmacology* (2000), vol. 39(12): pp. 2408 –2417 (cit. on p. 17).

87. Xia, Y. et al.: 'Histiotypic electrophysiological responses of cultured neuronal networks to ethanol'. *Alcohol* (2003), vol. 30(3): pp. 167–174 (cit. on p. 17).

88. Yeung, C. K. et al.: 'Drug profiling using planar microelectrode arrays'. *Analytical and bioanalytical chemistry* (2007), vol. 387(8): pp. 2673–2680 (cit. on p. 17).

89. Kolomiets, B. et al.: 'Late histological and functional changes in the P23H rat retina after photoreceptor loss'. *Neurobiology of disease* (2010), vol. 38(1): pp. 47–58 (cit. on p. 17).

90. Wagenaar, D. A. et al.: 'An extremely rich repertoire of bursting patterns during the development of cortical cultures'. *BMC neuroscience* (2006), vol. 7(1): p. 11 (cit. on p. 17).

91. Dworak, B. J. et al.: ‘Novel MEA platform with PDMS microtunnels enables the detection of action potential propagation from isolated axons in culture’. *Lab on a Chip* (2009), vol. 9(3): pp. 404–410 (cit. on pp. 17, 103).

92. Oka, H. et al.: ‘A new planar multielectrode array for extracellular recording: application to hippocampal acute slice’. *Journal of Neuroscience Methods* (1999), vol. 93(1): pp. 61 –67 (cit. on pp. 17, 27).

93. Suzuki, I. et al.: ‘Carbon nanotube multi-electrode array chips for noninvasive real-time measurement of dopamine, action potentials, and postsynaptic potentials’. *Biosensors and Bioelectronics* (2013), vol. 49: pp. 270 –275 (cit. on pp. 17, 27, 45).

94. Bergveld, P. et al.: ‘Extracellular Potential Recordings by Means of a Field Effect Transistor Without Gate Metal, Called OSFET’. *Biomedical Engineering, IEEE Transactions on* (1976), vol. BME-23(2): pp. 136–144 (cit. on pp. 18, 47).

95. Fromherz, P. et al.: ‘A neuron-silicon junction: a Retzius cell of the leech on an insulated-gate field-effect transistor’. *Science* (1991), vol. 252(510): pp. 1290–1293 (cit. on pp. 18, 19, 49, 50, 175).

96. Schmidt, C.: ‘Bioelectronics: The bionic material’. *Nature* (Mar. 2012), vol. 483(7389): S37–S37 (cit. on pp. 18, 21, 63).

97. Wrobel, G. et al.: ‘Transmission electron microscopy study of the cell–sensor interface’. *Journal of The Royal Society Interface* (2008), vol. 5(19): pp. 213–222 (cit. on pp. 18, 19).

98. Zeck, G. et al.: ‘Noninvasive neuroelectronic interfacing with synaptically connected snail neurons immobilized on a semiconductor chip’. *Proceedings of the National Academy of Sciences* (2001), vol. 98(18): pp. 10457–10462 (cit. on pp. 18, 19).

99. Eschermann, J. F. et al.: ‘Action potentials of HL-1 cells recorded with silicon nanowire transistors’. *Applied Physics Letters* (2009), vol. 95(8), 083703: p. 083703 (cit. on pp. 19, 20, 49, 53, 61, 130).

100. Offenhäusser, A. et al.: ‘Cell-transistor hybrid systems and their potential applications’. *Trends in Biotechnology* (2001), vol. 19(2): pp. 62 –66 (cit. on pp. 19, 49, 130).

101. Meyburg, S. et al.: ‘Single cell recordings with pairs of complementary transistors’. *Applied physics letters* (2006), vol. 89(1): p. 013901 (cit. on p. 19).

102. Wrobel, G. et al.: ‘Cell-transistor coupling: investigation of potassium currents recorded with p-and n-channel FETs’. *Biophysical journal* (2005), vol. 89(5): pp. 3628–3638 (cit. on pp. 19, 130).

103. Lambacher, A. et al.: ‘Fluorescence interference-contrast microscopy on oxidized silicon using a monomolecular dye layer’. *Applied Physics A* (1996), vol. 63(3): pp. 207–216 (cit. on p. 19).

104. Braun, D. et al.: ‘Fluorescence interferometry of neuronal cell adhesion on microstructured silicon’. *Physical review letters* (1998), vol. 81(23): p. 5241 (cit. on p. 19).

105. Fromherz, F.: ‘Extracellular recording with transistors and the distribution of ionic conductances in a cell membrane’. English. *European Biophysics Journal* (1999), vol. 28(3): pp. 254–258 (cit. on pp. 19, 49).

106. Prinz, A. A. et al.: ‘Electrical synapses by guided growth of cultured neurons from the snail Lymnaea stagnalis’. *Biological cybernetics* (2000), vol. 82(4): pp. L1–L5 (cit. on p. 19).

107. Felderer, F. et al.: ‘Transistor needle chip for recording in brain tissue’. English. *Applied Physics A* (2011), vol. 104(1): pp. 1–6 (cit. on pp. 19, 51).

108. Eversmann, B. et al.: ‘A 128 × 128 CMOS biosensor array for extracellular recording of neural activity’. *Solid-State Circuits, IEEE Journal of* (2003), vol. 38(12): pp. 2306–2317 (cit. on pp. 19, 22).

109. Lambacher, A. et al.: ‘Electrical imaging of neuronal activity by multi-transistor-array (MTA) recording at 7.8 um resolution’. *Applied Physics A* (2004), vol. 79(7): pp. 1607–1611 (cit. on pp. 19, 22).

110. Hutzler, M. et al.: ‘High-resolution multitransistor array recording of electrical field potentials in cultured brain slices’. *Journal of Neurophysiology* (2006), vol. 96(3): pp. 1638–1645 (cit. on pp. 19, 22, 51).

111. Patolsky, F. et al.: ‘Detection, stimulation, and inhibition of neuronal signals with high-density nanowire transistor arrays’. *Science* (2006), vol. 313(5790): pp. 1100–1104 (cit. on pp. 20, 51, 53, 61, 128, 129, 175).

112. Wu, Y. et al.: ‘Controlled growth and structures of molecular-scale silicon nanowires’. *Nano Letters* (2004), vol. 4(3): pp. 433–436 (cit. on p. 20).

113. Timko, B. P. et al.: ‘Electrical recording from hearts with flexible nanowire device arrays’. *Nano Letters* (2009), vol. 9(2). PMID: 19170614: pp. 914–918 (cit. on pp. 20, 51, 61, 175).

114. Tian, B. et al.: ‘Three-dimensional, flexible nanoscale field-effect transistors as localized bioprobes’. *Science* (2010), vol. 329(5993): pp. 830–834 (cit. on p. 20).

115. Vu, X. T. et al.: ‘Top-down processed silicon nanowire transistor arrays for biosensing’. *physica status solidi (a)* (2009), vol. 206(3): pp. 426–434 (cit. on pp. 20, 53, 61).

116. Roth, S. et al.: ‘Neuronal architectures with axo-dendritic polarity above silicon nanowires’. *Small* (2012), vol. 8(5): pp. 671–675 (cit. on pp. 20, 21, 51, 53, 103).

117. Schmidt, V. et al.: ‘Silicon nanowires: A review on aspects of their growth and their electrical properties’. *Advanced Materials* (2009), vol. 21(25-26): pp. 2681–2702 (cit. on pp. 20, 53, 59).

118. Kostarelos, K. et al.: ‘Graphene devices for life’. *Nat Nano* (Oct. 2014), vol. 9(10): pp. 744–745 (cit. on pp. 21, 63).

119. Li, X. et al.: ‘Large-area synthesis of high-quality and uniform graphene films on copper foils’. *Science* (2009), vol. 324(5932): pp. 1312–1314 (cit. on pp. 21, 64, 69).

120. Bae, S. et al.: ‘Roll-to-roll production of 30-inch graphene films for transparent electrodes’. *Nat Nano* (Aug. 2010), vol. 5(8): pp. 574–578 (cit. on pp. 21, 64, 69, 71).

121. Lee, Y. et al.: ‘Wafer-scale synthesis and transfer of graphene films’. *Nano Letters* (2010), vol. 10(2): pp. 490–493 (cit. on pp. 21, 64).

122. Prasai, D. et al.: ‘Graphene: Corrosion-inhibiting coating’. *ACS Nano* (2012), vol. 6(2). PMID: 22299572: pp. 1102–1108 (cit. on pp. 21, 51, 63).

123. Lee, C. et al.: ‘Measurement of the elastic properties and intrinsic strength of monolayer graphene’. *Science* (2008), vol. 321(5887): pp. 385–388 (cit. on pp. 21, 51, 63).

124. Geim, A. K. et al.: ‘The rise of graphene’. *Nature materials* (2007), vol. 6(3): pp. 183–191 (cit. on p. 21).

125. Uesugi, E. et al.: ‘Electric double-layer capacitance between an ionic liquid and few-layer graphene’. *Scientific Reports* (Apr. 2013), vol. 3: p. 1595 (cit. on pp. 21, 68, 69).

126. Hess, L. H. et al.: ‘High-transconductance graphene solution-gated field effect transistors’. *Applied Physics Letters* (2011), vol. 99(3), 033503: p. 033503 (cit. on pp. 21, 64, 88).

127. Cohen-Karni, T. et al.: ‘Graphene and nanowire transistors for cellular interfaces and electrical recording’. *Nano Letters* (2010), vol. 10(3): pp. 1098–1102 (cit. on pp. 21, 64, 142).

128. Hess, L. H. et al.: ‘Graphene transistor arrays for recording action potentials from electrogenic cells’. *Advanced Materials* (2011), vol. 23(43): pp. 5045–5049 (cit. on pp. 21, 51, 64, 142, 175).

129. Berdondini, L. et al.: ‘Active pixel sensor array for high spatio-temporal resolution electrophysiological recordings from single cell to large scale neuronal networks’. *Lab on a Chip* (2009), vol. 9(18): pp. 2644–2651 (cit. on p. 22).

130. Frey, U. et al.: ‘Switch-matrix-based high-density microelectrode array in CMOS technology’. *Solid-State Circuits, IEEE Journal of* (2010), vol. 45(2): pp. 467–482 (cit. on p. 22).

131. Huys, R. et al.: ‘Single-cell recording and stimulation with a 16k micro-nail electrode array integrated on a 0.18 μm CMOS chip’. *Lab on a Chip* (2012), vol. 12(7): pp. 1274–1280 (cit. on p. 22).

132. Bakkum, D. J. et al.: ‘Tracking axonal action potential propagation on a high-density microelectrode array across hundreds of sites’. *Nat Commun* (July 2013), vol. 4: p. 2181 (cit. on p. 22).

133. Müller, J. et al.: ‘High-resolution CMOS MEA platform to study neurons at subcellular, cellular, and network levels’. *Lab on a Chip* (2015), vol. (cit. on p. 22).

134. Ding, S. et al.: ‘Kv3-like potassium channels are required for sustained high-frequency firing in basal ganglia output neurons’. *Journal of neurophysiology* (2011), vol. 105(2): pp. 554–570 (cit. on p. 22).

135. Tonini, R. et al.: ‘Small-conductance Ca2+ activated K+ channels modulate action potential-induced Ca2+ transients in hippocampal neurons’. *Journal of Neurophysiology* (2013), vol. 109(6): pp. 1514–1524 (cit. on pp. 22, 125).

136. Bradley, J. et al.: ‘Submillisecond optical reporting of membrane potential in situ using a neuronal tracer dye’. *The Journal of Neuroscience* (2009), vol. 29(29): pp. 9197–9209 (cit. on pp. 22, 23).

137. Ogden, O. et al.: *Patch clamp techniques for single channel and whole-cell recording.* Vol. 2. 1994 (cit. on pp. 22, 27).

138. Bébarová, M.: ‘Advances in patch clamp technique: towards higher quality and quantity’. *General physiology and biophysics* (2012), vol. 31(2): pp. 131–140 (cit. on p. 22).

139. Berridge, M. J. et al.: ‘The versatility and universality of calcium signalling’. *Nat Rev Mol Cell Biol* (Oct. 2000), vol. 1(1): pp. 11–21 (cit. on pp. 23, 124).

140. Augustine, G. J. et al.: ‘Local Calcium Signaling in Neurons’. *Neuron* (2003), vol. 40(2): pp. 331 –346 (cit. on pp. 23, 124, 125).

141. Clapham, D. E.: ‘Calcium Signaling’. *Cell* (2007), vol. 131(6): pp. 1047 –1058 (cit. on pp. 23, 125).

142. Grienberger, C. et al.: ‘Imaging calcium in neurons’. *Neuron* (2012), vol. 73(5): pp. 862–885 (cit. on p. 23).

143. Chemla, S. et al.: ‘Voltage-sensitive dye imaging: Technique review and models’. *Journal of Physiology-Paris* (2010), vol. 104(1): pp. 40–50 (cit. on p. 23).

144. Peterka, D. S. et al.: ‘Imaging voltage in neurons’. *Neuron* (2011), vol. 69(1): pp. 9–21 (cit. on p. 23).

145. Akemann, W. et al.: ‘Imaging neural circuit dynamics with a voltage-sensitive fluorescent protein’. *Journal of neurophysiology* (2012), vol. 108(8): pp. 2323–2337 (cit. on p. 23).

146. Spira, M. E. et al.: ‘Multi-electrode array technologies for neuroscience and cardiology’. *Nat Nano* (Feb. 2013), vol. 8(2): pp. 83–94 (cit. on pp. 26, 27, 43, 141).

147. Fejtl, M. et al.: ‘On micro-electrode array revival: its development, sophistication of recording, and stimulation’. *Advances in Network Electrophysiology.* Springer, 2006: pp. 24–37 (cit. on p. 26).

148. Stett, A. et al.: ‘Two-way silicon-neuron interface by electrical induction’. *Phys. Rev. E* (2 1997), vol. 55: pp. 1779–1782 (cit. on pp. 27, 50).

149. Cohen, A. et al.: ‘Reversible transition of extracellular field potential recordings to intracellular recordings of action potentials generated by neurons grown on transistors’. *Biosensors and Bioelectronics* (2008), vol. 23(6): pp. 811–819 (cit. on pp. 27, 130).

150. Kim, J; et al.: ‘Surface-modified microelectrode array with flake nanostructure for neural recording and stimulation’. *Nanotechnology* (2010), vol. 21(8): p. 085303 (cit. on p. 27).

151. Bräggemann, D. et al.: ‘Nanostructured gold microelectrodes for extracellular recording from electrogenic cells’. *Nanotechnology* (2011), vol. 22(26): p. 265104 (cit. on p. 27).

152. Keefer, E. W. et al.: ‘Carbon nanotube coating improves neuronal recordings’. *Nat Nano* (July 2008), vol. 3(7): pp. 434–439 (cit. on pp. 27, 45).

153. Lee, B. et al.: ‘A primer onbrain-machine interfaces, concepts, and technology: A key element in the future of functional neurorestoration’. *World Neurosurgery* (2013), vol. 79(3-4): pp. 457 –471 (cit. on p. 27).

154. Lewis, P. M. et al.: ‘Restoration of vision in blind individuals using bionic devices: A review with a focus on cortical visual prostheses’. *Brain Research* (2015), vol. 1595: pp. 51 –73 (cit. on p. 27).

155. Chen, S. et al.: ‘Extracellular matrix-based materials for neural interfacing’. *MRS Bull.* (2012), vol.: pp. 606–613 (cit. on p. 28).

156. Dankerl, M. et al.: ‘Diamond transistor array for extracellular recording from electrogenic cells’. *Advanced Functional Materials* (2009), vol. 19(18): pp. 2915–2923 (cit. on pp. 28, 51, 175).

157. Mandal, S. et al.: ‘The diamond superconducting quantum interference device’. *ACS Nano* (2011), vol. 5(9): pp. 7144–7148 (cit. on p. 28).

158. Bautze, T. et al.: ‘Superconducting nano-mechanical diamond resonators’. *Carbon* (2014), vol. 72: pp. 100 –105 (cit. on p. 28).

159. Denisenko, A. et al.: ‘Diamond power devices. Concepts and limits’. *Diamond and Related Materials* (2005), vol. 14(3-7): pp. 491 –498 (cit. on p. 28).

160. Edgington, R. et al.: ‘Boron sigma-doped (1 1 1) diamond solution gate field effect transistors’. *Biosensors and Bioelectronics* (2012), vol. 33(1): pp. 152 –157 (cit. on p. 28).

161. Kawarada, H. et al.: ‘Electrolyte-solution-gate FETs using diamond surface for biocompatible ion sensors’. *physica status solidi (a)* (2001), vol. 185(1): pp. 79–83 (cit. on p. 28).

162. Denisenko, A. et al.: ‘pH sensor on O-terminated diamond using boron-doped channel’. *Diamond and Related Materials* (2007), vol. 16(4-7): pp. 905 –910 (cit. on p. 28).

163. Ahnood, A. et al.: ‘Ultrananocrystalline diamond-CMOS device integration route for high acuity retinal prostheses’. English. *Biomedical Microdevices* (2015), vol. 17(3), 50 (cit. on p. 28).

164. Tsunozaki, K. et al.: ‘Fabrication and electrochemical characterization of boron-doped diamond microdisc array electrodes’. *Chemistry Letters* (2002), vol. 31(5): pp. 502–503 (cit. on p. 28).

165. Lawrence, N. S. et al.: ‘Electroanalytical applications of boron-doped diamond microelectrode arrays’. *Talanta* (2006), vol. 69(4): pp. 829 –834 (cit. on p. 28).

166. Pecková, K. et al.: ‘Boron-doped diamond film electrodes: New tool forvoltammetric determination of organic substances’. *Critical Reviews in Analytical Chemistry* (2009), vol. 39(3): pp. 148–172 (cit. on p. 28).

167. Yoshimi, K. et al.: ‘Phasic reward responses in the monkey striatum as detected by voltammetry with diamond microelectrodes’. *Neuroscience Research* (2011), vol. 71(1): pp. 49 –62 (cit. on p. 28).

168. Smirnov, W. et al.: ‘Integrated all-diamond ultramicroelectrode arrays: Optimization of faradaic and capacitive currents’. *Analytical Chemistry* (2011), vol. 83(19): pp. 7438–7443 (cit. on p. 28).

169. Ganesan, K. et al.: ‘An all-diamond, hermetic electrical feedthrough array for a retinal prosthesis’. *Biomaterials* (2014), vol. 35(3): pp. 908–915 (cit. on p. 28).

170. Ganesan, K. et al.: ‘Diamond penetrating electrode array for Epi-Retinal Prosthesis’. *EMBC’10* (2010), vol.: pp. 6757–6760 (cit. on p. 28).

171. Hébert, C. et al.: ‘A composite material made of carbon nanotubes partially embedded in a nanocrystalline diamond film’. *Carbon* (2013), vol. 52: pp. 408 –417 (cit. on p. 28).

172. Héber, C. et al.: ‘Boosting the electrochemical properties of diamond electrodes using carbon nanotube scaffolds’. *Carbon* (2014), vol. 71: pp. 27 –33 (cit. on p. 28).

173. Gracio, J. J. et al.: ‘Diamond growth by chemical vapour deposition’. *Journal of Physics D: Applied Physics* (2010), vol. 43(37): p. 374017 (cit. on p. 29).

174. Vogl, P. et al.: ‘A Semi-empirical tight-binding theory of the electronic structure of semiconductors’. *Journal of Physics and Chemistry of Solids* (1983), vol. 44(5): pp. 365–378 (cit. on p. 29).

175. Pan, L. S. et al.: *Diamond: electronic properties and applications.* Springer Science & Business Media, 2013 (cit. on p. 29).

176. Haenen, K. et al.: ‘Phonon-assisted electronic transitions in phosphorus-doped n-type chemical vapor deposition diamond films’. *Diamond and related materials* (2001), vol. 10(3): pp. 439–443 (cit. on p. 29).

177. Lagrange, J-P. et al.: ‘Activation energy in low compensated homoepitaxial boron-doped diamond films’. *Diamond and Related Materials* (1998), vol. 7(9): pp. 1390–1393 (cit. on p. 29).

178. Matsumoto, S. et al.: ‘Vapor deposition of diamond particles from methane’. *Japanese Journal of Applied Physics* (1982), vol. 21(4A): p. L183 (cit. on p. 30).

179. Kamo, M. et al.: ‘Diamond synthesis from gas phase in microwave plasma’. *Journal of Crystal Growth* (1983), vol. 62(3): pp. 642 –644 (cit. on p. 30).

180. Arnault, J.C. et al.: ‘Mechanisms of CVD diamond nucleation and growth on mechanically scratched Si(100) surfaces’. English. *The European Physical Journal B - Condensed Matter and Complex Systems* (1999), vol. 11(2): pp. 327–343 (cit. on p. 30).

181. Daenen, M. et al.: ‘Seeding, growth and characterization of nanocrystalline diamond films on various substrates’. *Phys Stat Sol* (2006), vol. (203): pp. 3005–3010 (cit. on p. 30).

182. Yugo, S. et al.: ‘Generation of diamond nuclei by electric field in plasma chemical vapor deposition’. *Applied Physics Letters* (1991), vol. 58(10): pp. 1036–1038 (cit. on pp. 30, 31).

183. Goodwin, D. G. et al.: ‘Theory of diamond vapor deposition’. *Handbook of industrial diamonds and diamond films, CRC Press* (1997), vol. (cit. on p. 31).

184. McMaster, M. C. et al.: ‘Dependence of the gas composition in a microwave plasma-assisted diamond chemical vapor deposition reactor on the inlet carbon source: {CH4} versus {C2H2}’. *Diamond and Related Materials* (1995), vol. 4(7): pp. 1000 –1008 (cit. on p. 31).

185. Celii, F. G. et al.: ‘Infrared detection of gaseous species during the filament-assisted growth of diamond’. *Applied Physics Letters* (1988), vol. 52(24): pp. 2043–2045 (cit. on p. 31).

186. Stoner, B. R. et al.: ‘Characterization of bias-enhanced nucleation of diamond on silicon by *invacuo* surface analysis and transmission electron microscopy’. *Phys. Rev. B* (19 1992), vol. 45: pp. 11067–11084 (cit. on p. 31).

187. Wolter, S. D. et al.: ‘Textured growth of diamond on silicon via in situ carburization and bias-enhanced nucleation’. *Applied Physics Letters* (1993), vol. 62(11): pp. 1215–1217 (cit. on p. 33).

188. Smith, E. et al.: ‘Modern Raman spectroscopy - A practical approach’. *John Wiley & Sons Ltd.* (2005), vol. (cit. on pp. 33, 75).

189. Prawer, S. et al.: ‘Raman spectroscopy of diamond and doped diamond’. *Philosophical Transactions of the Royal Society of London A: Mathematical, Physical and Engineering Sciences* (2004), vol. 362(1824): pp. 2537–2565 (cit. on p. 34).

190. Wagner, J. et al.: ‘Resonance effects in Raman scattering from polycrystalline diamond films’. *Applied Physics Letters* (1991), vol. 59(7): pp. 779–781 (cit. on pp. 34, 35).

191. Héber, C.: ‘Matrice de microélectrodes tout diamant et ccomposite diamant/nanotubes de ccarbon pour la neurophysiologie: du matériau aux composants d’inteface’. PhD thesis. IMEP2 and Insitut Néel, CNRS Grenoble, 2012 (cit. on p. 36).

192. Bernard, M. et al.: ‘About the origin of the low wave number structures of the Raman spectra of heavily boron doped diamond films’. *Diamond and Related Materials* (2004), vol. 13(4-8). 14th European Conference on Diamond, Diamond-Like Materials, Carbon Nanotubes, Nitrides and Silicon Carbide: pp. 896 –899 (cit. on p. 37).

193. Bernard, M. et al.: 'Non-destructive determination of the boron concentration of heavily doped metallic diamond thin films from Raman spectroscopy'. *Diamond and Related Materials* (2004), vol. 13(2): pp. 282 –286 (cit. on p. 37).

194. Pruvost, F. et al.: 'Characteristics of homoepitaxial heavily boron-doped diamond films from their Raman spectra'. *Diamond and Related Materials* (2000), vol. 9(3-6): pp. 295 –299 (cit. on p. 37).

195. Hébert, C.: 'Matrice de microélectrodes tout diamant et composites diamant/nanotubes de carbon pour la neurophysiologie: du matériau aux composants d'interface'. PhD thesis. Institut Néel, CNRS Grenoble, France, 2012 (cit. on p. 38).

196. Bruckenstein, S. et al.: 'Diffusion currents to (ultra) microelectrodes of various geometries - ellipsoids, spheroids and elliptical disks'. *Journal of Electroanalytical Chemistry* (2002), vol. 538: pp. 3–12 (cit. on p. 42).

197. Suzuki, A. et al.: 'Fabrication, characterization, and application of boron-doped diamond microelectrodes for in vivo dopamine detection'. *Analytical chemistry* (2007), vol. 79(22): pp. 8608–8615 (cit. on p. 42).

198. Prasek, J. et al.: 'Methods for carbon nanotubes synthesis-review'. *J. Mater. Chem.* (40 2011), vol. 21: pp. 15872–15884 (cit. on p. 43).

199. Nasibulin, A. G. et al.: 'Correlation between catalyst particle and single-walled carbon nanotube diameters'. *Carbon* (2005), vol. 43(11): pp. 2251 –2257 (cit. on p. 43).

200. Kumar, M.: 'Carbon nanotube synthesis and growth mechanism'. *Carbon Nanotubes - Synthesis, Characterization, Applications, Edited by Siva Yellampalli* (2011), vol. (cit. on p. 43).

201. Baughman, R. H. et al.: 'Carbon nanotubes - The route toward applications'. *Science* (2002), vol. 297(5582): pp. 787–792 (cit. on p. 43).

202. Li, H. J. et al.: 'Multichannel ballistic transport in multiwall carbon nanotubes'. *Phys. Rev. Lett.* (8 2005), vol. 95: p. 086601 (cit. on p. 45).

203. Li, W. et al.: 'Raman characterization of aligned carbon nanotubes produced by thermal decomposition of hydrocarbon vapor'. *Applied Physics Letters* (1997), vol. 70(20): pp. 2684–2686 (cit. on p. 45).

204. Cellot, G. et al.: 'Carbon nanotubes might improve neuronal performance by favouring electrical shortcuts'. *Nat Nano* (Feb. 2009), vol. 4(2): pp. 126–133 (cit. on p. 45).

205. Cellot G. Toma, F. M. et al.: 'Carbon nanotube scaffolds tune synaptic strength in cultured neural circuits: novel frontiers in nanomaterial–tissue interactions'. *The Journal of Neuroscience* (2011), vol. 31(36): pp. 12945–12953 (cit. on p. 45).

206. Martinelli, V. et al.: 'Carbon nanotubes promote growth and spontaneous electrical activity in cultured cardiac myocytes'. *Nano Letters* (2012), vol. 12(4): pp. 1831–1838 (cit. on p. 45).

207. Karlsson, H. L. et al.: 'Copper oxide nanoparticles are highly toxic: A comparison between metal oxide nanoparticles and carbon nanotubes'. *Chemical Research in Toxicology* (2008), vol. 21(9). PMID: 18710264: pp. 1726–1732 (cit. on p. 45).

208. Jia, G. et al.: 'Cytotoxicity of carbon nanomaterials: Single-wall nanotube, multi-wall nanotube, and fullerene'. *Environmental Science & Technology* (2005), vol. 39(5). PMID: 15787380: pp. 1378–1383 (cit. on p. 45).

209. Sze, S. M.: *Physics of semiconductor devices*. John Wiley & Sons, 1981 (cit. on pp. 47, 48, 58).

210. Jenkner, M. et al.: 'Bistability of membrane conductance in cell adhesion observed in a neuron transistor'. *Phys. Rev. Lett.* (23 1997), vol. 79: pp. 4705–4708 (cit. on pp. 50, 130).

211. Khodagholy, D. et al.: 'In vivo recordings of brain activity using organic transistors'. *Nat Commun* (Mar. 2013), vol. 4: p. 1575 (cit. on p. 51).

212. Khodagholy, D. et al.: ‘High transconductance organic electrochemical transistors’. *Nat Commun* (July 2013), vol. 4: p. 2133 (cit. on p. 51).

213. Sahni, D. et al.: ‘Biocompatibility of pristine graphene for neuronal interface: Laboratory investigation’. *Journal of Neurosurgery: Pediatrics* (2013), vol. 11(5): pp. 575–583 (cit. on pp. 51, 64, 111, 117).

214. Kim K. S.and Zhao, Y. et al.: ‘Large-scale pattern growth of graphene films for stretchable transparent electrodes’. *Nature* (Feb. 2009), vol. 457(7230): pp. 706–710 (cit. on pp. 51, 63, 69).

215. Bergveld, P.: ‘Development of an Ion-Sensitive Solid-State Device for Neurophysiological Measurements’. *Biomedical Engineering, IEEE Transactions on* (1970), vol. BME-17(1): pp. 70–71 (cit. on p. 53).

216. Cui, Y. et al.: ‘Functional nanoscale electronic devices assembled using silicon nanowire building blocks’. *Science* (2001), vol. 291(5505): pp. 851–853 (cit. on p. 53).

217. Chen, Y. et al.: ‘Silicon-based nanoelectronic field-effect pH sensor with local gate control’. *Applied Physics Letters* (2006), vol. 89(22), 223512: p. 223512 (cit. on p. 53).

218. Knopfmacher, O. et al.: ‘Nernst limit in dual-gated Si-nanowire FET sensors’. *Nano Letters* (2010), vol. 10(6). PMID: 20499926: pp. 2268–2274 (cit. on pp. 53, 60).

219. Luo, L. et al.: ‘Silicon nanowire sensors for Hg2+ and Cd2+ ions’. *Applied Physics Letters* (2009), vol. 94(19), 193101: p. 193101 (cit. on p. 53).

220. Zheng, G. et al.: ‘Multiplexed electrical detection of cancer markers with nanowire sensor arrays’. *Nat Biotech* (Oct. 2005), vol. 23(10): pp. 1294–1301 (cit. on p. 53).

221. Park, I. et al.: ‘Top-down fabricated silicon nanowire sensors for real-time chemical detection’. *Nanotechnology* (2010), vol. 21(1): p. 015501 (cit. on p. 53).

222. Gao, Z. et al.: ‘Silicon nanowire arrays folabel-f-free detection of DNA’. *Analytical Chemistry* (2007), vol. 79(9). PMID: 17407259: pp. 3291–3297 (cit. on p. 53).

223. Elfström, N. et al.: ‘Silicon nanoribbons for electrical detection of biomolecules’. *Nano Letters* (2008), vol. 8(3): pp. 945–949 (cit. on p. 53).

224. Mishra, N. N. et al.: ‘Ultra-sensitive detection of bacterial toxin with silicon nanowire transistor’. *Lab Chip* (6 2008), vol. 8: pp. 868–871 (cit. on p. 53).

225. Beyers, R. et al.: ‘Titanium disilicide formation on heavily doped silicon substrates’. *Journal of Applied Physics* (1987), vol. 61(11): pp. 5110–5117 (cit. on p. 56).

226. Wunnicke, O.: ‘Gate capacitance of back-gated nanowire field-effect transistors’. *Applied Physics Letters* (2006), vol. 89(8), 083102: p. 083102 (cit. on p. 59).

227. Khanal, D. R. et al.: ‘Gate coupling and charge distribution in nanowire field effect transistors’. *Nano Letters* (2007), vol. 7(9). PMID: 17718588: pp. 2778–2783 (cit. on p. 59).

228. Sekaric, L. et al.: ‘Size-dependent modulation of carrier mobility in top-down fabricated silicon nanowires’. *Applied Physics Letters* (2009), vol. 95(2): p. 023113 (cit. on p. 59).

229. Stern, E. et al.: ‘Label-free immunodetection with CMOS-compatible semiconducting nanowires’. *Nature* (2007), vol. 445(7127): pp. 519–522 (cit. on p. 59).

230. Borkovec, M. et al.: ‘Ionization Processes and Proton Binding in Polyprotic Systems: Small Molecules, Proteins, Interfaces, and Polyelectrolytes’. *Surface and Colloid Science, Vol. 16, Kluwer Academic, New York, ed. E. Matijevic* (2001), vol. (cit. on p. 60).

231. Timko, B. P. et al.: ‘Response to comment on "Detection, stimulation, and inhibition of neuronal signals with high-density nanowire transistor arrays"’. *Science* (2009), vol. 323(5920): p. 1429 (cit. on p. 61).

232. Cui, Y. et al.: ‘High performance silicon nanowire field effect transistors’. *Nano Letters* (2003), vol. 3(2): pp. 149–152 (cit. on p. 61).

233. Patolsky, F. et al.: ‘Electrical detection of single viruses’. *Proceedings of the National Academy of Sciences of the United States of America* (2004), vol. 101(39): pp. 14017–14022 (cit. on p. 61).

234. Cohen-Karni, T. et al.: ‘Flexible electrical recording from cells using nanowire transistor arrays’. *Proceedings of the National Academy of Sciences* (2009), vol. 106(18): pp. 7309–7313 (cit. on p. 61).

235. Pang, S. W. et al.: ‘Damage induced in Si by ion milling or reactive ion etching’. *Journal of Applied Physics* (1983), vol. 54(6): pp. 3272–3277 (cit. on p. 62).

236. Misra, D. et al.: ‘Electrical damage to silicon devices due to reactive ion etching’. *Semiconductor Science and Technology* (1990), vol. 5(3): p. 229 (cit. on p. 62).

237. Belkacem, A. et al.: ‘Electronic defects induced in silicon by SF6 plasma etching’. *Journal of Vacuum Science & Technology B* (1993), vol. 11(3): pp. 709–716 (cit. on p. 62).

238. Liu, Y. et al.: ‘Ideal rectangular cross-section Si-Fin channel double-gate MOSFETs fabricated using orientation-dependent wet etching’. *Electron Device Letters, IEEE* (2003), vol. 24(7): pp. 484–486 (cit. on p. 62).

239. Dankerl, M. et al.: ‘Graphenesolution-ggated field-effect transistor array for sensing applications’. *Advanced Functional Materials* (2010), vol. 20(18): pp. 3117–3124 (cit. on p. 64).

240. Li, N. et al.: ‘The promotion of neurite sprouting and outgrowth of mouse hippocampal cells in culture by graphene substrates’. *Biomaterials* (2011), vol. 32(35): pp. 9374 –9382 (cit. on pp. 64, 100, 111, 119).

241. Park, S. Y. et al.: ‘Enhanced differentiation of human neural stem cells into neurons on graphene’. *Advanced Materials* (2011), vol. 23(36): H263–H267 (cit. on pp. 64, 111).

242. Tang, M. et al.: ‘Enhancement of electrical signaling in neural networks on graphene films’. *Biomaterials* (2013), vol. 34(27): pp. 6402–6411 (cit. on pp. 64, 100, 111).

243. Mattei, T. A. et al.: ‘Technological developments and future perspectives on graphene-based metamaterials: a primer for neurosurgeons’. *Neurosurgery* (2014), vol. 74(5): pp. 499–516 (cit. on p. 64).

244. Rocha, C. G. et al.: ‘Tailoring the physical properties of graphene’. *Graphene: Synthesis and Applications* (2011), vol.: p. 1 (cit. on p. 64).

245. Castro Neto, A. H. et al.: ‘The electronic properties of graphene’. *Rev. Mod. Phys.* (1 2009), vol. 81: pp. 109–162 (cit. on pp. 65, 66).

246. Katsnelson, M. I.: ‘Graphene: carbon in two dimensions’. *Materials today* (2007), vol. 10(1): pp. 20–27 (cit. on p. 65).

247. Boukhvalov, D. W. et al.: ‘Hydrogen on graphene: Electronic structure, total energy, structural distortions and magnetism from first-principles calculations’. *Physical Review B* (2008), vol. 77(3): p. 035427 (cit. on p. 65).

248. Martin, J. et al.: ‘Observation of electron-hole puddles in graphene using a scanning single-electron transistor’. *Nat Phys* (Feb. 2008), vol. 4(2): pp. 144–148 (cit. on p. 66).

249. Novoselov, K. S. et al.: ‘Electric field effect in atomically thin carbon films’. *Science* (2004), vol. 306(5696): pp. 666–669 (cit. on pp. 66, 69).

250. Das Sarma, S. et al.: ‘Electronic transport in two-dimensional graphene’. *Rev. Mod. Phys.* (2 2011), vol. 83: pp. 407–470 (cit. on pp. 66, 67).

251. Xia, F. et al.: ‘The origins and limits of metal-graphene junction resistance’. *Nat. nano.* (2011), vol. 6(3): pp. 179–184 (cit. on p. 66).

252. Kim, S. et al.: ‘Realization of a high mobility dual-gated graphene field-effect transistor with Al2O3 dielectric’. *Applied Physics Letters* (2009), vol. 94(6), 062107: p. 062107 (cit. on p. 67).

253. Grahame, D. C.: ‘The electrical double layer and the theory of electrocapillarity.’ *Chemical Reviews* (1947), vol. 41(3). PMID: 18895519: pp. 441–501 (cit. on p. 67).

254. Ye, J. et al.: ‘Accessing the transport properties of graphene and its multilayers at high carrier density’. *Proceedings of the National Academy of Sciences* (2011), vol. 108(32): pp. 13002–13006 (cit. on p. 68).

255. Efetov, D. K. et al.: ‘Controlling Electron-Phonon Interactions in Graphene at Ultrahigh Carrier Densities’. *Phys. Rev. Lett.* (25 2010), vol. 105: p. 256805 (cit. on p. 68).

256. Viculis, L. M. et al.: ‘A chemical route to carbon nanoscrolls’. *Science* (2003), vol. 299(5611): p. 1361 (cit. on p. 69).

257. Allen, M. J. et al.: ‘Honeycomb Carbon: A Review of Graphene’. *Chemical Reviews* (2010), vol. 110(1). PMID: 19610631: pp. 132–145 (cit. on p. 69).

258. Park, S. et al.: ‘Chemical methods for the production of graphenes’. *Nat Nano* (Apr. 2009), vol. 4(4): pp. 217–224 (cit. on p. 69).

259. Reina, A. et al.: ‘Large area, few-layer graphene films on arbitrary substrates by chemical vapor deposition’. *Nano Letters* (2009), vol. 9(1). PMID: 19046078: pp. 30–35 (cit. on pp. 69, 70).

260. Novoselov, K. S. et al.: ‘A roadmap for graphene’. *Nature* (Oct. 2012), vol. 490(7419): pp. 192–200 (cit. on p. 69).

261. Lang, B.: ‘A LEED study of the deposition of carbon on platinum crystal surfaces’. *Surface Science* (1975), vol. 53(1): pp. 317 –329 (cit. on p. 69).

262. Eizenberg, M. et al.: ‘Carbon monolayer phase condensation on Ni(111)’. *Surface Science* (1979), vol. 82(1): pp. 228 –236 (cit. on p. 69).

263. Obraztsov, A. N. et al.: ‘Chemical vapor deposition of thin graphite films of nanometer thickness’. *Carbon* (2007), vol. 45(10): pp. 2017 –2021 (cit. on p. 69).

264. Yu, Q. et al.: ‘Graphene segregated on Ni surfaces and transferred to insulators’. *Applied Physics Letters* (2008), vol. 93(11), 113103: p. 113103 (cit. on p. 69).

265. McLellan, R. B.: ‘The solubility of carbon in solid gold, copper, and silver’. *Scripta Metallurgica* (June 1969), vol. 3(6): pp. 389–391 (cit. on p. 69).

266. Han, Zheng (Vitto): ‘Macroscopic CVD graphene for nnanoelectronic: from growth to proximity induced 2D superconductivity’. PhD thesis. Insitut Néel, CNRS Grenoble, France, 2013 (cit. on pp. 70–72, 79, 139).

267. Han, Z. et al.: ‘Homogeneous optical and electronic properties of graphene due to the suppression of multilayer patches during CVD on copper foils’. *Advanced Functional Materials* (2014), vol. 24(7): pp. 964–970 (cit. on pp. 70, 71, 89, 115).

268. Liu, M. et al.: ‘A graphene-based broadband optical modulator’. *Nature* (June 2011), vol. 474(7349): pp. 64–67 (cit. on p. 71).

269. Zande, A. M. van der et al.: ‘Large-scale arrays of single-layer graphene resonators’. *Nano Letters* (2010), vol. 10(12). PMID: 21080681: pp. 4869–4873 (cit. on p. 71).

270. Kim, B. J. et al.: ‘High-performance flexible graphene field effect transistors with ion gel gate dielectrics’. *Nano Letters* (2010), vol. 10(9). PMID: 20704323: pp. 3464–3466 (cit. on p. 71).

271. Chung, C. et al.: ‘Biomedical applications of graphene and graphene oxide’. *Accounts of chemical research* (2013), vol. 46(10): pp. 2211–2224 (cit. on p. 71).

272. Nguyen, P. et al.: ‘Graphene interfaced with biological cells: opportunities and challenges’. *The Journal of Physical Chemistry Letters* (2012), vol. 3(8): pp. 1024–1029 (cit. on p. 71).

273. Kalita, D.: ‘Graphene produced by CVD: from control and understanding of atomic scale defects to production of macroscale functional devices’. PhD thesis. Insitut Néel, CNRS Grenoble, France, 2015 (cit. on p. 73).

274. Malard, L. M. et al.: ‘Raman spectroscopy in graphene’. *Physics Reports* (2009), vol. 473(5-6): pp. 51 –87 (cit. on pp. 75–77).

275. Cancado, L. G. et al.: ‘Quantifying Defects in Graphene via Raman Spectroscopy at Different Excitation Energies’. *Nano Letters* (2011), vol. 11(8). PMID: 21696186: pp. 3190–3196 (cit. on pp. 75, 78).

276. Niyogi, S. et al.: ‘Spectroscopy of covalently functionalized graphene’. *Nano Letters* (2010), vol. 10(10). PMID: 20738114: pp. 4061–4066 (cit. on p. 75).

277. Casiraghi, C. et al.: ‘Raman fingerprint of charged impurities in graphene’. *Applied Physics Letters* (2007), vol. 91(23), 233108: p. 233108 (cit. on pp. 75, 77).

278. You, Y-M. et al.: ‘Edge chirality determination of graphene by Raman spectroscopy’. *Applied Physics Letters* (2008), vol. 93(16), 163112: p. 163112 (cit. on p. 75).

279. Gupta, A. K. et al.: ‘Probing graphene edges via raman scattering’. *ACS Nano* (2009), vol. 3(1): pp. 45–52 (cit. on p. 75).

280. Huang, M. et al.: ‘Probin strain-induced electronic structure change in graphene by raman spectroscopy’. *Nano Letters* (2010), vol. 10(10). PMID: 20735024: pp. 4074–4079 (cit. on p. 75).

281. Mohiuddin, T. M. G. et al.: ‘Uniaxial strain in graphene by Raman spectroscopy: G’ peak splitting, Grüneisen parameters, and sample orientation’. *Phys. Rev. B* (20 2009), vol. 79: p. 205433 (cit. on pp. 75, 77).

282. Venezuela, P. et al.: ‘Theory of double-resonant Raman spectra in graphene: Intensity and line shape of defect-induced and two-phonon bands’. *Phys. Rev. B* (3 2011), vol. 84: p. 035433 (cit. on p. 75).

283. Ni, Z. H. et al.: ‘On resonant scatterers as a factor limiting carrier mobility in graphene’. *Nano Letters* (2010), vol. 10(10). PMID: 20795655: pp. 3868–3872 (cit. on p. 75).

284. Gokus, T. et al.: ‘Making graphene luminescent by oxygen plasma treatment’. *ACS Nano* (2009), vol. 3(12). PMID: 19925014: pp. 3963–3968 (cit. on p. 75).

285. Elias, D. C. et al.: ‘Control of graphene’s properties by reversible hydrogenation: Evidence for graphane’. *Science* (2009), vol. 323(5914): pp. 610–613 (cit. on p. 75).

286. Ferrari A. C. and. Basko, D. M: ‘Raman spectroscopy as a versatile tool for studying the properties of graphene’. *Nat Nano* (Apr. 2013), vol. 8(4): pp. 235–246 (cit. on p. 76).

287. Beams, R. et al.: ‘Raman characterization of defects and dopants in graphene’. *Journal of Physics: Condensed Matter* (2015), vol. 27(8): p. 083002 (cit. on pp. 76, 77).

288. Tuinstra, F. et al.: ‘Raman spectrum of graphite’. *The Journal of Chemical Physics* (1970), vol. 53(3): pp. 1126–1130 (cit. on p. 77).

289. Lee, J. E. et al.: ‘Optical separation of mechanical strain from charge doping in graphene’. *Nat Commun* (Aug. 2012), vol. 3: p. 1024 (cit. on pp. 77, 114, 117, 118).

290. Calizo, I. et al.: ‘Temperature dependence of the raman spectra of graphene and graphene multilayers’. *Nano Letters* (2007), vol. 7(9). PMID: 17718584: pp. 2645–2649 (cit. on p. 77).

291. Graf, D. et al.: ‘Spatially resolved raman spectroscopy of single- and few-layer graphene’. *Nano Letters* (2007), vol. 7(2). PMID: 17297984: pp. 238–242 (cit. on pp. 77, 79, 116).

292. Ferrari, A. C. et al.: ‘Raman spectrum of graphene and graphene layers’. *Phys. Rev. Lett.* (18 2006), vol. 97: p. 187401 (cit. on p. 77).

293. Cancado, L. G. et al.: ‘Geometrical approach for the study of G’ band in the Raman spectrum of monolayer graphene, bilayer graphene, and bulk graphite’. *Phys. Rev. B* (24 2008), vol. 77: p. 245408 (cit. on p. 77).

294. Eckmann, A. et al.: ‘Probing the nature of defects in graphene by raman spectroscopy’. *Nano Letters* (2012), vol. 12(8). PMID: 22764888: pp. 3925–3930 (cit. on p. 78).

295. Casiraghi, C. et al.: ‘Raman spectroscopy of graphene edges’. *Nano Letters* (2009), vol. 9(4). PMID: 19290608: pp. 1433–1441 (cit. on p. 78).

296. Nagashio, K. et al.: ‘Contact resistivity and current flow path at metal/graphene contact’. *Applied Physics Letters* (2010), vol. 97(14), 143514: p. 143514 (cit. on p. 83).

297. Huang, B-C. et al.: ‘Contact resistance in top-gated graphene field-effect transistors’. *Applied Physics Letters* (2011), vol. 99(3), 032107: p. 032107 (cit. on p. 83).

298. Song, S. M. et al.: ‘Determination of work function of graphene under a metal electrode and its role in contact resistance’. *Nano letters* (2012), vol. 12(8): pp. 3887–3892 (cit. on p. 84).

299. Hess, L. H. et al.: ‘Graphene transistors for bioelectronics’. *Proceedings of the IEEE* (2013), vol. 101(7): pp. 1780–1792 (cit. on pp. 88, 93, 142).

300. Handel, P. H.: ‘Fundamental quantum 1/f noise in semiconductor devices’. *Electron Devices, IEEE Transactions on* (1994), vol. 41(11): pp. 2023–2033 (cit. on p. 93).

301. Lin, Y-M. et al.: ‘Strong suppression of electrical noise in bilayer graphene nanodevices’. *Nano Letters* (2008), vol. 8(8). PMID: 18298094: pp. 2119–2125 (cit. on p. 93).

302. Liu, G. et al.: ‘Low-frequency electronic noise in the double-gate single-layer graphene transistors’. *Applied Physics Letters* (2009), vol. 95(3), 033103: p. 033103 (cit. on p. 93).

303. Xu, G. et al.: ‘Effect of spatial charge inhomogeneity on 1/f noise behavior in graphene’. *Nano Letters* (2010), vol. 10(9). PMID: 20684526: pp. 3312–3317 (cit. on p. 93).

304. Heller, I. et al.: ‘Charge noise in graphene transistors’. *Nano Letters* (2010), vol. 10(5). PMID: 20373788: pp. 1563–1567 (cit. on p. 93).

305. Imam, S.A. et al.: ‘Low-frequency noise and hysteresis in graphene field-effect transistors on oxide’. English. *Micro & Nano Letters* (1 2010), vol. 5: 37–41(4) (cit. on p. 93).

306. Balandin, A. A.: ‘Low-frequency 1/f noise in graphene devices’. *Nat Nano* (Aug. 2013), vol. 8(8): pp. 549–555 (cit. on p. 93).

307. Hung, K. K. et al.: ‘A unified model for the flicker noise in metal-oxide-semiconductor field-effect transistors’. *Electron Devices, IEEE Transactions on* (1990), vol. 37(3): pp. 654–665 (cit. on p. 93).

308. Rumyantsev, S. et al.: ‘Electrical and noise characteristics of graphene field-effect transistors: ambient effects, noise sources and physical mechanisms’. *Journal of Physics: Condensed Matter* (2010), vol. 22(39): p. 395302 (cit. on p. 93).

309. Shao, Q. et al.: ‘Flicker noise in bilayer graphene transistors’. *Electron Device Letters, IEEE* (2009), vol. 30(3): pp. 288–290 (cit. on p. 93).

310. Kaverzin, A. A. et al.: ‘Impurities as a source of 1/f noise in graphene’. *Phys. Rev. B* (7 2012), vol. 85: p. 075435 (cit. on p. 93).

311. Rumyantsev, S. et al.: ‘Low-frequency noise in graphene field-effect transistors’. *Noise and Fluctuations (ICNF), 2011 21st International Conference on.* 2011: pp. 234–237 (cit. on p. 93).

312. Farmer, D. B. et al.: ‘Chemical doping and electron-hole conduction asymmetry in graphene devices’. *Nano Letters* (2009), vol. 9(1): pp. 388–392 (cit. on p. 94).

313. Seliktar, D.: ‘Designing cell-compatible hydrogels for biomedical applications’. *Science* (2012), vol. 336(6085): pp. 1124–1128 (cit. on p. 95).

314. Vigetti, D. et al.: ‘Hyaluronan: Biosynthesis and signaling’. *Biochimica et Biophysica Acta (BBA) - General Subjects* (2014), vol. 1840(8). Matrix-mediated cell behaviour and properties: pp. 2452 –2459 (cit. on p. 95).

315. Burdick, J. A. et al.: ‘Hyaluronic acid hydrogels for biomedical applications’. *Advanced materials* (2011), vol. 23(12): H41–H56 (cit. on p. 95).

316. Seidlits, S. K. et al.: ‘The effects of hyaluronic acid hydrogels with tunable mechanical properties on neural progenitor cell differentiation’. *Biomaterials* (2010), vol. 31(14): pp. 3930–3940 (cit. on p. 95).

317. Baier Leach, J. et al.: 'Photocrosslinked hyaluronic acid hydrogels: Natural, biodegradable tissue engineering scaffolds'. *Biotechnology and Bioengineering* (2003), vol. 82(5): pp. 578–589 (cit. on p. 95).

318. Patterson, J. et al.: 'Hyaluronic acid hydrogels with controlled degradation properties for oriented bone regeneration'. *Biomaterials* (2010), vol. 31(26): pp. 6772 –6781 (cit. on p. 95).

319. Laurent, T. S. et al.: 'Hyaluronan.' *The FASEB Journal* (1992), vol. 6(7): pp. 2397–2404 (cit. on p. 95).

320. Di Bartolomeo, A. et al.: 'Charge transfer and partial pinning at the contacts as the origin of a double dip in the transfer characteristics of graphene-based field-effect transistors'. *Nanotechnology* (2011), vol. 22(27): p. 275702 (cit. on p. 95).

321. Merz, M.: 'Topologically defined neuronal networks controlled by silicon chips'. PhD thesis. Technische Universität München, Max-Plank-Institut für Biochemie, 2003 (cit. on p. 97).

322. Miller, K. J. et al.: 'Direct electrophysiological measurement of human default network areas'. *Proceedings of the National Academy of Sciences* (2009), vol. 106(29): pp. 12174–12177 (cit. on p. 99).

323. Viventi, J. et al.: 'Flexible, foldable, actively multiplexed, high-density electrode array for mapping brain activity in vivo'. *Nat Neurosci* (Dec. 2011), vol. 14(12): pp. 1599–1605 (cit. on p. 99).

324. Crone, N. E. et al.: 'High-frequency gamma oscillations and human brain mapping with electrocorticography'. *Event-Related Dynamics of Brain Oscillations*. Ed. by Neuper, Christa et al. Vol. 159. Progress in Brain Research. Elsevier, 2006: pp. 275 –295 (cit. on p. 99).

325. Ball, T. et al.: 'Movement related activity in the high gamma range of the human EEG'. *NeuroImage* (2008), vol. 41(2): pp. 302 –310 (cit. on p. 99).

326. Wang, W. et al.: 'Human motor cortical activity recorded with Micro-ECoG electrodes, during individual finger movements'. *Engineering in Medicine and Biology Society, 2009. EMBC 2009. Annual International Conference of the IEEE.* 2009: pp. 586–589 (cit. on p. 99).

327. Towle, V. L. et al.: 'ECoG gamma activity during a language task: differentiating expressive and receptive speech areas'. *Brain* (2008), vol. 131(8): pp. 2013–2027 (cit. on p. 99).

328. Keller, C. J. et al.: 'Heterogeneous neuronal firing patterns during interictal epileptiform discharges in the human cortex'. *Brain* (2010), vol. 133(6): pp. 1668–1681 (cit. on p. 99).

329. Truccolo, W. et al.: 'Single-neuron dynamics in human focal epilepsy'. *Nat Neurosci* (May 2011), vol. 14(5): pp. 635–641 (cit. on p. 99).

330. Burgess, N. et al.: 'A model of hippocampal function'. *Neural networks* (1994), vol. 7(6): pp. 1065–1081 (cit. on p. 100).

331. Eichenbaum, H. et al.: 'The hippocampus, memory, and place cells: is it spatial memory or a memory space?' *Neuron* (1999), vol. 23(2): pp. 209–226 (cit. on p. 100).

332. O'Reilly, R. C. et al.: 'Conjunctive representations in learning and memory: principles of cortical and hippocampal function.' *Psychological review* (2001), vol. 108(2): p. 311 (cit. on p. 100).

333. Morris, R. G. M. et al.: 'Place navigation impaired in rats with hippocampal lesions'. *Nature* (1982), vol. 297(5868): pp. 681–683 (cit. on p. 100).

334. Iaria, G. et al.: 'Cognitive strategies dependent on the hippocampus and caudate nucleus in human navigation: variability and change with practice'. *The journal of neuroscience* (2003), vol. 23(13): pp. 5945–5952 (cit. on p. 100).

335. West, M. J. et al.: 'Differences in the pattern of hippocampal neuronal loss in normal ageing and Alzheimer's disease'. *The Lancet* (1994), vol. 344(8925): pp. 769–772 (cit. on p. 100).

336. Jin, K. et al.: 'Increased hippocampal neurogenesis in Alzheimer's disease'. *Proceedings of the National Academy of Sciences* (2004), vol. 101(1): pp. 343–347 (cit. on p. 100).

337. Gloveli, T. et al.: ‘Neuronal activity patterns during hippocampal network oscillations in vitro’. *Hippocampal Microcircuits*. Springer, 2010: pp. 247–276 (cit. on p. 100).

338. Nave, K-A.: ‘Myelination and support of axonal integrity by glia’. *Nature* (2010), vol. 468(7321): pp. 244–252 (cit. on p. 100).

339. Deitmer, J. W.: ‘Strategies for metabolic exchange between glial cells and neurons’. *Respiration Physiology* (2001), vol. 129(1-2): pp. 71 –81 (cit. on p. 100).

340. Barres, B. A.: ‘The mystery and magic of glia: A perspective on their roles in health and disease’. *Neuron* (2008), vol. 60(3): pp. 430–440 (cit. on pp. 100, 101).

341. Pfrieger, F. W.: ‘Role of glia in synapse development’. *Current Opinion in Neurobiology* (2002), vol. 12(5): pp. 486 –490 (cit. on p. 100).

342. Ullian, E. M. et al.: ‘Role for glia in synaptogenesis’. *Glia* (2004), vol. 47(3): pp. 209–216 (cit. on pp. 100, 101).

343. Teng, Y. D. et al.: ‘Functional recovery following traumatic spinal cord injury mediated by a unique polymer scaffold seeded with neural stem cells’. *Proceedings of the National Academy of Sciences* (2002), vol. 99(5): pp. 3024–3029 (cit. on p. 100).

344. Jun, S. B. et al.: ‘Low-density neuronal networks cultured using patterned poly-l-lysine on microelectrode arrays’. *Journal of Neuroscience Methods* (2007), vol. 160(2): pp. 317 –326 (cit. on p. 100).

345. Geiger, B. et al.: ‘Environmental sensing through focal adhesions’. *Nature reviews Molecular cell biology* (2009), vol. 10(1): pp. 21–33 (cit. on pp. 100, 106).

346. Bugnicourt, G. et al.: ‘Nanoscale surface topography reshapes neuronal growth in culture’. *Langmuir* (2014), vol. 30(15): pp. 4441–4449 (cit. on pp. 100, 106).

347. Xie, C. et al.: ‘Noninvasive neuron pinning with nanopillar arrays’. *Nano letters* (2010), vol. 10(10): pp. 4020–4024 (cit. on p. 100).

348. Teixeira, A. I. et al.: ‘The promotion of neuronal maturation on soft substrates’. *Biomaterials* (2009), vol. 30(27): pp. 4567–4572 (cit. on p. 100).

349. Koh, H.S. et al.: ‘Enhancement of neurite outgrowth using nano-structured scaffolds coupled with laminin’. *Biomaterials* (2008), vol. 29(26): pp. 3574 –3582 (cit. on p. 100).

350. Hogan, B. et al.: *Manipulating the mouse embryo: a laboratory manual*. Vol. 34. Cold spring harbor laboratory Cold Spring Harbor, NY, 1986 (cit. on p. 100).

351. Beaudoin, G. M. J. et al.: ‘Culturing pyramidal neurons from the early postnatal mouse hippocampus and cortex’. *Nat. Protocols* (Sept. 2012), vol. 7(9): pp. 1741–1754 (cit. on p. 101).

352. Kaech, S. et al.: ‘Culturing hippocampal neurons’. *Nat. Protocols* (Dec. 2006), vol. 1(5): pp. 2406–2415 (cit. on p. 101).

353. Hughes, E. G. et al.: ‘Astrocyte secreted proteins selectively increase hippocampal GABAergic axon length, branching, and synaptogenesis’. *Molecular and Cellular Neuroscience* (Jan. 2010), vol. 43(1): pp. 136–145 (cit. on p. 101).

354. Hu, R. et al.: ‘Astrocyte-derived estrogen enhances synapse formation and synaptic transmission between cultured neonatal rat cortical neurons’. *Neuroscience* (2007), vol. 144(4): pp. 1229 –1240 (cit. on p. 101).

355. Christopherson, K. S. et al.: ‘Thrombospondins are astrocyte-secreted proteins that promote CNS synaptogenesis’. *Cell* (2005), vol. 120(3): pp. 421–433 (cit. on p. 101).

356. Boehler, M. D. et al.: ‘Added astroglia promote greater synapse density and higher activity in neuronal networks’. *Neuron glia biology* (2007), vol. 3(02): pp. 127–140 (cit. on p. 101).

357. Giepmans, B. N. G. et al.: ‘The fluorescent toolbox for assessing protein location and function’. *Science* (2006), vol. 312(5771): pp. 217–224 (cit. on p. 102).

358. Huang, B. et al.: ‘Breaking the diffraction barrier: Super-Resolution imaging of cells’. *Cell* (2010), vol. 143(7): pp. 1047 –1058 (cit. on p. 102).

359. Kane, Ravi S et al.: ‘Patterning proteins and cells using soft lithography’. *Biomaterials* (1999), vol. 20(23): pp. 2363–2376 (cit. on p. 103).

360. Nam, Y. et al.: ‘Epoxy-silane linking of biomolecules is simple and effective for patterning neuronal cultures’. *Biosensors and bioelectronics* (2006), vol. 22(5): pp. 589–597 (cit. on pp. 103, 104, 118).

361. Erickson, J. et al.: ‘Caged neuron MEA: A system for long-term investigation of cultured neural network connectivity’. *Journal of neuroscience methods* (2008), vol. 175(1): pp. 1–16 (cit. on p. 103).

362. Xie, C. et al.: ‘Noninvasive neuron pinning with nanopillar arrays’. *Nano letters* (2010), vol. 10(10): pp. 4020–4024 (cit. on p. 103).

363. Tomba, C. et al.: ‘Tuning the adhesive geometry of neurons: length and polarity control’. *Soft matter* (2014), vol. 10(14): pp. 2381–2387 (cit. on p. 104).

364. Hardelauf, H. et al.: ‘High fidelity neuronal networks formed by plasma masking with a bilayer membrane: analysis of neurodegenerative and neuroprotective processes’. *Lab Chip* (16 2011), vol. 11: pp. 2763–2771 (cit. on pp. 104, 118).

365. Chang, J. C. et al.: ‘Modulation of neural network activity by patterning’. *Biosensors and Bioelectronics* (2001), vol. 16(7): pp. 527–533 (cit. on pp. 105, 128).

366. Rutten W. L. C.and Ruardij, T. G. et al.: ‘Cultured neural networks: optimization of patterned network adhesiveness and characterization of their neural activity’. *Applied Bionics and Biomechanics* (2006), vol. 3(1): pp. 1–7 (cit. on pp. 105, 128).

367. Flanagan, L. A. et al.: ‘Neurite branching on deformable substrates’. *Neuroreport* (2002), vol. 13(18): p. 2411 (cit. on pp. 106, 110, 114).

368. Smith, D. H.: ‘Stretch growth of integrated axon tracts: Extremes and exploitations’. *Progress in Neurobiology* (2009), vol. 89(3): pp. 231 –239 (cit. on p. 106).

369. Lamoureux, P. et al.: ‘Mechanical tension can specify axonal fate in hippocampal neurons’. *The Journal of cell biology* (2002), vol. 159(3): pp. 499–508 (cit. on p. 106).

370. Dadsetan, M. et al.: ‘Stimulation of neurite outgrowth using positively charged hydrogels’. *Biomaterials* (2009), vol. 30(23-24): pp. 3874 –3881 (cit. on pp. 106, 114).

371. Fromherz, P.: ‘Semiconductor chips with ion channels, nerve cells and brain’. *Physica E: low-dimensional systems and nanostructures* (2003), vol. 16(1): pp. 24–34 (cit. on pp. 107, 130).

372. Blau, A.: ‘Cell adhesion promotion strategies for signal transduction enhancement in microelectrode array in vitro electrophysiology: an introductory overview and critical discussion’. *Current Opinion in Colloid & Interface Science* (2013), vol. 18(5): pp. 481–492 (cit. on p. 107).

373. Braun, D. et al.: ‘Fluorescence interferometry of neuronal cell adhesion on microstructured silicon’. *Phys. Rev. Lett.* (23 1998), vol. 81: pp. 5241–5244 (cit. on p. 107).

374. Amaral, M. et al.: ‘Cytotoxicity evaluation of nanocrystalline diamond coatings by fibroblast cell cultures’. *Acta biomaterialia* (2009), vol. 5(2): pp. 755–763 (cit. on p. 108).

375. Klauser, F. et al.: ‘Direct and Protein-Mediated Cell Attachment on Differently Terminated Nanocrystalline Diamond’. *Chemical Vapor Deposition* (2010), vol. 16(1-3): pp. 42–49 (cit. on p. 108).

376. Bendali, A. et al.: ‘Distinctive Glial and Neuronal Interfacing on Nanocrystalline Diamond’. *PLoS ONE* (Mar. 2014), vol. 9(3): e92562 (cit. on p. 108).

377. Thalhammer, A. et al.: ‘The use of nanodiamond monolayer coatings to promote the formation of functional neuronal networks’. *Biomaterials* (2010), vol. 31(8): pp. 2097 –2104 (cit. on pp. 108, 117).

378. Edgington, R. J. et al.: ‘Patterned neuronal networks using nanodiamonds and the effect of varying nanodiamond properties on neuronal adhesion and outgrowth’. *Journal of neural engineering* (2013), vol. 10(5): p. 056022 (cit. on pp. 108, 110).

379. Ojovan, S. M. et al.: ‘Nanocrystalline diamond surfaces for adhesion and growth of primary neurons, conflicting results and rational explanation’. *Frontiers in neuroengineering* (2014), vol. 7 (cit. on pp. 108, 175).

380. Tessier-Lavigne, M. et al.: ‘The molecular biology of axon guidance’. *Science* (1996), vol. 274(5290): pp. 1123–1133 (cit. on p. 110).

381. Franze, K. et al.: ‘Neurite branch retraction is caused by a threshold-dependent mechanical impact’. *Biophysical journal* (2009), vol. 97(7): pp. 1883–1890 (cit. on pp. 110, 114).

382. Dotti, C. G. et al.: ‘The establishment of polarity by hippocampal neurons in culture’. *The Journal of neuroscience* (1988), vol. 8(4): pp. 1454–1468 (cit. on pp. 111, 113).

383. Sun, Y. et al.: ‘Surface coating as a key parameter in engineering neuronal network structures in vitro’. *Biointerphases* (2012), vol. 7(1): p. 29 (cit. on p. 113).

384. Lo, C-M. et al.: ‘Cell movement is guided by the rigidity of the substrate’. *Biophysical journal* (2000), vol. 79(1): pp. 144–152 (cit. on p. 114).

385. Leach, J. B. et al.: ‘Neurite outgrowth and branching of PC12 cells on very soft substrates sharply decreases below a threshold of substrate rigidity’. *Journal of neural engineering* (2007), vol. 4(2): p. 26 (cit. on p. 114).

386. Arulmoli, J. et al.: ‘Static stretch affects neural stem cell differentiation in an extracellular matrix-dependent manner’. *Scientific reports* (2015), vol. 5 (cit. on p. 114).

387. Gilles, S. et al.: ‘Control of cell adhesion and neurite outgrowth by patterned gold nanoparticles with tunable attractive or repulsive surface properties’. *Small* (2012), vol. 8(21): pp. 3357–3367 (cit. on p. 114).

388. Tu, Q. et al.: ‘Effects of surface charges of graphene oxide on neuronal outgrowth and branching’. *Analyst* (2014), vol. 139(1): pp. 105–115 (cit. on pp. 114, 118).

389. Freudiger, C. W. et al.: ‘Label-free biomedical imaging with high sensitivity by stimulated Raman scattering microscopy’. *Science* (2008), vol. 322(5909): pp. 1857–1861 (cit. on p. 116).

390. Matthäus, C. et al.: ‘Infrared and Raman microscopy in cell biology’. *Methods in cell biology* (2008), vol. 89: pp. 275–308 (cit. on p. 116).

391. Shein, M. et al.: ‘Engineered neuronal circuits shaped and interfaced with carbon nanotube microelectrode arrays’. *Biomedical microdevices* (2009), vol. 11(2): pp. 495–501 (cit. on p. 117).

392. Lovat, V. et al.: ‘Carbon nanotube substrates boost neuronal electrical signaling’. *Nano letters* (2005), vol. 5(6): pp. 1107–1110 (cit. on p. 117).

393. Das, A. et al.: ‘Monitoring dopants by Raman scattering in an electrochemically top-gated graphene transistor’. *Nature nanotechnology* (2008), vol. 3(4): pp. 210–215 (cit. on p. 118).

394. Banhart, F. et al.: ‘Structural defects in graphene’. *ACS nano* (2010), vol. 5(1): pp. 26–41 (cit. on p. 118).

395. Fletcher, T. L. et al.: ‘The distribution of synapsin I and synaptophysin in hippocampal neurons developing in culture’. *The Journal of Neuroscience* (1991), vol. 11(6): pp. 1617–1626 (cit. on p. 122).

396. Berliocchi, L. et al.: ‘Botulinum neurotoxin C initiates two different programs for neurite degeneration and neuronal apoptosis’. *The Journal of Cell Biology* (2005), vol. 168(4): pp. 607–618 (cit. on p. 122).

397. Xu, F. et al.: ‘Silver nanoparticles (AgNPs) cause degeneration of cytoskeleton and disrupt synaptic machinery of cultured cortical neurons’. *Molecular Brain* (2013), vol. 6(1): p. 29 (cit. on p. 122).

398. Perkins, K. L.: ‘Cell-attached voltage-clamp and current-clamp recording and stimulation techniques in brain slices’. *Journal of Neuroscience Methods* (2006), vol. 154(1 - 2): pp. 1 –18 (cit. on pp. 123, 124).

399. Ebashi, S. et al.: ‘Calcium and muscle contraction’. *Progress in Biophysics and Molecular Biology* (1968), vol. 18: pp. 123 –183 (cit. on p. 124).

400. Zhou, B. et al.: ‘Epicardial progenitors contribute to the cardiomyocyte lineage in the developing heart’. *Nature* (July 2008), vol. 454(7200): pp. 109–113 (cit. on p. 124).

401. Jouaville, L. S. et al.: ‘Regulation of mitochondrial ATP synthesis by calcium: Evidence for a long-term metabolic priming’. *Proceedings of the National Academy of Sciences* (1999), vol. 96(24): pp. 13807–13812 (cit. on p. 124).

402. Neher, E. et al.: ‘Multiple roles of calcium ions in the regulation of neurotransmitter release’. *Neuron* (2008), vol. 59(6): pp. 861 –872 (cit. on p. 124).

403. Zucker, R. S.: ‘Calcium- and activity-dependent synaptic plasticity’. *Current Opinion in Neurobiology* (1999), vol. 9(3): pp. 305 –313 (cit. on p. 124).

404. Ferragamo, M. J. et al.: ‘Ca2+ dependent, stimulus-specific modulation of the plasma membrane Ca2+ pump in hippocampal neurons’. *Journal of Neurophysiology* (2009), vol. 101(5): pp. 2563–2571 (cit. on pp. 124, 125).

405. Hallworth, N. E. et al.: ‘Apamin-sensitive small conductance calcium-activated potassium channels, through their selective coupling to voltage-gated calcium channels, are critical determinants of the precision, pace, and pattern of action potential generation in rat subthalamic nucleus neurons in vitro’. *The Journal of Neuroscience* (2003), vol. 23(20): pp. 7525–7542 (cit. on p. 124).

406. Gee, K. R. et al.: ‘Chemical and physiological characterization of fluo-4 Ca2+-indicator dyes’. *Cell Calcium* (2000), vol. 27(2): pp. 97 –106 (cit. on p. 124).

407. Gu, X. et al.: ‘Spontaneous neuronal calcium spikes and waves during early differentiation’. *The Journal of Neuroscience* (1994), vol. 14(11): pp. 6325–6335 (cit. on p. 125).

408. Dejean, C. et al.: ‘Synchronous high-voltage spindles in the cortex–basal ganglia network of awake and unrestrained rats’. *European Journal of Neuroscience* (2007), vol. 25(3): pp. 772–784 (cit. on p. 127).

409. Dejean, C. et al.: ‘Dynamic changes in the cortex-basal ganglia network after dopamine depletion in the rat’. *Journal of Neurophysiology* (2008), vol. 100(1): pp. 385–396 (cit. on p. 127).

410. Hai, A. et al.: ‘Long-term, multisite, parallel, in-cell recording and stimulation by an array of extracellular microelectrodes’. *Journal of neurophysiology* (2010), vol. 104(1): pp. 559–568 (cit. on p. 130).

411. Wen, L. et al.: ‘Neuregulin 1 regulates pyramidal neuron activity via ErbB4 in parvalbumin-positive interneurons’. *Proceedings of the National Academy of Sciences* (2010), vol. 107(3): pp. 1211–1216 (cit. on p. 131).

412. Somogyl, P.: ‘Synchronization of neuronal activity in hippocampus by individual GABAergic interneurons’. *Nature* (1995), vol. 378: p. 2 (cit. on p. 131).

413. Jung, H-Y. et al.: ‘Prolonged sodium channel inactivation contributes to dendritic action potential attenuation in hippocampal pyramidal neurons’. *The Journal of Neuroscience* (1997), vol. 17(17): pp. 6639–6646 (cit. on p. 131).

414. Colbert, C. M. et al.: ‘Slow recovery from inactivation of Na+ channels underlies theactivity-dependent attenuation ofdendritic action potentials in hippocampal CA1 pyramidal neurons’. *The Journal of Neuroscience* (1997), vol. 17(17): pp. 6512–6521 (cit. on p. 131).

415. Lorenzoni, M. et al.: ‘Simple and effective graphene laser processing for neuron patterning application’. *Scientific reports* (2013), vol. 3 (cit. on p. 132).

416. Ghibaudo, G. et al.: 'Electrical noise and RTS fluctuations in advanced CMOS devices'. *Microelectronics Reliability* (2002), vol. 42(4-5): pp. 573 –582 (cit. on p. 132).

417. Li, J. et al.: 'Sensitivity enhancement of Si nanowire field effect transistor biosensors using single trap phenomena'. *Nano Letters* (2014), vol. 14(6): pp. 3504–3509 (cit. on pp. 132, 135, 139).

418. Gasparyan, F. et al.: 'Single trap in liquid gated nanowire FETs: Capture time behavior as a function of current'. *Journal of Applied Physics* (2015), vol. 117(17), 174506: pp. – (cit. on pp. 132, 135).

419. Sharf, T. et al.: 'Single electron charge sensitivity of liquid-gated carbon nanotube transistors'. *Nano Letters* (2014), vol. 14(9): pp. 4925–4930 (cit. on p. 132).

420. Karnatak, P. et al.: 'Fermi-edge transmission resonance in graphene driven by a single coulomb impurity'. *Phys. Rev. Lett.* (2 2014), vol. 113: p. 026601 (cit. on p. 132).

421. Kaverzin, A. A.: 'Electronic transport and flicker noise in graphene structures'. PhD thesis. University of Exeter, 2011 (cit. on pp. 132, 133).

422. Magistretti, J. et al.: 'High conductance sustained single-channel activity responsible for the low-threshold persistent Na+ current in entorhinal cortex neurons'. *The Journal of neuroscience* (1999), vol. 19(17): pp. 7334–7341 (cit. on pp. 137, 138).

423. Yasaei, P. et al.: 'Chemical sensing with switchable transport channels in graphene grain boundaries'. *Nature communications* (2014), vol. 5 (cit. on pp. 138, 139, 142).

424. Ago, H. et al.: 'Epitaxial growth and electronic properties of large hexagonal graphene domains on Cu (111) thin film'. *Applied Physics Express* (2013), vol. 6(7): p. 075101 (cit. on p. 138).

425. Huang, P. Y. et al.: 'Grains and grain boundaries in single-layer graphene atomic patchwork quilts'. *Nature* (2011), vol. 469(7330): pp. 389–392 (cit. on p. 139).

426. Chorev, E. et al.: 'In vivo dual intra- and extracellular recordings suggest bidirectional coupling between CA1 pyramidal neurons'. *Journal of Neurophysiology* (2012), vol. 108(6): pp. 1584–1593 (cit. on p. 141).

427. Storm, J. F.: 'Action potential repolarization and a fast after-hyperpolarization in rat hippocampal pyramidal cells.' *The Journal of Physiology* (1987), vol. 385(1): pp. 733–759 (cit. on p. 141).

428. Erisir, A. et al.: 'Function of specific K+ channels in sustainehigh-frequency firing of fast-spiking neocortical interneurons'. *Journal of Neurophysiology* (1999), vol. 82(5): pp. 2476–2489 (cit. on p. 141).

429. Poolos, N. P. et al.: 'Calcium-activated potassium conductances contribute to action potential repolarization at the soma but not the dendrites of hippocampal CA1 pyramidal neurons'. *The Journal of Neuroscience* (1999), vol. 19(13): pp. 5205–5212 (cit. on p. 141).

430. Cheng, J. et al.: 'Flexible Solution-Gated Graphene Field Effect Transistor for Electrophysiological Recording'. *Microelectromechanical Systems, Journal of* (2014), vol. 23(6): pp. 1311–1317 (cit. on p. 142).

431. Park, D. et al.: 'Graphene-based carbon-layered electrode array technology for neural imaging and optogenetic applications'. *Nat Commun* (Oct. 2014), vol. 5: p. 5258 (cit. on p. 175).

432. Carabelli, V. et al.: 'Nanocrystalline diamond microelectrode arrays fabricated on sapphire technology for high-time resolution of quantal catecholamine secretion from chromaffin cells'. *Biosensors and Bioelectronics* (2010), vol. 26(1): pp. 92–98 (cit. on p. 175).

433. Qing, Q. et al.: 'Nanowire transistor arrays for mapping neural circuits in acute brain slices'. *Proceedings of the National Academy of Sciences* (2010), vol. 107(5): pp. 1882–1887 (cit. on p. 175).

434. Gao, Z. et al.: 'Transparent diamond microelectrodes for biochemical application'. *Diamond and Related Materials* (2010), vol. 19(7): pp. 1021–1026 (cit. on p. 175).

A All-diamond microelectrode arrays

A. 1 CVD diamond: growth parameters

1. Growth of intrinsic nanocrystalline diamond

1.1 Bias enhanced nucleation (BNE)
Pressure: 16 torr
Substrate temperature: 700°C
Plasma power: 1000W
H2/CH4: 285 sccm/15 sccm
Bias voltage: -260V to -300 V
Time: 20 min

1.2 Diamond deposition
Bias voltage: 0V
H2/CH4: 3 sccm/297 sccm
Pressure: 30 torr
Substrate temperature: 700°C
Plasma power: 1000W
Growth rate: 6-8 nm/min

2. Growth of boron-doped nanocrystalline diamond

Pressure: 33 torr
Substrate temperature: 870°C
Plasma power 260W
H2/CH4: 1.05 sccm/200 sccm
B/C: 0.58% (boron from B2H6)
Growth rate: 6-8 nm/min

A. 2 Embedded CNTs: growth parameters

Catalyst: 3 nm Pd
1. Catalytic etching:
Pressure: 60 torr H2 atmosphere
Substrate temperature: 950°C (filament temperature: 1950°C)
Etch time: 30min

2. Carburization:
Pressure: 60 torr
H2/CH4: 100 sccm/9 sccm,
Substrate temperature: 300°C (filament temperature: 1300°C)
time: 1h

3. CNT growth:
Pressure: 60 torr
H_2/CH_4: 100/9,
Substrate temperature: 800°C (filament temperature: 1800°C)

A. 3 All-diamond MEA: Fabrication recipe

1. Mesa:
Photoresist S1818 or S1805
Metal deposition: 100nm Ni
Lift-off: acetone
Etching: O_2 plasma
Stripping the etch mask: commercial Ni-etchant

2. Selective growth:
Photoresist: AZ5214
Sputter: 2µm SiO_2 and 200 nm Cr
Lift-off: acetone
Grow diamond as in A. 2, but without boron
Stripping the mask: commercial Cr etch and HF

3. Metallization:
Photoresist: S1818
Metal deposition: Ti-Pt-Au (30-40-30 nm)
Lift-off: acetone

B Silicon nanowire FETs: fabrication protocol

1. Metallic contacts

Substrate preparation: subsequent washings in acetone, isopropanol and DI water, followed drying with nitrogen gun and 5 min long baking at 200°C hot plate
Resists: spin first LOR3A and bake at 170°C for 1 min, then spin UV3 and bake at 130°C for 1 min
Exposure: has to be adjusted depending on the power
Development: MF-26
Shortly before metal deposition: 10s HF dip to remove the native oxide
Metal deposition: Ti - Pt - Au (17 nm - 30 nm - 30 nm)
Lift-off: acetone

2. E-Beam NW definition

Resist: PMMA 4%
Development: subsequent development in MIBK and isopropanol, followed by a rinse in DI water
Metal deposition: 70 nm Al
Lift-off: NMP 2h at 80°C, followed by a subsequent rinsing in acetone, isopropanol and DI water

3. Etching silicon nanowires

Etching in reactive ion plasma: SF_6 plasma for 35 s
Stripping the etch mask: 1-3 min in MF6, rinse in DI water

4. Contact annealing

4min at 400°C in Ar/H_2 atmosphere

5. Gate oxide deposition

Protect the contact pads with a photoresist and deposit 10 nm HfO_2 using ALD

6. Passivation of contact leads

Deposit 200 nm parylene-C on the entire chip surface
Etch parylene above the nanowires and contact pads using oxygen plasma and a photoresist mask (UV3) to protect parylene elsewhere

C Graphene FETs: fabrication flow

1. Etching transistor channel

1.1 Using photoresist mask on pristine graphene:
Transfer graphene using PMMA assisted wet transfer technique
remove PMMA in acetone (overnight) and anneal the sample at 300°C/$0.5{\cdot}10^{-7}$ mbar for 3h
Define photoresist mask to protect the future transistor channel: resist - S1818, developer - Microdeveloper:DI water (1:1))
Etch graphene in oxygen plasma
Remove S1818 in acetone

1.2 Using gold mask on pristine graphene
Transfer graphene using PMMA assisted wet transfer technique
remove PMMA in acetone (overnight) and anneal the sample at 300°C/$0.5{\cdot}10^{-7}$ mbar for 3h
Deposit 10 nm gold etch mask above the future transistor channel (resist: S1818, developer: Microdeveloper:DI water (1:1), evaporation: 10 nm Au, lift-off: acetone)
Etch graphene in oxygen plasma
Remove gold in KI solution (30-45 s), rinse the sample in acetone, isopropanol and DI water

1.3 Using photoresist mask on PMMA covered graphene
Transfer graphene using PMMA assisted wet transfer technique
Do not remove the PMMA
define photoresist mask to protect the future transistor channel: resist - S1818, developer - Microdeveloper:DI water (1:1))
Etch graphene (PMMA) in oxygen plasma
remove S1818/PMMA in acetone and and anneal the sample at 300°C/$0.5{\cdot}10^{-7}$ mbar for 3h

2. Metallic contacts

Substrate preparation: 5 min long baking at 180°C hot plate
Resists: spin S1805 and bake for 4 min at 115°C
Exposure: has to be adjusted depending on the power
Development: Microdeveloper:DI water (1:1)
Shortly before metal deposition: 10s HF dip to remove the native oxide
Metal deposition: Pd - Au (40 nm - 30 nm)
Lift-off: acetone

6. Passivation of contact leads

Isolate the metallic contact leads using SU8 with standard processing parameters

D General properties of used materials

Table summarizing the general properties of materials used in this work, revealing the outstanding potential of graphene for biomedical applications.

Table .1: Properties of materials used in this work for realization of versatile neural interfaces. $^{+}$ the material exhibits the required property, $^{(+)}$) technologically challenging or after certain modifications, ^{0} the requirement is not met, * this work.

Property	Diamond	*ref.*	Silicon	*ref.*	Graphene	*ref.*
Compatibility with MEA technology	+	[80]	(+)	[22]	+	[431]
Compatibility with FET technology	(+)	[156]	+	[95]	+	⋆
Integration on flexible polymers	(+)	[74]	(+)	[113]	+	⋆
Integration on transparent substrates	(+)	[432]	(+)	[433]	+	⋆
Intrinsic flexibility	(+)	[79]	0		+	⋆
Intrinsic transparency	(+)	[434]	0		+	⋆
Sub-cellular resolution	0		+	[111]	(+)	⋆
Biocompatibility	(+)	⋆ [379]	0	⋆	+	⋆
Impedance at 1 kHz (kΩ)	400	⋆	-			⋆
Mobility ($cm^2V^{-1}s^{-1}$)	120	[128]	250	⋆	5000	⋆
Capacitance ($\mu F/cm^2$)	2	[128]	0.35	[128]	2	[128]
Gate noise (µV)	-		30	[128]	10	[128]

Resumé

Abstract: In line with the technological progress of last decades a variety of adapted bioelectrical interfaces was developed to record electrical activity from the nervous system reaching from whole brain activity to single neuron signaling. Although neural interfaces have reached clinical utility and are commonly used in fundamental neuroscience, their performance is still limited. In this work we investigated alternative materials and techniques, which could improve the monitoring of neuronal activity of cultured networks, and the long-term performance of prospective neuroprosthetics. While silicon nanowire transistor arrays and diamond based microelectrodes are proposed for improving the spatial resolution and the electrode stability in biological environment respectively, the main focus of this thesis is set on the evaluation of graphene based field effect transistor arrays for bioelectronics. Due to its outstanding electrical, mechanical and chemical properties graphene appears as a promising candidate for the realization of chemically stable flexible electronics required for long-term neural interfacing. Here we demonstrate the outstanding neural affinity of pristine graphene and the realization of highly sensitive fast graphene transistors for neural interfaces.

Resumé: Dans la lignée des progrès technologiques récents en électronique, ces dernières décennies ont vu l'émergence d'une variété de systèmes permettant l'interface bioélectronique, allant de la mesure de l'activité électrique émise par l'ensemble du cerveau jusqu'à la mesure du signal émis par un neurone unique. Bien que des interfaces électroniques avec les neurones ont montré leur utilité pour des applications cliniques et sont communément utilisés par les neurosciences fondamentales, leurs performances sont encore très limitées, notamment en raison de l'incompatibilité relative entre les systèmes à l'état solide et le vivant. Dans ce travail de thèse, nous avons étudié des techniques et des matériaux nouveaux permettant une approche alternative et qui pourraient améliorer le suivi de l'activité de réseaux de neurones cultivés in situ et à terme la performance des neuroprothèses in vivo. Dans ce travail, des réseaux de nanofils de silicium et des microélectrodes en diamant sont élaborés pour respectivement améliorer la résolution spatiale et la stabilité des électrodes dans un environnement biologique. Un point important de cette thèse est également l'évaluation des performances de transistors à effet de champ en graphène pour la bio électronique. En raison des performances remarquables et combinées sur les aspects électrique, mécanique et chimique du graphène, ce matériau apparaît comme un candidat très prometteur pour la réalisation d'une électronique permettant une interface stable et sensible avec un réseau de neurones. Nous montrons dans ce travail l'affinité exceptionnelle des neurones avec une surface de graphène brut et la réalisation d'une électronique de détection rapide et sensible à base de transistor en graphène.